This is to certify that the

dissertation entitled

PULSED ELECTRON PARAMAGNETIC RESONANCE STUDIES OF THE HISTIDINE AND WATER LIGATION OF TYPE 1 AND TYPE 2 COPPER SITES IN FET3 PROTEIN, A MULTICOPPER OXIDASE FROM YEAST

presented by

Constantino Ponsaran Aznar, III

has been accepted towards fulfillment
of the requirements for

Ph.D. degree in Chemistry

John L McCracken
Major professor

Date 8/28/00

PULSED ELECTRON PARAMAGNETIC RESONANCE STUDIES OF THE HISTIDINE AND WATER LIGATION OF TYPE 1 AND TYPE 2 COPPER SITES IN FET3 PROTEIN, A MULTICOPPER OXIDASE FROM YEAST

By

Constantino Ponsaran Aznar, III

A DISSERTATION

Submitted to
Michigan State University
in partial fulfillment of the requirements
for the degree of

DOCTOR OF PHILOSOPHY

Department of Chemistry

2000

ABSTRACT

PULSED ELECTRON PARAMAGNETIC RESONANCE STUDIES OF THE HISTIDINE AND WATER LIGATION OF TYPE 1 AND TYPE 2 COPPER SITES IN FET3 PROTEIN, A MULTICOPPER OXIDASE FROM YEAST

By

Constantino Ponsaran Aznar, III

Electron spin echo envelope modulation (ESEEM) spectroscopy has been used to study two variants of Fet3p generated by site-directed mutagenesis. A homolog of ceruloplasmin, Fet3p is a multicopper oxidase from the yeast *Saccharomyces cerevisiae*. Like human ceruloplasmin (hCp), Fet3p catalyzes the reduction of molecular oxygen to water with ferrous ion as the reducing agent. This ferroxidase activity is essential to the physiologic role the two enzymes play in organismal iron homeostasis. The two mutant Fet3p studied were proteins in which either the type 1 or type 2 Cu(II)-binding sites had been depleted so that EPR/ESEEM studies could be accomplished without the complication of spectral overlap. ^{14}N ESEEM was used to determine possible histidine ligation to type 1 and type 2 Cu(II) sites. Computer simulations of three-pulse spectra taken at magnetic field positions corresponding to $g_{\|}$ and $g_{\perp}$ suggest that the type 2 Cu(II) shows one equatorially-bound histidine imidazole ligand contributing to the echo-envelope modulation. For the type 1 Cu(II), two magnetically distinct histidine imidazole ligands were found. Water ligation to these copper sites was also studied by the deuterium-exchange technique. The results suggest that both the type 1 and type 2 sites are readily accessible to water. However, water is an inner-sphere ligand to only the type

2 copper site with one axial and one equatorial D_2O. The ^2H modulation function of the type 1 copper site is due entirely to ambient deuterons with the nearest metal-to-deuteron distance being 3.7Å. Comparison of the data obtained in this work to the x-ray crystal structures of the multicopper enzyme homologs ascorbate oxidase, laccase and human ceruloplasmin was made.

To Mama and Papa

ACKNOWLEDGEMENTS

MARAMING SALAMAT! It is a Filipino way of expressing their gratitude. There are several people I need to thank for their contribution to the completion of this dissertation.

Thanks to Professor John McCracken, my advisor, for patiently guiding and supporting me throughout my five- (and more ?)year stay at MSU. He is not only a very good researcher, but an excellent lecturer as well. His lecture and talk during group and one-on-one meetings were very helpful and enlightening. Not to forget to mention were his amusing stories, mostly about his experiences.

Thanks to our collaborators, Richard Hassett; Daniel Yuan; and specially Prof. Daniel J. Kosman. Without the Fet3sample from Kosman's Lab, this dissertation would not be possible.

Thanks to the guys in the electronic shop for gladly providing me the electronic devices that I needed to finish up the pulse-generating boxes.

Thanks also to Vada O'Donell.

Thanks to the past and present group members of the McCracken Lab, specially Dr. V. Bouchev, Dr. V. Singh, Dr. E. Saari, Dr. R. Muthukumaran, and Dr. S. Smith. I thank Pearl (R. Muthukumaran) for his help in the collection of CW-EPR and ENDOR data.

Thanks to my Filipino and non-Filipino friends, students and non-students, here in East Lansing, specially to Aileen, Cecilia, Vivienne, Charisse (for the sotanghon and bilo-bilo, ☺), Beni, Chris, Ian and Oggie. Activities such as tennis, volleyball, get together for the purposes of eating and playing card games or charades, out of town and state trips, the ever exciting practices and performances for Michigan and Global Festival, etc. made my stay here less lonely, fun and exciting.

Thanks to my family - mama and papa, brothers and sisters, lolo and lola, aunts and uncles, for their love and prayers. I want to thank Auntie Eva and her family, they are the nearest family I have here in the US.

And To God, a very sincere MARAMING MARAMING SALAMAT!

TABLE OF CONTENTS

LIST OF TABLES

LIST OF FIGURES

INTRODUCTION

Multicopper oxidases (*e.g.* laccase, ceruloplasmin, ascorbate oxidase) are enzymes that couple four, one-electron oxidations of a substrate to the four-electron reduction of molecular oxygen to water. A recent addition to this group of enzymes is Fet3 (Fe = iron, t = transport) protein from the budding yeast *Saccharomyces cerevisiae.* Among the multicopper oxidases, only Fet3p and ceruloplasmin possess ferroxidase activity, that is, specificity towards Fe(II) as the substrate. This unique enzymatic activity underscores the specific role that these two multicopper oxidases play in the iron homeostasis of their respective organisms. Yeast is an excellent model for the study of metal homeostasis because the genetics of the organism is easily manipulated.

Two of the copper sites in Fet3 protein, in their divalent oxidation states, are paramagnetic and therefore, can be probed by the Electron paramagnetic resonance (EPR) techniques. This thesis will present the biological application of electron spin echo envelope modulation (ESEEM) with Fet3 protein the system studied. Chapter 1 describes spectroscopic techniques used in the study. The fundamentals of continuous wave (CW) and pulse-EPR will be discussed. In Chapter 2, the chemistry of copper; properties of multicopper oxidase; and the biochemistry of Fet3 protein will be introduced. Chapter 3 is a description of the pulsed-EPR instrument at Michigan State University. Recent changes and modifications on the instrument are discussed. The last two chapters give details on the experiment, results and analysis. Chapter 4 discusses the ^{14}N ESEEM studies of the histidine ligation to the type 1 and

type 2 copper sites in Fet3 protein. The coordination of these copper sites to water and their accessibility to water solvent, determined using ^{2}H-ESEEM technique, are the main the focus of Chapter 5. Chapter 5 also integrates the results obtained from the ^{14}N ESEEM and ^{2}H-ESEEM experiments to give the proposed structures of the type 1 and type 2 copper sites in Fet3 protein.

Chapter 1

INTRODUCTION TO CONTINUOUS WAVE- AND PULSE-ELECTRON PARAMAGNETIC RESONANCE

Magnetic resonance spectroscopy has proven to be an essential spectroscopic tool in the investigation of many biochemical and biological systems. Electron paramagnetic resonance (EPR) spectroscopy, for example, has found wide range of application in the studies of photosynthesis, bioenergetics, membranes and electron transport.

EPR Spectroscopy was experimentally observed in 1945 by a Russian scientist, Zavoisky.[1] Gradually, it developed to be a powerful tool for studying atoms, ions and molecules that have unpaired electrons. Systems with unpaired spin are said to be paramagnetic. The paramagnetism could be inherent to the system or could be produced by irradiation or other physical or chemical treatment of nonmagnetic substances. Paramagnetism implies a nonzero angular momentum and therefore the existence of magnetic dipole moment. EPR deals with the interaction of this magnetic moment with an external magnetic field. The interaction is termed the electronic Zeeman Interaction and is probed by applying an oscillating microwave magnetic field perpendicular to the applied external magnetic field.

The first objective of this chapter is to present a brief description of the phenomenon of EPR. Magnetic interactions , other than the Zeeman interaction, that contribute to the spectra will be discussed.[2-8] The second goal is to describe the pulse version of EPR, in particular, Electron Spin Echo Envelope Modulation (ESEEM).[9-16] ESEEM is an EPR technique used to resolve hyperfine interactions

that are masked in the continuous wave-EPR (CW-EPR) spectrum. Combination of the CW-EPR, and ESEEM can provide a better picture of the geometric and electronic structure of paramagnetic substance.

1.1 Interaction of Free Electron with a Magnetic Field

Classically, the energy as a result of the interaction of the magnetic moment, vector, μ, and applied magnetic field vector, **B**, is mathematically described as

$$E = -\mu \bullet \mathbf{B} \qquad (1.1a)$$

or equivalently,

$$E = -\mu B \cos\theta, \qquad (1.1b)$$

where θ is the angle between the magnetic moment and direction of the magnetic field (Figure 1.1). For macroscopic magnetic moment, the energy is a continuum as θ can assume any value from 0 to 2π.

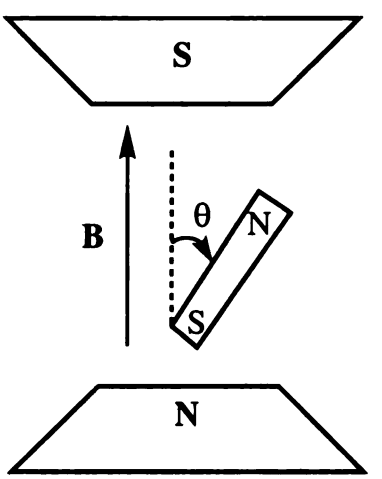

Figure 1.1. Dependence of the energy of interaction of a classical magnetic dipole and external magnetic field on θ. θ is the angle between the axis of the magnetic dipole and the direction of the applied field.

Equation 1.1-1 has a quantum-mechanical counterpart, or operator, for the microscopic system of the electron. The magnetic moment of an electron is expressed as an operator in equation (1.2).

$$\hat{\mu} = -g_e \beta \hat{\mathbf{S}} \tag{1.2}$$

$\hat{\mathbf{S}}$ is the operator for the electron's intrinsic angular momentum, while g_e is the electron g-value (2.0023) and β is the Bohr magneton and is equal to $eh/2m_ec = 9.27401 * 10^{-24}$ J T^{-1}. Using the value of μ, we can write the quantum-mechanical counterpart of equation (1.1-1a) as

$$\mathcal{H} = g_e \beta \hat{\mathbf{S}} \bullet \mathbf{B} \tag{1.3}$$

If the z-direction is chosen to be the direction of the magnetic field ($\mathbf{B}=B_z\mathbf{k}=B_o\mathbf{k}$, $B_x=B_y=0$), then equation (1.3) reduces to

$$\mathcal{H} = g_e \beta \hat{\mathbf{S}}_z \bullet \mathbf{B}_o \tag{1.4}$$

Borrowing from the results of the rigid rotor model problem for describing the quantum mechanics of angular momentum:

$$\hat{\mathbf{S}}|Sm_s\rangle = \sqrt{S(S+1)}\hbar^2|Sm_s\rangle$$

$$\hat{S}_z|Sm_s\rangle = m_s\hbar \quad \text{where } m_s = -S, -S+1, \ldots +S$$

$$\text{and } \langle S_x\rangle = \langle S_y\rangle = 0,$$

where $\hat{\mathbf{S}}$ is the total angular momentum operator and m_s represents the z-component of the angular momentum. Experimentally, it is known that a single unpaired electron spin gives rise to two Zeeman energy states. Following the results of the rigid rotor problem, S=1/2 so that the unpaired spin can exist as two energy states described by $m_s = \pm 1/2$. These two energy states are typically labelled $|\alpha\rangle =$

$|1/2,1/2\rangle$ and $|\beta\rangle = |1/2,-1/2\rangle$. Operating with the Hamiltonian operator of equation (1.4) on the $|\alpha\rangle$ and $|\beta\rangle$ states yields

$$E_\alpha = \frac{1}{2}\beta g_e B_o \tag{1.5a}$$

and $$E_\beta = -\frac{1}{2}\beta g_e B_o \tag{1.5b}$$

1.2 A Simple CW-Experiment

Figure 1.2 shows the diagram describing the splitting of the two degenerate electron spin states in the presence of an external magnetic field. The low-energy spin state corresponds to the states with spin projection $m_s = -1/2$ and the high-energy spin states corresponds to spin projection $m_s=1/2$. The population of the spin states follows Boltzmann distribution so that the relative population of $|\alpha\rangle$ to $|\beta\rangle$ state is

$$\frac{n_\alpha}{n_\beta} = \exp[-\Delta E/kT] \tag{1.6}$$

where $n_{s'}$ is the population of the state, k the Boltzmann constant, T the absolute temperature and ΔE (equal to $g_e\beta B_o$) the energy difference between the two states. It is essential that the ratio should be less than one ($n_\beta > n_\alpha$) for a net absorption of the microwave field energy to occur. Decreasing the temperature is one way of increasing the population difference.

In a typical EPR experiment, the energy difference is the measurable property. It corresponds to the energy required to the change the orientation of the electron's magnetic moment. In general the energy difference is probed by irradiating the paramagnetic species with a fixed microwave frequency with magnetic field strength, B_1, while the varying the external magnetic field, B_o, to yield an absorption

CW-EPR signal as shown in Figure 1.2. For a transition to occur, B_1 should be directed perpendicular to the B_o field, following the selection rule, $\Delta m_s = \pm 1$ and $\Delta m_I = 0$. Depending on the detection system used in the instrument, a first-derivative EPR signal can also be recorded. Resonance is achieved when the energy of the radiation matches the energy difference between the two states,

$$h\nu = g_e \beta B_o \text{ or} \qquad [1.7a]$$

$$\omega_o = g_e \beta B_o / \hbar . \qquad [1.7b]$$

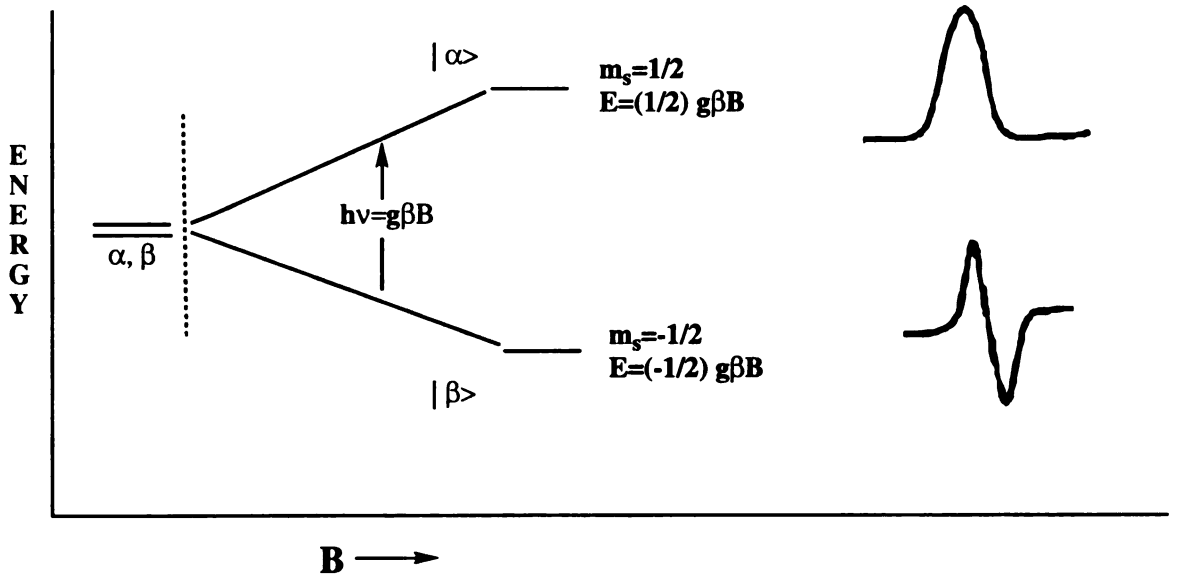

Figure 1.2. A typical CW-EPR experiment. A variable external magnetic field splits the degeneracy of α and β electron spin states, while a fixed microwave radiation induces transition between the two states to trace an absorption or first derivative EPR spectrum.

Classically, ω_o, the electron Larmor frequency, corresponds to the precession of the magnetic moment of the electron about the external magnetic field. In quantum mechanics, it corresponds to the frequency required to flip spin states of the electron from $m_s = -1/2$ to $m_s = 1/2$.

1.3 Spin Hamiltonian

The Hamiltonian operator that describes the energy of an atom or radical with unpaired electron spin in the presence of nuclei that also have magnetic moments consists of several energy terms,[6,7]

$$\mathcal{H} = \mathcal{H}_{el} + \mathcal{H}_{CF} + \mathcal{H}_{LS} + \mathcal{H}_{SS} + \mathcal{H}_{Ze} + \mathcal{H}_{HF} + \mathcal{H}_{Zn} + \mathcal{H}_{II} + \mathcal{H}_{Q}, \quad \text{where}$$

$\mathcal{H}_{el}$ = electronic Hamiltonian operator consisting of the sum of the kinetic energy of each electron and the potential energy of the electron relative to the nuclei and the coulombic interaction (10^4-10^5 cm^{-1}),

$\mathcal{H}_{CF}$ = Hamiltonian describing the interaction of the electron orbital with the electric fields of the crystal or the chemical bond of the molecules (10^3-10^4 cm^{-1}),

$\mathcal{H}_{LS}$ = spin-orbit interaction Hamiltonian , $\lambda \mathbf{L} \bullet \mathbf{S}$ (10^2 cm^{-1}),

$\mathcal{H}_{SS}$ = electron spin-spin interaction (0-10 cm^{-1}),

$\mathcal{H}_{Ze}$ = electron Zeeman interaction operator (0-10cm^{-1}),

$\mathcal{H}_{HF}$ =hyperfine interaction operator describing the coupling of electron-nuclear spin (0-$10^2 cm^{-1}$),

$\mathcal{H}_{Zn}$ = nuclear Zeeman (0-10^{-3} cm^{-1}),

$\mathcal{H}_{II}$ = nuclear spin-spin interaction,

$\mathcal{H}_{Q}$ = nuclear quadrupolar interaction Hamiltonian (0-$10^{-2} cm^{-1}$).

$\mathcal{H}_{el}$ and $\mathcal{H}_{CF}$ operate only on the spatial term of the total electronic wavefunctions . Both, plus the $\mathcal{H}_{LS}$, are often much greater than magnetic interactions that give rise to an EPR signal so that their specific forms need not be known. The relevant terms that contribute to the spin Hamiltonian, therefore, are

$$\mathcal{H}= \mathcal{H}_{Ze} + \mathcal{H}_{SS} + \mathcal{H}_{HF} + \mathcal{H}_{Zn} + \mathcal{H}_{Q} + \mathcal{H}_{II}.$$

The effect of spin-orbit coupling on the g-value is included in the effective electron Zeeman , $\mathcal{H}_{Ze}$. For the copper system studied in this work, however, the energy operators that give rise to the observed EPR are

$$\mathcal{H}= \mathcal{H}_{Ze} + \mathcal{H}_{HF} + \mathcal{H}_{Zn} + \mathcal{H}_{Q} . \qquad (1.8)$$

These four Hamiltonian operators will be discussed in the succeeding sections.

1.3.1 Electron Zeeman Interaction

The resonance condition, equation (1.7) was derived for the case of an electron coupled to an external magnetic field. In addition to its intrinsic spin angular momentum, the electron in an atom has orbital angular momentum, **L**. This orbital angular momentum couples with **S** to yield a resultant angular momentum **J**. For light elements such as Cu^{+2} and other transition metals, the coupling of **L** and **S** is adequately described by the Russell-Saunders coupling scheme,[3]

$$\mathbf{J}= \mathbf{L} + \mathbf{S} .$$

The vectorial addition of the two angular momenta (Figure 1.3) results in an effective magnetic moment vector which can be derived to be equal to

$$\mu= -g_J b\mathbf{J},$$

where $g_J = \frac{3J(J+1) + S(S+1) - L(L+1)}{2J(J+1)}$ assuming $g_e = 2.0$. Hence, an appropriate electron Zeeman Hamiltonian would be ,

$$\mathcal{H}_{Ze} = g_J \beta \mathbf{J} \cdot \mathbf{B} \tag{1.9}$$

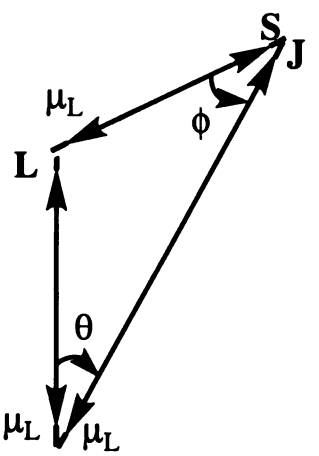

Figure 1.3. Schematic diagram for the vector addition of electron spin angular momentum, S and orbital angular momentum, L to yield an effective angular momentum J.

and the corresponding resonant condition would be

$$\Delta E = h\nu = g_J \beta B_o. \tag{1.10}$$

The g-factor, g_J, is characteristic of the sample and should be experimentally determined.

When atoms are part of the molecular framework, the degeneracy of the orbitals are lifted and orbital angular momentum becomes zero. We say then, that the orbital angular momentum is "quenched" and therefore expect that the g-factor will

be equal to the electron g-value. However, spin-orbit coupling restores some orbital angular momentum by admixing orbitals.

Another way of writing the equation is $\mathcal{H}_{Ze} = (\beta\hat{\mathbf{L}} + g_e\hat{\mathbf{S}}) \bullet \mathbf{B}$. A more succinct form of the equation is

$$\mathcal{H}_{Ze} = \beta\hat{\mathbf{S}} \bullet \underline{\mathbf{g}} \bullet \mathbf{B} \tag{1.21}$$

In the equation, **S** is the effective spin and **g** is a 3×3 tensor that takes into account the dependence of effective moment μ_j on the orientation of external magnetic field. The elements of the symmetric g-tensor,

$$\underline{\mathbf{g}} = \begin{bmatrix} g_{xx} & g_{xy} & g_{xz} \\ g_{xy} & g_{yy} & g_{yz} \\ g_{xz} & g_{yz} & g_{zz} \end{bmatrix}$$

can be derived to be equal to[3]

$$g_{\alpha\beta} = g_e\delta_{\alpha\beta} + 2\lambda\sum_{n''}\frac{\langle n|L_\alpha|n''\rangle\langle n''|L_\beta|n\rangle}{E_n - E_{n''}}. \tag{1.22}$$

In a coordinate system that diagonalizes g, the electron Zeeman becomes

$$\mathcal{H}_{Ze} = \beta\begin{bmatrix}\hat{S}_x & \hat{S}_y & \hat{S}_z\end{bmatrix} \bullet \begin{bmatrix} g_{xx} & 0 & 0 \\ 0 & g_{yy} & 0 \\ 0 & 0 & g_{zz} \end{bmatrix} \bullet \begin{bmatrix} h_1B_o \\ h_2B_o \\ h_3B_o \end{bmatrix}, \tag{1.23}$$

where the $h_{i's}$ are the direction cosines in polar coordinate so that the electron Zeeman Hamiltonian becomes,

$$\mathcal{H}_{Ze} = \beta B_o\left[(g_{xx}\sin\theta\cos\phi)\hat{S}_x + (g_{yy}\sin\theta\sin\phi)\hat{S}_y + (g_{zz}\cos\theta)\hat{S}_z\right] \tag{1.24}$$

In an axial g-tensor, meaning $g_{xx} = g_{yy} = g_\perp$ and $g_{zz} = g_\parallel$, the electron Zeeman Hamiltonian reduces to

$$\mathcal{H}_{Ze} = \beta B_o\left[g_\perp\sin\theta(\cos\phi\hat{S}_x + \sin\phi\hat{S}_y) + (g_\parallel\cos\theta)\hat{S}_z\right]. \tag{1.25}$$

The corresponding energy eigenvalue for the above Hamiltonian is

$$E_{Ze} = \beta\, m_s\, (g_\perp^2 \sin^2\theta + (g_\parallel^2 \cos^2\theta)^{1/2}\, B_o = \beta\, m_s\, g\, B_o \qquad (1.26)$$

$$g = (g_\perp^2 \sin^2\theta + g_\parallel^2 \cos^2\theta)^{1/2}.$$

The energy equation assumes the form that we are more familiar with where g_e is replaced by the effective g-factor. Clearly, equation (1.26) implies (2S + 1) energy levels that equally space even in the presence of an anisotropic g.

Anisotropy in g is lost in a system in which molecules tumble and rotate rapidly, so that an average g-value equal to the average of the trace of the g-tensor is observed. This averaging will allow us to simplify the electron Zeeman Hamiltonian,

$$\mathcal{H}_{Ze} = g_{iso}\beta\hat{\mathbf{S}} \bullet \mathbf{B}$$

$$\mathcal{H}_{Ze} = g_{iso}\beta\begin{pmatrix}\hat{S}_x & \hat{S}_y & \hat{S}_z\end{pmatrix}\begin{pmatrix}h_1B_o \\ h_2B_o \\ h_3B_o\end{pmatrix} \qquad (1.27a)$$

or simply , in the case of the external applied in the z-direction,

$$\mathcal{H}_{Ze} = g_{iso}\beta\hat{S}_z(h_3B_o) = g_{iso}\beta\hat{S}_zB_z \qquad (1.27b)$$

1.3.2 Nuclear Zeeman Interaction

Several nuclei have nuclear spin and an associated magnetic moment, μ_N. Similar to the electron, the nuclear magnetic moment of the magnetic nucleus is proportional to its nuclear spin angular momentum,

$$\mu_N = g_N\beta_N\mathbf{I}_N, \qquad (1.29)$$

where g_N is the nuclear g-factor which is usually assumed to be isotropic and whose magnitude depends on the identity of the nucleus, β_N ($5.05078 * 10^{-27}$ JT^{-1}) is the

nuclear magneton which is 1838 times smaller than the electron Bohr magneton and, $\mathbf{I}_N$, is the spin angular momentum for the nucleus which can assume an integral or half-integral value. The absence of the negative sign in the right hand of the equation implies that the nuclear magnetic moments and nuclear spin are parallel, although that is not always the case. The magnitude of β_N relative to β is very small because of the large rest mass of the proton with respect to the electron. Consequently, the electron Zeeman is about 10^3 stronger than the nuclear Zeeman.

The Hamiltonian for describing the nuclear Zeeman is given by,

$$\mathcal{H}_{ZN} = -g_N\beta_N\hat{\mathbf{I}}_N \bullet \mathbf{B}. \tag{1.30}$$

This Hamiltonian adds to the electron Zeeman to yield the total spin Hamiltonian,

$$\mathcal{H}_T = g\beta\hat{\mathbf{S}} \bullet \mathbf{B} - g_N\beta_N\hat{\mathbf{I}}_N \bullet \mathbf{B}. \tag{1.31}$$

The above equation tell us that α and β electron spin states are split according to the projection of I, m_I, in space.

1.3.3 Hyperfine interaction

The nuclear magnetic moment creates a local magnetic field (B_{local}) which may couple to the moment of the unpaired electron spin to enhance or oppose the external magnetic field (B_{ext}) yielding an effective magnetic field (B_{eff}). The resonance condition is still valid if B is replaced by B_{eff}. Because there exists a 2I+1 multiplicity nuclear spin states for a nucleus with spin I, there would be 2I+1 different values of the resonance field strength..

The interaction of the electron spin and nuclear spin magnetic moments is termed the hyperfine interaction. It is responsible for the additional (2I+1) splittings

that we observed in the CW-EPR spectrum. The energy of the hyperfine interaction is defined by the Hamiltonian,

$$\mathcal{H} = \hat{\mathbf{S}} \bullet \underline{\mathbf{A}} \bullet \mathbf{B} \quad \text{or} \tag{1.32a}$$

$$H = \begin{bmatrix} \hat{S}_x & \hat{S}_y & \hat{S}_z \end{bmatrix} \bullet \begin{bmatrix} A_{xx} & A_{xy} & A_{xz} \\ A_{xy} & A_{yy} & A_{yz} \\ A_{xz} & A_{yz} & A_{zz} \end{bmatrix} \bullet \begin{bmatrix} \hat{I}_x \\ \hat{I}_y \\ \hat{I}_z \end{bmatrix}, \tag{1.32b}$$

where **S** and **I** are the electron and nuclear spin operators and the **A** the hyperfine tensor. **A**, a 3× 3 matrix, is a sum of the anisotropic interaction and the Fermi contact interaction,

$$\mathbf{A} = \mathbf{T} + A_{iso}\,\mathbf{1}. \tag{1.33}$$

A_{iso} , a scalar quantity, is the isotropic hyperfine coupling and is proportional to the probability of finding an electron in a nucleus,

$$A_{iso} = \frac{8\pi}{3} g\beta g_N \beta_N |\psi(0)|^2 \tag{1.34}$$

It vanishes for orbitals with $l > 0$ because $|\psi(0)|^2$ is zero. The anisotropic part of the hyperfine interaction is most simply modelled according to the classical interaction of two point dipoles. The energy of interaction of two point dipoles is described classically as

$$E_{dipolar} = -\left\{ \frac{3(\mu_e \bullet \mathbf{r})(\mu_N \bullet \mathbf{r})}{r^5} - \frac{(\mu_e \bullet \mu_N)}{r^3} \right\} \tag{1.35}$$

In the above equation, **r** represents the vector joining the unpaired electron and nucleus. Vectors μ_e and μ_n are the classical electron and nuclear magnetic moments. For a quantum mechanical system, the magnetic moments in equation (1.35) must be

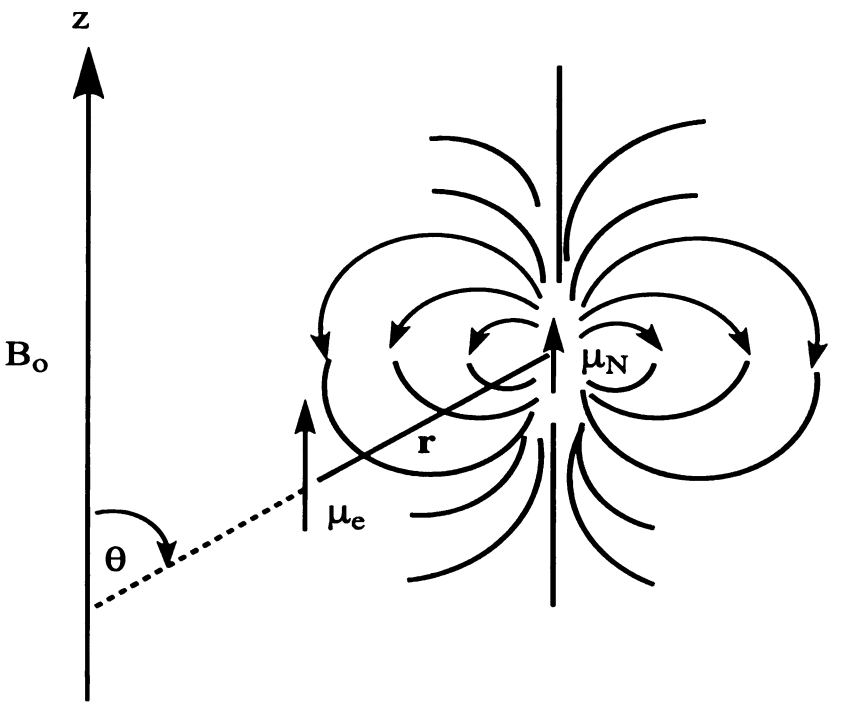

Figure 1.4. Dipolar interaction between the electron magnetic moment, μ_e and nearby nuclear magnetic moment, μ_N. The pictorial description assumes that μ_e and μ_N are aligned along the direction of the magnetic field. The vector r represents the separation between the two dipoles and θ is the angle between r and the direction of the magnetic field. The dipole-dipole energy can be approximated to be $E_{dip} = \left[(1-3\cos^2\theta)/r^3\right]\mu_{Nz}\mu_{ez} = B_{local}\mu_{ez}$. Depending on the value of θ, the B_{local} may enhance or oppose the applied external magnetic field.

replaced by their corresponding spin operators to give,

$$\mathcal{H}_{\text{dipolar}} = g_N\beta_N g_e\beta\left\{\frac{3(\hat{\mathbf{S}}\bullet\mathbf{r})(\hat{\mathbf{I}}\bullet\mathbf{r})}{r^5} - \frac{(\hat{\mathbf{S}}\bullet\hat{\mathbf{I}})}{r^3}\right\}. \tag{1.36}$$

Equation (1.36) can be expanded in Cartesian coordinates to yield,

$$\mathcal{H} = g_N\beta_N g_e\beta\left\{\begin{array}{l}\dfrac{3x^2-r^2}{r^5}\hat{S}_x\hat{I}_x + \dfrac{3y^2-r^2}{r^5}\hat{S}_y\hat{I}_y + \dfrac{3z^2-r^2}{r^5}\hat{S}_z\hat{I}_z \\ +\dfrac{3xy}{r^5}\left(\hat{S}_y\hat{I}_x+\hat{S}_x\hat{I}_y\right)+\dfrac{3yz}{r^5}\left(\hat{S}_z\hat{I}_y+\hat{S}_y\hat{I}_z\right)+\dfrac{3xz}{r^5}\left(\hat{S}_z\hat{I}_x+\hat{S}_x\hat{I}_z\right)\end{array}\right\}. \tag{1.37}$$

Integrating the Hamiltonian over the spatial variable yields a compact Hamiltonian that depends only on spin operators,

$$\mathcal{H}_{HF} = \hat{\mathbf{S}}\bullet\underline{\mathbf{T}}\bullet\hat{\mathbf{I}}. \tag{1.38}$$

T is a traceless tensor whose diagonal elements are given by,

$$T_{ii} = g_N\beta_N g_e\beta\left\langle\frac{3i^2-r^2}{r^5}\right\rangle, \quad i= x,y,z \tag{1.39}$$

and the off-diagonal elements are given by

$$T_{ij} = g_N\beta_N g_e\beta\left\langle\frac{3_{ij}}{r^5}\right\rangle. \tag{1.40}$$

In liquid phase, the molecules are in constant motion. If the rate of rotation and tumbling of the paramagnets is larger than the microwave frequency, the anisotropic hyperfine averages out leaving only the Fermi contact, A_{iso},

$$A_{iso} = (A_{xx} + A_{yy} + A_{zz})/3\ , \tag{1.41}$$

as consequence of **T** being traceless. Figure 1.5 depicts the splitting of energy levels that will be observed for an S=1/2, I=1/2 system characterized by isotropic hyperfine interaction. Shown also is the expected CW-EPR spectrum.

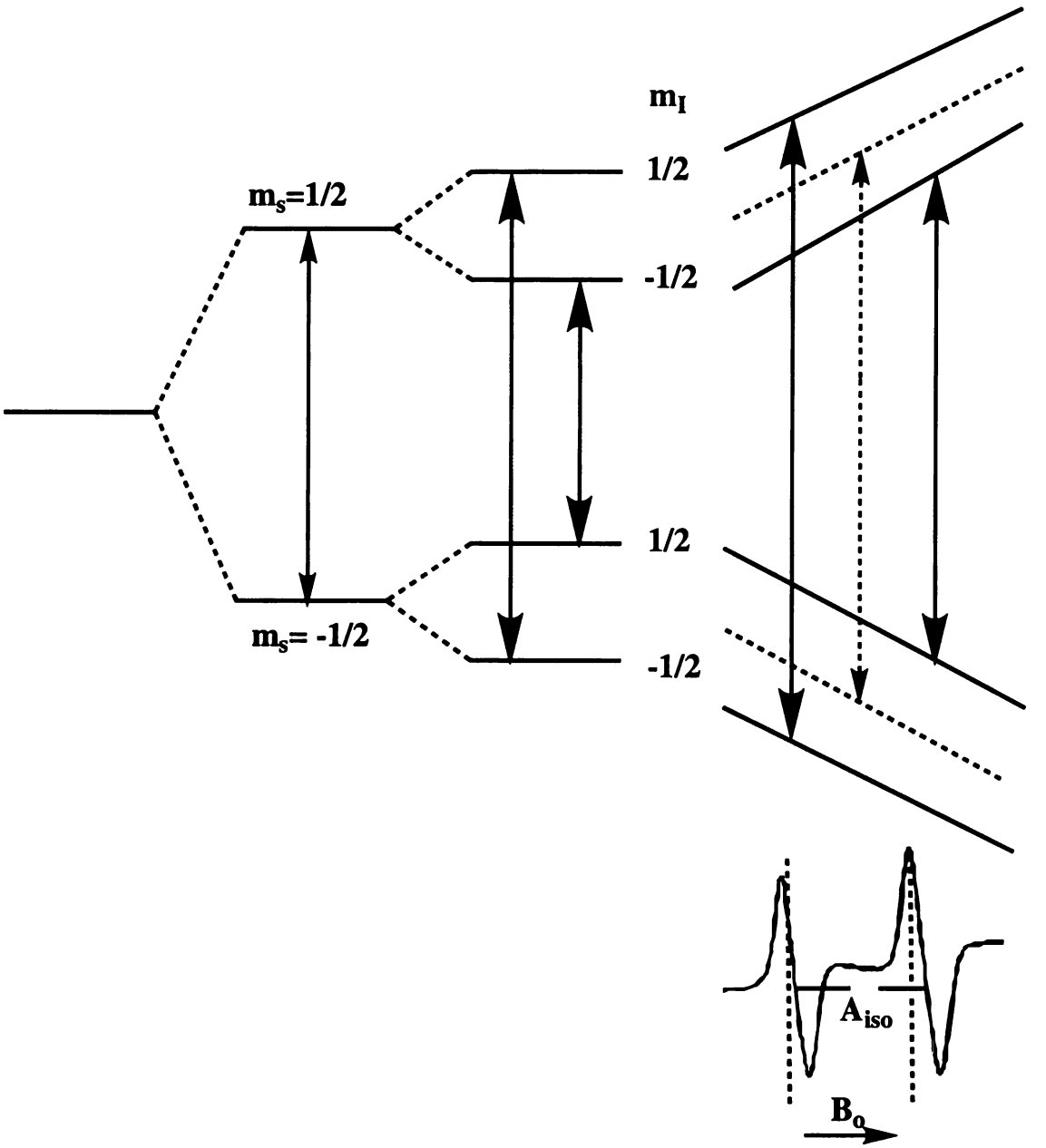

Figure 1.5. Isotropic hyperfine interaction. Energy diagram showing splitting of energy states for the case of S=1/2, I=1/2 system. The splitting due to nuclear Zeeman interaction is not shown.

1.3.4 Nuclear Quadrupole Interaction (NQI)

Nuclei with spin $I \geq 1/2$ have a quadrupolar moment, eQ, that is collinear with the nuclear magnetic moment. Quadrupolar nuclei may have either oblate or prolate charge distributions (Figure 1.6) compared to nuclei with I = 1/2 which have a spherical charge distribution. The magnitude of eQ is a measure of the deviation from a spherical charge distribution in the nucleus. Mathematically, eQ is [3]

$$eQ = 2\pi \int_0^{\infty} \int_0^{\pi} \rho_N(r,\theta)\left(3\cos^2\theta - 1\right) r^4 dr \sin\theta d\theta \,, \tag{1.42}$$

where the dependence of r on ϕ is removed and ρ_N is the charge distribution function of nuclear charge.

Nuclear quadrupole interaction is the interaction of the quadrupolar moment with electric field gradients at the nucleus. These electric field gradients arise from the non-uniform electronic charge distribution caused by the atoms in the vicinity of

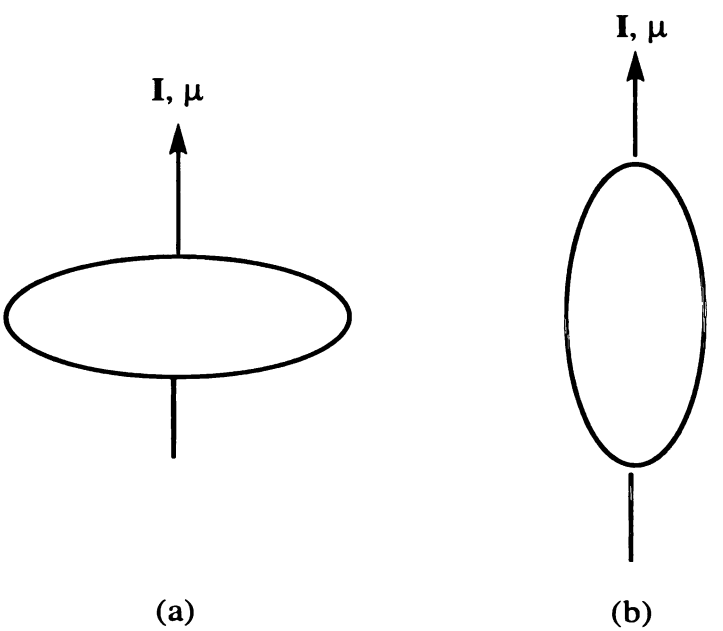

Figure 1.6 Nuclei with quadruple moment, (a) oblate and (b) prolate.

the nucleus. The magnitude and orientation of these gradients are determined by the electronegativity and the geometry of the atoms surrounding the nucleus.

Since the axis of the of the quadrupole moment and the nuclear dipolar moment are coincident, we can describe the nuclear quadrupolar interaction as the nuclear spin self-coupling,

$$\mathcal{H} = \begin{pmatrix} \hat{I}_x & \hat{I}_y & \hat{I}_z \end{pmatrix} \begin{pmatrix} Q_{xx} & Q_{xy} & Q_{xz} \\ Q_{xy} & Q_{yy} & Q_{yz} \\ Q_{xz} & Q_{yz} & Q_{zz} \end{pmatrix} \begin{pmatrix} \hat{I}_x \\ \hat{I}_y \\ \hat{I}_z \end{pmatrix} \tag{1.43}$$

where Q is the traceless quadrupole tensor that describes the anisotropy of the quadrupole interaction. In the coordinate system that diagonalizes the Q-tensor, the principal values of the tensor are given by

$$\begin{aligned} Q_{xx} &= -\frac{1}{2}A(1-\eta) \\ Q_{yy} &= -\frac{1}{2}A(1+\eta) \\ Q_{zz} &= A, \end{aligned} \tag{1.44}$$

where $A = \frac{e^2qQ}{2I(2I-1)}$, and $\eta = \frac{Q_{xx} - Q_{yy}}{Q_{zz}}$. NQI will be discussed further in chapter 4 where ^{14}N coupling with the electron spin is considered.

1.4 ESEEM

Knowledge of the hyperfine and NQI tensors would give us information about electronic and geometric environment of our paramagnetic system. These magnetic parameters are often difficult to extract from the CW-EPR. Biological samples are usually prepared as frozen solutions so that the CW-EPR spectra are

broad, powder-like spectra. These spectra are comprised of EPR spectra of individual single crystal-like paramagnetic species whose molecular axes are randomly oriented with respect to the direction of the external magnetic field. Consequently, the hyperfine and NQI tensors are obscured because they contribute to the broadening of the spectra. To circumvent the poor resolution of the hyperfine tensors, one may resort to studying single-crystal samples . However, preparation of single crystals of biological samples is a difficult task. A more reasonable solution is to make use of the sensitivity of the Electron Spin Echo Envelope Modulation (ESEEM) technique in measuring weak hyperfine couplings.

ESEEM is pulsed- EPR method that requires the application of a sequence of intense microwave pulses to induce a paramagnetic signal in the form of a spin echo. The intensity of the spin echo is measured as function of time separating two microwave pulses. Spin echoes monotonically decay with time. In addition, they are modulated by neighboring magnetic nuclei. An envelope of modulated echoes contains information about the electron-nuclear interaction as well the nuclear quadrupole interaction. The two most commonly used pulse schemes in ESEEM are the two- and three-pulse sequence. The physics and mathematics of spin echo formation will be discussed in the next sections.

1.4.1 Effects of Microwave Pulses

The formation of spin echo is based on the concept of an inhomogeneously broadened EPR spectrum as shown in Figure 1.7.[10] The EPR spectrum centered at B_o has a full width half maximum (FWHM) of ΔB. It is an envelope of many

homogeneously broadened lines of width ΔB_i and center B_i. These individual lines are known as spin packets. A spin packet represents electron spins that experience the same average effective magnetic field.

The effect of microwave (mw) pulses of duration t_p is to burn a "hole" in the inhomogeneously broadened EPR resonance line (Figure 1.6b).[10] A typical EPR spectrum covers a frequency range of several megahertz (10-10^2 MHz for radicals and 10^3 MHz for metals) so that even the shortest microwave pulse (10ns) that can be generated cannot cover the entire EPR spectrum. In contrast, NMR spectrum spans only a few kilohertz so that radiofrequency (RF) pulses can adequately excite almost all the nuclear spins in the sample to the same extent. Narrowing the microwave pulses can widen the burnt hole as the narrower the pulse, the wider the frequency distribution ($1/t_p \cong \Delta\omega$). However, a narrow microwave pulse needed to excite the entire EPR spectrum may result in low intensity of the microwave field so that electrons are weakly excited. Thus, unless the height of the pulse is simultaneously increased, the depth of the hole becomes shallower and consequently signals are too weak to be observed. This can be viewed better by considering the mw pulse as a oscillating magnetic field that torques the magnetic moment of the electrons in the paramagnetic sample by an angle $\omega_1 t_p$ where ω_1 is the frequency of oscillation about the microwave B_1 field and t_p is the width of the microwave pulse.[3,10] In this view the purpose of the microwave pulses is to provide a magnetic field B_1 oscillating in resonance with as many of the spin packets as possible. If B_1 is very weak and t_p is

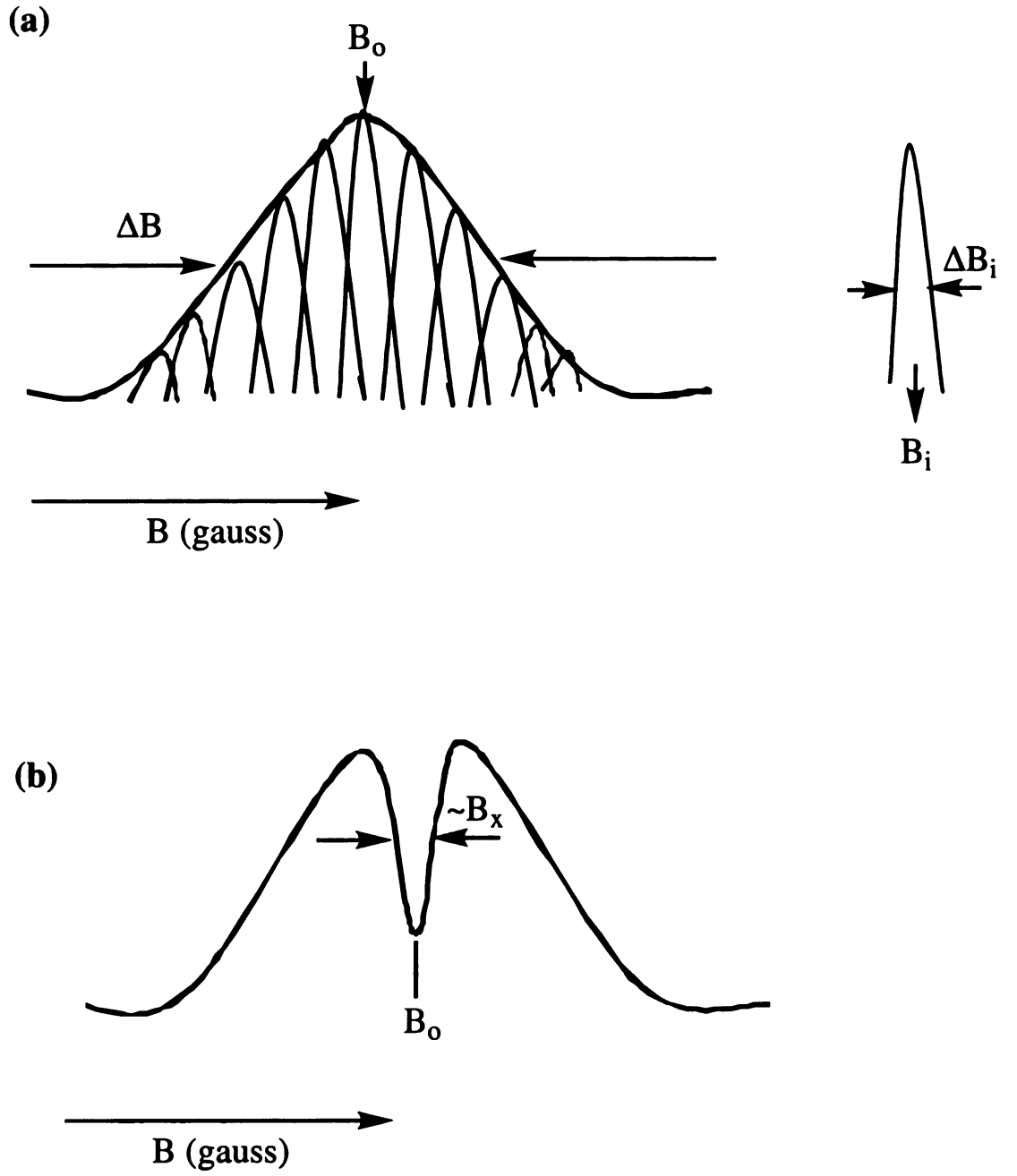

Figure 1.7. (a) An inhomogeneously broadened EPR spectrum comprising of several homogenous spin packets with linewidth ΔB_i. (b) "Burning of a hole" of some width in the a inhomogeneously broadened EPR spectrum as a result of applying a microwave pulse of some duration.

long, only a very few spin packets will be affected by the microwaves. A large B_1 field with short t_p, however, can excite spin packets over a broad range of resonance frequencies about the microwave frequency (30-50 MHz bandwidths are common). Therefore, the microwave pulse, of frequency ω_o, can be completely described as an envelope of a time(t)-varying field of intensity $B_1\cos(\omega_o t)$, where $\omega_o = g_e\beta B_o$ and can burn a hole of some width in the EPR spectrum.

1.4.2 Formation of an Echo in Two-pulse (The Hahn's Echo)

In 1950, Erwin Hahn discovered the first nuclear spin echo using the $\pi/2$-τ-π RF pulse sequence.[17] The first electron spin echo (ESE) was observed by R. Blume in 1958 in his studies of electron-spin relaxation time of sodium-ammonia solution.[18] In the experiment, he used the Carr-Purcell π-τ-$\pi/2$ pulse sequence.

Any sequence of two microwave pulses can give rise to an echo, but the maximum echo intensity occurs in a $\pi/2$-τ-π pulse sequence. The formation of a 2-pulse electron spin echo can be described pictorially using the vector model (Figure 1.8) and quantitatively by the Bloch equation. In this description, a rotating coordinate system (X,Y,Z) is chosen. The coordinate system rotates at angular frequency equal to the frequency of the microwave pulse whose magnetic field, B_1, is directed in the X-direction and is perpendicular to the external magnetic field, B_o ($B_o \| Z$). Prior to the application of the first $\pi/2$ pulse, the spin packets assume an equilibrium value, the bulk magnetization M_o, in the presence of the external magnetic field. M_o is the sum of the magnetization of the homogeneous spin packets.

The time-dependent evolution of M_o upon the application of the microwave can be evaluated using the Bloch equation,

$$\frac{dM_o}{dt} = \gamma B_{eff} \times M, \tag{1.45}$$

where B_{eff} is the effective field ($B_{ext} + B_1$) in the rotating frame. Solution to this equation can be viewed as the precession of the bulk magnetization about B_{eff}. At resonance (i.e. the B_1 field oscillate at ω_o), the magnetization will precess about B_1 at $\omega_1 = \gamma B_1$. Following this constraint, the exact solutions to the Bloch equation are,

$$M_z(\tau_p) = M_o \cos\omega_1\tau_p \qquad \text{and} \quad \upsilon(\tau_p) = M_o \sin\omega_1\tau_p \ , \tag{1.46}$$

where τ_p is the time duration of the microwave pulse and υ is the transverse component of the magnetization defined along the Y-axis of the rotating frame. If the microwave pulse is applied such that $\omega_1\tau_p = \pi/2$, the M_z component is zero while $\upsilon = M_o = M'$ and is lying on the Y-axis of the rotating coordinate system. When the first $\pi/2$ microwave pulse is turned off, the magnetization starts to dephase because the individual spin packets comprising M' have different precession frequencies about B_o. This process is called a free induction decay (FID) and it is what is most often measured in solution NMR. Those spins packets that have precession frequency (ω_i) greater than ω_o will rotate away from Y counterclockwise at a rate $\Delta\omega = \omega_i - \omega_o$, while those spin packets with precessional frequency less than ω_o will rotate clockwise away from Y -axis by $-\Delta\omega = \omega_o - \omega_i$. After some τ, spin packets a and b have rotated through an angle $\Delta\omega_a\tau$ and $\Delta\omega_b\tau$, respectively, and spin packets c and d - $\Delta\omega_c\tau$ and $-\Delta\omega_d\tau$, respectively. The dephasing or decay of the magnetization is determined by the phase memory time T_M which is in the range of the spin-spin

Figure 1.8. Vector model description of the formation of two-pulse electron spin echo. A). Equilibrium condition, the paramagnetic system has a characteristic bulk magnetization prior to the application of the first pulse. B) A 90° pulse is applied so that a transverse bulk magnetization is created in the Y-axis of the rotating frame. C). Decay of the magnetization to individual spin packets' magnetization during waiting period, τ. D) Reflection of the dephased pattern of magnetization about the XZ plane upon the application of a 180° pulse. E) Formation of an 2-pulse echo when the spin packets refocused at 2τ after the first pulse.

Two-pulse echo formation

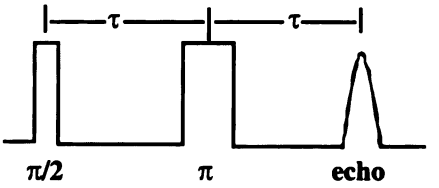

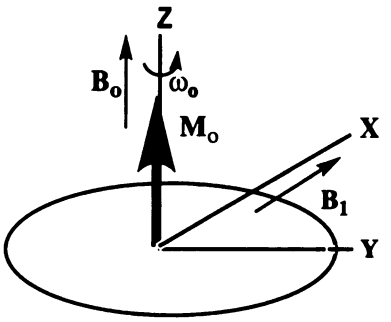

A) t = 0

pulse 1
$t_p = \pi/2$

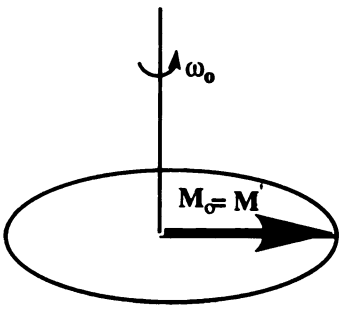

B) application of π/2 pulse

τ

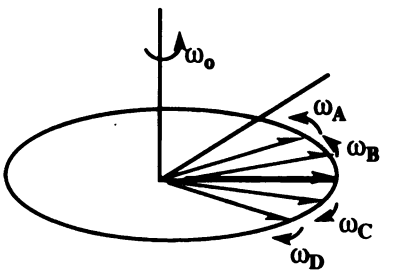

C) dephasing of spin packets

pulse 2
$t_p = \pi$

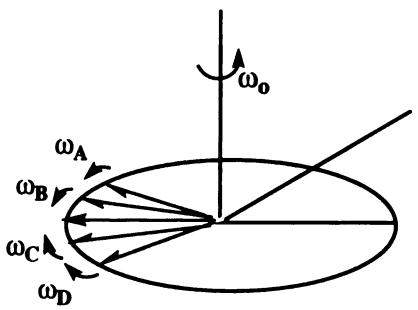

D) application of π pulse

2τ

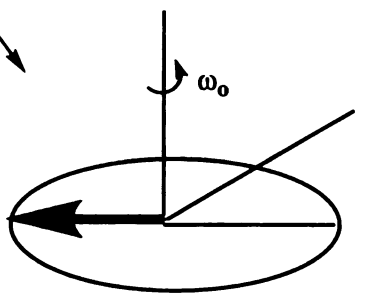

E) refocusing of net magnetization

relaxation T_2. At time τ after the application of the first pulse, the second π pulse is applied. The effect of the second pulse is to reflect the dephased pattern of the magnetization about the X-Z plane. This results in the change of the accumulated phase angle for the spin packets a and b from $\Delta\omega_{a,b}\tau$ to $(\pi - \Delta\omega_{a,b}\tau)$. Similarly, the phases of the spin packets c and d are changed to $(\pi + \Delta\omega_{c,d}\tau)$. The spin packets still precess at their former rate and direction so that at time 2τ after the application of the first pulse, spin packets a and b have accumulated phase equal to $[(\pi - \Delta\omega_{a,b}\tau + \Delta\omega_{a,b}\tau = \pi)]$ and spin packets c and d have the same phase, $[(\pi + \Delta\omega_{c,d}\tau - \Delta\omega_{c,d}\tau = \pi)]$. Thus, the spin packets converge to form transverse magnetization, $M'(2\tau)$, in the -Y axis. The refocussing of spin packets results in the emission or radiation detected in a form of spin-echo.

1.4.3 Three-Pulse Echo formation (Stimulated Echo)

The classical description of he evolution of magnetization in the ($\pi/2$-τ-$\pi/2$-T-$\pi/2$-echo(τ)) three-pulse sequence[16] is shown in Figure 1.9. The same coordinate system will be used in the description. As expected, the 90° pulse will rotate the bulk magnetization to the Y-axis. After some time τ, the transverse magnetization M' will dephase into its components. Spin packet A will form an phase angle, $\Delta\omega_A\tau$ (where $\Delta\omega_A = \omega_A - \omega_o$) while spin packet B, $-\Delta\omega_B\tau$ (where $-\Delta\omega_B = \omega_o - \omega_B$) with respect to the Y-axis. A second 90° pulse is applied at time τ, rotating the dephased pattern of the M' magnetization into the XZ plane where they are allowed to precess for time T. During the long waiting period T, further dephasing occurs and a series of cones are

Figure 1.9. Classical description of the formation of three-pulse ESE.
A) Equilibrium condition. B) Application of the first 90° pulse creating a transverse magnetization along Y. C) The transverse magnetization M' is allowed to dephase during time τ. D) Application of the second 90° pulse, this time the dephasing magnetization pattern is on the XZ plane. E). Formation of precessional cones/storage of magnetization along Z axis during time T. F) Cone formation right after the third 90° pulse is applied. G) A stimulated echo is formed.

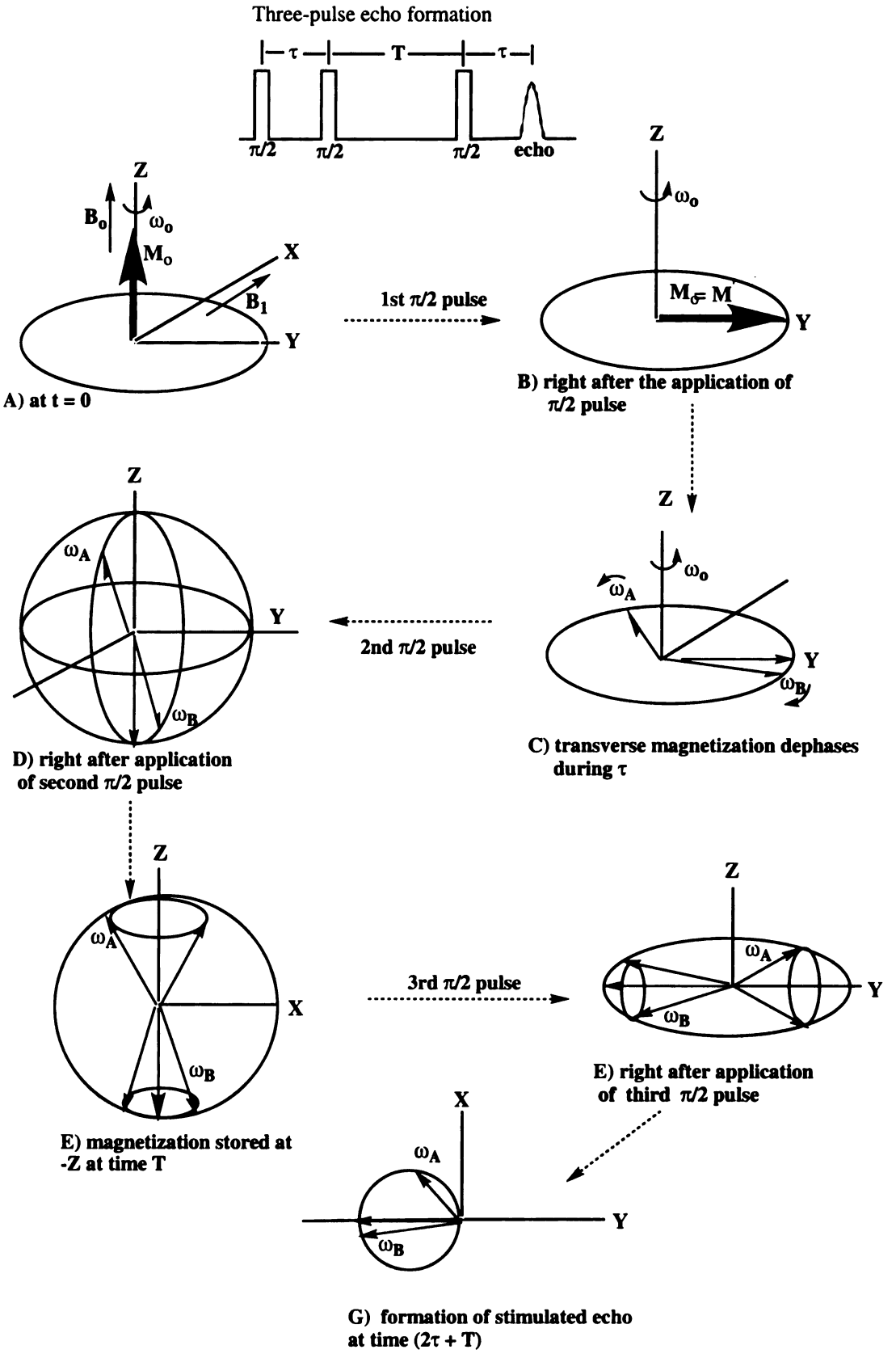
Three-pulse echo formation
τ
T
τ
π/2
π/2
π/2
echo
Z
B0
ω0
M0
X
B1
Y
A) at t = 0
1st π/2 pulse
Z
ω0
Mσ= M'
Y
B) right after the application of π/2 pulse
Z
ω0
ωA
Y
ωB
C) transverse magnetization dephases during τ
2nd π/2 pulse
Z
ωA
Y
ωB
D) right after application of second π/2 pulse
3rd π/2 pulse
Z
ωA
Y
ωB
E) right after application of third π/2 pulse
Z
ωA
X
ωB
E) magnetization stored at -Z at time T
X
ωA
Y
ωB
G) formation of stimulated echo at time (2τ + T)

formed as projections of spin magnetization along the direction of B_o. These cones allow the phase information contained in $\Delta\omega_A\tau$ and $-\Delta\omega_B\tau$ of each spin packet to be stored along the Z axis. Application of the third 90° pulse after time T, will bring the stored Z-magnetization back to the XYplane where the spin packets will refocus at time τ after the third pulse. The three-pulse echo is called a stimulated echo because the second 90° pulse puts the spins into a "holding" pattern in the Z direction until the third pulse generates the rephasing in the XY plane to stimulate echo production.

The actual shape and width of the electron spin echo are dependent on the sample and spectrometer parameters. In a typical ESE experiment, the integrated echo intensity is recorded as function of τ, in the case of two-pulse echo, and T in the case of three-pulse echo. In a typical three-pulse experiment τ is held fixed and T is varied to generate an echo decay curve. The three-pulse echo as a function of T decays with the spin-lattice time, T_1 since during time T the electron spins are oriented in the z direction. Thus, the three pulse echo decays much more slowly than the two-pulse echo.

1.4.4 Nuclear Modulation

In an Electron Spin Echo Envelope Modulation experiment, the intensity of the electron spin echoes are studied as function of increasing one of the microwave pulse spacings. For two-pulse ESEEM experiment, the time τ is incremented, and in a three-pulse ESEEM measurement, T, the spacing between the second and third pulse is varied. In both experiments, an overall decrease in echo intensity is observed This decrease is due to random and irreversible loss of magnetization by each

individual packet which is dependent on T_2, spin-spin relaxation, for the case of the two-pulse experiment and T_1, spin-lattice relaxation, for the case of three-pulse measurement. Interference effects that originate from electron-nuclear hyperfine coupling lead to modulation of these intensities and provide a means for recovering this information that is lost due to inhomogeneous broadening. The physics of these modulations will be discussed in this section. Both classical and quantum mechanical descriptions will be discussed.

The classical explanation[12,13] is as follows (Figure 1.10). We assume that S_z is quantized along the direction of the external magnetic field. Nearby nuclei with spin I of some distance r from the electron will experience an effective field B_{1eff} equal to the sum of the external magnetic field and the dipolar magnetic field, B_e, due to the electron. The magnetic nuclei will precess about this effective field. Similarly, the magnetic nucleus will generate a dipolar field, B_N whose magnitude is almost negligible compared to the B_o so that the electron will precess about ~B_o. However, the precession of the magnetic nuclei about B_{1eff} will cause variation in B_N. This time-dependent variation of the field, $\Delta B_{N1}(t)$, causes modulation of the electron Larmor frequency by the nuclear Larmor frequency ω_{N1}. When a microwave pulse is applied, the projection of S_z will change and consequently will alter the effective magnetic field experienced by the magnetic nucleus from B_{1eff} to B_{2eff}. If the microwave pulse width is shorter than the nuclear Larmor frequency, not all nuclei can adiabatically precess around the new B_{2eff} direction. Some nuclei will precess about B_{1eff} at w_{N1} and some nuclei will precess about B_{2eff} at w_{N2}. Thus, microwave

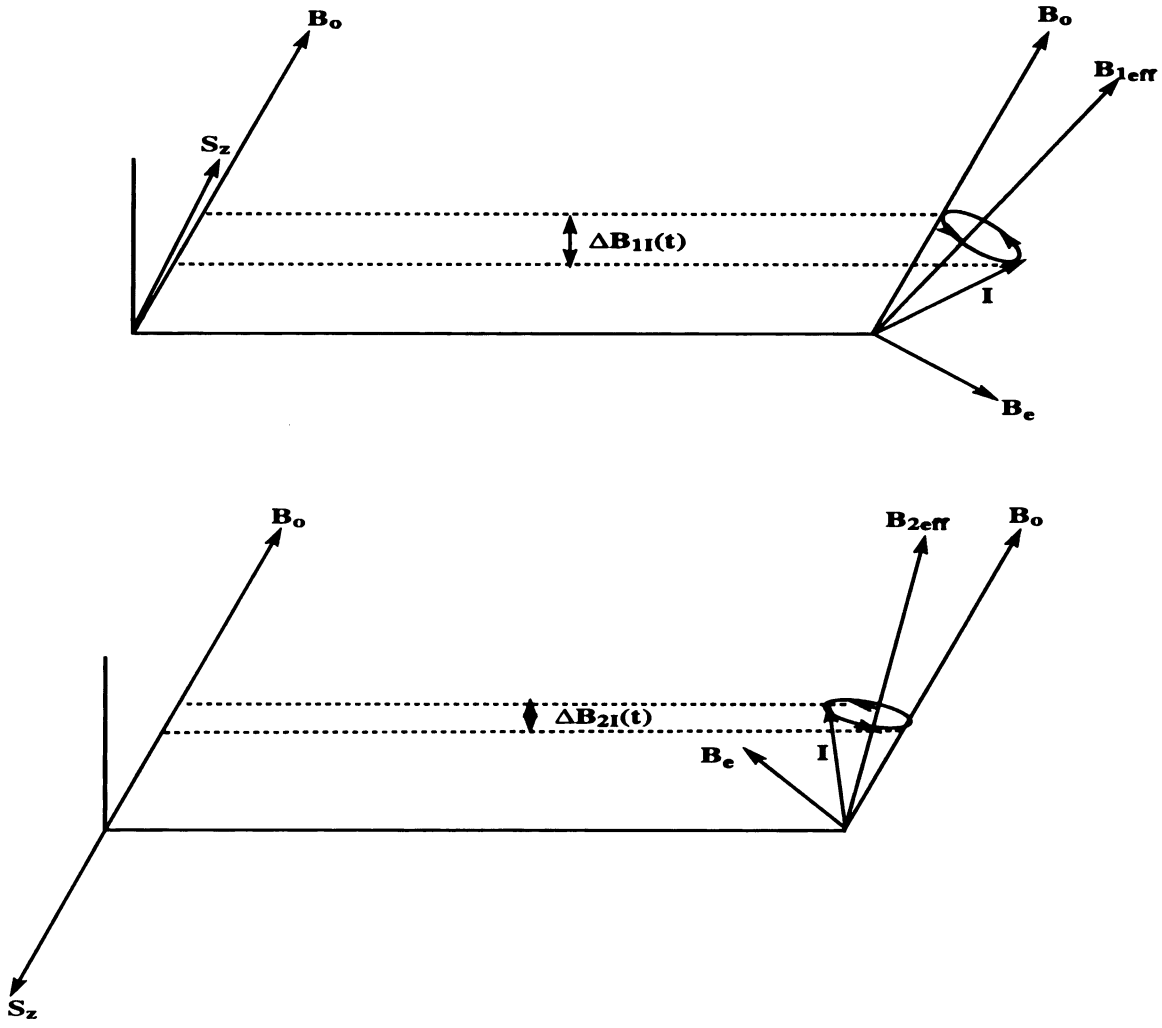

Figure 1.10. Classical explanation of the origin echo modulation. An isotropic g-factor is assumed implying that the S_z is aligned along the direction of the applied field. (A) An electron in motion produces a local magnetic field, B_{1e} at the nearby magnetic nuclei. H_{1e} adds to the external magnetic field B_o to yield an effective magnetic field, B_{1eff}. The precession of the nuclei I about B_{1eff} produces a time varying local field $\Delta H_{1I}(t)$ at the electron and consequently modulates the electron Larmor frequency. (B) Application of the resonance pulse reverses S_z to $-S_z$ resulting in a new effective magnetic field, B_{2eff} about which the nucleus precesses. If the duration of the pulse is shorter than the nuclear Larmor frequency, not all the nucleus will able to precess about B_{2eff}. Thus the electron Larmor frequency is modulated by $\Delta B_{1I}(t)$ and $\Delta B_{2I}(t)$ at nuclear frequencies proportional to B_{1eff} and B_{2eff}, respectively. Interference of these nuclear frequencies produces beats in the electron prescession signal at the nuclear frequencies. The modulation of S_z can be detected in a form of an echo if a second resonant pulse is applied.

pulse causes a branching of the precessing nuclei into two sets that produce two different nuclear-modulation frequencies at the electron. Interference between these two nuclear frequencies produces beats in the electron precesssion signal at the nuclear frequencies. The modulation of S_z can be detected by applying a second microwave pulse to generate an echo. The amplitude of the echo depends on the orientation of the B_{eff},, and hence on the electron-nuclear distance r and on the number of equivalent nuclei at r. Thus, an analysis of an echo-modulation pattern gives information on the number and distance of magnetically coupled nuclei as well as their identity from the modulation frequency.

A quantum-mechanical view of echo modulation can be described using the energy level diagram for an S=1/2 and I=1/2 spin system shown in Figure 1.11.[11] Anisotropy in hyperfine interaction contributes to the inhomogeneous broadening of the EPR linewidth as electron spins experience different local magnetic field due to the magnetic nucleus randomly oriented with respect to the direction of the external magnetic field. This anisotropy also results in the spin states whose wavefunctions are mixtures of nuclear spin states. As a consequence of the mixing of states, the two forbidden transitions can be observed in addition to the two allowed transitions ($\Delta m_s = \pm 1$ and $\Delta m_I = 0$). Clearly from the energy level diagram, it is possible to induce transition from one initial spin states to different final spin states upon the application of the microwave pulse. This branching of transitions is responsible for the modulation of electron spin echoes.

The origin of nuclear echo modulation can be explained by combining the vector model explanation of two-pulse ESE formation and the quantum mechanical

Figure 1.11. Combination of quantum mechanics and vector model of echo formation to explain the origin of echo modulation. A) Four-energy level diagram showing branching of transitions. B) Vector model showing the interference of spin packets as result of branching of transition in a two-pulse echo sequence.

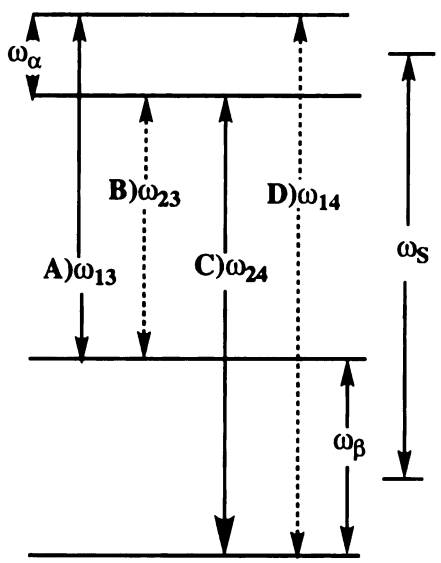

$|1\rangle = \cos(\theta_\alpha/2)\,|1/2\ 1/2\rangle + \sin(\theta/2)\,|1/2\ -/2\rangle$

$|2\rangle = -\sin(\theta_\alpha/2)\,|1/2\ 1/2\rangle + \cos(\theta/2)\,|1/2\ -/2\rangle$

$|3\rangle = \cos(\theta_\beta/2)\,|-1/2\ 1/2\rangle + \sin(\theta/2)\,|-1/2\ -/2\rangle$

$|4\rangle = -\sin(\theta_\beta/2)\,|-1/2\ 1/2\rangle + \sin(\theta/2)\,|-1/2\ -/2\rangle$

θ=quantization axis

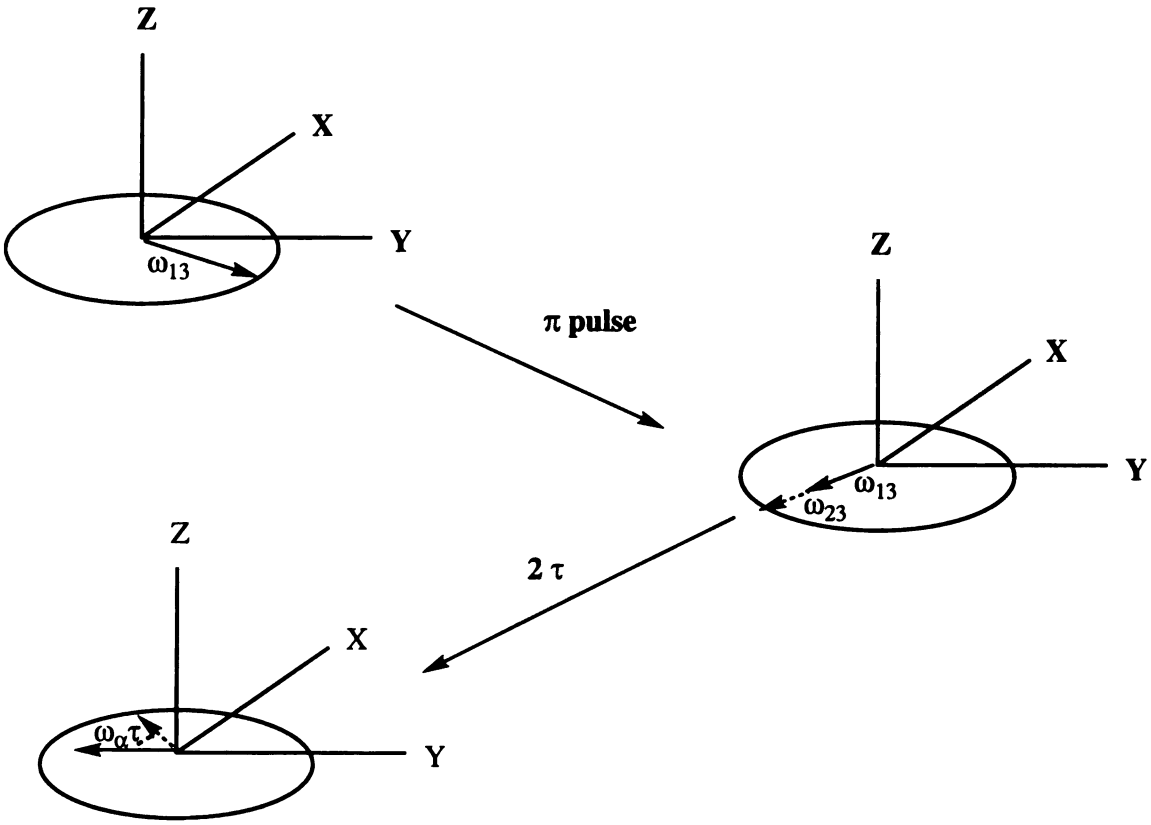

description of branching of transitions. For simplicity, the spin packet that undergoes transition from E_1 to E_3 at frequency ω_{13} will be considered. After the first precession, the spin packet will a develop a phase angle with respect to the Y axis. Application of second pulse at time τ after the first pulse will rotate the spin packet to 180°. In addition to this rotation, splitting of the magnetization vector will occur as a result of branching of transition. The new spin packet that was generated will precess at ω_{23}. Because of the difference in the precessional frequency, the new spin packet will precess at a different frequency while the original spin packet will maintain its original frequency. At time τ after the second pulse, the original spin packet will align at the Y axis and contribute to the echo. The echo, however, was modulated because the second spin packet does not refocus and therefore interferes with the formation of the echo. The extent of interference that results from the branching of the EPR transitions depends on the projection of the branched spin packet on to the Y-axis, $\cos\{(\omega_{13}-\omega_{23})\}\tau$, weighted by the probability for the branching. The echo, therefore, is modulated as one varies the time between the 90° and 180° pulses with a frequency $|(\omega_{13}-\omega_{23})| = \omega_\beta$.

The origin of modulation of the three-pulse electron spin echo is the same as for the two-pulse echo. It essentially depends on transient excitation of branched EPR transitions involving two nuclear spin orientations. One difference is that three-pulse ESEEM is modulated by the nuclear frequencies ω_α and ω_β, whereas the two-pulse ESEEM is modulated by the sum and difference of ω_α and ω_β in addition to modulation by the nuclear frequencies at each electron spin manifold. This difference

will be understood better by discussing formulation of the modulation of function of the two and three-pulse ESEEM using the density matrix formalism.

1.4.5 Density Formalism of ESEEM

1.4.5.1 Density Operator

In ESEEM, we are concerned with measuring the bulk magnetization in the form of a spin echo. Calculation of the time-dependent evolution of an ensemble average can be done without knowing the exact state of the system by invoking the concept of the density matrix.[19-22]

Consider a system described by a set of orthonormal states and that the probabilities that the system is in each of these states are w_i. The expectation value of an observable A is

$$\langle \mathbf{A} \rangle = \sum_i w_i \left\langle \psi_i \middle| \hat{\mathbf{A}} \middle| \psi_i \right\rangle, \tag{1.47}$$

which is a quantum and statistical average. A density operator, ρ, can be defined as

$$\hat{\rho} = \sum_i w_i |\psi_i\rangle\langle\psi_i|. \tag{1.48}$$

We can express the set of orthonormal states as linear combinations of basis state so that,

$$|\psi_j\rangle = \sum_j c_j^{(i)} |\phi_j\rangle. \tag{1.49}$$

The statistical average, therefore, can be rewritten as,

$$\langle A \rangle_{stat} = \sum_i w_i \sum_j c_j^{(i)*} \left\langle \phi_j \middle| \hat{A} \sum_k c_k^{(i)} \middle| \phi_k \right\rangle \tag{1.50}$$

$$= \sum_j \sum_k \left[\sum_i c_j^{(i)*} w_i c_k^{(i)} \right] \left\langle \phi_j \middle| \hat{A} \middle| \phi_k \right\rangle$$

$$= \sum_j \sum_k \rho_{jk} A_{jk} = Tr(\rho A)$$

in which the density-matrix ρ_{kj}, the matrix representation of the density operator in this basis, is defined by

$$\rho_{kj} = \sum_i c_j^{(i)*} w_i c_k^{(i)} = \left\langle \phi_k \middle| \hat{\rho} \middle| \phi_j \right\rangle. \tag{1.51}$$

If the physical observable evolves with time, then we should write the orthonormal states as $|\psi_i(t)\rangle$, the basis states as $|\phi_i(t)\rangle$, the coefficient as $c_l(t)$, and the observable as $\langle A(t)\rangle$. We should also described the time-dependence of the density operator as,

$$\hat{\rho}(t) = \sum_i w_i |\psi_i(t)\rangle\langle\psi_i(t)|, \tag{1.52}$$

whose matrix-elements ρ_{kj}, is

$$\rho_{kj}(t) = \sum_i c_j^{(i)*}(t) w_i c_k^{(i)}(t) = \left\langle \phi_k(t) \middle| \hat{\rho}(t) \middle| \phi_j(t) \right\rangle. \tag{1.53}$$

In a case in which the state of the system is known, all probabilities are zero except for one (i.e. pure state), so that density operator becomes,

$$\hat{\rho}(t) = |\psi(t)\rangle\langle\psi(t)| \tag{1.54}$$

and the matrix elements as

$$\rho_{kj}(t) = c_j^*(t) c_k(t) = \left\langle \phi_k(t) \middle| \hat{\rho}(t) \middle| \phi_j(t) \right\rangle. \tag{1.55}$$

Important properties of density matrix operator that need to be mentioned are that a) the Tr(ρ)=1, b) it is a Hermitian operator, and c) in all its representation the diagonal elements are always real and lie in the interval [0,1].

The density operator equation of motion is given by ,

$$\frac{d\rho}{dt} = \frac{i}{\hbar}\{\rho(t)H - H\rho(t)\} = \frac{i}{\hbar}[\rho(t), H], \tag{1.56}$$

where H may time-dependent or time-independent Hamiltonian. If H is time-independent, $\rho(t)$, the density operator at time, t, can be determined from $\rho(0)$ at time zero by ,

$$\rho(t) = \exp\left\{\frac{-iHt}{\hbar}\right\}\rho(0)\exp\left\{\frac{iHt}{\hbar}\right\}. \tag{1.57}$$

Therefore, if $\rho(0)$ is known we will be able to calculate the average eigenvalue of the some observable $\langle A \rangle$ at time t.

1.4.5.2 Application of Density Matrix to ESEEM

The detailed discussion for the derivation of the modulation function for two-pulse and three-pulse ESEEM is presented in the manuscripts of W. Mims.[9,23] In this section, a brief explanation will be presented.

In ESEEM, we let our spin system (i.e magnetization) evolves in time during the application of microwave pulses (nutation period) and when the microwave pulses are absent (free precession period) as shown in Figure 1.12. We can track the time-dependent motion of the magnetization of our perturbed system using the density operator equation of motion. At some time, t_{echo}, we observe an echo which is due to the refocused y-component, (M_y), of the transverse magnetization. The echo signal, E_{mod}, can be quantitatively known, if $\rho(t_{echo})$, density operator at the time echo appears, is known. This echo signal is proportional to the $Tr\{\rho(t_{echo})S_y\}$.

The general form of echo signal is given by,

$$E_{mod} = \eta Tr\{\rho(t_{echo})\mathcal{H}\}$$

where η is constant that depends on the experimental arrangements and $\mathcal{H}_1$ is the time-dependent Hamiltonian portion of the total Hamiltonian,

$$\mathcal{H}_{tot} = \mathcal{H}_0 + \mathcal{H}_1. \tag{1.58}$$

$\mathcal{H}_0$ is the static interactions in the sample that include the Zeeman interaction, hyperfine interaction and nuclear quadrupole interaction. $\mathcal{H}_1$, on the other hand,

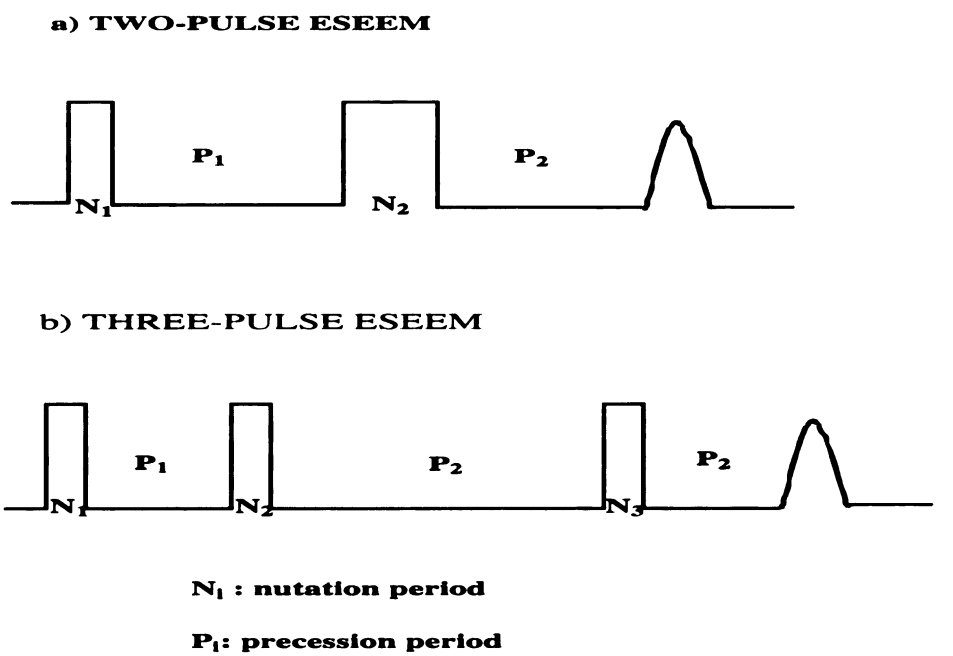

Figure 1.12 Nutation and free-precession periods in two- and three-pulse ESEEM.

describes the interaction of our system with the field of the microwave pulse. The explicit form of these Hamiltonians are

$$\mathcal{H}_0 = \beta\hat{\mathbf{S}}\cdot\underline{\mathbf{g}}\cdot\hat{\mathbf{B}} - \beta_N g_N \hat{\mathbf{I}}\cdot\mathbf{B} + \hat{\mathbf{S}}\cdot\underline{\mathbf{A}}\cdot\hat{\mathbf{I}} + \hat{\mathbf{I}}\cdot\underline{\mathbf{P}}\cdot\hat{\mathbf{I}}... \tag{1.59}$$

$$\mathcal{H}_1 = g_e\beta B_1\hat{S}_x\cos(\omega_1 t). \tag{1.60}$$

The trace should be summed over (a) the $|\alpha_i>$ and $|\beta i>$ states (Figure 1.13a) and the sum over the systems which make up the inhomogeneous line (Figure 1.13b). These sums can be calculated separately assuming that a) the spread in the inhomogeneous shifts $\Delta B_{o,k}$ ($B_{o,k} = B_{o,avg} + \Delta B_{o,k}$) is large compared to the intervals in the α and β manifolds and (b) $\Delta B_{o,k}$ only varies the spacing between the α and β manifolds and does not lead to an inhomogeneous distribution of intervals within each manifold. With these assumptions, the sum over α and β manifolds gives the envelope modulation function and the sum over the inhomogeneous line yields the form of the echo signal.

It is necessary to express $\mathcal{H}_{tot}$, $\mathcal{H}_1$ and $\mathcal{H}_o$ in a rotating-frame coordinate system. The transformation to this coordinate means that we fix the direction of the microwave field B_1, say along X, thereby removing its dependence on time, t. This transformation can be done by applying the similarity rotation operator,

$$R(\theta = \omega t) = Exp\left[\frac{i}{2}\omega t \Sigma_z\right], \tag{1.61}$$

where $\Sigma_z = \begin{bmatrix} I & 0 \\ 0 & -I \end{bmatrix}$

has an analogous meaning as the Pauli matrix σ_z. I is identity submatrix of dimension equal to the number of nuclear spin states (2I + 1). In the rotating frame, $\mathcal{H}_o$ and $\mathcal{H}_1$ are expressed as $\mathcal{H}'_o$ and $\mathcal{H}'_1$, respectively. After the appropriate transformation to the rotating frame, the density operator during the nutation period can be expressed as,

$$\tilde{\rho}(t_f) = R_N^* \tilde{\rho}(t_i) R_N, \tag{1.62}$$

where $R_N = \exp\{i(\mathcal{H}'_o + \mathcal{H}'_1)(t_f - t_i)/\hbar\} = \exp\{i(\mathcal{H}'_o + \mathcal{H}'_1)t_p/\hbar$ (1.63)

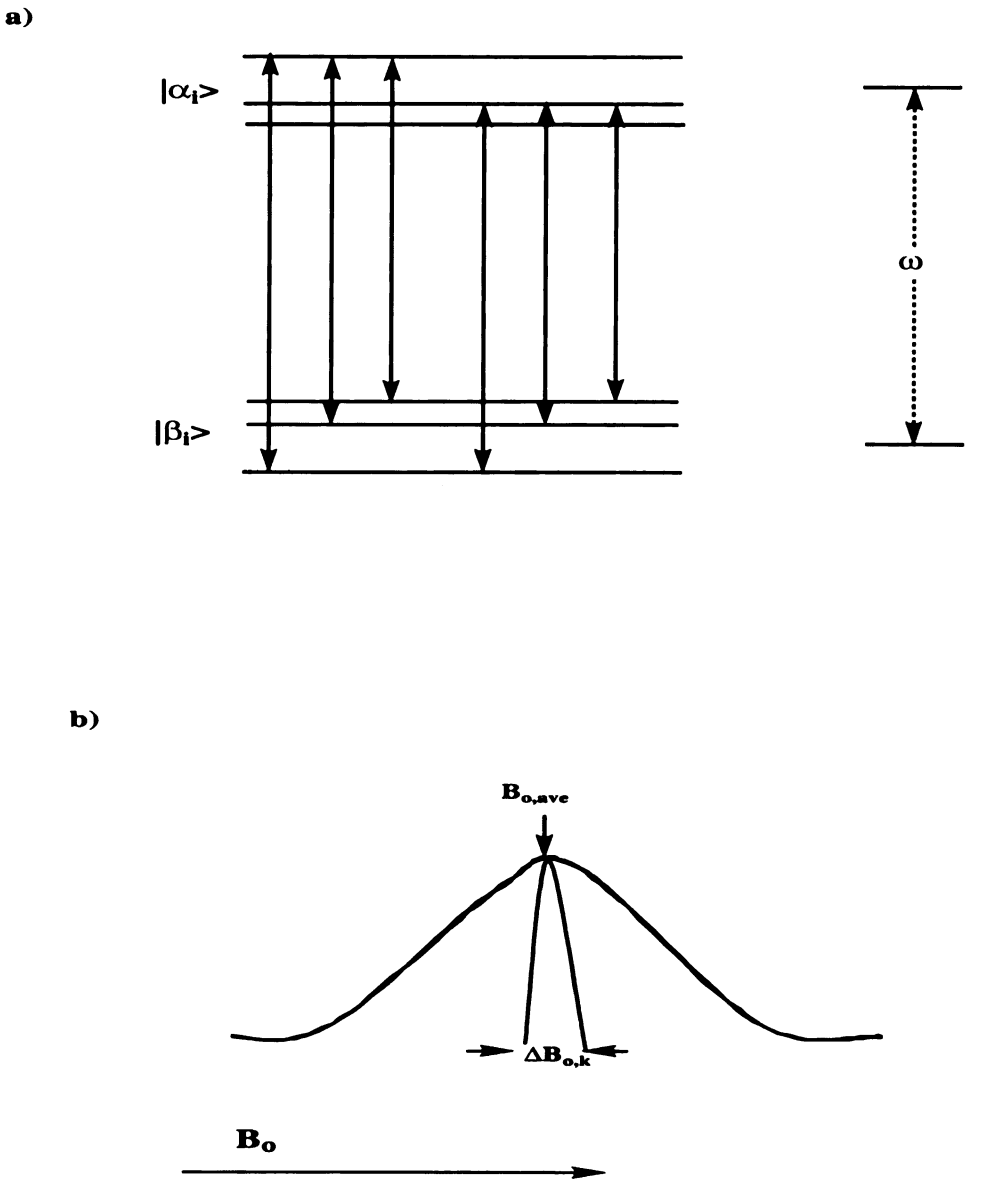

Figure 1.13. A) Set of energy levels that interact with a resonant microwave pulse. For spin echo modulation to be observed, it is essential that branching occurs. That is, there must be transitions from on one given state in α electron spin manifold to more than one final states in the β manifold. B) Distribution of values of B_o in an inhomogeneously broadened line.

and the free precession as

$$\tilde{\rho}(t_f) = R_t^* \tilde{\rho}(t_i) R_t \tag{1.64}$$

where $R_t = \exp\{i(\mathcal{H}_o')(t_f - t_i)/\hbar\}$. (1.65)

Using these exponential operators, the density operator when echo appears, $\tilde{\rho}_{echo}$, can be determined after the sequence of nutation and precession with respect to the initial density, $\tilde{\rho}_o$, by the transformation

$$\tilde{\rho}_{echo} = R^+ \tilde{\rho} R \tag{1.66}$$

where for the two-pulse sequence ,

$$R = R_{N_1} R_\tau R_{N_2} R_{\tau+t} \tag{1.67}$$

and for three pulse

$$R = R_{N_2} R_\tau R_{N_2} R_T R_{N_3} R_\tau. \tag{1.68}$$

The initial density, $\tilde{\rho}_o$, is a time-independent equilibrium density matrix prior to the application of the first pulse. It is diagonalized in the representation that diagonalizes $\mathcal{H}_o'$ and the diagonal elements represents the thermal equilibrium initial population of the alpha and beta electron spin states . Assuming all the sublevels in alpha and beta electron spin manifolds are equally populated, the initial density in matrix form is

$$\rho_{o,diag} = \begin{bmatrix} \rho_\alpha^o & 0 \\ 0 & \rho_\beta^o \end{bmatrix} = \begin{bmatrix} aI & 0 \\ 0 & bI \end{bmatrix} \tag{1.69}$$

We can think of a and b as the average Boltzmann population of the several sublevels in the alpha and beta electron spin manifolds.

$\mathcal{H}_o'$ can be diagonalized (i.e. transformed into $|m_S m_I\rangle$ basis), by using the unitary transformation operators, M_α and M_β. M_α and M_β are $(2I + 1) \times (2I + 1)$ matrices describing the mixing of nuclear spin states caused by the hyperfine

interaction in the alpha and beta manifolds. Diagonalization of $\mathcal{H}'_0$ is essentially diagonalizing its two block diagonal (2I + 1) ((2I +1) submatrices for each alpha and beta spin state. The exponential operator, R, and $\mathcal{H}'_1$ should also be expressed in this representation.

After all the transformations, we can figure out the density matrix at the time of the appearance of the echo in the diagonalized representation for the two- and three-pulse echo sequence. For the two pulse experiment, the echo is generated at time 2τ and therefore we are interested at knowing the ρ_{echo} at time 2τ

$$\rho_{echo}(2\tau)= R^{\dagger}\rho(0)R$$

The corresponding normalized modulation function for $E(2\tau)$ is,

$$E_{mod}(\tau)=\left(\frac{1}{2(2I+1)}\right)Tr\left(Q_{\tau}^{+}M^{+}P_{\tau}^{+}MQ_{\tau}M^{+}P_{\tau}M+H.C.\right). \qquad (1.70)$$

In the equation, H.C. stands for Hermitian conjugate. I has the usual meaning, it is the spin of the nucleus that gives rise to the observed superhyperfine couplings. P_τ and Q_τ are (2I +1) × (2I+1) diagonal matrices describing the evolution of the electron spin manifolds during the preceesional period. They consist of elements $(P_\tau)_{ii} = P_{ii} = \exp(i\omega_{i,\alpha}\tau)$ and $(Q_\tau)_{kk} = Q_{kk} = \exp(i\omega_{k,\beta}\tau)$. M is the unitary matrix $M_\alpha^{\dagger}M_\beta$. If more than one nucleus is coupled to the unpaired electron spin, the echo modulation function assumes the form,

$$E_{mod}(\tau)=\prod_{i=1}^{n}E_{mod}^{i}(\tau). \qquad (1.71)$$

For the case of the three-pulse echo, the echo appears at time $(2\tau +T)$. The normalized E_{mod} is then,

$$E_{\mathrm{mod}}(\tau,T)=\left(\frac{1}{4(2I+1)}\right)Tr\begin{pmatrix}Q_\tau^+M^+(P_T^+P_\tau^+)MQ_\tau M^+(P_TP_\tau)M+\\(Q_T^+Q_\tau^+)M^+P_\tau^+M(Q_TQ_\tau)M^+P_\tau M+H.C.\end{pmatrix}. \tag{1.72}$$

When more than one nucleus is coupled, the product rule applies. However, the product rule is obeyed within the same electron spin state so that

$$E_{\mathrm{mod}}(\tau,T)=\frac{1}{2}\left[\prod_i^n E_\alpha^i(\tau,T)+E_\beta^i(\tau,T)\right]. \tag{1.73}$$

It should be noted that the generalized modulation function for S =1/2 (equations 1.70-1.73) are derived with the assumption that $\mathcal{H}_1 >> \mathcal{H}_0$. With this assumption the exponential operator for the nutation period is simplified because the $\mathcal{H}_0$ is neglected.

1.4..5.3 Modulation Formula for an S=1/2, I =1/2 System

In the rotating frame, the Hamiltonian describing the interaction of the nucleus of spin I = 1/2 and the electron spin S = 1/2 is given by,[9,24,25]

$$\mathcal{H}_0' = \hbar\left[(\omega_o-\omega)\hat{S}_z-\omega\hat{I}_z+\hat{S}_z\hat{I}_z+\hat{S}_zB\hat{I}_z\right]. \tag{1.74}$$

The above equation assumes g to be isotropic. Likewise, $\mathcal{H}_1$ in the rotating frame is expressed as

$$\mathcal{H}_1' = \hbar\omega_1\hat{S}_x\ ,\ (\hbar\omega_1 = g_e\beta B_1). \tag{1.75}$$

The eigenvalue of $\mathcal{H}'_0$, can be determined in a representation that diagonalizes the S_z and I_z. This can be carried out using the unitary transformation operator, $\exp(i\varphi I_y)$,

$$\mathcal{H}_{diag} = \exp(i\varphi\hat{I}_y)\mathcal{H}_o'\exp(-i\varphi\hat{I}_y) = \hbar(\omega_o-\omega)\hat{S}_z-\hbar\omega_\varphi\hat{I}_z \tag{1.76}$$

The transformation is equivalent to rotation about the y axis through an angle φ. The angle φ is determined by

$$\tan\varphi = \frac{B \cdot m_s}{A \cdot m_s - \omega_I}, \tag{1.78}$$

and assumes the values φ_α and φ_β when $m_s = \alpha$ and $m_s = \beta$, respectively. Physically, these angles determine the quantization axes of the nuclear spin, the Larmor frequency of which assumes two values corresponding to two electron spin states, the alpha and beta states,

$$\omega_{\alpha,\beta} = \left[\left(\omega_I \mp \frac{A}{2}\right)^2 + \frac{B^2}{4}\right]^{1/2}. \tag{1.79}$$

We can view exp(iφIy) as an operator that mixes nuclear states at the same electron spin projections and can write it in matrix form using the $|m_I>$ representation.

$$\exp\left(-i\varphi_\alpha \hat{I}_y\right) = \begin{bmatrix} \cos\frac{\varphi_\alpha}{2} & -\sin\frac{\varphi_\alpha}{2} \\ \sin\frac{\varphi_\alpha}{2} & \cos\frac{\varphi_\alpha}{2} \end{bmatrix} = M_\alpha \tag{1.80}$$

$$\exp\left(-i\varphi_\beta \hat{I}_y\right) = \begin{bmatrix} \cos\frac{\varphi_\beta}{2} & -\sin\frac{\varphi_\beta}{2} \\ \sin\frac{\varphi_\beta}{2} & \cos\frac{\varphi_\beta}{2} \end{bmatrix} = M_\beta. \tag{1.81}$$

Therefore, the unitary matrix M assumes the form,

$$M = M_\alpha M_\beta^+ = \begin{bmatrix} \cos\frac{\varphi_\alpha - \varphi_\beta}{2} & \sin\frac{\varphi_\alpha - \varphi_\beta}{2} \\ -\sin\frac{\varphi_\alpha - \varphi_\beta}{2} & \cos\frac{\varphi_\alpha - \varphi_\beta}{2} \end{bmatrix} = \begin{bmatrix} v & u \\ -u^* & v^* \end{bmatrix}. \tag{1.82}$$

The column of the matrix M_α are actually the eigenvectors that corresponds to the two eigenvalues in the alpha manifold. This also applies to M_β. In mathematical form, the energy eigenvalues are given by,

$$E(-1/2,1/2) = E_{\beta,4} = \frac{-\hbar(\omega_o - \omega)}{2} - \frac{\hbar}{2}\left[\left(\omega_I + \frac{A}{2}\right)^2 + \frac{B^2}{4}\right]^{1/2} \tag{1.83a}$$

$$E(-1/2,-1/2) = E_{\beta,3} = \frac{-\hbar(\omega_o - \omega)}{2} + \frac{\hbar}{2}\left[\left(\omega_I + \frac{A}{2}\right)^2 + \frac{B^2}{4}\right]^{1/2} \tag{1.83b}$$

$$E(1/2,1/2) = E_{\alpha,2} = \frac{\hbar(\omega_o - \omega)}{2} - \frac{\hbar}{2}\left[\left(\omega_I - \frac{A}{2}\right)^2 + \frac{B^2}{4}\right]^{1/2} \tag{1.83c}$$

$$E(1/2,-1/2) = E_{\alpha,1} = \frac{\hbar(\omega_o - \omega)}{2} + \frac{\hbar}{2}\left[\left(\omega_I - \frac{A}{2}\right)^2 + \frac{B^2}{4}\right]^{1/2}. \tag{1.83d}$$

Corresponding to the above energy eigenvalues are the eigenvectors,

$$\Psi(-1/2,1/2) = \Psi_{\beta,4} = -\sin\frac{\varphi_\beta}{2}|-1/2,\ 1/2\rangle + \cos\frac{\varphi_\beta}{2}|-1/2,-1/2\rangle \tag{1.84a}$$

$$\Psi(-1/2,-1/2) = \Psi_{\beta,3} = \cos\frac{\varphi_\beta}{2}|-1/2,\ 1/2\rangle + \sin\frac{\varphi_\beta}{2}|-1/2,-1/2\rangle \tag{1.84b}$$

$$\Psi(1/2,1/2) = \Psi_{\alpha,2} = -\sin\frac{\varphi_\alpha}{2}|1/2,\ 1/2\rangle + \cos\frac{\varphi_\alpha}{2}|1/2,-1/2\rangle \tag{1.84c}$$

$$\Psi(1/2,-1/2) = \Psi_{\alpha,1} = \cos\frac{\varphi_\alpha}{2}|1/2,\ 1/2\rangle + \sin\frac{\varphi_\alpha}{2}|1/2,-1/2\rangle \tag{1.84d}$$

The notations $E(m_S, m_I)$ and $\Psi(m_S,m_I)$ are incorrect for the case described above. They are correct for the case in which the electron and nuclear spins are quantized along the same direction. They are shown for the purpose of showing the transformation of the eigenvalues and eigenvectors when hyperfine anisotropy is present.

Having known the elements of M_α and M_α allows us to express the exponential operator for both the precession and nutation period in the eigenvalue representation,

$$R_j = \begin{bmatrix} M_\alpha & \\ & M_\beta \end{bmatrix} \exp\left[\frac{-iHt}{\hbar}\right] \begin{bmatrix} M_\alpha^+ & \\ & M_\beta^+ \end{bmatrix}, \tag{1.85}$$

where $H=\mathcal{H}'_0$ when pulse is off and $H=\mathcal{H}'_1$ when pulse is on. Using the explicit form of M for I=1/2, the analytic solution for two-pulse echo,

$$E_{\text{mod}}(\tau) = 1 - \frac{k}{2}\left\{\begin{array}{l} 1-\cos(\omega_\alpha\tau)-\cos(\omega_\beta\tau)+ \\ \frac{1}{2}\cos\cos([\omega_\alpha+\omega_\beta]\tau)-\frac{1}{2}\cos\cos([\omega_\alpha-\omega_\beta]\tau) \end{array}\right\} \tag{1.86}$$

and for three pulse,

$$E_{\text{mod}}(\tau,T) = 1 - \frac{k}{2}\left\{\begin{array}{l} \sin^2(\frac{\omega_\alpha\tau}{2})\{1-\cos[\omega_\alpha(\tau+T)]+ \\ \sin^2(\frac{\omega_\alpha\tau}{2})\{1-\cos[\omega_\beta(\tau+T)] \end{array}\right\}. \tag{1.87}$$

In both equations, k is the modulation depth parameter and is equal to

$$k = 4|v|^2|u|^2 = \sin^2(\varphi_\beta - \varphi_\alpha) = \left(\frac{\omega_I B}{\omega_\alpha \omega_\beta}\right)^2, \tag{1.88}$$

where $|u|^2$ and $|v|^2$ are the transition probabilities for the forbidden and allowed spin transition. $|u|$ and $|v|$ are also known as branching parameters. They describe the mixing, which may be due anisotropy in hfi interaction, of each zeroth-order nuclear spin function into each spin function of the total electron-nuclear system and are essential for the appearance of the ESEEM. When either $|v|$ or $|u|$ are zero (i.e. no mixing), only the spin-allowed transitions are excited and no ESEEM will be observed.[9,26]

1.5 Two-Pulse ESEEM vs. Three-pulse ESEEM

As discussed earlier, two factors determine the intensity of the echo. The experimental echo decay of is a product of a monotonically decreasing relaxation decay function and the modulation function,

$$E_{echo} = E_{decay} E_{\mathrm{mod}}. \tag{1.89}$$

The exact form of the decay function is not known. Approximately, it is modelled to an exponential function, $\exp(-\tau/\tau_o)^n$ where n=1,1.5,2 or 0.5.[27]

The analytic solution to the two-pulse echo suggests that the modulation of the two-pulse echo occurs at hyperfine frequencies and their sum and difference combination frequencies. These frequencies will manifest in the Fourier transform of the time domain data. Because of the product rule, frequencies due to the combinations of frequencies arising from the different nuclei will also manifest in addition to fundamental and combination frequencies of one nucleus. Thus, adding complexities. These additional frequencies compounded by the short phase memory time, T_M (approximately in the order of the spin-spin relaxation, T_2) that describes the decay of echo with time will contribute to poor resolution of two-pulse ESEEM data. The E_{mod} of the three-pulse echo, on the other hand, is modulated only by the fundamental frequencies. When several nuclei are coupled, the product rule is applied to alpha and beta electron spin manifolds separately. Also the decay of the echo is governed by longer relaxation processes (electron spin-lattice relaxation, electron cross relaxation and nuclear spin-spin relaxation) at liquid helium temperature leading to a better frequency resolution than typically found for the two-pulse experiment.

One important property of the three-pulse echo modulation function is the suppression effect which is helpful in the assignment of superhyperfine frequencies belonging to alpha or beta electron spin manifold. The choice of τ has an effect on the intensity of the modulation amplitude. By setting τ over the range of values determined by the period of the complementary hyperfine frequencies, we may be able to enhance or suppress the shf frequencies from an electron spin manifold. This suppression effect is useful in experiment when one want to suppress the modulation frequencies of protons to find out the modulation due to another nucleus, say ^{14}N. This can be done by setting τ proportional to the period of oscillation of a proton nucleus at a given external magnetic field intensity.

One drawback from three-pulse ESEEM is that the sequence can generate several two-pulse echoes which may overlap with the three-pulse echo resulting in distortion in the ESEEM pattern. To eliminate the effect of overlapping echoes, a phase cycling technique was introduced. The contribution of these unwanted echoes is removed by cycling the phase of the mw pulses to produce alternating negative and positive two-pulse echoes while the three-pulse echo remains always positive.[28]

Although it may appear that three-pulse is better than two-pulse experiment, the use of a particular echo sequence will depend on what one wants to obtain. For example, water ligation in a metal center will be determined better with two-pulse ESEEM because information about the coupling of water proton to an electron is contained in the sum combination peak. Also, two-pulse is more reliable in D_2O-exchange experiment where division of modulation functions consisting of product of modulations functions of individual nuclei coupled to the electron, is involved. For

the accurate determination of the ^{14}N hyperfine frequencies, three-pulse ESEEM has the advantage over two-pulse because the three-pulse ESEEM gives better resolution of peaks than the two-pulse ESEEM. In the work that I am going to present, two-pulse ESEEM was used to characterize water ligation to copper center and three-pulse was used to determine histidyl-imidazole ligation. The copper system studied will be discussed in the next chapter.

List of References

1)Orton, J. W. *Electron Paramagnetic Resonance An Introduction To Transition Group Ions in Crystals*; Iliffe Books Ltd: London, 1968.

2)Abragram, A.; Bleaney, B. *Electron Paramagnetic Resonance of Transition Ions*; Dover Publications, Inc.: Mineola, New York, 1970.

3)Atherton, N. M. *Principles of Electron Spin Resonance*; Ellis Horwood & PTR Prentice Hall: New York, 1993.

4)Wertz, J. E.; Bolton, J. R. *Electron Spin Resonance: Elementary Theory and Practical Applications*; 2 ed.; Chapman and Hall: New York, 1986.

5)Gordy, W. *Theory and Applications of Electron Spin Resonance*; John Wiley & Sons, Inc.: New York, 1980; Vol. 15.

6)Poole, C. P. *Electron Spin Resonance: A Comprehensive Treatise on Experimental Techniques*; 2 ed.; John Wiley & Sons, Inc.: New York, 1983.

7)Poole, C. P.; Farach, H. A. *Theory of Magnetic Resonance*; 2 ed.; John Wiley & Sons, Inc.: New York, 1987.

8)McMillan, J. A. *Electron Paramagnetism*; Reinhold Book Corporation: New York, 1968.

9)Mims, W. B. *Phys. Rev. B* **1972**, *5*, 2409-2419.

10)Norris, J. R.; Thurnauer, M. C.; Bowman, M. K. *Electron Spin Echo Spectroscopy and the Study of Biological Structure and Function*; in Advances in Biological and Medical Physics, Lawrence, J. H., Gofman, J. W. and Hayes, T. L. ed.; Academic Press, Inc.: New York, 1980; Vol. 17, pp 365-416.

11)McCracken, J. *Electron Spin Echo Envelope Modulation*; in Handbook of Electron Spin Resonance, Poole, C. P. and Farach, H. A. ed.; Springer-Verlag: New York, 1999; Vol. 2, pp 69-84.

12)Kevan, L. *Modulation of Electron Spin-Echo Decay in Solids*; in Time Domain Electron Spin Resonance, Kevan, L. and Schwartz, R. N. ed.; John Wiley & Sons, Inc.: New York, 1979, pp 280-341.

13)Kevan, L. *Development in Electron Spin-Echo Modulation Analysis*; in Modern Pulsed and Continuous Electron Spin Resonance, Kevan, L. and Bowman, M. K. ed.; John Wiley & Sons, Inc.: New York, 1990, pp 231-266.

14)Schweiger, A. *New Trends In Pulsed Electron Spin Resonance*; in Modern Pulsed and Continous Electron Spin Resonance, Kevan, L. and Bowman, M. ed.; John Wiley & Sons, Inc.: New York, 1990, pp 43-118.

15)Keijers, C. P.; Reijerse, E. J.; Schmidt, J. *Pulsed EPR: A New Field of Applications*; North-Holland: Amsterdam, 1989.

16)Liao, P. F.; Hartman, S. R. *Phys. Rev. B* **1973**, *8*, 69-80.

17)Hahn, E. L. *Phys. Rev.* **1950**, *80*, 580-594.

18)Blume, R. J. *Phys. Rev.* **1958**, *109*, 1867-1873.

19)Blum, K. *Density Matrix Theory and Application*; Plenum Press: New York, 1996.

20)Cohen-Tannoudji, C.; Diu, B.; Laloe, F. *Quantum Mechanics*; Herman: Paris, 1977; Vol. 1.

21)Feynman, R. P. *Statistical Mechanics: A Set of Lecture Notes*; W.A. Benjamin: Reading, Massachusetts, 1972.

22)Slichter, C. P. *Principle of Magnetic Resonance*; Springer-Verlag: Berlin, 1978.

23)Mims, W. B. *Phys. Rev. B* **1972**, *6*, 3543-3545.

24)Dikanov, S. A.; Shubin, A. A.; Parmon, V. N. *J. Magn. Reson.* **1981**, *42*, 474-487.

25)Rowan, L. G.; Hahn, E. L.; Mims, W. B. *Phys. Rev. A* **1965**, *137*, A61-A71.

26)De Groot, A.; Evelo, R.; Hoff, A. J. *J. Magn. Reson.* **1986**, *66*, 331-343.

27)Blumberg, W. E.; Mims, W. B.; Zuckerman, D. *Rev. Sci. Instrum.* **1973**, *44*, 546-555.

28)Fauth, J. M.; Schweiger, A.; Braunschweiler, L.; Forrer; Ernst, R. R. *J. Magn. Reson.* **1986**, *66*, 74-85.

Chapter 2

INTRODUCTION TO FET3 PROTEIN , A MULTICOPPER OXIDASE FROM YEAST *SACCHAROMYCES CEREVISIAE*

Copper-containing enzymes and proteins are ubiquitously distributed among animals and plants. The copper ions of these proteins maybe involved in electron transfer, participate directly in the catalytic process or may act only as internal cofactors. Copper enzymes involved in the activation of molecular oxygen are classified as oxygenases or oxidases. Oxygenases activate molecular oxygen for incorporation into organic substrates. If one atom of the dioxygen is incorporated it is classified as a monooxygenase, while dioxygenases catalyzes incorporation of both the two atoms of molecular oxygen into the substrate. Oxidases, on the other hand, couple one-, two- or four- electron oxidation of substrates to one-, two- or four-electron reduction of dioxygen to hydrogen peroxide or water.[1]

The Fet3 protein,[2,3] an extracellular membrane-bound enzyme found in yeast, is an oxidase. It is a multicopper oxidase meaning it has multiple copper active sites that are structurally and spectroscopically different from one another. It plays role in iron homeostasis in yeast and has been studied to gain insight into the iron regulation and metabolism of higher eukaryotes.

This chapter presents an introduction to the Fet3 enzyme. The coordination chemistry of copper of copper, its EPR and absorption properties, and its redox properties will be discussed. The second part of this chapter will focus on

multicopper oxidases, with emphasis to Fet3 and ceruloplasmin, both of which exhibit ferroxidase activity.

2.1 Coordination of Cu(I) and Cu(II)

Regardless of whether copper ions are directly involved in the catalytic process, they change redox states during reaction with a substrate as electrons are transferred between the copper ion and the substrate or between copper ion and other redox partner. The predominant oxidation states of copper in biological systems are the +2 and +1 oxidation states. A neutral copper has a valence-shell configuration of $3d^{10}4s^{1}$. Removal of one electron will result in Cu^{+1} with $3d^{10}$ electron configuration. Because the electrons are paired in the d orbitals, Cu^{+1} is diamagnetic. Removal of another electron from Cu^{+1} will yield the paramagnetic Cu^{+2} ($3d^{9}$) species. Although further oxidation to Cu^{+3} is possible, Cu^{+3} compounds are short lived.

The oxidation state of copper determines the stereochemistry of the copper complex. Table 2.1 lists the common coordinations and stereochemistries of Cu^{+1} and Cu^{+2} complexes. Normally, Cu^{+1}-ligands favor tetrahedral coordination, while those of Cu^{+2} favor a square planar bonding geometry.[4,5]

In biological systems, the ligands of Cu^{+1} and Cu^{+2} can be classified as endogenous and exogenous ligands. The amino acids that bind to the copper ions are called endogenous ligands. Copper binds to these ligands through the nitrogen, oxygen and sulfur atoms which may be located at the N- or C-termini of the polypeptide chain, within the chain or in the side chains. Ligands not derived from

proteins are considered exogenous ligands. Water, hydroxide, oxide and sulfide are examples of these ligands.[1,5]

Table 2.1. Coordination and stereochemistries of Cu^{+1} and Cu^{+2}.

common oxidation	d^n	d shell Z_{eff}	common coord. no.	effective geometry	spin State (s)	ionic radii (Å)
+1	d^{10}	7.85	2	linear	0	0.46
			3	trigonal	0	
			4	T_d*	0	0.60
			6	O_h	0	0.77
+2	d^9	8.20	4	T_d	1/2	0.57
				D_{4h}*	1/2	
			5	C_{4v}	1/2	0.65
				D_{3h}	1/2	
			6	O_h*	1/2	0.73

*favored conformation

The concept of "hard and soft acids and bases" (HSAB)[5] is useful in assigning ligands that may coordinate to a metal center to form stable complex. In this concept, small metal ions and acids that are not easily polarized are classified as "hard" while large and easily polarized metal ions or acids are classified as "soft". Ligands with highly electronegative donor atom are hard bases while polarizable ligands are soft. Generally, stable complexes are either formed by hard acids (metal ions) and hard bases (ligands) or soft acids(metal ions) and soft bases (ligands). HSAB can be applied to copper ligands as well. Thus, we expect that in a copper-protein complex,

the soft ion Cu^{+1} will preferably coordinate ligands having soft donor atoms such as Cys, Cys^- and Met. In the same logic, the harder Cu^{+2} will complex with water Tyr, Tyr^-, Ser, Thr or His which have 'hard' donor atoms, O and N.

Cu^{+3} is the hardest among copper oxidation states. It will only form complexes with hard ligands such as Tyr, Tyr^- and OH^-, because soft ligands will reduce Cu^{+3}. Although amino acid ligands that form stable complexes with Cu^{+3} are available, Cu^{+3} has yet to be found in a protein or enzyme. One reason is that, redox reactions involving Cu^{+3} active site require extremely high reduction potential. Such high magnitude of potential has not yet been needed biologically. The simple reason, however, could be that while Tyr, OH^-, and Tyr^- are hard enough to stabilize Cu^{+3}, such complexes may not be stable enough to provide part of the active site of an enzyme.[4]

2.2 Classification of Copper-Binding Sites

Based on spectroscopic data obtained from copper in its d^9 (i.e. Cu^{+2}) electronic configuration, copper binding sites are traditionally classified as type -1, type-2 and type-3 sites.[6-9] These spectroscopic properties reflect differences in their electronic and geometric structures.

According to ligand-field theory, when copper and other transition metals are placed in an octahedral ligand field, the five degenerate 3d-orbitals will be lifted into two sets of degenerate orbitals - (a) t_{2g} (triply generate) and (b) e_g (double generate) sets.[10] The manner of splitting is consequence of the way the lobes of the different d-orbitals are directed to the ligands. The d_{xy}, d_{xz}, d_{yz} orbitals are directed

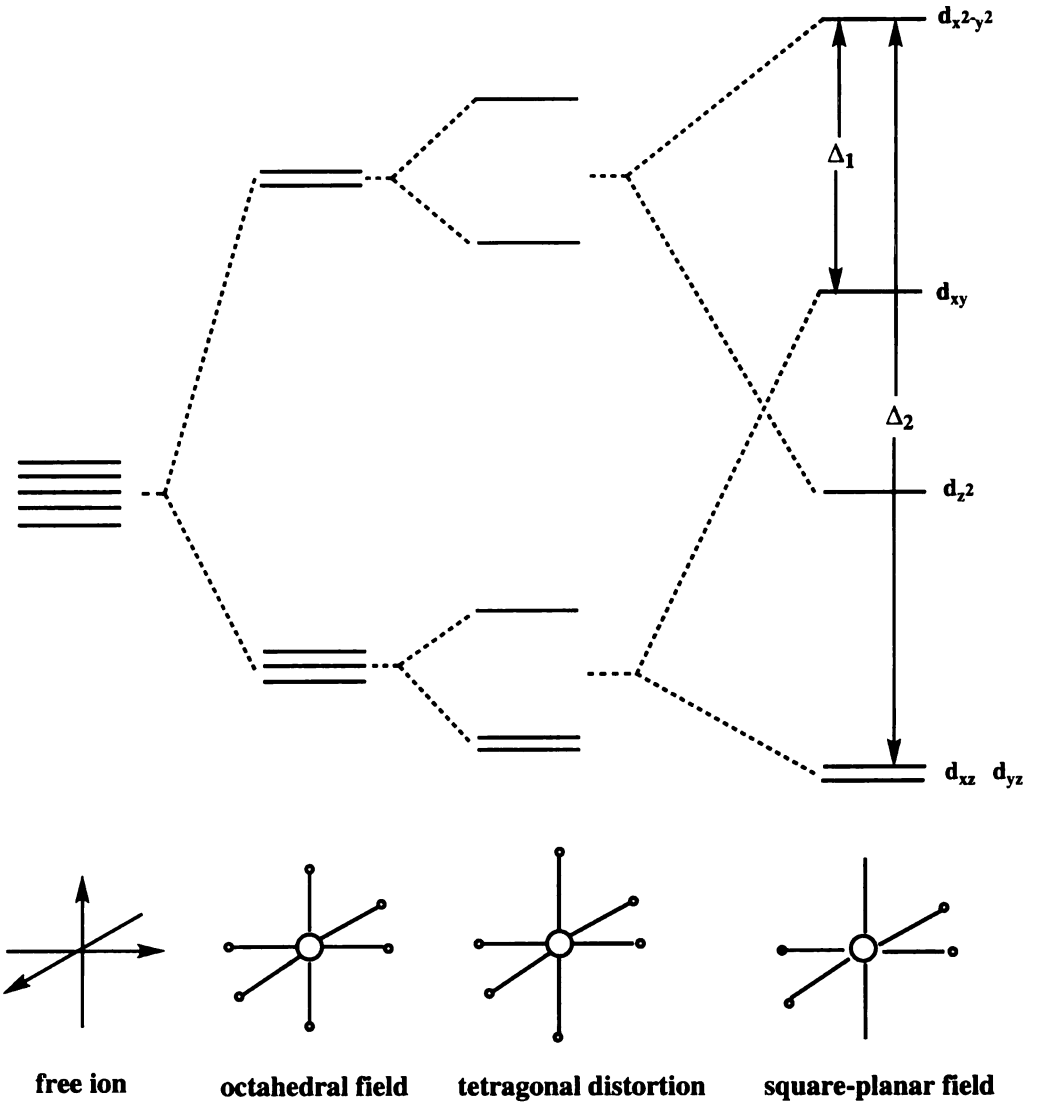

Figure 2.1. Splitting of a d-orbitals in an octahedral, tetragonal or square-planar ligand field.

between the ligands whereas the lobes of the d_z^2 and d_x^2-$_y^2$ are directed toward the ligands. Consequently, the d_z^2 and d_x^2-$_y^2$ orbitals are repelled more than the d_{xy}, d_{xz}, d_{yz}. Following Jahn-Teller theorem,[10,11] further splittings will occur as a result of tetragonal distortion in which distance of the ligand at the z-axis is lengthen and the ligand at x and y are contracted. In the limit of tetragonal distortion, the ligands at z-axis are completely withdrawn leaving a square planar arrangement. Distribution of the valence electrons in Cu^{+2} among the 3d-orbitals will result in the unpaired spin residing in the d_x^2-$_y^2$ orbital (Figure 2.1).

The unpaired electron makes Cu^{+2} amenable to EPR studies. Shown in Figure 2.2 is a typical powder EPR signal of Cu^{+2} in frozen solution. It is a characterized by an axial g-tensor with $g_{\|} > g_{\perp} > g_e = 2.0023$. As explained in the first chapter, the deviation of the g-values form the g_e is attributed to spin-orbit coupling. For an axial Cu^{+2} system in a square planar ligand field, the g values at the canonical orientations are,[12-15]

$$g_z = g_{\|} = g_e + 8\lambda/\Delta_1 \qquad (2.1a)$$

$$g_x = g_y = g_e + 2\lambda/\Delta_2 \,. \qquad (2.1b)$$

where the Δ's are energy differences as defined in Figure 2.1. The above equations were derived assuming an electrostatic interaction, that is the unpaired electron spend most of its time in the $3d_x^2$-$_y^2$ orbital. Usually, the calculated g values using these equations are greater than the experimental g-values, indicating that there is too

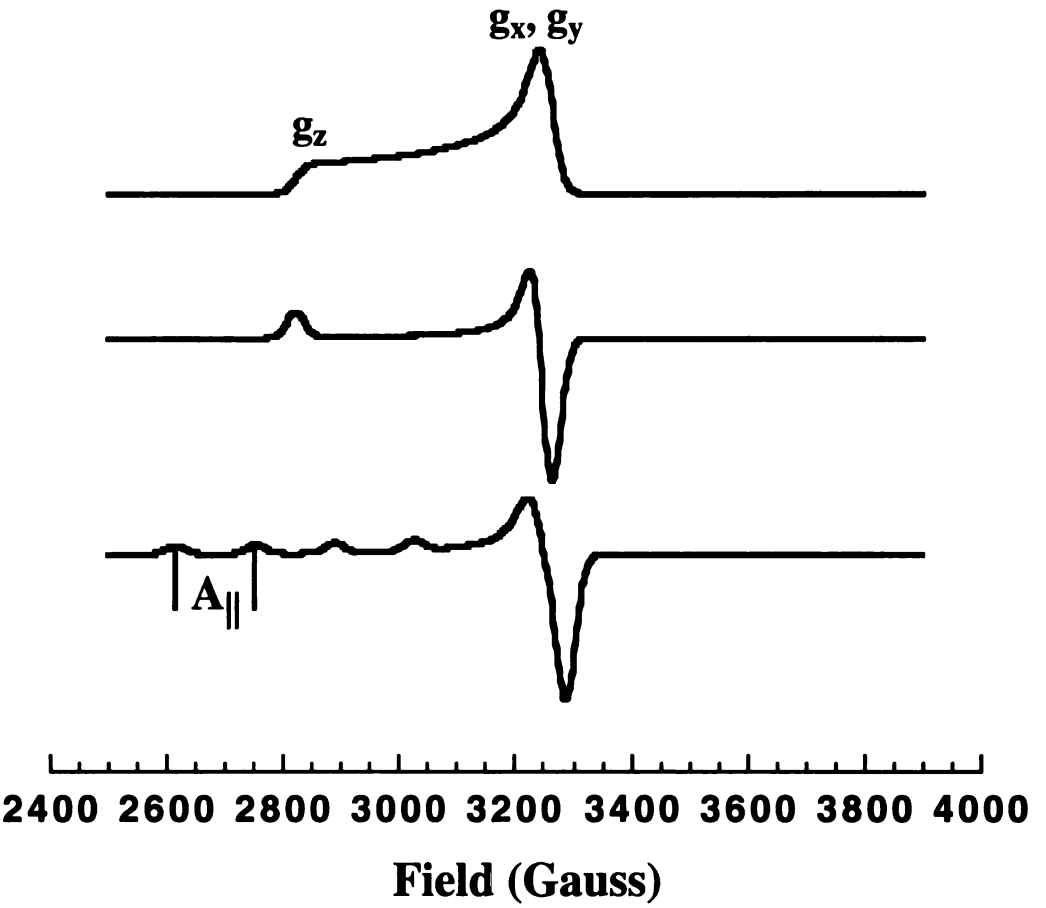

Figure 2.2. Theoretical CW-EPR spectra of Cu(II)-aquo complex. A) Absorption spectum, B) first derivative spectrum of A, and C) first derivative spectrum showing hyperfine interaction in the $g_{||}$ region.

much angular momentum added to the ligand field ground state wavefunction. This deviation arises from the fact that ligand field calculation uses pure d orbitals. One way to correct this discrepancy is to write the ground state function in terms of molecular orbital of the d orbital and ligand orbital. Covalency or delocalization of the electron into the ligand reduces the angular momentum associated with a molecular orbital and therefore calculation should include its effect. A ligand molecular orbital (MO) treatment for calculating Cu^{+2} g values are discussed in several papers.[13,16-18]

In the $g_{\|}$ region of the EPR spectrum, additional peaks are observed because of the Cu^{+2} hyperfine interaction. Cu^{+2} possesses a nuclear spin I = 3/2, which will couple to the unpaired electron spin to yield (2I + 1) resonances. Often times, the principal axes of the metal hfi and the g-tensor are coincident so that assignment of the hyperfine coupling constant is not complicated. Generally, the hyperfine parallel splittings, $A_{\|}$, for normal tetragonal Cu^{+2} complex are large ranging from 150 to 250 $\times 10^{-4}$ cm^{-1}. The perpendicular hyperfine coupling constants, $A_{\perp}$, are small (<35×10-4 cm-1) and most often will not be resolved but will appear as broadening in the powder spectrum. Mathematically, the hyperfine coupling constants are given by[14,19]

$$A_{\|} = -Pd(\kappa + \frac{4\alpha^2}{7} - \frac{3\Delta g_{\perp}}{7} - \Delta g_{\|}), \qquad (2.2a)$$

$$A_{\perp} = -Pd(\kappa - \frac{2\alpha^2}{7} - \frac{11\Delta g_{\perp}}{14}) \qquad (2.2b)$$

where $P = 2\beta g_n \beta_n \langle r^{-3} \rangle = 396 \times 10^{-4}$ cm^{-1}, κ is the Fermi contact and α^2 is the percent metal character in the $d_{x^2-y^2}$ orbital.

Cu^{+2} is also accessible to UV/Vis absorption studies. Absorption bands (Figure 2.3) can be assigned as d-d transitions and ligand-to-metal charge transfer (LMCT) transitions. Because the orbitals are split by the ligand field, the d-d

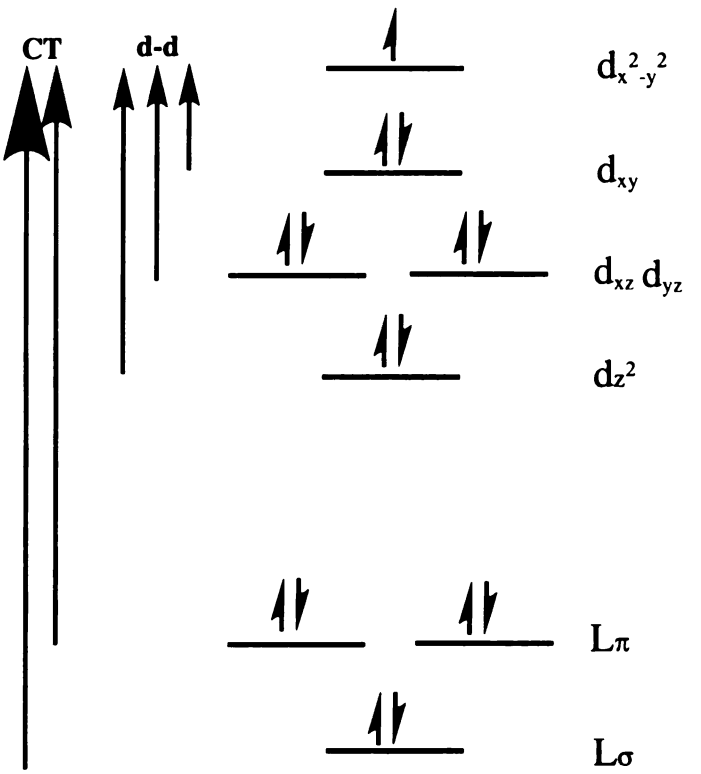

Figure 2.3. Absorption Spectroscopy. d-d and ligand to metal charge transfer (LMCT) transitions observed for a d^9 copper.

transitions are a sensitive probe of geometry of the copper-complex. For example, tetragonal complexes exhibit d-d transitions in the region from region ~500nm to 1 μm. Copper-complexes that are constrained to assume tetrahedral geometry have d-d

transition in the range of 1-2 μm. LMCT are high energy transitions. They provide information on the degree of overlap between the metal and ligand orbital.[8,19]

Type-1, type-2 and type-3 copper sites have characteristic EPR and absorption properties.[4,6-9] The deep-blue colored type-1 copper centers show characteristic absorption bands at approximately 600nm with molar extinction coefficients, ε, of about $5000M^{-1}\ cm^{-1}$. This band is assigned to a cysteine-sulfur to copper charge transfer transition. The cysteine-copper bond is covalent and is one of the reasons why the $A_{\|}$ of copper ($43\text{-}95 \times 10^{-4}cm^{-1}$) is smaller compared to those of tetragonal complexes. Because of the covalent character of this bond, the unpaired spin is delocalized into cysteine ligand and thus reduces the interaction of the Cu nuclear spin with that of the unpaired electron spin. Plastocyanin is an example of a well-studied type-1 copper site. Like other type-1 coppers, it functions as an electron transfer agent. The metal is characterized by a high positive reduction potential and ligands which are diposed in space to assume a structure that is a compromise of Cu^{+1} and Cu^{+2} stereochemistries. Type-2 copper sites feature tetragonally-distorted octahedral coordination geometries similar to those typically found for Cu^{+2} in solution. They exhibit EPR spectrum that have $A_{\|}$ in the range from 158 to $201\times10^{-4}cm^{-1}$. Although they exhibit d-d transitions, they are very weak so that they are often not detected in the optical spectrum These copper sites are found in oxidases, oxygenases, nitrite reductases and Cu/Zn superoxide dismutase where they are directly involved in oxygen metabolism. With regards to ligation, type-2 copper sites are not as uniform as type-1 copper sites which have generally a conserved 2Histidine and 1Cysteine equatorial ligation. One common feature, however, is that

at least one histidine ligand is coordinated and there is one coordination site that is always free for oxygen binding. Type-3 copper sites are binuclear centers that are antiferromagnitacally coupled. The two copper ions are covalently linked by bridging ligand OR^-, allowing the unpaired spins to couple and thus making the binuclear sites EPR-silent. Type-3 copper sites show a strong absorption band at about 330nm with ε~3000-5000$M^{-1}cm^{-1}$ and is believed to be due to ligand(OR^-)-metal charge transfer transition. These copper sites can be found in hemocyanin and tyrosinase.

There are other copper-binding centers that do not belong to the above classifications. Among these are the trinuclear sites comprised of a single type-2 and single type-3 copper center,[20-26] the binuclear Cu_A found in cytochrome oxidase[27-30] and nitrous oxide reductase,[30,31] Cu_B-heme in cytochrome c[32] and recently the Cu_Z in nitrous oxide reductase[33,34]. Except for the trinuclear copper sites, these copper centers will not be discussed in this dissertation. Trinuclear copper centers will be discussed in the multicopper oxidase section of this chapter.

2.3 Redox Behavior of Copper Complexes

As mentioned previously, Cu^{+1} ligand complexes will favor a tetrahedral conformation, while those of Cu^{+2} will favor a square planar conformation. However, in the copper-binding sites of proteins, ligands and conformations may differ greatly from those normally preferred. To be a relevant component in biological catalysis, the copper-binding centers must be able to change oxidation states with relative ease thermodynamically. A compromise between ligands and

conformations of Cu^{+1} and Cu^{+2} must occur to optimize the redox potentials for specific processes. This is particularly true for type 1 copper whose primary function is long-range electron transfer.

In aqueous solution, the redox potential of the redox couple Cu^{+2}/Cu^{+1} is E°_{red} = +153 mV[35]. This is in contrast to the relatively high positive reduction potentials, E°_{red} ,that are found in copper proteins complexes specially in type 1 copper which varies from 183 mV for stellacyanin to 765 mV in type 1 copper site laccase.[4] The relatively high reduction potentials of copper sites means that Cu^{+1} is stabilized more than the Cu^{+2} species. Ligand-binding interactions, hydrophobicity of environment and solvent accessibility of the metal site are variables that affect the reduction potential of the Cu^{+2}/Cu^{+1} protein complex.[36-48]

Studies on model copper complexes were made to determine the effect of replacing water ligands with ligands having N and S donors on the E°_{red} of the Cu^{+2}/Cu^{+1} half-redox reaction. Yandell et al. were able to correlate the potentials observed for the copper complex models to the equation[37],

$$E^{\circ}_{red} = E^{\circ}_{Cu+2/Cu+1} + \Sigma(n_L \Delta E_L) \qquad (2.3)$$

where $E^{\circ}_{Cu+2/Cu+1}$ is the standard reduction potential of the aqueous Cu^{+2}/Cu^{+1} couple, ΔE_L is the variation in redox potential introduced by a donor atom in ligand L which displaces the water ligand and n_L is the number of occurrences of ligand L. Replacement of water by thioether sulfur substantially increases E°_{red}. The effect of nitrogen donor is dependent whether they are aromatic or saturated.

The disposition of the ligands which define the geometry of the complex also affects the reduction potential of the copper complex. Tripodal ligands that force the

copper(II) complex to assume a distorted tetrahedral geometry increase the reduction potential of the Cu^{+2}/Cu^{+1} couple appreciably.[39] We may expect therefore that for the same set of ligands, higher reduction potentials for complexes with almost tetrahedral structure than for those complexes whose ligands are distributed in square-planar arrangement will be observed. A study on the effect of the geometry on redox potential was done by Addison and Yokoi.[38]

The observed variation of E^{o}_{red} in model complexes can be translated to copper proteins. The E^{o}_{red} of a protein Cu^{+2}/Cu^{+1} couple can be increased by introducing π-acceptor or "soft" ligands such as the thioether (Met) and thiolate(Cys) which favor Cu^{+1} to the copper binding sites. Therefore some copper bindings sites are ligated with soft ligands that favor Cu^{+1} and hard ligands that favor Cu^{+2}. A positive E^{o}_{red} can also be achieved by destabilization of the Cu^{+2} ion and this can be done by constraining the geometry of the metal center to those of low LFSE which usually favor Cu^{+1}. A typical example of this is the small type 1 copper plastocyanin in which the structure of the oxidized form is a distorted tetrahedron. Plastocyanin has the typical conserved ligation His_2Cys comprising the equatorial ligands. An axial Met ligand which is ~3.0 Å from the copper center is also present. From electronic structure studies of both Cu^{+1} and Cu^{+2} species by Solomon et al, it was suggested that the elongated axial Cu-Met bond contribute to the high-reduction potential of the plastocyanin. This elongated bond allows for a small change in the geometry as copper changes oxidation states and consequently a low Frank-Condon barrier or reorganizational energy suitable for fast electron transfer.[45,46]

In addition to choice of ligands and the geometry imposed by the ligands on the metal center, the reduction potential of the copper protein couple is also dependent on the dielectric constant of the protein matrix and/or solvent accessibility of the copper site. Because of low charge of Cu^{+1} complex, a hydrophobic environment will favor Cu^{+1} with respect to the Cu^{+2} species. This will result in the more positive reduction potential as compared to those observed in aqueous solution. Access of solvent water to the metal center can be limited by the choice of ligands. Amino acids with bulky hydrophobic side chains will inhibit entry of water to the metal site and will result in the stabilization of Cu^{+1} with respect to Cu^{+2}. Experimentally, these ideas have been proven using systems with type 1 copper proteins.[44]

A theory to account the effect of solvation of metal-protein complex was developed by Churg and Warshel.[41] Their explanation is based the on the thermochemical concept that the standard free-energy change, ΔG°_{red} when adding one electron to an oxidized molecule A^{ox}, to give the reduced form, A^{red}, is related to E°_{red} through the well-known equation

$$\Delta G^{\circ}_{red} = -\mathcal{F}E^{\circ}_{red} + \text{constant.} \qquad (2.4)$$

$\mathcal{F}$ in the above equation is the Faraday constant. The above equation can be used to determine the environmental effects of different solvents upon the reduction of the of some molecule A^{ox}. The relation of solvation energy and change in redox potential is given by,

$$-\mathcal{F}E^{\circ}_{red} = \Delta[\Delta G^{\circ}_{solv}(A^{ox}) - \Delta G^{\circ}_{solv}(A^{red}) = \Delta\Delta G_{solv} = \Delta\Delta G^{\circ}_{red}. \qquad (2.5)$$

$\Delta\Delta G_{solv}$ is approximated to be equal to the sum of (i) the interaction of complex

charge and protein permanent dipoles, (ii) the interaction of complex charge and the induced dipoles of associated with polarizable atom, (iii) solvation energy of the complex by the surrounding water molecules and the (iv) interaction of complex with ionizable groups. This mathematical approach has been applied to explain the redox variation of redox potential of cytochrome c and the octapeptide-methionine/histidine complex formed by the hydrolysis of cytochrome.

To sum up the points discussed in this section, metalloproteins (i.e. copper protein) tune their redox potentials for specific reactions by the appropriate choice of ligand, a compromise between the structure of oxidized and reduced forms of the metalloproteins and control of solvent access to the metal center.

2.4 Multicopper Oxidases

Multicopper oxidases are class of enzymes that contain type-1, type-2 and type-3 copper centers.[8,9] These blue oxidases couple the four-electron reduction of dioxygen to water to the four-electron oxidation of a substrate. Among the well-characterized multicopper enzymes are laccase (Lc), ascorbate oxidase(AO) and ceruloplasmin (Cp). Recently, an enzyme from yeast, Fet3[2,3], has been identified as belonging to this group. All of these enzymes oxidize their substrate by one electron processes.

Laccases are widely distributed in plants and fungi where they catalyze the oxidation of numerous aromatic phenols, amino phenols and diamines via complete reduction of dioxygen to water. By far the most studied plant laccase is the *Rhus vernicifera*. It was discovered by Yoshida in 1883[9]. Plant laccases are believed to be

involved in lignin formation and wound healing. Fungal laccases have been isolated and purified from various sources such as basidiomycetes, ascomycetes and deueromycetes. They are postulated to be involved in sporolation, pigment formation, lignin degradation, and pathogenesis.

Ascorbate oxidase occurs exclusively in higher plants. The two most common sources of these enzymes are cucumber and green zucchini squash. It is thought the enzyme play a role in ripening, growth control and disease control.

Ceruloplasmin is an enzyme that is found in the plasma of mammals and birds. At least four functions have been attributed to ceruloplasmin, those of copper transport and, ferroxidase activity[49], amine oxidase activity and as an antioxidant.[9,50] A wide range of organic and inorganic compounds may be utilized as substrates. However, biological and kinetic data indicate that the physiologically

Table 2.2. Distribution of Copper in Some Multicopper Oxidases.

Enzyme	Type 1	Type 2	Type 3	Reference
Laccase	1	1	1	8,71
Ascorbate Oxidase	2	2	2	24,25
Human Ceruloplasmin	3	1	1	26
Fet3	1	1	1	57,59

relevant substrate of ceruloplasmin is Fe (II). Plasma ferroxidase activity is essential to iron homeostasis in human.[51,52]

1.5 Fet3 as a multicopper oxidase

As a multicopper oxidase, Fet3 oxidizes four moles of iron and concomitantly reduces molecular oxygen to water. The role of Fet3 as a multicopper oxidase is supported by several studies. Sequence analysis revealed an open reading frame with homology to other multicopper oxidases such as laccase, ascorbate oxidase and ceruloplasmin. Homology is particularly strong in the regions that are involved in the binding of the catalytic Cu^{+2} prosthetic groups. The copper catalytic domain is exposed on the extracellular side of the plasma membrane and is attached to the plasma membrane by a single transmembrane unit. This configuration implies that another molecule is needed to transport iron across the cell membrane. Ftr1 with multiple transmembrane domains and a potential ferric binding motif is the apparent transporter which is believed to form complex with Fet3.[53-55] Enzymatic activity studies also supported Fet3 as a multicopper oxidase and confirmed its ferroxidase activity.[3,56,57] Experiments have shown that the best substrate for Fet3 is the ferrous ion.[55] Yeast cells that were grown in copper-deficient media, had profound deficiency in iron transport which was directly related to the absence of ferrous activity[3,58]. Addition of copper restored iron transport activity. This implies that copper loading of apo-Fet3 is essential for multicopper activity. Studies on Fe(II)-dependent O_2 consumption[3] by yeast cells provided evidence of Fet3's ferroxidase activity in that an approximate 4:1 ratio of the rate of Fe(II) oxidation to O_2

consumption was revealed. Its relevance to high-affinity transport is supported by the absence or reduction of O_2 consumption in cells with mutated Fet3, cells grown in high iron-media and cells grown in copper-free media. O_2 consumption using cells stripped of cell walls also indicated that the ferroxidase domain of Fet3 is located on the extracellular surface because removal of the yeast cell wall did not hinder iron-induced increase in O_2 consumption but addition of trypsin did.

In addition to sequence analysis and catalytic activity studies, support for the multicopper sites of Fet3 comes from the characteristic UV/VIS absorption bands and CW-EPR spectra of wild-type Fet3.[57,59] Four copper cofactors have been determined based on the atomic absorption spectroscopy analysis. Spectroscopically, these copper sites can be differentiated as type-1, type-2 and a binuclear cluster, type-3. Type-1 and type-2 are paramagnetic whereas type-3 site is EPR-silent. This is evident in the overlap of EPR signals coming from type-1 and type -2 copper sites. The type-3 copper site is EPR inactive because a hydroxide (OH^-) bridges the copper. Absorption spectroscopy was used to detect the presence of a type-3 copper in Fet3. The absorption band at 300 nm is assigned to OH^- to metal charge-transfer transition. Another intense absorption band is observed at 600 nm and assigned to type -1 copper site. As expected, no detectable UV-Vis absorption due to type-2 copper site was observed.

2.6 Tri-nuclear cluster

Type-2 and type-3 copper sites in multicopper oxidases are believed to form a trinuclear site. This trinuclear copper site is considered to be the binding and

reduction site for molecular oxygen. Support for the existence of a trinuclear site includes the azide binding and oxygen reactivity studies on laccase, the crystal structure of AO from Zucchini and the kinetic and crystallography studies on human ceruloplasmin (hCp).[20-26]

The copper sites in plant laccase from *Rhus Vernicifera* have been extensively studied by Prof. Solomon's group at Stanford University. With the help of laccase variants, they were able to suggest that type-2 and type-3 Cu sites form a trinuclear cluster necessary for oxygen binding.[22,64,65] The type-2 copper can be selectively chelated to produce a type-2 depleted (T2D) laccase variant containing only type 1 and type 3 copper centers. Type-1 copper can be selectively replaced by Hg^{+2} (T1Hg) leaving the type-2 and type-3 copper sites intact. The use of these variants avoids difficulty in spectral analysis as the contribution of either one of the paramagnetic copper sites is eliminated. As we will find later, similar technique was used in the spectral analysis of Fet3 by EPR.

Azide binding studies in both native laccase and T1Hg laccase utilized low-temperature magnetic circular dichroism (LTMCD), absorption and EPR spectroscopies. Results of these studies indicated that azide bridges the type 2 and the type 3 copper suggesting that type 2 copper is near to type 3, (<5.2 Å) and therefore capable of forming a trinuclear cluster.[20,21,23] A combination of these spectroscopic techniques allowed ligand field (d-d) and charge-transfer (CT) spectral features associated with the paramagnetic type-2 center to be differentiated from those of the antiferromagnetically coupled type-3 center.

Further proof of a trinuclear site came from the study dioxygen reactivity using X-ray absorption edge spectroscopy.[22] Qualitatively, a preedge 1s-4p transition, assigned empirically from polarized single-crystal studies by Smith et al.[66], near 8984 eV is present in the X-ray edge absorption spectra of Cu(I) but is absent in Cu(II) spectra. Thus, the 8984 eV feature is useful in probing the reduced copper site and its coordination environment. Exposure of T2D with oxidized type 1 and reduced type 3 copper sites to air, did not result into the substantial change in the appearance of the 8984 eV feature. Similar results were obtained for the T2D laccase where both the type-1 and type-3 copper sites were reduced. This means that none of the reduced copper sites were oxidized and therefore no reaction with O_2 occurred. However, exposure of fully reduced T1Hg laccase to air resulted in the total lost of the 8984 eV transition. The results implies that the trinuclear cluster represents the minimum structural unit for the reduction of molecular oxygen.

The existence of a type2-type3 trinuclear cluster is also supported by the x-ray crystallographic studies on ascorbate oxidase by Albrecht Messerschimdt et al.[24,25] The crystal structure resolved at 1.9 Å of AO from Zucchini revealed that the multicopper oxidase is a homodimeric enzyme with subunits weighing 70 kD and a chain length of 552 amino acids. Each of the subunits or each monomer, like laccase, consists of three domains and contains four copper atoms. These domains are characterized by β-strand. Domain 1 is made up of two four-stranded β-sheets forming a β-sandwich structure. Six-stranded and a five-stranded β-sheet comprise domain 2. The final domain 3 is shaped by two five-stranded sheets forming a β-barrel and a four-stranded β -sheet. The type 1 copper is located in domain 3 and the

trinuclear copper center is situated between domains 1 and 3. The binding site for the reductant is on the surface of the enzyme, near the type 1 copper center. The oxygen binding site, i.e. the trinuclear copper center, is embedded inside the enzyme and accessible by two channels of different sizes.

The mononuclear type- 1 copper in domain 3 is coordinated by His445(Nδ), His512(Nδ), Cys507(S), and Met517(S). These ligands are the canonical ligands that are found the mononuclear type-1 copper sites of plastocyanin[67,68] and azurin[69]. Like these two type-1 copper centers, the methionine forms a distant noncoordinating axial ligand. The trinuclear copper site, consisting formally of type 2 and type 3 copper centers, requires eight histidines, one OH^- or (O^{2-}) and a second OH^- (or H_2O) coordination. Six of the eight histidine ligands coordinate to both copper ions of the type 3 copper center to form a trigonal prismatic structure. The two copper centers of the type-3 site are inequivalent with respect to histidine nitrogen ligation. Histidine ligands of the first copper ion include His102(Nε), His450(Nε) and His506(Nε) and those of the second copper ion are His62(Nδ), His104(Nε) and His508(Nε). Additionally, a OH^- (or O^{2-}) bridge links these two copper atoms resulting in a strong antiferromagnetic coupling. The type 2 copper ion is coordinated by two histidine residues, His60(N^2) and His448(N^2) and possibly by hydroxide or water. These coordinations are shown in Figure 2.4.

In 1996, a 3.1 Å resolution X-ray crystal structure of human serum ceruloplasmin was published and confirmed the presence of a trinuclear cluster in the enzyme.[26] The trinuclear cluster of type-2 and type3- copper sites may therefore be

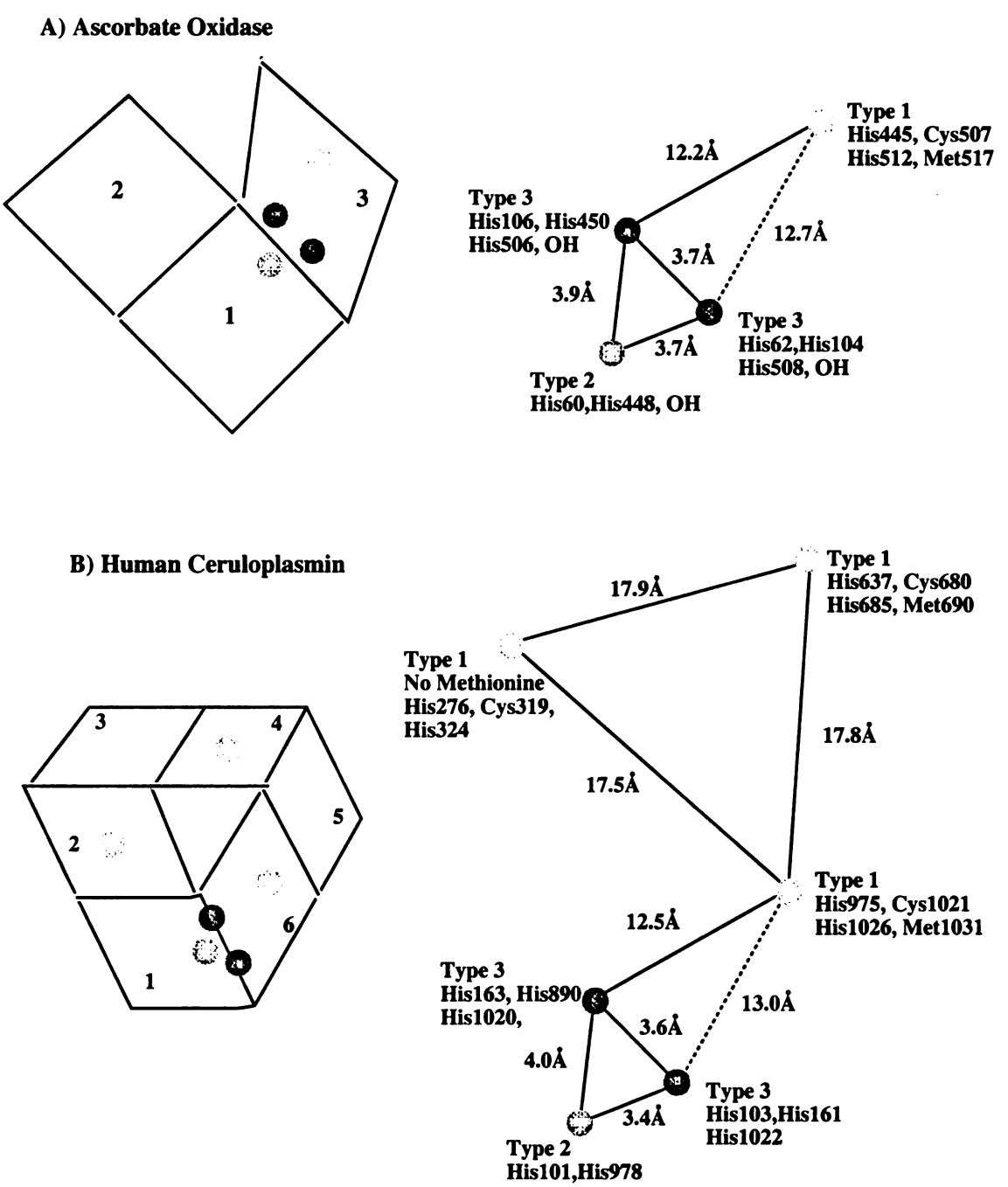

Figure 2.4. Comparison of spatial arrangement of the different copper sites in ascorbate oxidase(AO) and human ceruloplasmin (hCp).

present to all multicopper oxidases. The crystal structure reveals that the molecule is comprised of six plastocyanin-type beta barrel domains arranged in a triangular array (Figure 2.4). It has about 1046 amino acids. There are six copper atoms; three form a trinuclear cluster situated at the interface of domains 1 and 6 and there are three mononuclear sites in domains 2,4 and 6. Each of the mononuclear coppers is coordinated to a cysteine and two histidine residues and those in domains 4 and 6 also coordinate to a methionine; in domain 2 the methionine is replaced by a leucine residue which may form a van der Waals type contact with the copper. The latter type-1 copper was found to be permanently reduced and therefore not relevant to catalysis.[70]

2.7 Mechanism of O_2 Reduction

Figure 2.4 provides the schematic representations of the structure of hCp and AO. The spatial arrangement of the coppers sites domain 1 and 6 of the hCp bears resemblance to the arrangement of the copper sites in the monomeric unit of AO. This leads to the idea that the three copper sites in laccase and Fet3 are geometrically arranged in a similar fashion to AO. In fact, the X-ray crystal structure of type-2 copper depleted laccase from *Coprinus cinerus*[71] confirmed that its type-1 site is approximately 13 Å from the type-3 center.

With resolution of the structure of AO, a mechanism for the catalytic activity of the multicopper oxidase has been proposed. The widely accepted mechanism involves the type-1 site as the primary electron acceptor, abstracting an electron from the reducing substrate and transferring it to the trinuclear site. One relevant structural

feature is that type-1 copper cystiene ligand is placed in between the two histidines that are ligand to type-3 site. This together with the covalent character of the Cys-(type-1 copper) bond, as determined experimentally and theoretically from the studies on plastocyanin[8,46,72], provide an efficient pathway for the delivery of the electron from type-1 to the trinuclear center (Figure 2.5).

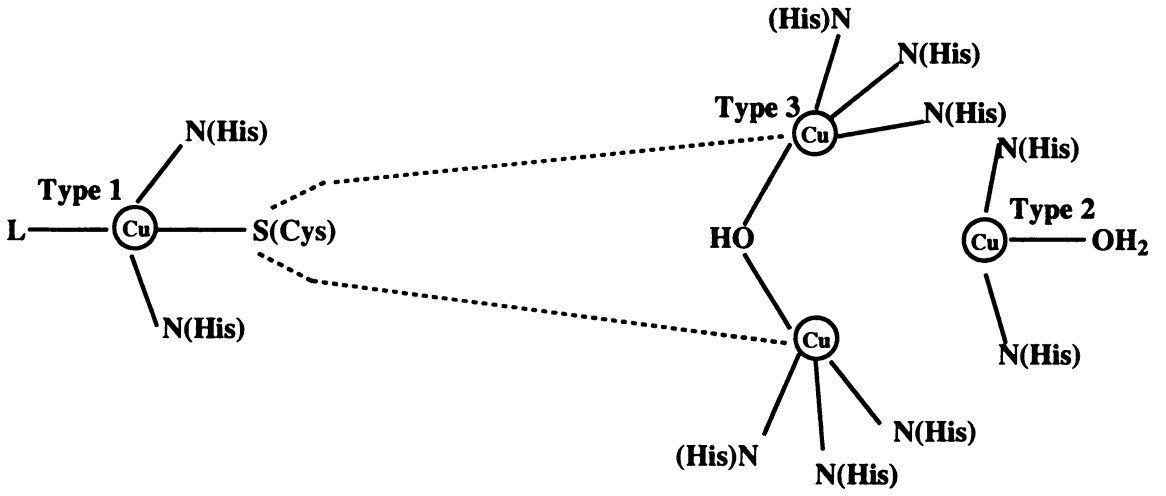

Figure 2.5. A proposed pathway for the transfer of electron from type-1 copper center to type 2-type3 trinuclear center in multicopper oxidases based on the X-crystal structure of ascorbate oxidase from zucchini. The X-ray structure showed the S(Cys) ligand is flanked by two histidines ligands from the two copper ions of the type-3 copper binunclear site. Theoretical calculations predicted the large overlap between the Cu d_{x2-y2} and S(Cys) $p\pi$ orbitals. These two findings provide an efficient pathway for the transfer of electron from the type 1 to the trinuclear copper site.

Binding to oxygen requires all of the copper sites in the enzyme to be fully reduced. This can be achieved by four single-electron reductions of type 1 copper with substrate and transfer of three electrons to the trinuclear copper site. The formation of water upon reaction of dioxygen with the fully reduced substrate may involve formation of an oxygen intermediate, hydro-peroxide or oxygen radical.

2.8 Regulation of Iron Transport in Yeast

Transition metals such iron, copper and zinc play a vital role in biochemical processes in eukaryotes. They stabilize protein structures and act as cofactors in catalysis. Because of their high-redox potentials, they are important components of biochemical redox reactions. Their redox properties, however, also make them potentially harmful because they are capable of generating toxic free radicals if the concentration of these metals in the cell is not tightly regulated. Therefore, a balance between the amount of metal essential for biochemical processes and the amount that is potentially toxic must be maintained. To meet the required concentration, cells utilize a specialized mechanism, controlled transmembrane metal transport.[73 74-76]

The yeast *Saccharomyces cerevisiae* provides an excellent model for the study of metal homeostasis in eukaryotes because its genetics can be easily manipulated. This simple eukaryote employs two transmembrane transport systems, one of low- and the other of high-affinity (Figure 2.6).[73-76] The high-affinity transport system is very specific to its metal target and is regulated according to metal needs, whereas the low-affinity system is less specific for the metal it transports and

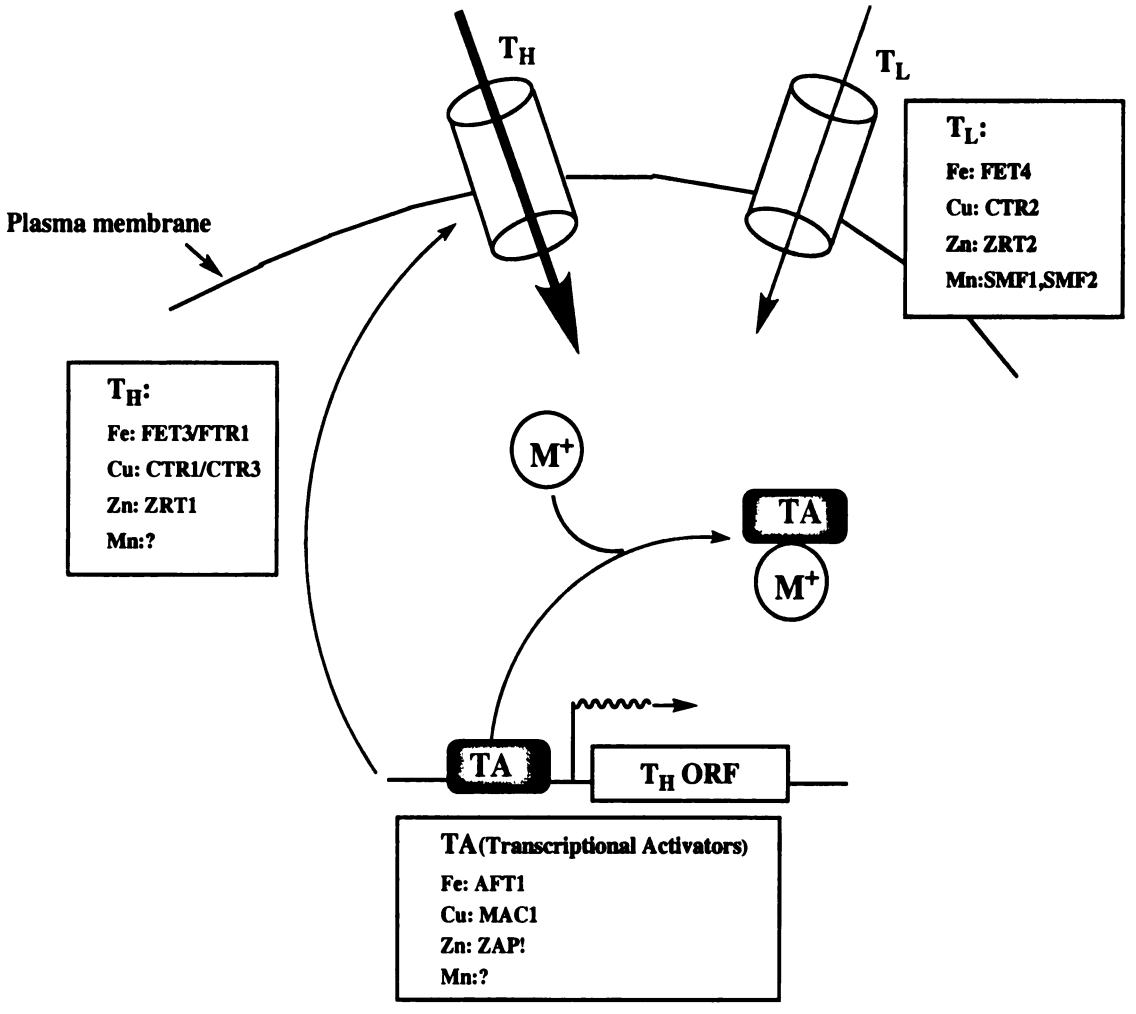

Figure 2.6. Model for the regulation of metal transport in yeast (adopted from Radisky et al., *J. Biol. Chem.*, 1999, 274, 4481-4484). High affinity metal transporters (T_H) are selective for the target metal and are transcribed according to metal need by transcriptional activators (TA) which release DNA upon metal binding. Low affinity transporters (T_L) are less responsive to metal need and are less metal selective. Although Fet4 was identified as low-affinity transporters, it can transport other metals. ORF, open reading frame.

and less responsive to metal requirement. These two transport systems provide for metal homeostasis.

In an iron-replete condition, the low-affinity transport system, (Michaelis-Menten constant, K_m = 30 μM) mediated by the product of Fet4 gene, [77,78] is activated for the transport of iron across the cellular membrane. Fet4, an integral membrane protein localized in the plasma membrane, is a Fe(II) transporter. The low affinity-transport system for iron can also acquire other metals such as manganese and cadmium. Under conditions where iron is limiting, high-affinity iron transport (K_m = 0.15 μM) takes place. An essential component of this transport system is Fet3.

2.9 High-affinity Transport of Iron in Yeast

Two major proteins are involved in the high-affinity transport of iron (Figure 2.7). These are the Fet3 enzyme, an integral membrane protein with an extracellular multicopper domain and Ftr1 (Fe transport) protein, a transmembrane iron permease. Genetics studies[50,53,54] have suggested that these proteins work in concert and that simultaneous expression of these proteins is necessary and sufficient for high-affinity iron transport. Fet3 enzyme acts as a ferroxidase by sequentially converting four moles of Fe^{+2} into Fe^{+3}. The four moles of electrons that are released in the process are transferred to molecular oxygen, thereby reducing it to water. The oxidized iron, then, enters into the cell, where it may then be utilized for cellular processes, via the transmembrane permease, Ftr1. Ftr1 has six potential transmembrane units and an iron-binding motif similar to that found in mammalian ferritin.[53] Similar to low-affinity iron transport, the activity of the cell surface ferrireductases, Fre1 and

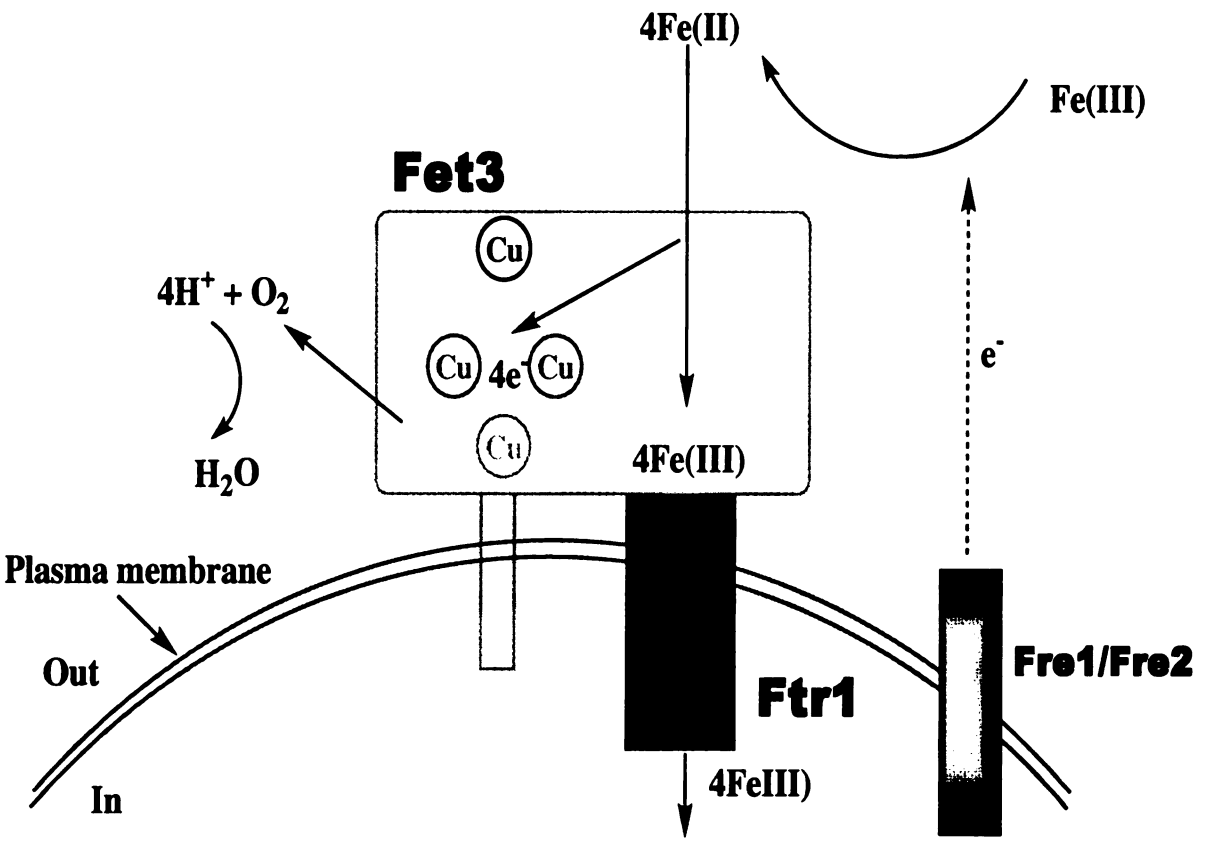

Figure 2.7. High-affinity uptake of iron across the cell of yeast. The essential components of the transport system include Fet3, integral membrane exhibiting a ferroxidase catalytic activity, Ftrl the iron transporter and Frel and Fre2, which generate the substrate, Fe(II) for Fet3. The ferroxidase activity of Fet3 is dependent on the three copper centers (one type 1, one type 2 and one type 3) that are localized outside the plasma membrane protein.

Fre2,[79-82] is also required in the high-affinity iron uptake because they convert iron into a soluble form, Fe^{+2} and hence make iron available for transport. The components of the high-affinity transport system are transcriptionally regulated by the product of AFT1 gene[76], an iron responsive DNA-binding protein. Transport of iron via the high-affinity system occurs only under aerobic condition.[83] In an anaerobic environment, the low-affinity transport is operative.

2.10 The Iron-Copper Connection

The ferroxidase activity of the Fet3 protein depends on the presence of the four copper ions. Any defects in the genes and enzymes that are involved in the delivery and loading of copper to apo-Fet3 result in defects in iron uptake. These copper delivery and loading genes/enzymes were identified in the process of searching for the genes involved in iron transport in yeast .

The CTR1 gene encodes the enzyme required for high-affinity transport of copper in yeast. A plasma-membrane protein, Ctr1 is responsible for the trafficking and delivery of copper to various cellular targets.[58,84] One of the cellular destinations is the mitochondria where it is needed to activate cytochrome oxidase. Loading of cytochrome oxidase with copper is mediated by intracellular transporter protein Cox17[85]. Copper can also be loaded via Lys7[86] to the cystolic copper protein, superoxide dismutase. Furthermore, copper ions are also delivered to secretory pathways and one of the targets for this mode of delivery is Fet3. Loading of copper to Fet3 is mediated by a cystolic enzyme Ccc2[87]. The CCC2 gene is

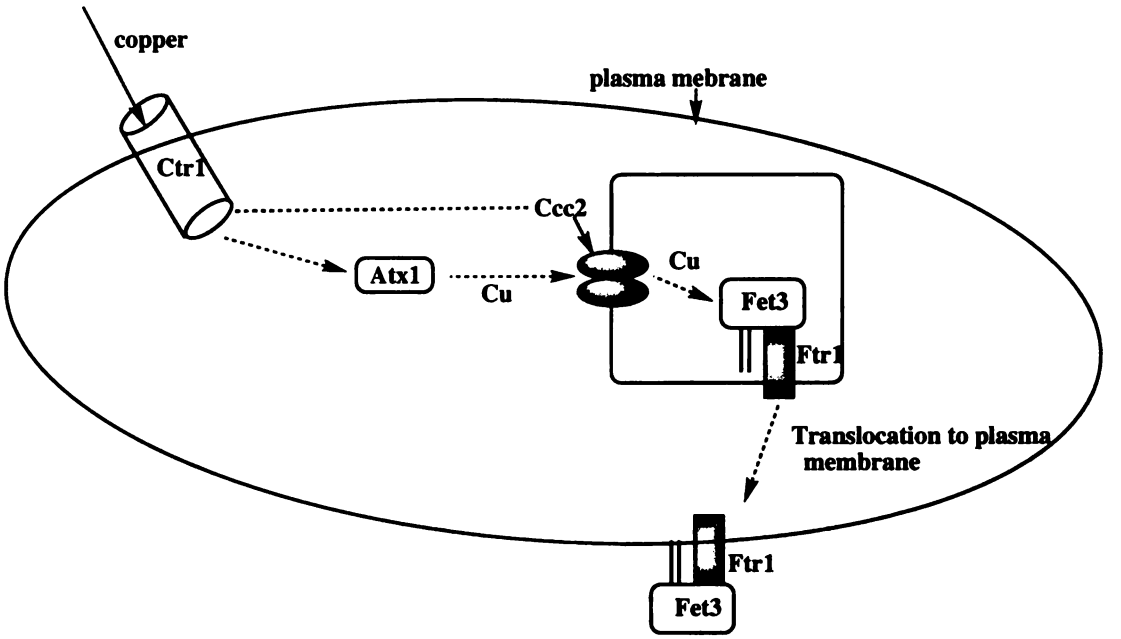

Figure 2.8. Scheme for the delivery and loading of copper to apo Fet3. Two pathways are proposed. The primary route is Ctr1p-Atx1p-Ccc2p-Fet3p. The secondary route involves Ctr1p-Ccc2-Fet3p.

homologous to the human Wilson and Menkes disease genes. Both the yeast and human genes are believed to function in the translocation of copper across intracellular membranes into the secretory pathways. In another pathway, copper can be loaded to apo-Fet3 via the Ctr1-Atx1-Ccc2 route.[88] The ATX1 gene is believed to the cystolic carrier of copper specific for the Ccc2 protein. Therefore, copper can be delivered to Fet3 in two pathways as shown in Figure 2.8. Any defects in the genes involved in the delivery and loading of copper to apo-Fet3 will abrogate the ferroxidase activity of Fet3 and consequently the iron uptake will cease.[58,83-88]

2.11 Ferroxidase Activity Ceruloplasmin

The other multicopper oxidase that exhibits a ferroxidase activity analogous to Fet3 is the serum enzyme from animals, ceruloplasmin. This enzyme is synthesized in the liver and secreted into the serum with six copper atoms, required for the ferroxidase activity, during biosynthesis.[50,51,89] Figure 2.9 shows the involvement of ceruloplasmin in iron mobilization by acting as a ferroxidase, converting ferrous ion to ferric ion. The substrate ferrous ion is released from the cell through a yet to be known enzyme. Two moles of the oxidized iron binds with the transferrin (Tf), an 80-kDa glycoprotein that circulates in vertebrate blood.[89] To transport iron into the cell, the diferric Tf then binds with membrane glycoprotein , transferrin receptor (TfR) . The Tf-TfR complex enters the cell via endocytosis. At the right pH, the ferric ion is released from the complex in the acidified endosome, and transferred to the cell cytoplasm. The iron in the form of Fe^{+3} is then stored in ferritins (Fts). From Ft, iron can be transported to other cellular components. The mechanism of intracellular transport is still ambiguous.[89-92] In the acidified endosome, the apoTf is still complexed with TfR. Ultimately, the apoTf-TfR returns to the surface and in the basic environment of the blood, apoTf is released to harbor more iron.

The ferroxidase activity of ceruloplasmin is supported by several studies.[8,50,89] In 1968, a hematology study, with pigs as the subjects, showed that copper-deficient pigs developed an iron-deficiency anemia. Copper-deficient animals were capable of absorbing iron but were incapable of releasing iron to plasma. Oral and intravenous administration of iron failed to correct the anemia but

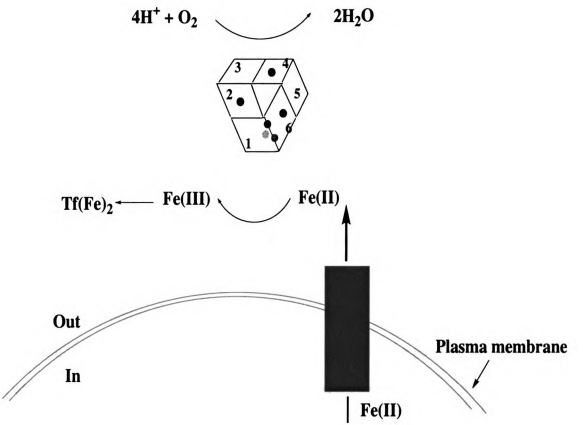

Figure 2.9. Iron mobilization in mammalian plasma. Acting as ferroxidase, ceruloplasmin converts Fe(II), released from the cell via an unknown transporter, to Fe(III). Two moles of Fe(III) subsequently binds with transferrin (Tf) and transported to different cells.

results in the accumulation of iron in duodenal enterocytes and reticulo-endothelial cells. Examination of the animal's blood revealed a deficiency in ceruloplasmin. Administration of ceruloplasmin resulted in the release of iron to the blood and corrected the observed anemia. It is apparent that copper deficiency caused the blockage of iron release from the cell. Implicated in this deficiency is ceruloplasmin, a copper-protein with ferroxidase activity. Copper-deficient pigs have impaired ceruloplasmin activity and cannot oxidize ferrous iron to the ferric state. Therefore, the transfer of iron to the plasma did not occur. The human analogue of this disorder is aceruloplasminemia[93] and is characterized by diabetes, retinal degeneration and neurologic symptoms. Affected patients have parenchymal iron accumulation in conjunction with the absence of serum ceruloplasmin. Molecular genetics analysis reveals inherited mutations in the ceruloplasmin. All of these findings point to the essential role played by ceruloplasmin, ferroxidase activity in iron metabolism.

2.12 Fet3 vs. hCp

Genes that are involved in the loading of copper to Fet3 have human homologues. A putative human plasma-membrane copper transporter with homology to Ctr1 has been identified and is called as hCTR1[94]. As stated before, Menkes and Wilson disease proteins, ATP7A and ATP7B respectively, are homologues of Ccc2.[75,87] Menkes disease is characterized by copper deficiency and Wilson disease by copper overload. ATP7b is expressed in the liver. Defects in and loss of Wilson disease protein, Atp7 result in defective transport into the intercellular vesicle where

ceruloplasmin normally becomes copper loaded. Wilson disease patients show low levels of active ceruloplasmin and may exhibit anemia similar to that observed in copper deficient pigs. Hah1, human homologue of the yeast Atx1 has also been identified.[95] Thus, the genes involved in the transport of copper to the multicopper oxidases appear to be completely conserved between yeast and human. These human genes may be able to substitute for their yeast counterparts allowing the study of the structure and functions of these genes in the host yeast.

The multicopper proteins Fet3 and ceruloplasmin therefore catalyze similar reactions. Both of them exhibit ferroxidase activity. This ferroxidase activity is necessary for the mobilization or transport of iron. They differ in that Fet3 mediates iron uptake whereas ceruloplasmin mediates iron egress.

The main goal of this dissertation is to characterize the structure of two copper sites, the type 1 and type 2 sites of Fet3 using the ESEEM technique in conjunction with CW-EPR. In particular the ligation of these two paramagnetic sites are determined.

List of References:

1)Holm, R. H.; Kennepohl, P.; Solomon, E. I. *Chem. Rev.* **1996**, *96*, 2239-2314.

2)Askwith, C.; Eide, D.; Van Ho, A.; Bernard, P. S.; Li, L.; Davis-Kaplan, S.; Sipe, D. M.; Kaplan, J. *Cell* **1994**, *76*, 403-410.

3)de Silva, D. M.; Askwith, C. C.; Eide, D.; Kaplan, J. *J. Biol. Chem.* **1995**, *270*, 1098-1101.

4)Abolmaali, B.; Taylor, H. V.; Weser, U. *Evolutionary Aspects of Copper Binding Centers in Copper Proteins*; in Structure and Bonding, Williams, R. J. P. ed.; Springer: Berlin, 1998; Vol. 91, pp 91-190.

5)Hughes, M. N. *The Inorganic Chemistry of Biological Processes*; 2nd ed.; John Wiley & Sons: New York, 1981.

6)Reinhammar, B.; Malmstrom, B. G. *"Blue" Copper-Containing Oxidases*; in Copper Protein, Spiro, T. G. ed.; John Wiley & Sons, Inc.: New York, 1981; Vol. 3, pp 110-149.

7)Jameson, R. F. *Coordination Chemistry of Copper with Regard to Biological System*; in Properties of Copper, Sigel, H. ed.; Marcel Dekker: New York, 1981; Vol. 12.

8)Solomon, E. I.; Sundaram, U. M.; Machonkin, T. E. *Chem. Rev.* **1996**, *96*, 2563-2605.

9)Messerschmidt, A. *Blue Copper Oxidases*; in Advances in Inorganic Chemistry, Skykes, G. ed.; Academic Press, Inc.: San Diego, California, 1994; Vol. 40, pp 121-185.

10)Huheey, J. E. *Inorganic Chemistry Principles of Structure and Reactivity*; 3rd ed.; Harper & Row, Publishers, Inc.: New York, 1983.

11)Jahn, H. A.; Teller, E. *Proc. Roy. Soc.* **1937**, *A161*, 220 - 235.

12)Atherton, N. M. *Principles of Electron Spin Resonance*; Ellis Horwood & PTR Prentice Hall: New York, 1993.

13)McGarvey, B. R. *Electron Spin Resonance of Transition-Metal Complexes*; in Transition Metal Chemistry, Carlin, R. L. ed.; Marcel Dekker, Inc.: New York, 1966; Vol. 3, pp 89-201.

14)Abragram, A.; Pryce, M. H. L. *Proc. R. Soc. London* **1951**, *205A*, 135-153.

15)Abragram, A.; Pryce, M. H. L. *Proc. R. Soc. London* **1951**, *205A*, 164-172.

16)Kivelson, D.; Neiman, R. *J. Chem. Phys.* **1961**, *35*, 149-135.

17)Maki, A. H.; McGarvey, B. R. *J. Chem. Phys.* **1958**, *29*, 31-34.

18)Maki, A. H.; McGarvey, B. R. *J. Chem. Phys.* **1958**, *29*, 35-38.

19)Solomon, E. I. *Commun. Inorg. Chem.* **1984**, *3*, 225-319.

20)Allendroff, M. D.; Spira, D. J.; Solomon, E. I. *Proc. Natl. Acad. Sci. USA* **1985**, *82*, 3063-3067.

21)Spira-Solomon, D. J.; Allendroff, M. D.; Solomon, E. I. *J. Am. Chem. Soc.* **1986**, *108*, 5318-5328.

22)Cole, J. L.; Tan, G. O.; Yang, E. K.; Hodgson, K.; Solomon, E. I. *J. Am. Chem. Soc.* **1990**, *112*, 2243-2249.

23)Cole, J. L.; Clark, P. A.; Solomon, E. I. *J. Am. Chem. Soc.* **1990**, *112*, 9534-9548.

24)Messerschmidt, A.; Rossi, A.; Ladenstein, R.; Huber, R.; Bolognesi, M.; Gatti, G.; Marchesini, A.; Petruzelli, R.; Finazzi-Agro, A. *J. Mol. Biol.* **1989**, *206*, 513-529.

25)Messerschmidt, A.; Ladenstein, R.; Huber, R.; Bolognesi, M.; Avigliano, L.; Petruzzelli, R.; Rossi, A.; Finazzi-Agro, A. *J. Mol. Biol.* **1992**, *224*, 179-205.

26)Zaitzeva, I.; Zaitzev, V.; Card, G.; Moshkov, K.; Box, B.; Ralph, A.; Lindley, P. *J. Biol. Inorg. Chem.* **1996**, *1*, 15-23.

27)Andrew, C. R.; Fraczkiewicz, R.; Czernuszewics, R. S.; Lappalainen, P.; Saraste, M.; Sanders-Loehr, J. *J. Am. Chem. Soc.* **1996**, *118*, 10436-10445.

28)Blackburn, N. J.; de Vries, S.; Barr, M. E.; Houser, R. P.; Tolman, W. B.; Sanders, D.; Fee, J. A. *J. Am. Chem. Soc.* **1997**, *119*, 6135-6143.

29)Gamelin, D. R.; Randall, D. W.; Hay, M. T.; Houser, R. P.; Mulder, T. C.; Canters, G. W.; de Vries, S.; Tolman, W.; Lu, Y.; Solomon, E. I. *J. Am. Chem. Soc.* **1998**, *120*, 5246-5263.

30)Houser, R. P.; Youbg, V. G.; Tolman, W. B. *J. Am. Chem. Soc.* **1996**, *118*, 2101-2102.

31)Neese, F.; Zumft, W. G.; Antholine, W. E.; Kroneck, P. M. H. *J. Am. Chem. Soc.* **1996**, *118*, 8692-8699.

32)Malmstrom, B. G. *Chem. Rev.* **1990**, *90*, 1247-1260.

33)Rosenzweig, A. C. *Nat. Struct. Biol.* **2000**, *7*, 169-171.

34)Brown, K.; Tegoni, M.; Prudencio, M.; Pereira, A. S.; Besson, S.; Moura, J. J.; Moura, I.; Cambillau, C. *Nat. Struct. Biol.* **2000**, *7*, 191-195.

35)Cotton, F. A.; Wilkinson, G. *Advanced Inorganic Chemistry*; 5th ed.; John Wiley & Sons, Inc.: New York, 1988.

36)Kassner, R. *Proc. Nat. Acad. Sci.* **1972**, *69*, 2263-2267.

37)Yandell, M. A. A.; Addison, A. W.; Karlin, K. D. *Inorg. Chim. Acta* **1981**, *55*, L35-L37.

38)Yokoi, H.; Addison, A. W. *Inorg. Chem.* **1977**, *16*, 1341-1348.

39)Karlin, K. D.; Yandell, J. K. *Inorg. Chem.* **1984**, *23*, 1184-1188.

40)Addison, A. W.; Rao, T. N.; Sinn, E. *Inorg. Chem.* **1984**, *23*, 1957-1966.

41)Churg, A. K.; Warshel, A. *Biochemistry* **1986**, *25*, 1675-1681.

42)Addison, A. W. *Inorg. Chim. Acta* **1989**, *162*, 217-220.

43)Canters, G. W.; Gilardi, G. *FEBS Letters* **1993**, *325*, 39-48.

44)Malmstrom, B. G. *Eur. J. Biochem.* **1994**, *223*, 711-718.

45)Solomon, E. I.; Penfield, K. W.; Gewirth, A. A.; Lowery, M. D.; Shadle, S. E.; Guckert, J. A.; LaCroix, L. B. *Inorg. Chim. Acta* **1996**, *243*, 67-78.

46)Guckert, J. A.; Lowery, M. D.; Solomon, E. I. **1994**.

47)Battistuzzi, G.; Borsari, M.; Loschi, L.; Righi, F.; Sola, M. *J, Am. Chem. Soc.* **1999**, *121*, 501-506.

48)Messerschmidt, A. *Metal Sites in Small Blue Copper Proteins, Blue Copper Oxidases and Vanadium-Containinng Enzymes*; in Structure and Bonding, Hill, H. A. O., Sadler, P. J. and Thomson, A. J. ed.; Springer: Berlin, 1998; Vol. 90, pp 37-68.

49)Osaki, S.; Johnson, D. A.; Frieden, E. *J. Biol. Chem.* **1966**, *241*, 2746.

50)Kaplan, J.; O'Halloran, T. *Science* **1996**, *271*, 1510-1512.

51)Gitlin, J. D. *Pediatric Research* **1998**, *44*, 271-276.

52)Mukhopadhyay, C. K.; Attieh, Z. K.; Fox, P. L. *Science* **1998**, *279*, 714-717.

53)Stearman, R.; Yuan, D. S.; Yamaguchi-Iwai, Y.; Klausner, R. D.; Dancis, A. *Science* **1996**, *271*, 1552-1557.

54)Askwith, C.; Kaplan, J. *J. Biol. Chem.* **1997**, *271*, 401-405.

55)Askwith, C. C.; Kaplan, J. *J. Biol. Chem.* **1998**, *273*, 22415-22419.

56)de Silva, D.; Sandra, D.-K.; Fergestad, J.; Kaplan, J. *J. Biol. Chem.* **1997**, *272*, 14208-14213.

57)Hasset, R. F.; Yuan, D. S.; Kosman, D. J. *J. Biol.Chem.* **1998**, *273*, 23274-23282.

58)Dancis, A.; Yuan, D. S.; Haile, C.; Askwith, C.; Eide, D.; Moehle, C.; Kaplan, J.; Klausner, R. D. *Cell* **1994**, *76*, 393-402.

59)Kosman, D. J.; Hassett, R.; Yuan, D. S.; McCracken, J. *J. Am. Chem. Soc.* **1998**, *120*, 4037-4038.

60)Graziani, M. T.; Morpugo, L.; Giuseppe, R.; Mondovi, B. *FEBS Letter* **1976**, *70*, 87-90.

61)Malkin, R.; Malmstrom, B. G.; Vanngard, T. *Eur. J. Biochem.* **1969**, *7*.

62)Reinhammar, B.; Oda, Y. *J. Inorg. Biochem.* **1979**, *11*, 115-127.

63)Spira-Solomon, D. J.; Solomon, E. I. *J. Am. Chem. Soc.* **1987**, *109*, 6421-6432.

64)Morie-Bebel, M. M.; Morris, M. C.; Menzie, J. L.; McMillin, D. R. *J. Am. Chem. Soc.* **1984**, *106*, 3677-3678.

65)Morie-Bebel, M. M.; Menzie, J. L.; McMillin, D. R. *The Preparation and Characterization of a Mixed Metal Derivative of Laccase*; in Biological and Inorganic Copper Chemistry, Proceedings of the Conference on Copper Coordination Chemistry, Karlin, K. D. and Zubieta, J. ed.; Adenine Press, Inc.: Guilderland, NY, 1986; Vol. 1, pp 89-95.

66)Smith, T. A.; Penner-Hahn, J. E.; Hodgson, K. O.; Berding, M. A.; Doniach, S. *Springer Proc. Phys.* **1984**, *2*, 58-60.

67)Guss, J. M.; Freeman, H. C. *J. Mol. Biol.* **1993**, *169*, 521-563.

68)Penfield, K. W.; Gay, R. R.; Himmelwright, R. S.; Eickman, N. C.; Solomon, E. I. *J. Am. Chem. Soc.* **1981**, *103*, 4382-4388.

69)Norris, G. E.; Anderson, B. F.; Baker, E. *J. Am. Chem. Soc.* **1986**, *108*, 2784-2785.

70)Machonkin, T. E.; Zhang, H. H.; Hedman, B.; Hodgson, K.; Solomon, E. I. *Biochemistry* **1998**, *37*, 9570-9578.

71)Ducros, V.; Brozowski, A. M.; Wilson, K. S.; Brown, S. H.; Ostergaard, P.; Schneider, P.; Yaver, D. S.; Pedersen, A. H.; Davies, G. J. *Nat. Struct. Biol.* **1998**, *5*, 310-316.

72)Pierloot, K.; De Kerpel, J. O. A.; Ryde, U.; Roos, B. O. *J. Chem. Phys. B* **1998**, *102*, 4638-4647.

73)Askwith, C. C.; de Silva, D.; Kaplan, J. *Mol. Microbiol.* **1996**, *20*, 27-34.

74)Eide, D. *Curr. Opin. Cell Biol.* **1997**, *9*, 573-577.

75)Askwith, C.; Kaplan, J. *Trends Biol. Sci.* **1998**, *23*, 135-138.

76)Radisky, D.; Kaplan, J. *J. Biol. Chem.* **1999**, *274*, 4481-4484.

77)Dix, D.; Bridgham, J.; Broderius, M.; Eide, D. *J. Biol. Chem.* **1997**, *272*, 11770-11777.

78)Dix, D. R.; Bridgham, J. T.; Broderius, M. A.; Byersdorfer, C. A.; Eide, D. J. *J. Biol. Chem.* **1994**, *269*, 26092-26099.

79)Dancis, A.; Klausner, R. D.; Hinnebusch, A. G.; Barriocanal, J. G. *Mol. Cell Biol.* **1990**, *10*, 2294 -2301.

80)Dancis, A.; Roman, D. G.; Anderson, G. J.; Hinnebusch, A. G.; Klausner, R. D. *Proc. Natl. Acad. Sci. USA* **1992**, *89*, 3869-3873.

81)Eide, D.; Davis-Kaplan, S.; Jordan, I.; Sipe, D.; Kaplan, J. *J. Biol. Chem.* **1992**, *267*, 20774-20781.

82)Shatwell, K. P.; Dancis, A.; Cross, A. R.; Klausner, R. D. *J. Biol. Chem.* **1996**, *271*, 14240-14244.

83)Hasset, R. F.; Romeo, A. M.; Kosman, D. J. *J. Biol. Chem.* **1998**, *273*, 7628-7636.

84)Dancis, A.; Haile, D.; Yuan, D. S.; Klausner, R. D. *J. Biol. Chem.* **1994**, *269*, 25660-25667.

85)Glerum, D. M.; Shtanko, A.; Tzagoloff, A. *J. Biol. Chem.* **1996**, *271*, 14504-14059.

86)Cullota, V. C.; Klomp, L. W. J.; Strain, J.; Casareno, R. L. B.; Krems, B.; Gitlin, J. D. *J. Biol. Chem.* **1997**, *272*, 23469-23472.

87)Yuan, D.; Stearman, R.; Dancis, A.; Dunn, T.; Beller, T. *Proc. Natl. Acad. Sci.* **1995**, *92*, 2632-2636.

88)Lin, S.-J.; Pufahl, R. A.; Dancis, A.; O'Halloran, T. V.; Culotta, V. C. *J. Biol. Chem.* **1997**, *272*, 9215-9220.

89)Winzerling, J. J.; Law, J. H. *Annu. Rev. Nutr.* **1997**, *17*, 501-526.

90)Watkins, J. A.; Altazan, J. D.; Elder, P.; Li, C.-Y.; Nunez, M.-T.; Xue-Xiang, C.-T. ; Glass, J. *Biochemistry* **1992**, *31*, 5820-5830.

91)Thorstensen, K.; Romslo, I. *J. Biol. Chem.* **1988**, *263*, 8844-8850.

92)Nunez, M. T.; Escobar, A.; Ahumada, A.; Gonzales-Sepulveda, M. *J. Biol. Chem.* **1992**, *267*, 11490-11494.

93)Harris, Z. L.; Takahashi, Y.; Miyajima, H.; Serizawa, M.; MacGillivray, R. T. A.; Gitlin, J. *Proc. Natl. Acad. Sci.* **1995**, *92*, 2539-2543.

94)Zhou, B.; Gitschier, J. *Proc. Natl. Acad. Sci.* **1997**, *94*, 7481-7486.

95)Klomp, L. W. J.; Lin, S.-J.; Yuan, D. S.; Klausner, R. D.; Culotta, V. C.; Gitlin, J. D. *J. Biol. Chem.* **1997**, *272*, 9221-9226.

Chapter 3

INSTRUMENTATION

In both optical and magnetic resonance spectroscopy, a source of electromagnetic radiation is used to irradiate a sample placed in specialized sample vessel. Changes in the properties of the incident radiation (frequency, energy, intensity etc.) detected by an appropriate detector will reveal some information about the sample. One obvious difference between optical and magnetic resonance spectroscopies is the need for an external magnetic field. A static magnetic field is required to align the magnetic moments of the sample and to split the energy levels to observe resonance. In EPR spectroscopy, other differences could be pointed out. One is that in EPR, monochromator such as prism or grating is not needed to emit monochromatic radiation. The microwave source (e.g. klystron or synthesizer) in EPR is capable of emitting monochromatic microwave radiation. Also, in a typical optical spectroscopy, a spectrum is obtained by varying the frequency of the electromagnetic radiation and observing the change in the radiation as it passes through the sample. An EPR spectrometer measures a spectrum by fixing the radiation frequency and scanning the applied magnetic field.

As mentioned in chapter 1, the first EPR experiment was done in 1945 by a Russian scientist, Zavoisky who detected a radio frequency absorbance from a copper dichloride sample. The availability of microwave components brought about by World War II led to the widespread use of paramagnetic resonance. Advances in design of microwave components and in electronics paved the way to modern

instruments and the construction of pulse-EPR instruments. The first part of this chapter will present a brief description of the CW-EPR spectrometer used in our study. Then, it will be followed by a description of the home-built pulse-EPR machine at Michigan State University. A comprehensive discussion on EPR instrumentation is presented by C. Poole[1] in his book and would serve as an excellent reference for those who wish to fully understand EPR instrumentation. A chapter on CW-EPR instrumentation is also explored in the book by Wertz and Bolton[2]. Discussion about pulse-EPR instrumentation can be found in several papers and books.[3-7]

3.1. CW-EPR

Data collection was done using the commercial Bruker ESP-300E instrument.[8] A simple schematic of the important components comprising the CW instrument is depicted in Figure 3.1.

The microwave (MW) radiation source is a klystron (1), which is housed in the microwave bridge. The microwave power is divided into a "power" arm and reference arm. MW coming from the power arm are used to irradiate the sample, placed in a resonant cavity, through a nonreciprocal device, the circulator (3). An attenuator (2) is used to vary the power used to excite the sample. The reflected MW from the cavity (7) are directed into a Schottky barrier diode detector (8), via port 3 of the circulator, where it is combined with MW coming from the reference arm. The reference arm has an attenuator (4) to bias the diode current making sure that the detector diode operates in a region of linear response (i.e. diode current is about 200

μA). It also has a phase shifter (5) that matches the phase of the reference MW with that of the reflected MW. The current from the detector diode then is fed to the signal channel (9) for phase-sensitive detection, amplification and processing. In our experiment, a TE102 cavity (7) was used and the temperature is maintained using an Oxford ESR-900 continuous flow cryostat. The current needed for the generation of the magnetic field of the external magnet is provided by an ER032 magnet power supply. Using a Hall probe, the magnitude of the magnetic field is monitored and regulated by ER032 magnetic field controller.

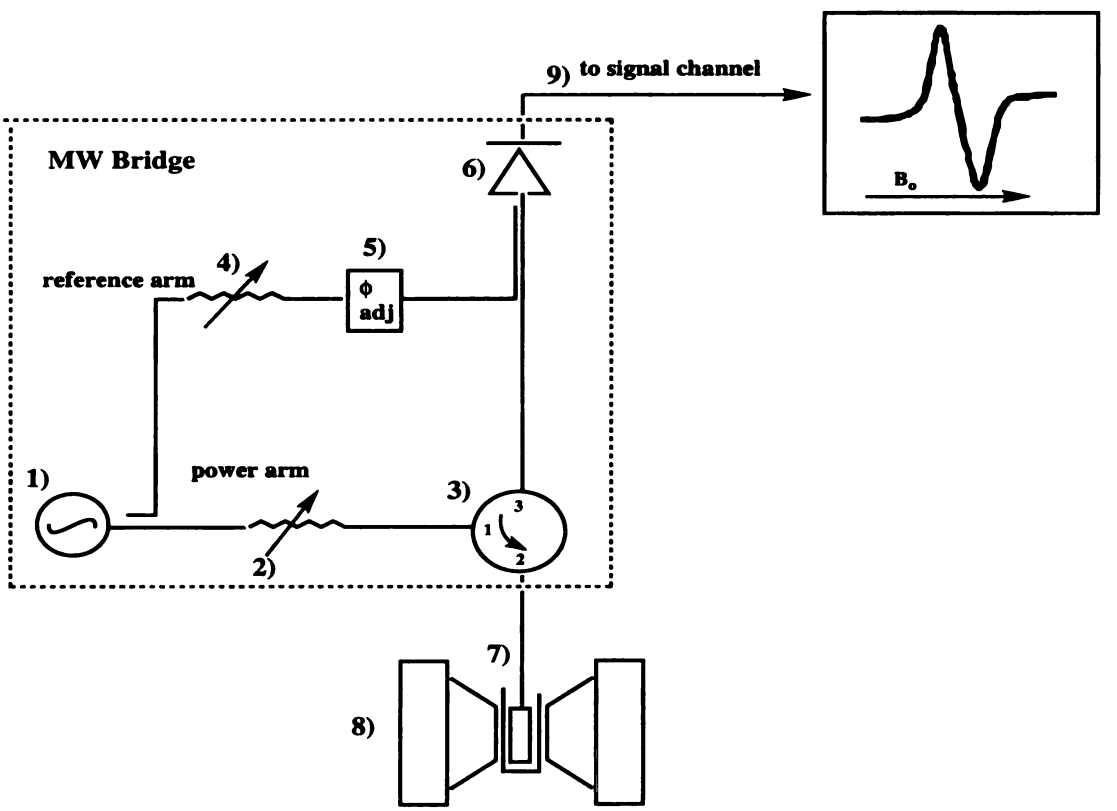

Figure 3.1. Diagram of the Bruker EPR spectrometer.

3.2 Pulse-EPR Machine at MSU

A layout of the pulse-EPR machine is shown in Figure 3.2. The machine was originally designed by Prof. John McCracken in 1990.[9] Essentially, the pulse-EPR machine has similar basic components as the CW-EPR machine.

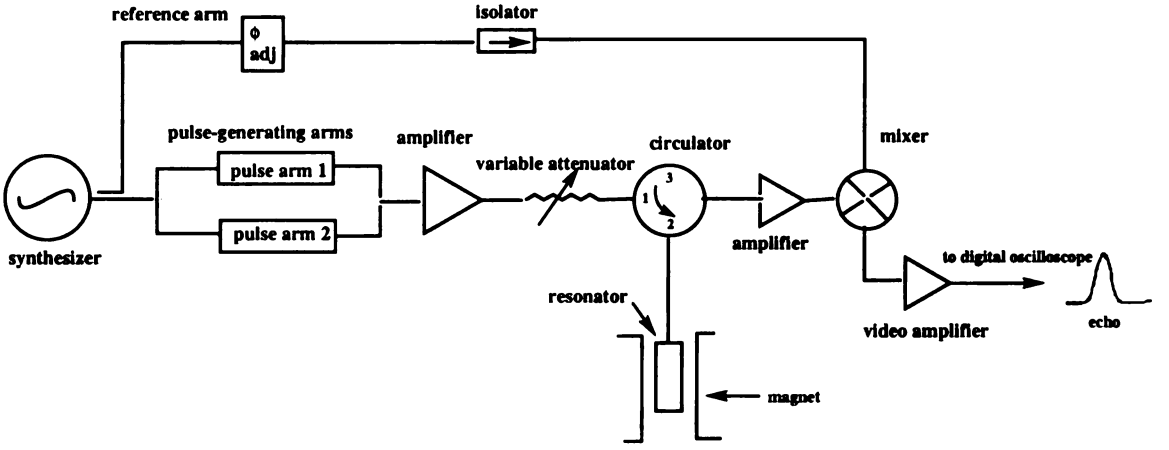

Figure 3.2. Design of the pulse-EPR machine at Michigan State University (MSU).

3.2.1 Microwave Bridge

The microwave bridge is comprised of a transmitter used to generate and control microwave radiation, and a receiver, which has a detector for detecting MW radiation. It also has rotary vane attenuator for varying the MW power that is fed to the sample through a circulator.

3.2.1.1 Transmitter

Figure 3.3 shows the schematic diagram of the transmitter part of the microwave bridge. A Microwave synthesizer (Giga-Tronics, Model 610) provides

the microwave radiation and is capable of operation over a frequency range of 6-18 GHz. A directional coupler (Omni Spectra, Model MN2025-6018-10) splits the microwave power with 90% of it being directed to the reference arm and the remainder to the pulse-forming channels. Acting as a current-bias and a phase-reference, the reference arm has an adjustable phase shifter (ARRA, Model 9828A). It also has an isolator (Innowave, Model 111R) which makes sure that there is no microwave radiation reflected back to the source. The remaining 10% of the microwave power from the source is fed to a power divider (Omni Spectra, Model PN2089-6209-00) further splitting the microwave radiation into two independent pulse-generating channels. Both of these channels have low-power, high-speed PIN diode switches (General Microwave, Model FM864-BH) and high-speed 0°/180° wide band phase modulators (General Microwave, Model F1938) whose width and phases, respectively, are controlled by a home-made pulse logic circuit. One of the channels has an attenuator (ARRA Model P9804-20), while the other one has a phase shifter. The low-power MW pulses (~100μW) generated are combined, passed through an isolator, and then amplified by a medium-power GaAs FET amplifier (Avantek, Model SWL-89-0437). Through an attenuator, the GaAS FET-amplified MW pulses ~(100mW) are fed into the travelling wave tube (TWT) amplifier (Applied Systems Engineering, Model 117). In order to vary the amount of MW power irradiating the sample, the TWT amplified pulse (1kW) is allowed to pass through a rotary vane attenuator (Hewlett Packard, Model X382A). In between the rotary vane attenuator and the TWT amplifier is an isolator, designed especially for high-power MW pulses.

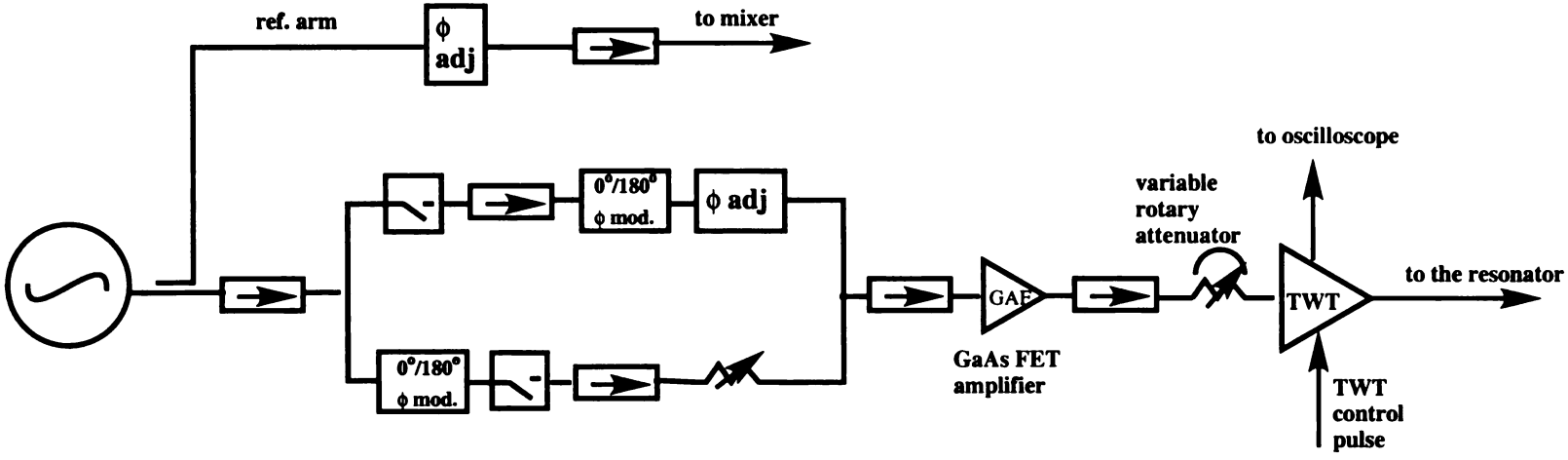

Figure 3.3. Transmitter section of the microwave bridge of the pulse-EPR machine.

The MW pulses are then fed to a circulator (Microwave Associates, Model MA-8K269), a non-reciprocal device like the isolator, which directs the microwave power in one terminal into the cavity containing the sample and then directs the reflected MW from the cavity to the detector through the next terminal in the sequence.

3.2.1.2 Receiver

The schematic diagram of the detection system is shown in Figure 3.4. The reflected MW signal from the sample resonator is first fed to a GaAs FET amplifier (Avantek, Model AWT-18635) through an isolator, a high-speed PIN diode limiter (Innowave, Model VPL-6018) and a fast PIN diode switch (General Microwave, Model F9114) which is triggered by the pulse-logic circuit. The diode limiter and switch serve to protect the GaAs FET amplifier from high-power microwave pulses. For tuning purposes, 1% of the microwave power is extracted via a direction coupler. Most of the microwave power is allowed to pass through a bandpass filter (K& L Microwave, Model 3H10-2000/18000-0/0) to remove unwanted radio frequency noises introduced by PIN switches, prior to its being directed to a double balance mixer (RHG, MODEL DM2-18 AB). In the mixer, the reflected MW signal from the resonator is mixed with the MW power coming from the reference arm. The homodyne arrangement of the double balance mixed generates signals at sum and difference of the frequencies of the signal coming from the receiver and the reference arm. The intensity of the echo signal is proportional to the difference between the amplitude of the two input signals as well as their relative phases. It is then amplified

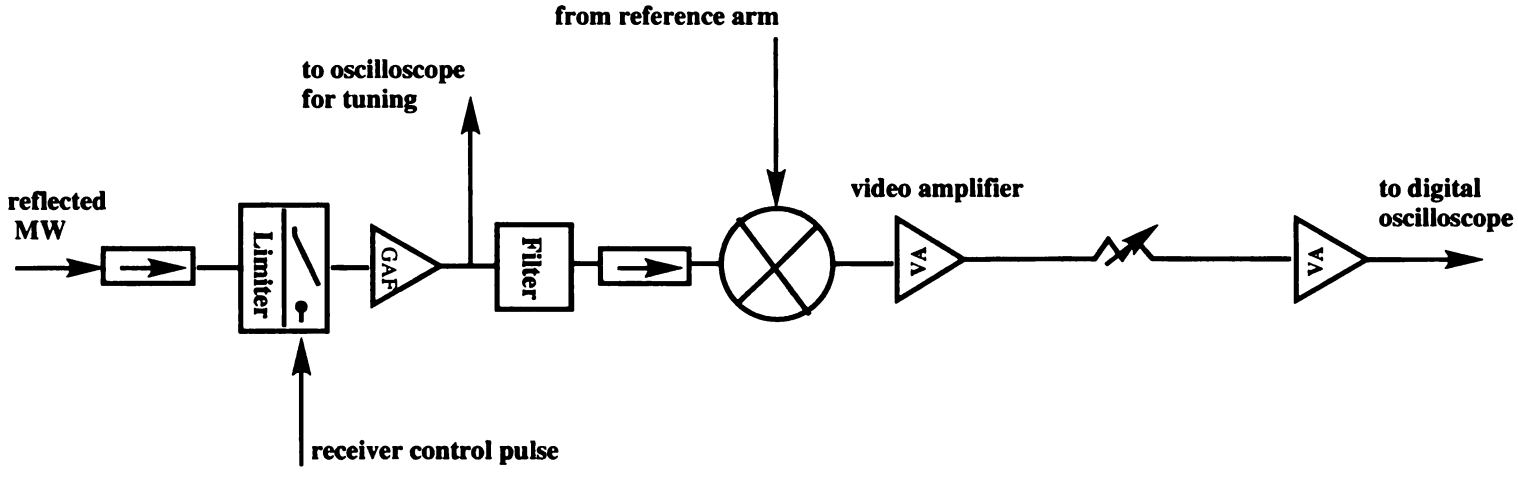

Figure 3.4. Receiver section of the microwave bridge of the pulse-EPR instrument.

and adjusted through series of video amplifier (Comlinear, Model E220)-attenuator (JFW, Model 50DR-003)-video amplifier and then finally fed to a digital oscilloscope(Tektronix 620 B) to convert the analog signals to digital signals.

3.2.2 Cavity and Cryogenic

For ESEEM experiments, a reflection-type cavity with folded stripline half-wave resonator[10] is used. The use of the folded stripline resonator lowers the quality factor, Q_L,[1,2] of the cavity. A low Q_L is desirable for ESE experiment to cut down the ring down time of the resonant pulse in the cavity and also to the decrease the dead-time. Q_L is related to amount of energy stored in the cavity and thus to the magnitude of B_1. A low Q_L implies small B_1 field and consequently low sensitivity. However, the use of this resonant element allows the increase of filling factor, η, by concentrating the B_1 field seen by the sample. Coupling of the microwave pulse with resonator is accomplished by a Gordon Coupler.[11,12] By adjusting the position of the this coupler, the Q_L of the cavity can be varied.

The cavity is immersed in a homemade liquid helium immersion dewar allowing us to work at 4.2 Kelvin. At this temperature, the relaxation processes, T_1 and T_2 are increased allowing us to detect echoes at longer times.

3.2.3 Magnet

The external magnetic field is supplied by an electromagnet (Walker Scientific, Model HF-12H) capable of generating magnetic field from 50 to 16000

gauss. The field values are monitored and regulated by a Hall-effect field controller (Bruker, Model B-H15).

3.2.4 Computer Interface, Experiment Timing and Data Collection

Figure 3.5 shows a detailed schematic diagram of the set-up of the pulse machine. The scope, field controller and the delay generator (Research Stanford Systems, Model DG535) are connected to the PowerComputing Mac computer via IEEE-488 interface (National Instruments). The delay and gate generator controls the timing of the echo experiment. It is used to trigger the pulse logic unit and therefore determines the pulse sequence. It is also used to trigger the oscilloscope for measuring the intensity of the electron spin echo. The data acquisition is implemented using LabVIEW 5.0.1(National Instruments).

3.2.5 Modification of the Pulse Logic Module

As mentioned earlier, the pulse logic module has three functions. It (1) determines the width and phases of the pulses coming out from the two microwave pulse-generating arms, (2) turns on the TWT amplifier, and (3) turns on and off the receiver diode switch to protect the detection system

The original design of the circuitry for this pulse logic unit was made by Prof. John McCracken and Dr. Hong-In Lee.[13] It was modified for the present work to allow for the generation of longer microwave pulses and reduce timing jitter introduced by poor circuit layout. Non-availability of some IC's used in the old pulse logic module at present time is also a reason for modifying the circuitry.

Figure 3.5. A schematic diagram of the pulse-EPR instrument built at Michigan State University. Schemes in Figure 3.3 and 3.4 are incorporated.

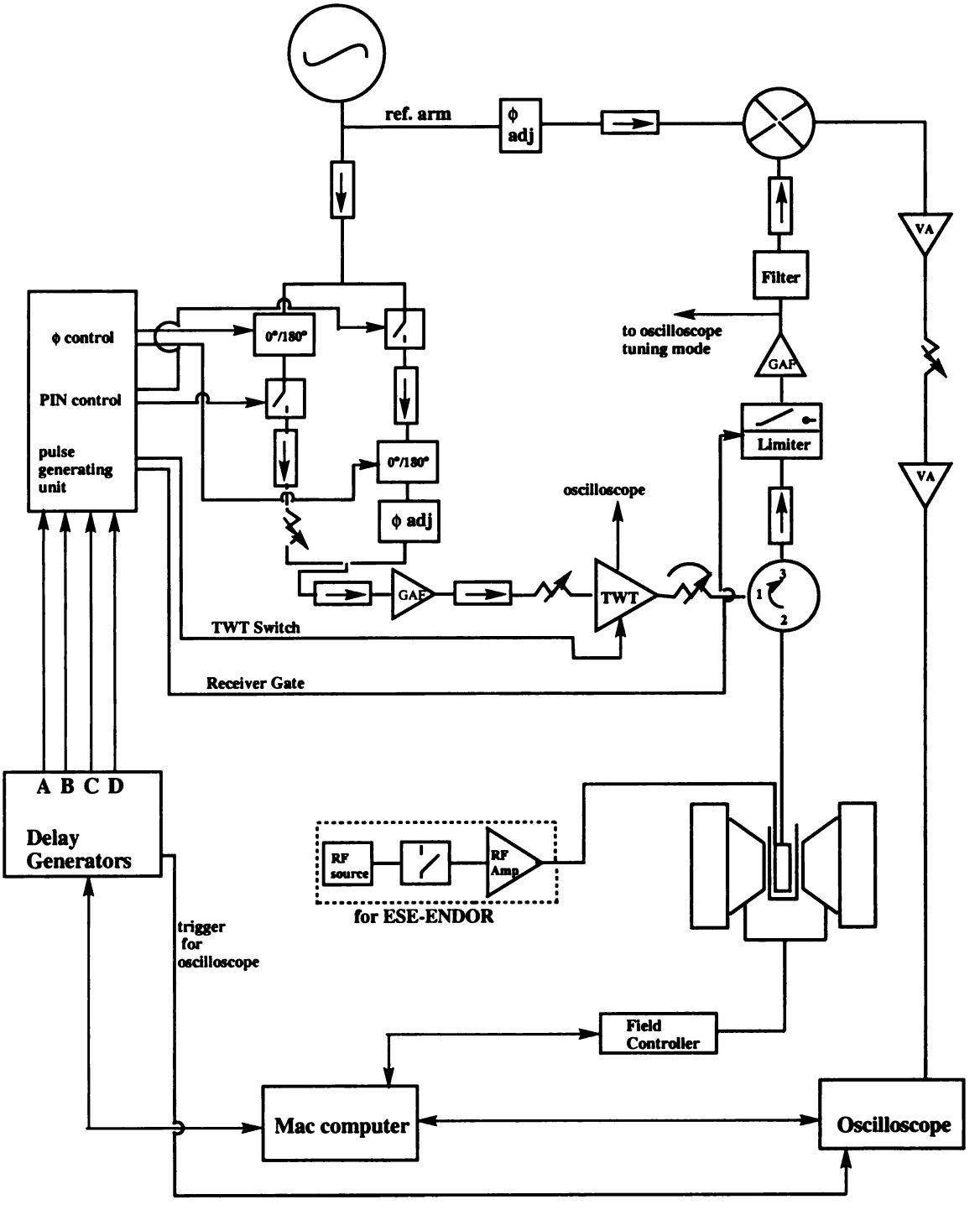
ref. arm
ϕ adj
VA
Filter
to oscilloscope tuning mode
GAF
Limiter
ϕ control
PIN control
pulse generating unit
0°/180°
0°/180°
ϕ adj
oscilloscope
GAF
TWT
TWT Switch
Receiver Gate
A B C D
Delay Generators
RF source
RF Amp
for ESE-ENDOR
trigger for oscilloscope
Field Controller
Mac computer
Oscilloscope

Using TTL textbooks and logic tables,[15,16] the design for the present circuit was made and their schematic diagrams are shown in the appendix section of this chapter.

APPENDICES

Appendix 3A
Pulse Logic Module

Timing Diagram for a Two-pulse ESEEM Measurement

Figure 3A.A1 shows a timing diagram for the creation of microwave pulses in a 2-pulse ESEEM experiment. The A and B inputs are generated by a delay and gate generator (DG535) which sets the separation between the two microwave pulses. Shown also in the figure are the output pulses used to turn on and off the PIN diode switches (General Microwave, Model FM864-BH), phase modulators (General Microwaves, Model f1938), TWT control, and the receiver PIN diode switch (General Microwave, Model F9114). The PIN diode switches are closed by a positive logic 0 input. A positive logic 1 input turns on the phase modulators and the TWT control.

Module Interconnections

A general scheme on how these trigger inputs and pulse outputs are integrated for the formation and amplification of microwave pulses is shown in Figure A3.A2. Basically, inputs from DG535 are fed into a pulse forming unit. This unit creates "0" logic pulses to drive the PIN diode switches (pulse P) and the TWT control circuit (pulse TWT), and logic "1" to control the phase modulators (pulse ϕ). Pulses P and TWT are directed to the pulse combiner unit which generates output pulses shown in

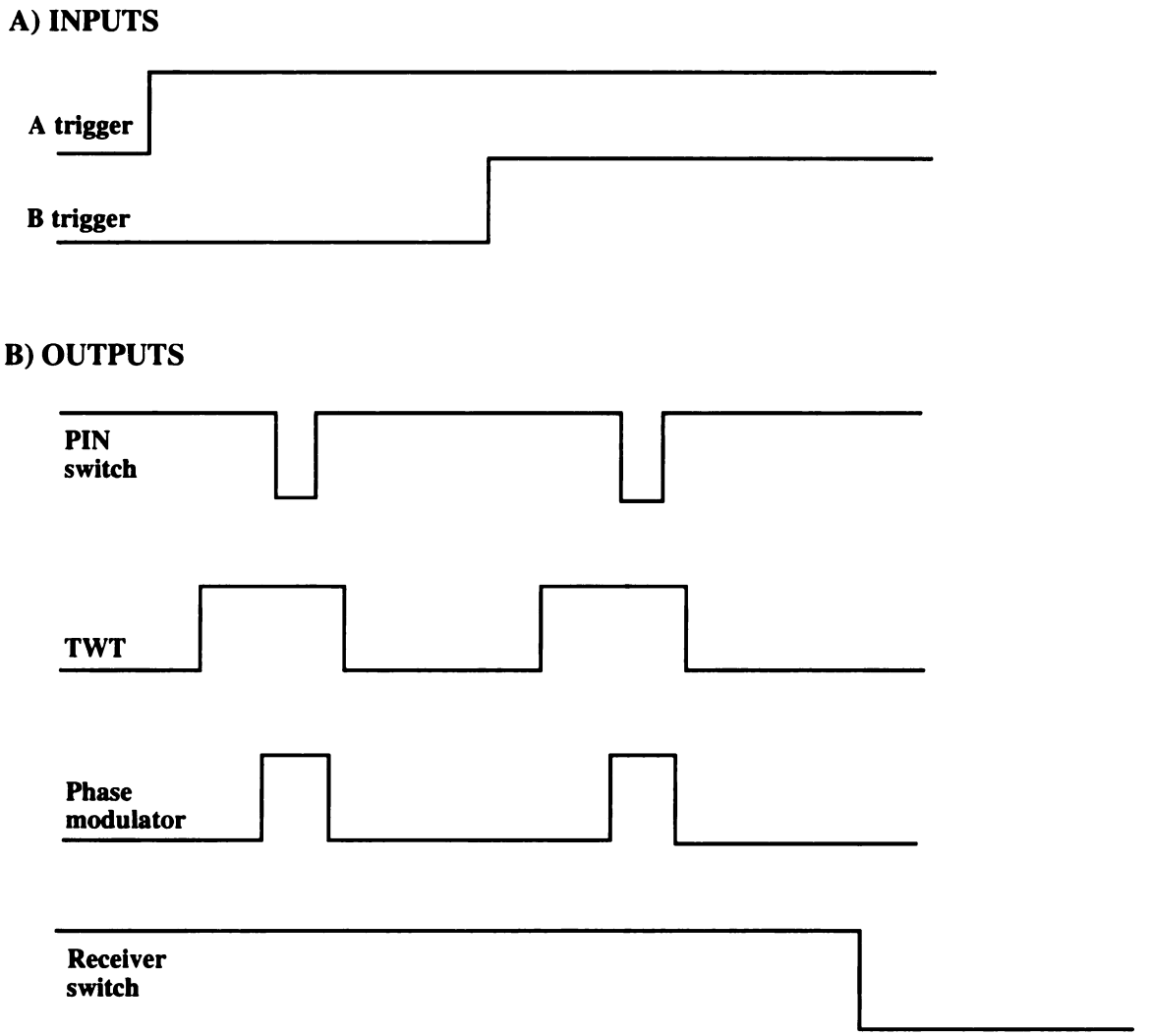

Figure A3.A1. Timing diagram for a 2-pulse ESEEM measurement.

Figure A3.A1, while pulse ϕ is fed to the phase sorter unit which generates the output pulse train for the phase modulators (Figure A3.A1). A pulse from the combiner unit is tapped and directed to the receiver control unit, which operates the PIN diode switch that gates the receiver.

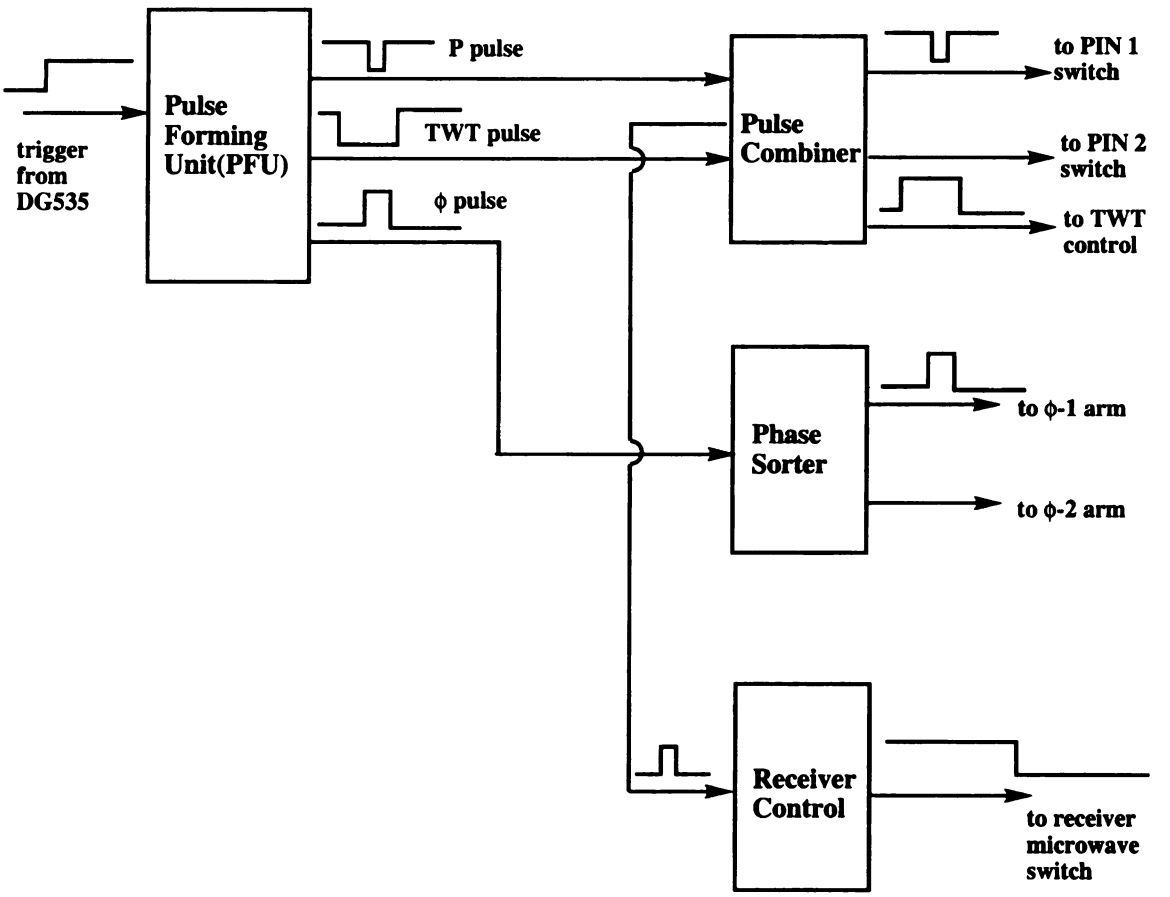

Figure A3.A.2. Module Interconnections.

Descriptions and Circuit Diagrams of PFU, Pulse Combiner, Phase Sorter and Receiver Control Switch

The pulse forming, pulse combiner, the receiver control, and the phase sorter units constitute the pulse logic module. Their circuitry is shown in Figure A3.A3, A3.A4, A3.A5 and A3.A6, respectively.

Pulse Forming Unit. Currently, the pulse forming unit (Figure A3.A3) can create six P (PA-PF), TWT (TWT A-F) and ϕ (ϕA-F) pulses. The width of the six P pulses (output 7-1 and 7-4, Figure A3.B3a-c) can be varied according to the logic inputs of pins 8, 9 and 10 of PPG33F-50, a 3-Bit programmable pulse generator (IC#4A and 4A). The duration of the TWT (output 5-12 and 5*-12, Figure A3.A3a-c) and ϕ pulses (output of 6-5 and 6*-5, Figure A3.A3a-c), on the other hand, are determined by the resistance between pins 7 and 16 of monostable multivibrator, 74LS123 (IC#5 and 6, respectively).

Pulse Combiner Unit. The TWT pulses (TWT A-F) that corresponds to each microwave pulse generated, are combined by an 8-input positive NAND (IC#8) gate of the pulse combiner (Figure 3A.A4) to form train of pulses for turning on the TWT amplifier. Three P pulses, designated as P-A, P-B and P-D, are combined in a dual 4-input positive-NAND (IC#11) gate (Figure A3.A4) to create train of pulses for triggering the PIN1 diode switch of the pulse-generating arm of the transmitter (Figure 3.5). Similarly, the pulses P-C, P-E and P-F are combined in the other half of the dual 4-input positive-NAND gate for triggering the PIN 2 diode switch.

Receiver Control Unit. The train of pulses from IC# 11-6 and 11-8 are tapped and directed to the receiver control unit (Figure A3.A5). This unit counts the number

pulses created and turns on the receiver switch (General Microwave, Model F9114, Figure 3.5) only when an electron spin echo appears.

Phase Sorter Unit. The six ϕ pulses from the pulse forming unit are fed to a phase sorter unit (Figure A3.A6) whose function is to phase cycle microwave pulses for the elimination of unwanted echoes found in a 3-pulse ESEEM experiment.

Figure A3.A3a. Pulse Generating Subunit (A input, page 116 and B input, page 117).

The IC's used are numbered. They are 1, 1* (74F00, Quadruple 2-input positive-NAND gate); 2, (74F04, Hex-Inverter); 3, 3*, 5, 5*, 6 and 6* (74LS123, Dual retriggerable monostable multivibrator); 4, 4* (PPG 33F-10, 3-bit programmable pulse generator); 4A, 4A* (PPG33F-50, 3-Bit programmable pulse generator); and 7 (74F02, Quadruple 2-input positive-NOR gate).

IC #4 and #4A (4* ans 4A*) create the narrow and wide pulses, respectively. The width of the pulses coming from 4-2 (A*-2) and 4A-2 (4A*-2) is determined by the logic input in pins 8, 9, 10 of IC#4 (4*) and #4A (4A*). Logic states of these pins are depended on the states of the binary switch (BIN-SW). PPG's 4 (4*) and 4A (4A*) are enabled by the double-pole-double-throw (DPDT) on/off/on toggle switch. A logic 0 enables 4 (4*), while a logic 1 enables 4A (4A*). The width of the TWT and ϕ pulses are depended on the resistance of the rotary switches.

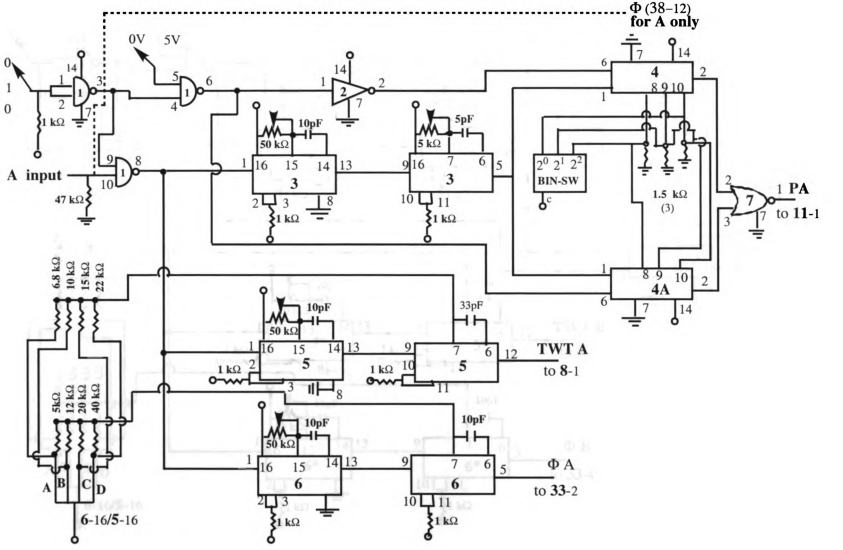

Figure A3.A3a. A input.

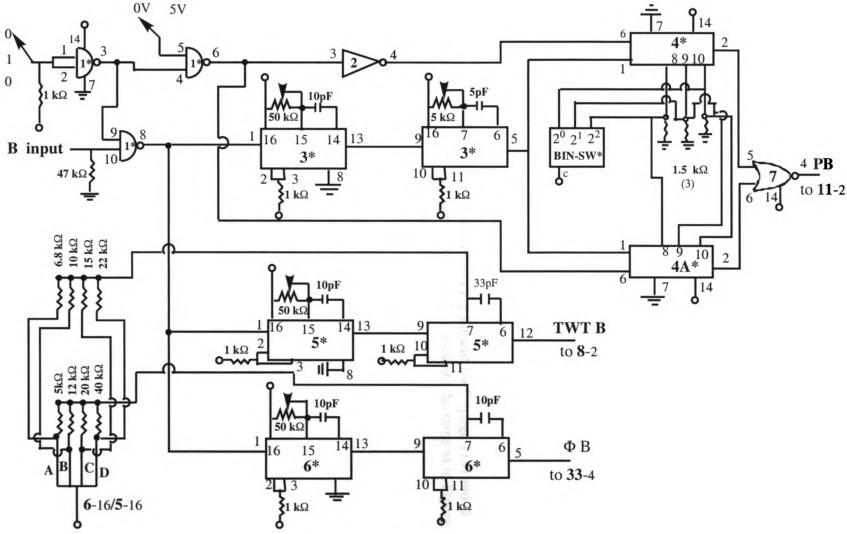

Figure A3.A3a. B input.

Figure A3.A3b. Circuit design of the pulse generating subunit for C (page 119) and D (page 220) inputs. The numbers and identification of IC's used are the same as in Figure A3.A3a.

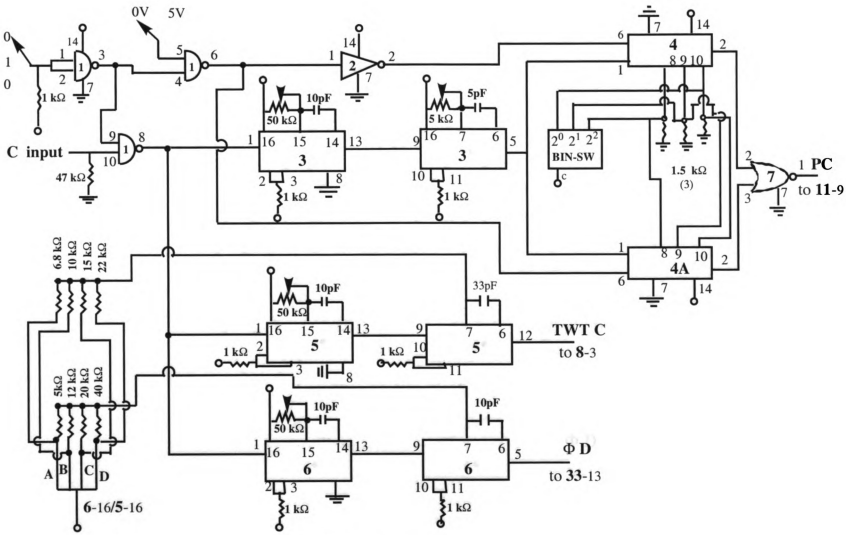

Figure A3.A3b. C input.

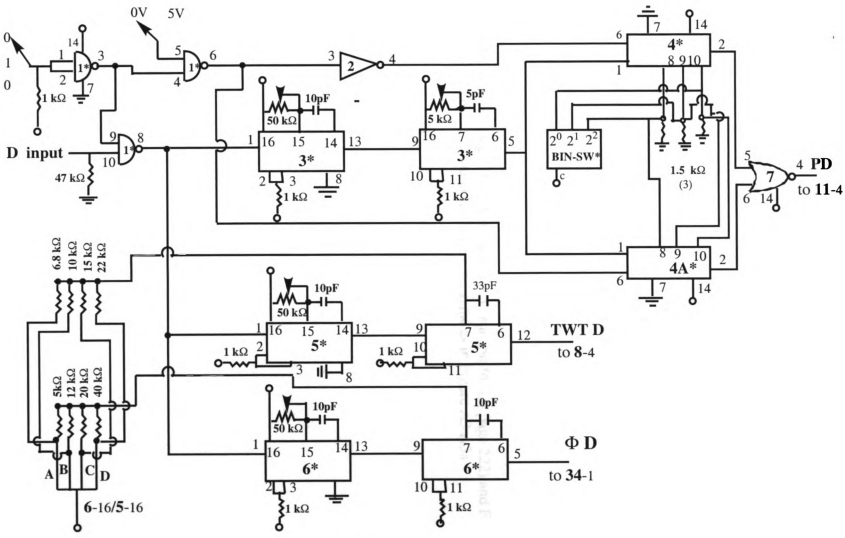

Figure A3.A3b. D input.

Figure A3.A3c. Circuit design of the pulse generating subunit for E (page 222) and F (223) inputs. IC numbers and identification are the same as in Figure A3.A3a

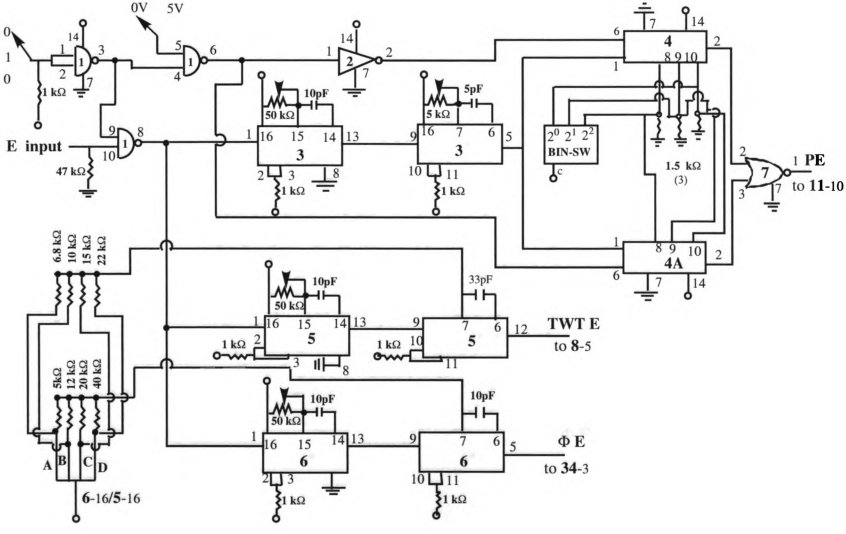

Figure A3.A3c. E input.

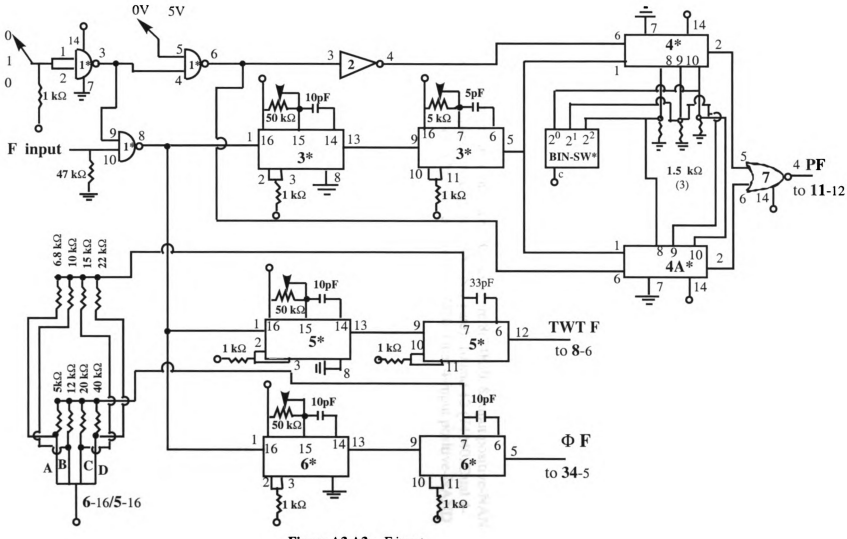

Figure A3.A3c. F input.

Figure A3.A4. Pulse combiner unit. The IC's used are 8(74F30, 8-input positive-NAND gate); 9 (74F00, Quadruple 2 -input positive-NAND gate); 10 and 12 (74140, Dual 4-input positive-NAND 50-ohm line driver); and 11 (7420, Dual 4-input positive-NAND gate).

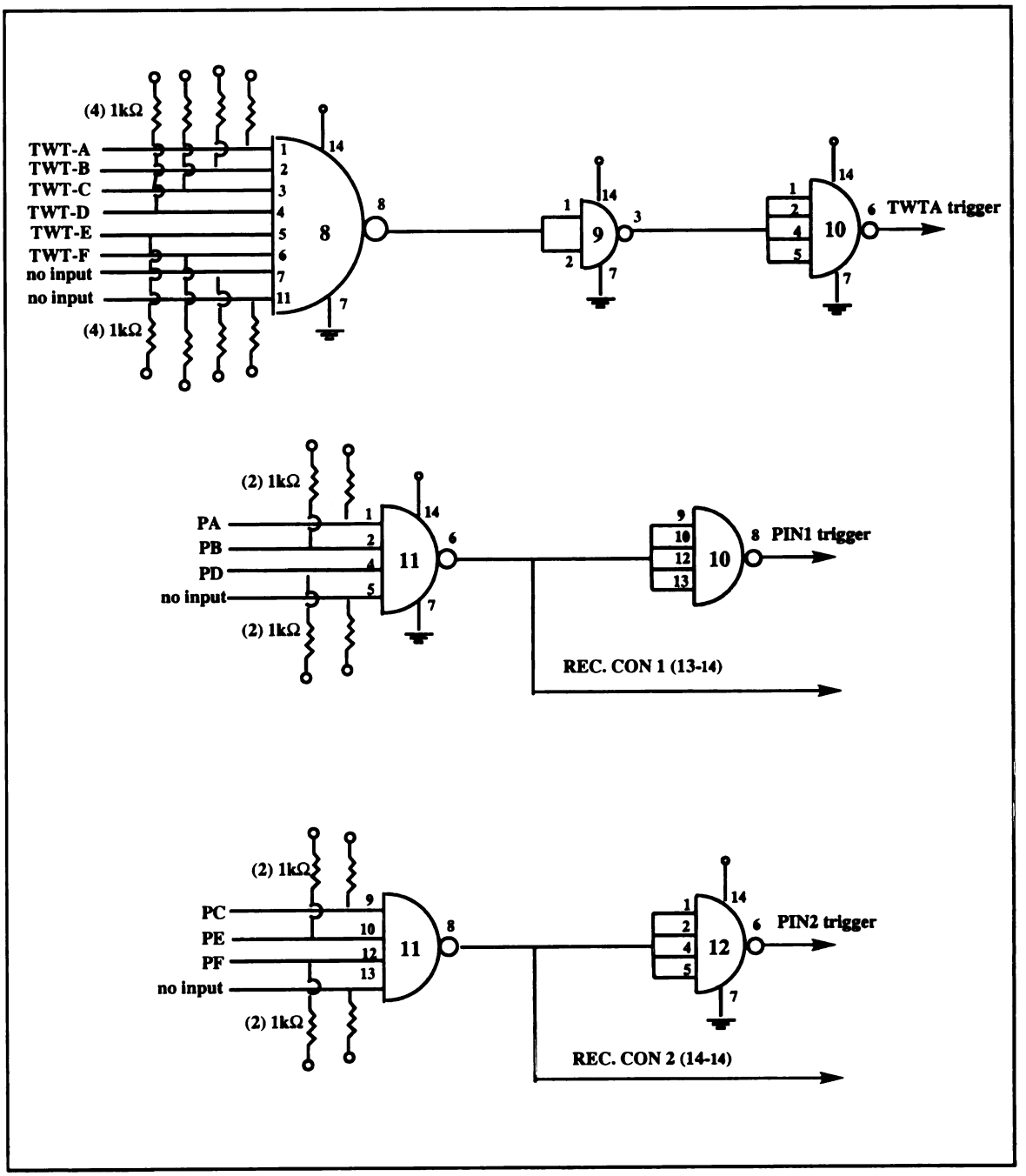
(4) 1kΩ
TWT-A
TWT-B
TWT-C
TWT-D
TWT-E
TWT-F
no input
no input
(4) 1kΩ
8
9
10
TWTA trigger
(2) 1kΩ
PA
PB
PD
no input
(2) 1kΩ
11
10
PIN1 trigger
REC. CON 1 (13-14)
(2) 1kΩ
PC
PE
PF
no input
(2) 1kΩ
11
12
PIN2 trigger
REC. CON 2 (14-14)

Figure A3.A5. Receiver Control Subunit. IC's used are 13 and 14 (7493, 4-bit binary counter); 15 and 23 (74LS123, Dual retriggerable monostable multivibrator); 16 and 17 (7404, Hex-Inverter); 18, 19, and 22 (7400, Quadruple 2-input positive-NAND gate); 20 (7420, Dual 4-input positive-NAND gate); and 21 (74140, Dual 4-input positive-NAND gate).

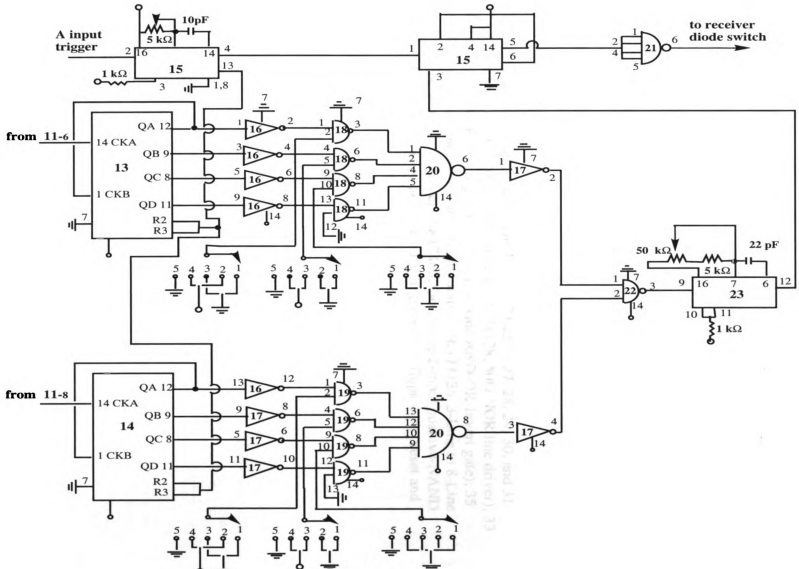
A input trigger
10pF
5 kΩ
1 kΩ
15
to receiver diode switch
21
from 11-6
from 11-8
13
14
14 CKA
1 CKB
QA 12
QB 9
QC 8
QD 11
R2
R3
16
17
18
19
20
50 kΩ
5 kΩ
22 pF
22
23
1 kΩ

Figure A3.A6. Phase Control Subunit. The IC's are 24,25,26,27, 28, 29, 30, and 31 (74LS373, In-phase module Octal-D type latches); 32 (74128, 50Ω NOR line driver); 33 (74LS54, 4-wide AND-OR-Invert gate); 34 (7454, 4-wide AND-OR-Invert gate); 35 (74LS123, Dual retriggerable monostable multivibrator); 36 (74138, 3-Line to 8-Line decoder); 37 (7494, 4-bit shift register), 38 (7400, Quadruple 2-input positive-NAND gate); and 39 (7474, Dual-D-Type positive-edge-triggered flip-flops with preset and clear).

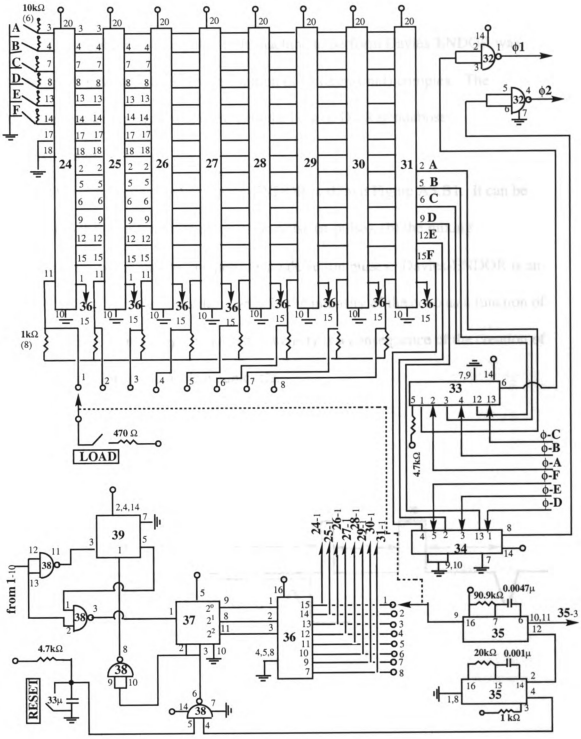
10kΩ
(6)
A
B
C
D
E
F
24
25
26
27
28
29
30
31
2 A
5 B
6 C
9 D
12 E
15 F
1kΩ
(8)
36
470 Ω
LOAD
ϕ1
ϕ2
32
33
4.7kΩ
ϕ-C
ϕ-B
ϕ-A
ϕ-F
ϕ-E
ϕ-D
34
39
38
37
36
35
from 1-10
90.9kΩ
0.0047μ
35-3
20kΩ
0.001μ
1 kΩ
4.7kΩ
33μ
RESET

Appendix 3B
Davies -ENDOR on Cu-dien-imidazole Complex

The capability of the pulse-EPR machine to perform Davies-ENDOR was tested using 5mM sample of frozen solution of Cu(dien-imid) complex. The experiment described here was done with the help of Dr. Rajendabose Muthukumaran.

The pulse sequence for Davies-ENDOR is shown Figure A3.B1. It can be divided into the (a) microwave preparation pulse (π-pulse), (b) the mixing radiofrequency pulse and, (c) the pulse-echo detection pulses. Davies-ENDOR is an ESE-ENDOR which measures the change in the intensity of the echo as a function of radio frequency. The change in the echo intensity is a consequence of the creation of the spin population in the nuclear sublevels.

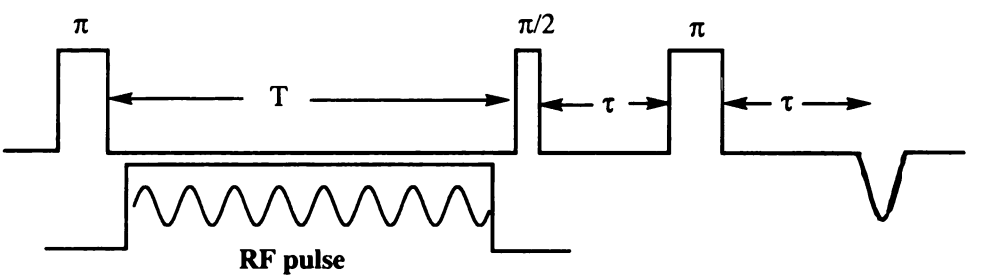

Figure A3.B1. Davies-ENDOR pulse sequence.

The effect of different pulses can be explained by what they do to the electron spin populations in a four-energy level system (S=1/2, I=1/2, Figure A3.B2). Initially, the spin system assumes an equilibrium population that follows the Boltzmann Distribution Law,

$$\frac{n_\alpha}{n_\beta} = \exp[-\Delta E/kT].$$

Because $g_e\beta_e B_o >> g_n\beta_n B_o$, spin population in the E_1 and E_2 levels, and E_3 and E_4 levels are essentially equal. The preparation microwave pulse is a π pulse of a duration chosen to make it selective for one of the EPR transitions. For example if

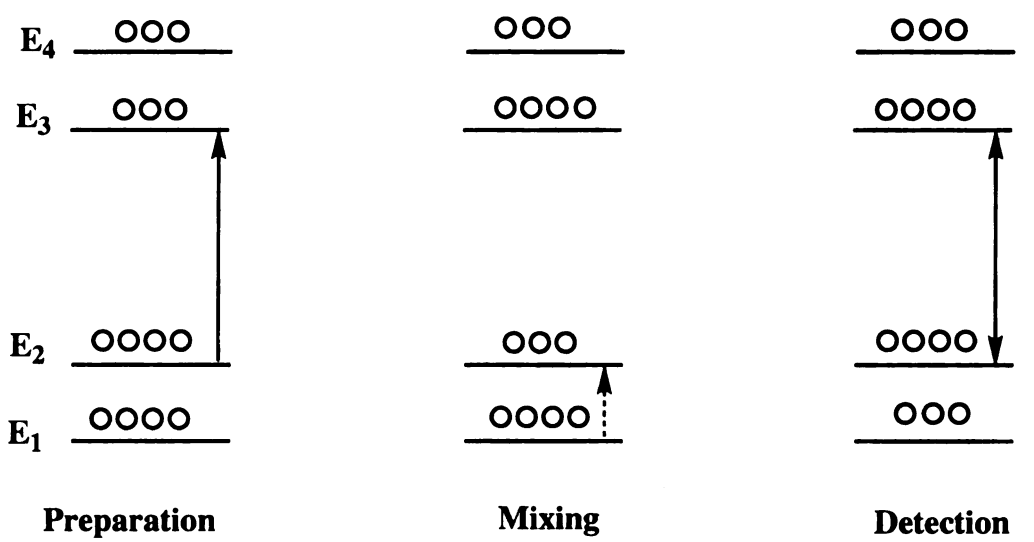

Figure A3.B2. Transfer of spin populations, represented by small circles, in Davies-ENDOR measurement for an S = 1/2 and I = 1/2 spin system during the preparation, mixing and detection periods.

the transition between E_2 and E_3 is irradiated, the population between these two levels is inverted. Consequently, a population difference is created between nuclear sublevels E_1 and E_2 and E_3 and E_4. This difference can be detected by applying a long radio frequency pulse during the mixing period. If the RF pulse is resonant with one of the NMR transitions, E_1-> E_2 for example, a nuclear spin flip will occur inverting the populations between these sublevels and equalizing the population between E_1 and E_4 and E_2 and E_3. If a $\pi/2$-τ-π-τ-echo sequence is applied right after the RF pulse, no primary echo will be observed. However, if the RF is not resonant, an echo will be detected as long as a population difference between EPR transition E_2 and E_3 (or E_1 and E_4) exists.

Figure A3.B3 shows a Davies-ENDOR of 5mM frozen solution of Cu-diethylene-imidazole complex at B_o = 3200 Gauss. Figure A3.B3a is collected using the pulse sequence: mw π pulse, 220ns; rf pulse, 7000ns; and detection pulse τ, 900ns. Two peaks are observed. The narrow peak at ~13.5 MHz is due to weakly coupled proton which can be from proton of ambient water. The broad peak of low intensity at around 18 MHz can be assigned to the nuclear modulation frequency of the directly coordinated ^{14}N of the imidazole ligand. Using a narrower preparation pulse, the contribution of the weakly coupled proton can be suppressed as shown in Figure A3.B3b. This Davies-ENDOR data was collected using the pulse sequence: mw π pulse, 450ns; rf pulse, 4400ns; and detection pulse τ, 450ns. The experimental data is simulated (solid line) spint1.mat (Matlab program) with the following Hamiltonian parameters: $A_{xx} = A_{yy} = A_{zz}$ =34.5, e^2qQ = 3.3 MHz, η = 0.13 and NQI Euler angles with respect to B_o of (0,0,0). A spectrum obtained using Mims-ENDOR

sequence is shown in Figure A3.B4 for comparison. In Mims-ENDOR spectrum, the ENDOR signals from weakly coupled protons dominate. These signal, however, are suppressed in Davies-ENDOR spectrum. Application of these ENDOR methods to the Fet3 protein were not successful, probably because of low sensitivity.

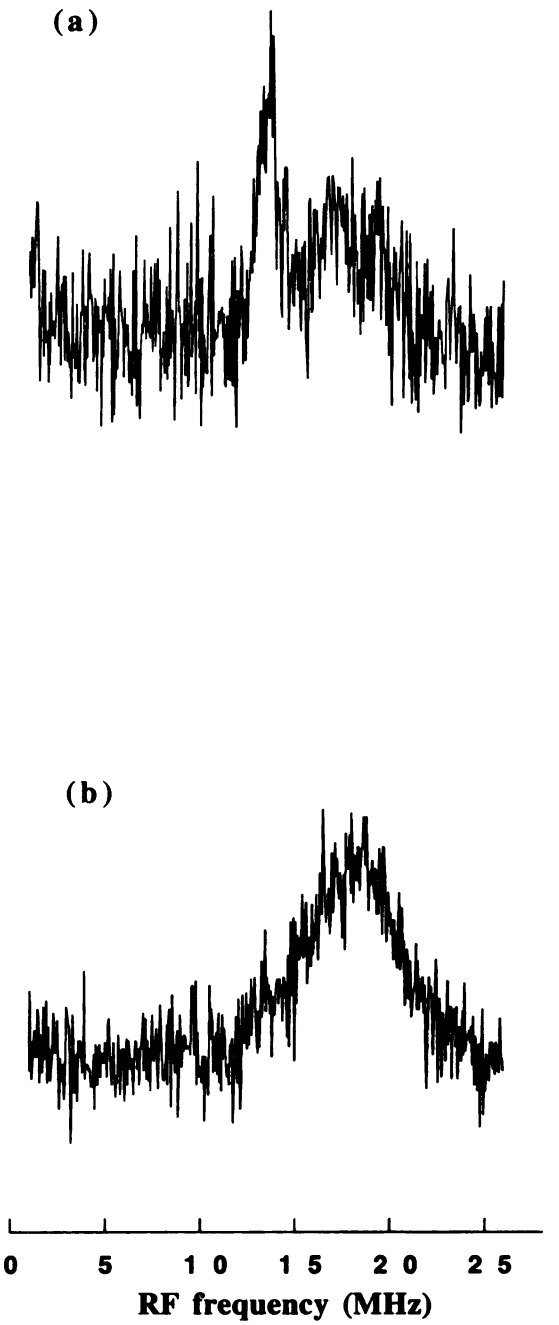

Figure A3.B3. Davies-ENDOR spectra of Cu-dien-imid complex recorded at 3200 G using the inversion and detection microwave pulse widths of (a) 220, 116 and 220 ns and (b) 40, 20 and 40 ns. Other experimental conditions: ν = 9.241 GHz, τ = 900 ns and t_{rf} = 7000 ns for (a) and τ = 450 ns and t_{rf} = 4400 ns for (b).

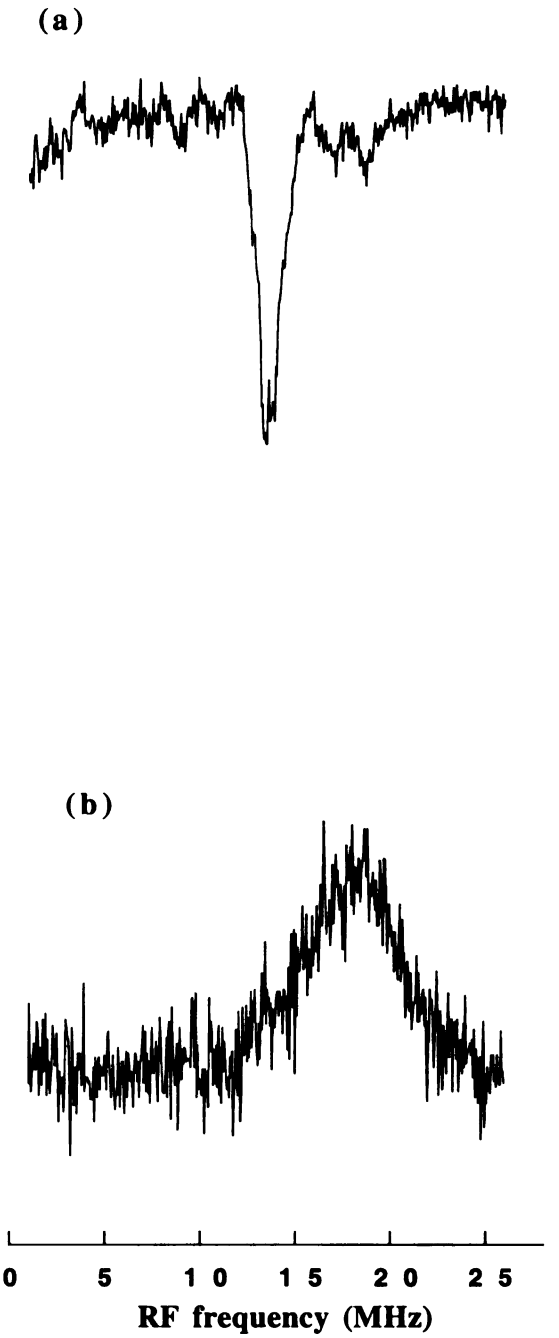

Figure A3.B4. (a) Mims ENDOR spectrum of Cu-dien-imid complex at 3200 Gauss, obtained using preparation pulse of 20 ns, t = 250 ns and RF pulse of 36800 ns. (b) Davies ENDOR collected at similar conditions as in figure A3.B3b.

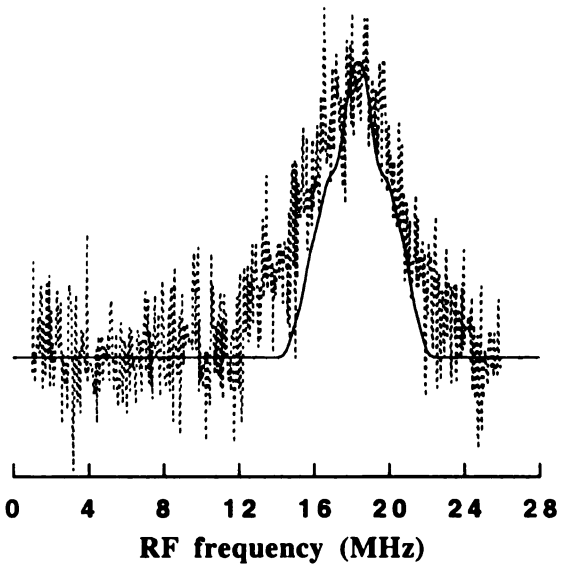

Figure A3.B5. Computer simulation (solid lines) of Davies ENDOR data shown in figure A3.B3b. The parameters used for the simulation are: $A_{xx} = A_{yy} = A_{zz} =$ 34.5MHz, $e^2qQ = 3.3$ MHz, $\eta = 0.13$ and NQI Euler angles with respect to B_o of (0,0,0).

LIST OF REFERENCES

1)Poole, C. *Electron Spin Resonance: A Comprehensive Treatise on Experimental Techniques*; 2 ed.; John Wiley & Sons, Inc.: New York, 1983.

2)Wertz, J.; Bolton, J. *Electron Spin Resonance: Elementary Theory and Practical Applications*; 2 ed.; Chapman and Hall:New York, 1986.

3)Mims, W. B. *Rev. Sci. Instrum.* **1965**, *36*, 1472-1479.

4)Brown, I. M.; Sloop, D. J. *Rev. Sci. Instrum.* **1970**, *41*, 1774-1777.

5)Blumberg, W. E.; Mims, W. B.; Zuckerman, D. *Rev. Sci. Instrum.* **1973**, *44*, 546-555.

6)Norris, J. R.; Thurnauer, M. C.; Bowman, M. K. *Electron Spin Echo Spectroscopy and the Study of Biological Structure and Function*; in Advances in Biological and Medical Physics, Lawrence, J. H., Gofman, J. W. and Hayes, T. L. ed.; Academic Press, Inc.: New York, 1980; Vol. 17, pp 365-416.

7)Keijers, C. P.; Reijerse, E. J.; Schmidt, J. *Pulsed EPR: A New Field of Applications*; North-Holland: Amsterdam, 1989.

8)Weber, R. T.; Heiss, A. A. *ESP 300E EPR Spectrometer User's Manual*; Bruker Analytische Messtechnik, 1992.

9)McCracken, J.; Shin, D. H.; Dye, D. l. *Appl. Magn. Reson.* **1992**, *3*, 305-316.

10)Lin, C. P.; Bowman, M. K.; Norris, J. R. *J. Magn. Reson.* **1985**, *65*, 369-374.

11)Britt, D.; Klein, M. *J. Magn. Reson.* **1987**, *74*, 535-540.

12)Gordon, J. P. *Rev. Sci. Instrum.* **1961**, *32*, 658-661.

13)Lee, H. I. *Electron Spin Echo Envelope Modulation Studies of Some Transition Metal Model Complexes*; Ph.D. Thesis; Michigan State University: East Lansing, 1994.

14)Davies, E. R. *Phys. Lett.* **1974**, *47A*, 1-2.

15) *The TTL Logic Data Book*; Custom Printing Company: Owensville, Missouri 1998.

16)Lancaster, D. *TTL Cookbook*; Howard W. Sams & Co., Inc.: Indianapolis, 1974.

Chapter 4

^{14}N ESEEM: Histidine Ligation to Type-1 and Type-2 Copper Centers in Fet3p

The R side chain unit in the amino acid histidine is imidazole. Imidazole can coordinate to various metal centers through its donor nitrogen atom. Nitrogen has two isotopic forms, ^{14}N and ^{15}N, both of which are magnetic. ^{14}N has nuclear spin, I=1 and ^{15}N has I=1/2. Therefore, histidyl imidazole ligation to a metal center can be identified by EPR techniques. CW-EPR spectroscopy, however, may not be appropriate because ligand hyperfine interactions are typically small compared to metal hyperfine and g-factor anisotropy. As a result, these important features contribute only to the broadening of absorption peaks in the CW-EPR spectrum. In this situation, Electron Spin Echo Envelope Modulation (ESEEM) becomes handy. ESEEM can measure weak hyperfine interactions that are otherwise masked by inhomogeneous broadening of the CW-EPR spectrum.

Mims and Peisach pioneered the application of X-band ESEEM for the study of copper proteins. Their studies on stellacyanin proved that copper with histidine/imidazole ligands exhibited a strong modulation due the remote nitrogen of the bound histidyl imidazole.[1] At X-band (~3000G), the directly coordinated N is strongly coupled so that the electron-nuclear coupling exceeds those of the ^{14}N nuclear Zeeman and the quadrupole term. Consequently, no modulation will be observed from the directly coordinated nitrogen as only the allowed transitions are excited by the microwave pulse. The couplings are also too strong to excite the "branching" of transitions for the weak forbidden lines that do exist. The first

assignments were made based on qualitative comparison of the two-pulse modulation pattern of stellacyanin with those of Cu(II)-aquo complex, Cu(II)- glycylglycine, Cu(II)-$(imidazole)_4$, Cu(II)-$(guanidine)_4$ complexes, and for Cu(II) bovine serum albumin which was previously found to have imidazole coordinated to copper(II). The quantum mechanics and mathematical description of this ^{14}N-ESEEM was also done by Mims and Peisach as they successfully simulated the two pulse and three-pulse spectra of Cu(II)-diethylene-imidazole and Cu(II)-$(imidazole)_4$ complexes.[2,3] Since these initial studies, several copper proteins have been studied using ESEEM.[4-8]

Here, we report the study of histidyl imidazole ligation to the type-1 and type-2 copper centers of the multicopper oxidase Fet3p using ^{14}N ESEEM. Because both type 1 and type 2 centers are paramagnetic, the determination of histidine ligation requires that the contribution of one be eliminated. This was accomplished through site-directed mutagenesis. The two mutants studied were proteins where either the type-1 or type-2 Cu-binding sites had been depleted so that EPR/ESEEM studies can be accomplished without the complication of spectral overlap. To quantify the number of histidine ligands coordinated to the copper sites and determine how they are coordinated, computer simulations of the three-pulse spectra taken at magnetic field positions corresponding to the $g_{\|}$ and $g_{\perp}$ were done. The type-2 copper site was found to have one equatorially bound histidyl imidazole ligand contributing to the echo-envelope modulation. For the type-1 Cu(II), two magnetically distinct histidyl imidazole ligands were found.

4.1 Experimental

Construction of Fet3p mutants and production of soluble protein. Mutant *FET3* alleles were constructed by site-directed mutagenesis by Prof. D.J. Kosman at SUNY-Buffalo. Type-1 depleted (T1D) Fet3p was prepared by Cys484Ser mutation at the type 1 copper site, and type-2 depletion (T2D) was achieved by mutation at the His81Gln mutation at the type 2 copper site. These mutations were selected on the basis of sequence alignment with the other multicopper oxidases. Following amplification of the mutant-encoding vectors in bacteria, the *FET3* sequences were confirmed by dideoxysequencing (Sequenase 2.0) and the vectors transformed into yeast host strain M2*. Culture growth and mutant protein purification were performed as has been described in detail for the wild type protein.[9]

CW-EPR. The continuous-wave EPR spectra of the Fet3 and its variants were obtained at X-Band on a Bruker ESP300E EPR spectrometer equipped with an Oxford ESR-900 liquid helium cryostat and utilizing a TE102 EPR. An EIP Microwave 25B frequency counter was used to monitor the microwave frequency and a Bruker ER 035 NMR gaussmeter was used to measure the external magnetic field. The QPOWA[10-12] (acquired from R.L. Belford at Illinois EPR Research Center) simulation program was used to extract the Cu(II) magnetic parameters for ESEEM simulation.

ESEEM. Pulsed EPR experiments were performed on a home-built spectrometer described previously.[13] Three-pulse ($\pi/2$-τ-$\pi/2$-T-$\pi/2$-τ-echo) ESEEM data were collected at X-band using a reflection cavity that employed a folded stripline resonant element. To eliminate unwanted echoes, a (0,0,0), (π,π,0) two- step phase cycling of the microwave pulses was used. The values of τ were set at period in which the nuclear modulations due to weakly coupled the proton were minimized. All experiments were performed at liquid helium temperature, 4.2 K. Frequency domain spectra were obtained by a Fourier transformation procedure that included dead-time reconstruction[14] as described elsewhere.

4.2 ^{14}N Modulation and Computer Simulation

Computer simulations of the ^{14}N ESEEM data were done using the density matrix formalism developed by Mims[15,16] together with the angle-selection protocol described by Hurst, Henderson and Kreilick[17,18] for Cu^{+2} ENDOR spectroscopy. The CW-EPR spectrum of a frozen solution of Cu^{+2} complexes consists of contributions from all possible orientations of the metal's magnetic axis with respect to the external magnetic field. In ESEEM, the external magnetic field is fixed and hence the simulation starts with determination of the various molecular orientations that satisfy the resonance field condition

$$B_r = \frac{h\nu - M_I A(\theta, \phi)}{B_e g(\theta,\phi)} \qquad (4.1)$$

where h is the Plank's constant, ν is excitation frequency, M_I is the metal's nuclear spin quantum number, θ and ϕ are angles that describe the orientation of the external

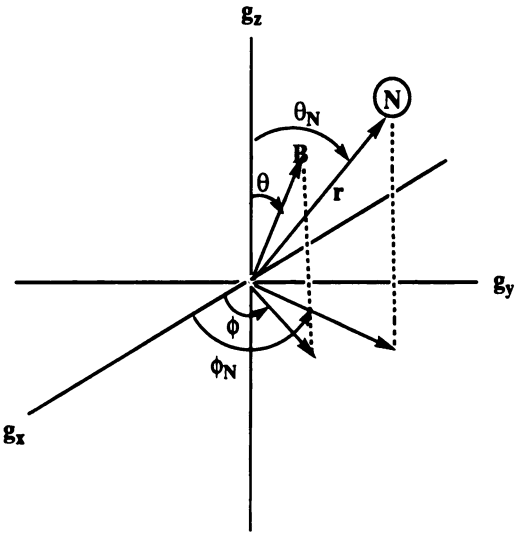

Figure 4.1. Reference coordinate system for ESEEM calculations. The rotation angle θ and the azimuthal angle ϕ describe the direction of the static magnetic field with respect to the g PAS. The nuclear position of the remote nitrogen of imidazole is defined by θ_N and ϕ_N.

magnetic field with respect to the g-tensor principal axis system (Figure 4.1), and $g(\theta,\phi)$ and $A(\theta,\phi)$ satisfy the following condition,

$$g(\theta,\phi)=\left[\sum_{i=1}^{3}(g_i h_i)^2\right]^{1/2}$$

$$A(\theta,\phi)=\frac{\left[\sum_{i=1}^{3}\sum_{j=1}^{3}\left(A_{ji}g_i h_i\right)^2\right]}{g(\theta,\phi)}$$

where the $h_{i's}$ are the direction cosines. Explicitly, the direction cosines in the spherical coordinate system are, $h_1=\cos\phi\sin\theta$, $h_2=\sin\phi\cos\theta$, and $h_3=\cos\theta$. Equation 4.1 tells us that for each set of (θ,ϕ) at a given M_I, there is a field at which resonance can occur. A pictorial explanation of equation (4.1) is shown in Figure 4.2. At fixed B, a curve S is traced on the surface of the sphere. S represents all the

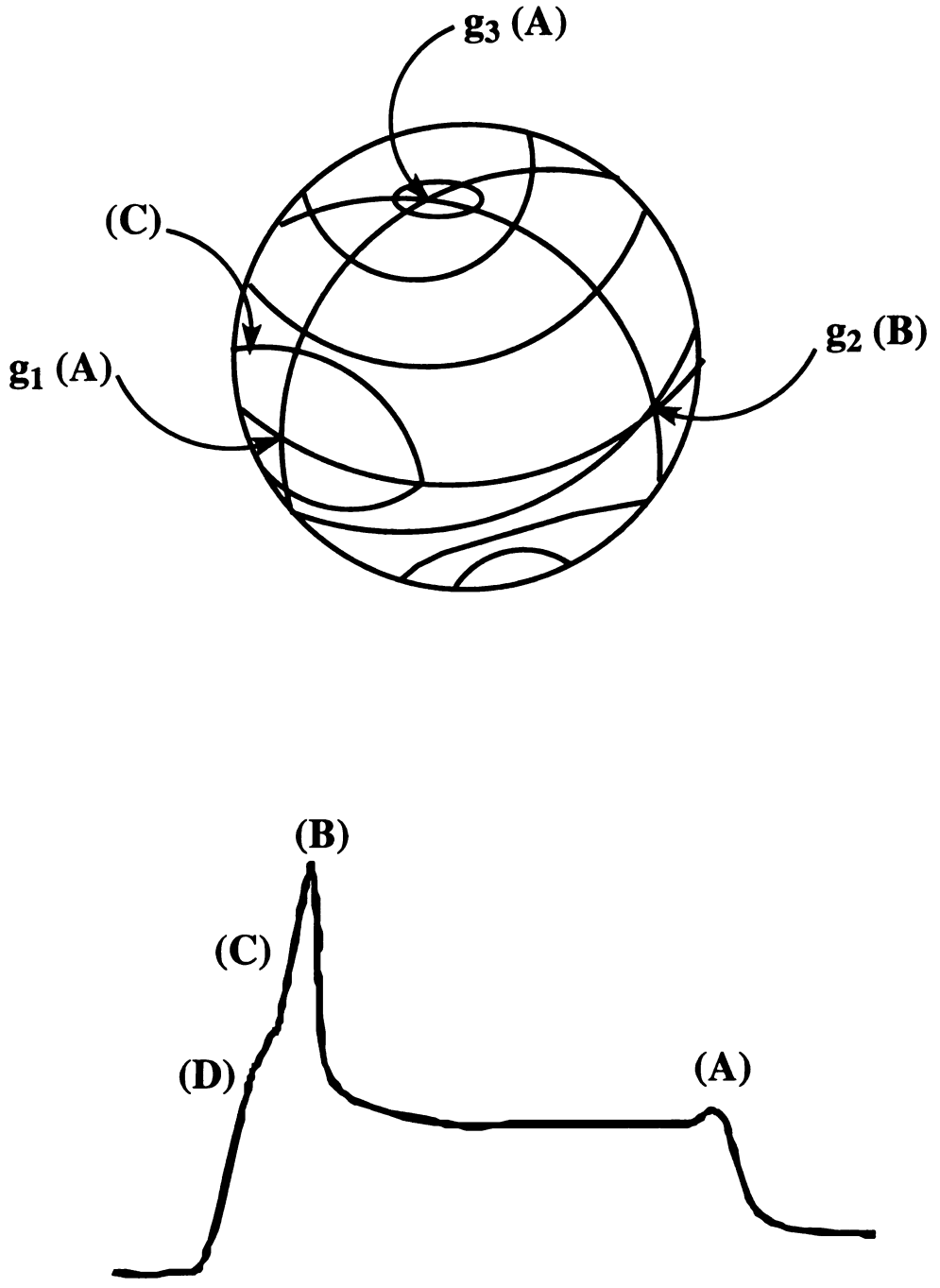

Figure 4.2. Plot of constant g factors (rhombic symmetry case, $g_1 < g_2 < g_3$) in a unit sphere showing correspondence to a magnetic field position in the CW-EPR spectrum.

molecular orientations having the same value of g but different values θ and ϕ.[19,20] For an axial g and A and assuming their PAS are coincident, these molecular orientations can easily be calculated because the dependence of B_r on ϕ vanishes. A graphical solution, for the case of frozen solution of Cu(II) complex is shown in Figure 4.3. It should be noted that an ESEEM spectrum, characteristic of a single crystal, can be obtained if data are obtained at lower field corresponding to transitions involving only the M_I=3/2 sublevel.

The molecular orientations that satisfy equation 4.1 are then used to calculate the ESEEM modulation function. From chapter one, the general stimulated echo envelope modulation function is given by,

$$E_{mod}(\tau,T) = [2(2I + 1)]^{-1} \, Tr\{G_\alpha + G_\beta\} \qquad (4.2)$$

where $G_\alpha = Q_\tau^{+} M^{+} P_T^{+} P_\tau^{+} M Q_\tau M^{+} P_T P_\tau M$

and $G_\beta = Q_\tau^{+} Q_T^{+} M^{+} P_\tau^{+} M Q_\tau Q_T M^{+} P_\tau M$.

In equation 4.2, Q,P and M are matrices of dimension 2I + 1, with P and Q being submatrices of the rotation operators that describe the time evolution of the density matrix during the free precession periods for the two electron spin manifolds. The modulation depths of the frequencies contained in P and Q are given by the elements of M where, $M = M_\alpha^{\dagger} M_\beta$. M_α and M_β are matrices that diagonalize the spin Hamiltonian describing the superhyperfine splittings in the M_s=1/2 and -1/2 electron spin manifolds, respectively.

For ^{14}N modulation the spin Hamiltonian that describes the superhyperfine splittings consists of the nuclear Zeeman, electron-nuclear superhyperfine interaction and the nuclear quadruple interaction.

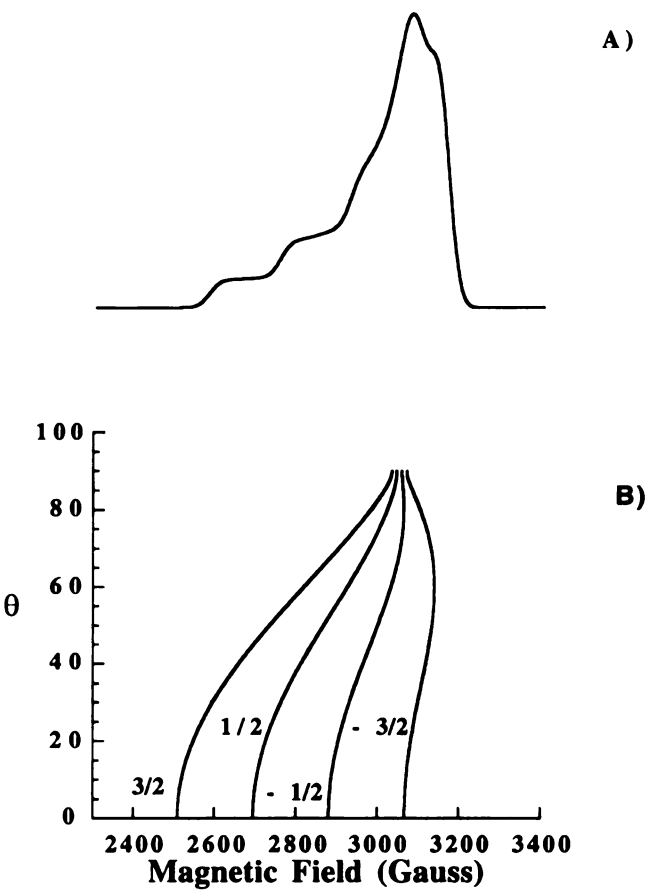

Figure 4.3. Discrete orientations defined by θ as a function of external magnetic field for copper complex with axial g-tensor. The EPR spectrum is generated with $g_x = g_y = 2.05$, $g_z = 2.25$, $A_x = A_y = 35$ MHz and $A_z = 586$ MHz Hamiltonian parameters.

$$\mathcal{H}_n = -g_n\beta_n \mathbf{B}\bullet\hat{\mathbf{I}} + \hat{\mathbf{S}}\bullet\underline{\mathbf{A}}\bullet\hat{\mathbf{I}} + \hat{\mathbf{I}}\bullet\underline{\mathbf{Q}}\bullet\hat{\mathbf{I}} \tag{4.3}$$

In the calculation, the hyperfine tensor is restricted to be axial and the elements are given by

$$A_{ij} = \frac{\beta_N g_N \beta\left[g_i(3n_i n_j - \delta_{ij})\right]}{hr^3} + A_{iso}\delta_{ij}\,21 \tag{4.4}$$

where $n_1 = \cos\phi_N \sin\theta_N$, $n_2 = \sin\phi_N \sin\theta_N$ and $n_3 = \cos\theta_N$. The angles θ_N and ϕ_N specify the orientation of the ^{14}N-hyperfine tensor principal axis with respect to the g-tensor while r, is the effective dipolar distance. Assuming only the hyperfine interaction accounts for the echo modulation, the fundamental modulation frequencies can be derived to be equal to,

$$\omega(B, m_s) = \left[\sum_{i=1}^{3}\left[\frac{m_s}{g(\theta,\phi)}\left(\sum_{j=1}^{3} g_j h_j A_{ji}\right) - h_i\omega_o\right]\right]^{1/2}, \tag{4.5}$$

where $\omega_o = \frac{g_N\beta_N B_o}{\hbar}$.

In its principal axis system, the ^{14}N nuclear quadrupole interaction can be written as,

$$\mathcal{H}q = \frac{e^2qQ}{4}[3I_z^2 - 2 + \eta(I_x^2 - I_y^2)] \tag{4.6}$$

To describe this interaction and relate the orientation of its PAS to that of the g-tensor five parameters are needed. These are the quadrupole coupling constant(e^2qQ); η (asymmetry parameter) and the three Euler angles (α,β,γ).

After the appropriate transformation of the hyperfine and quadrupole tensors to the g-axis system, the Hamiltonians in the alpha and beta electron spin manifolds are separately diagonalized to give the eigenvalues and eigenvectors. The

eigenvalues are used to compute the elements of P and Q while the eigenvectors which determine the intensities are used to calculate the elements of M. With P,Q, and M known, the modulation function at a certain M_I, $E_{mod, MI}$, can be calculated. It is given by the equation,

$$E_{mod, M_I}(\tau, T) = \int_S E_{mod}(\tau, T, S)dS \qquad (4.7a).$$

S can be expressed as a function of g and ϕ , $S(g,\phi)$, so that

$$E_{mod,M_I}(\tau, T) = \int_0^{2\pi} E_{mod}(\tau, T, \phi)_g \frac{dS}{d\phi} d\phi. \qquad (4.7b)$$

$(dS/d\phi)d\phi$ gives the probability the paramagnetic assumes an orientation at a given g. Consideration of distribution in field, (4.7b) expands to,

$$E_{mod, M_I}(\tau, T) = \int_{B_o-\Delta B}^{B_o+\Delta B} \int_0^{2\pi} E_{mod}(\tau, T, \phi)_g \, R(B) \frac{dS}{d\phi} d\phi dB \qquad (4.8)$$

R(B) in equation is a gaussian lineshape function. At a static magnetic field corresponding to $g_\perp$, transitions involving all M_I's of copper maybe possible so that the resultant E_{mod} consists of four line integrals of the form described by (4.7b). The resulting modulation function is then multiplied by the decay function , $\exp[-(\tau/t)^n]$ where values of τ, t and n were chosen such that the decay of modulation of our simulation is similar to the experimental time-domain data.

4.3 Comparison of Nuclear Transition Spectra

Prior to using the ESEEM angle-selection program, its output was compared to simulations of spectra obtained by other methods. The purpose of this exercise was to test the output of our orientation selection ESEEM simulations program by

comparing it to the predictions made by the more established routines developed for ENDOR spectroscopy. An ENDOR powder spectrum for an assumed S = 1/2, I =1 spin system described by the Hamiltonian parameters: $g_n = 2.261$, $A_{iso} = 4.0$, $r_{eff} =$ 2.6Å, $B_o = 3200$ Gauss, $\nu = 9.2$ GHz, is shown in Figure 4.4A. Two powder lineshapes centered about the nuclear Larmor frequency of 5.52MHz are predicted. The lineshapes are of the familiar "Pake" type that result from the $\sin\theta$ weighting of the electron magnetic moments. The most intense portion of each Pake lineshape occurs when $\theta = 90°$, or when the electron magnetic moments are perpendicular to the lab field. The frequency difference between those perpendicular features yields the $A_\perp$ principal element of the hyperfine tensor. If the electron magnetic moments are aligned with the lab field, $\theta = 0°$, and one observes the largest splitting in the ENDOR spectrum of $A_\parallel = 7.1$MHz.

A corresponding powder ESEEM spectrum is shown in Figure 4.4B. Just as with the ENDOR spectrum, one finds two broad peaks, from the two electron spin manifold, centered at the nuclear Larmor frequency. The ESEEM lineshapes differ from the ENDOR powder spectrum pattern in that they are weighted by EPR transition probability products.[22] Because the branching of transition is most favored for $\theta = 45°$ and tails of to zero at $\theta = 0°$ and 90°, a more complex response is predicted. Now if g-anisotropy is added to this problem so that powder averaging of the spin system is no longer appropriate, the ESEEM simulation of Figure 4.4C-E are obtained. For these simulations an axial g-tensor with principal elements of $g_{xx} = g_{yy} = 2.25$, and $g_{zz} = 2.05$ were used. Figure 4.4C shows the output obtained near g = 2.05, where only the $\theta = 90°$ orientation is sampled. At g = 2.25, the $\theta = 0°$

Figure 4.4. Comparison of different nuclear transition spectra. A) ENDOR spectrum calculated by a Matlab program Spint1.mat, B) and ESEEM spectrum calculated by orientation averaging using the Fortran program SESPN1, C) ESEEM spectrum at a discrete orientation, $\theta = 90°$, D) ESEEM spectrum at a discrete orientation, $\theta = 0°$, and E) ESEEM spectrum at a discrete orientation, $\theta = 45.°$ C-D spectra are calculated using the Fortran program ANGSESPN1. All spectra are generated using the same magnetic parameter for an assumed S = 1/2, I = 1 system: $g_n = 2.26$, $A_{iso} = 4.0$, $r_{eff} = 2.6$Å, $B_o =$ 3200 Gauss, $\nu = 9.2$ GHz, $\tau = 200$ns an T = 40ns. The g principal values used to calculate spectra C, D and E are $g_x = 2.25$, $g_y = 2.25$ and $g_z = 2.05$.

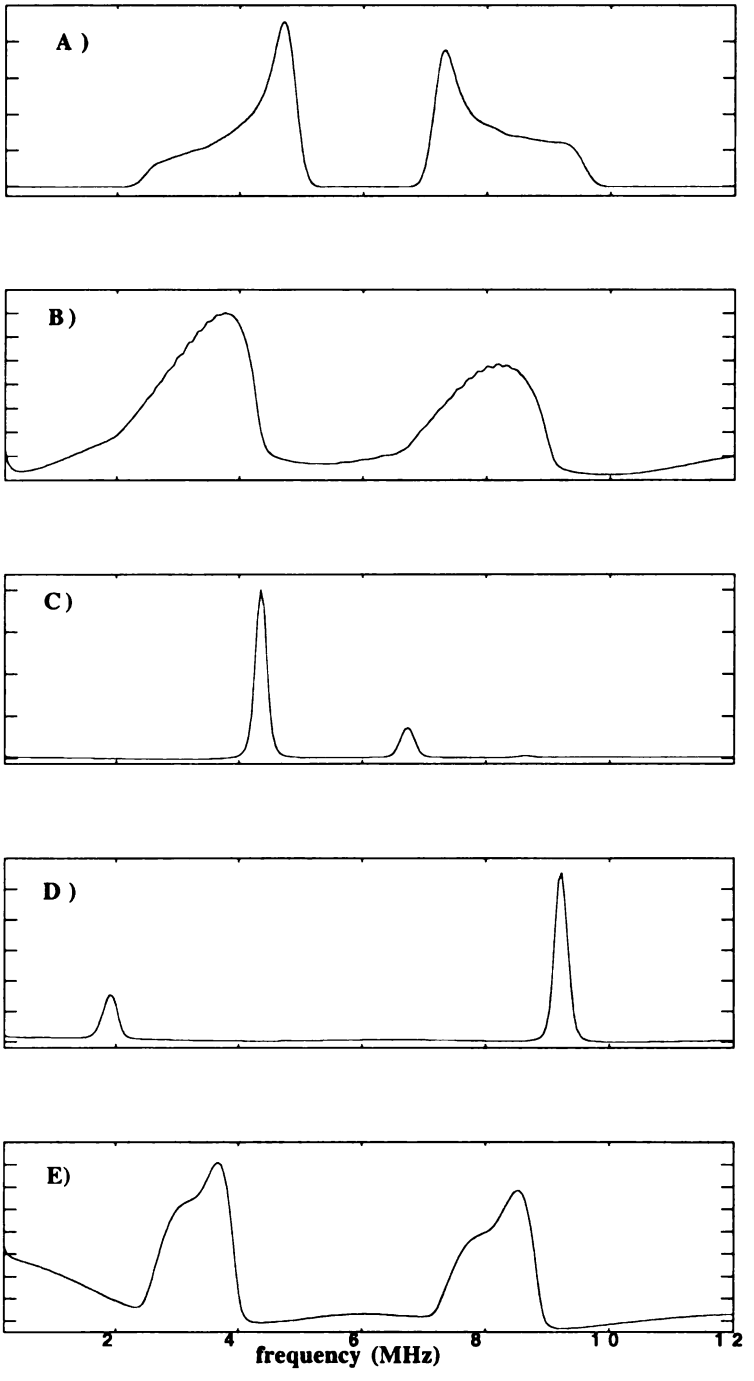
A)
B)
C)
D)
E)
2
4
6
8
10
12
frequency (MHz)

orientation is studied and these results are shown in Figure 4.4D. The $\theta = 45°$ orientation is resolved at g = 2.15 and the predicted ESEEM is provided in Figure 4.4E. Part of the inequivalence in amplitudes for the peaks predicted in the ESEEM spectrum stems from the τ-suppression behavior of three-pulse ESEEM.

4.4 Results and Discussion

4.4.1 CW-EPR

X-band CW-EPR spectra of Fet3p and its variants are shown in Figure 4.5. Figure 4.5A shows the spectrum of wild type protein with both type 1 and type 2 centers contributing. Figure 4.5B and 4.5C are of T2D Fet3p [spectrum of the type 1 Cu(II) only] and T1D Fet3p [spectrum of the type 2 Cu(II) only], respectively. The spectra are characterized by axial g tensors with no hyperfine structure being observed at $g_{\perp}$. Both mutants lacked enzymatic activity. These and other data demonstrate that the sequence homology upon which the mutagenesis was based correctly predicts the amino acid ligands to the type 1 and type 2 copper atoms in Fet3p. The results of Figure 4.5C are supported by the visible absorbance data that have also demonstrated that Cys484Ser mutation resulted in the loss of the type 1 Cu(II).[23]

These CW-EPR data were analyzed using the QPOWA program. In Fig. 4.5B, the spectrum of the type 1 Cu(II) site is simulated (dotted line) using the parameters, $g_{||} = 2.050$; $g_{\perp} = 2.198$; $A_{||} = 271$ MHz and $A_{\perp} = 25$ MHz, while the type 2 Cu(II) spectrum is simulated in Fig. 4.5C (dotted line) using the values $g_{||} = 2.054$; $g_{\perp} = 2.250$; $A_{||} = 586$ MHz and $A_{\perp} = 35$ MHz. The observed principal g values ($g_{||} >$

Figure 4.5. Continuous-wave EPR spectra of (A)wild-type Fet3, (B) type 2 depleted (T2D) Fet3 and, (C) type 1 depleted (T1D) Fet3. For (A), measurement conditions were: microwave frequency, 9.478GHz; microwave power, 2mW; modulation frequency, 100kHz; modulation amplitude, 10G; temperature, 16K. For (B), measurement conditions were: microwave frequency, 9.481GHz; microwave power, 0.998mW; modulation frequency, 100kHz; modulation amplitude, 5.054G; temperature, 16K. The simulated spectrum (dotted line) of (B) was obtained using $g_x = g_y = 2.050$, $g_z = 2.198$, $A_x = A_y = 25$ MHz and $A_z = 271$ MHz. For (C), measurement conditions were: microwave frequency, 9.481GHz; microwave power, 0.998mW; modulation frequency, 100kHz; modulation amplitude, 5.054G; temperature, 16K. The simulated spectrum (dotted line) of (C) was obtained using $g_x = g_y = 2.054$, $g_z = 2.250$, $A_x = A_y = 35$MHz and $A_z =$ 586MHz.

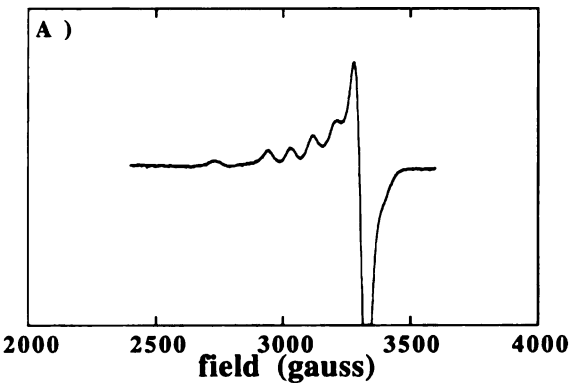
A)
2000
2500
3000
3500
4000
field (gauss)

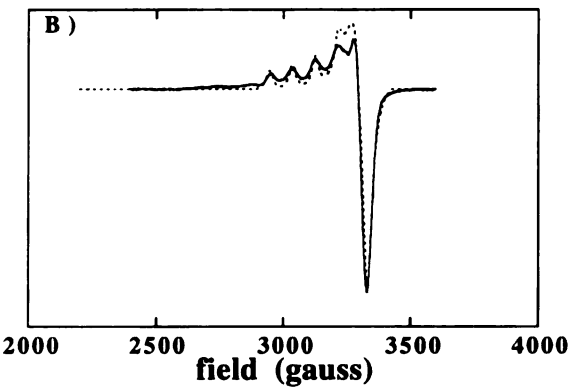
B)
2000
2500
3000
3500
4000
field (gauss)

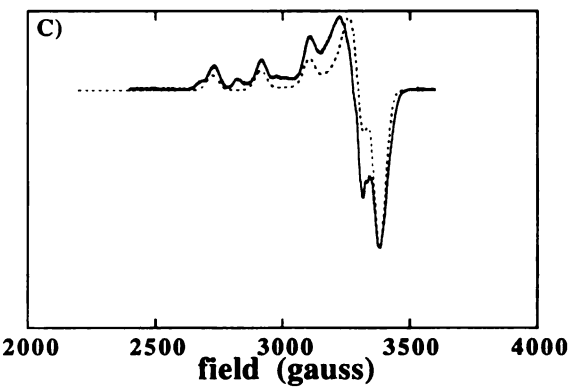
C)
2000
2500
3000
3500
4000
field (gauss)

$g_{\perp} > 2.0023$) of both type 1 and type 2 copper sites indicate that at each copper the unpaired electron primarily occupies the $3d_{x^2-y^2}$ atomic orbital on the metal.[24,25] The smaller g values of the type 1 Cu(II) in relation to the values for the type 2 Cu(II), particularly $g_{||}$, is a result of the strong covalent bonding between Cu^{+2} and the cysteine-sulfur ligand at the type 1 site. This covalent bonding leads to more electron delocalization onto the ligand and consequently the metal hyperfine coupling constant decreases.

4.4.2 ^{14}N ESEEM

4.4.2.1 T1D Fet3p

Figure 4.6 and 4.7 shows the three-pulse ^{14}N-ESEEM data collected for T1D Fet3p at magnetic field positions in the $g_{||}$ (B_o = 2690 Gauss) and $g_{\perp}$ (B_o = 3050 Gauss) regions, respectively. At both field strengths, the frequency-domain spectra show sharp low frequency peaks at ~0.6, ~0.9 and ~1.5 MHz. A broad peak that shifts from ~3.6 to ~4.2 MHz as the magnetic field is varied from 2690G to 3050G is also observed. The spectra are similar to those obtained for ascorbate oxidase (AO) at low field where only the type 2 Cu(II) contributes to the envelope modulation function.[26]

The overall appearance of the experimental modulation pattern are similar to those obtained by ESEEM studies on model copper complexes and copper proteins exhibiting ^{14}N modulation arising from the interaction of the unpaired electron spin of Cu(II) and the remote (non-coordinated) nitrogen of an equatorially coordinated imidazole.[2,4,8] Furthermore, the appearance of these spectra is typical of ^{14}N nuclei characterized by an isotropic hyperfine coupling that is approximately equal to twice

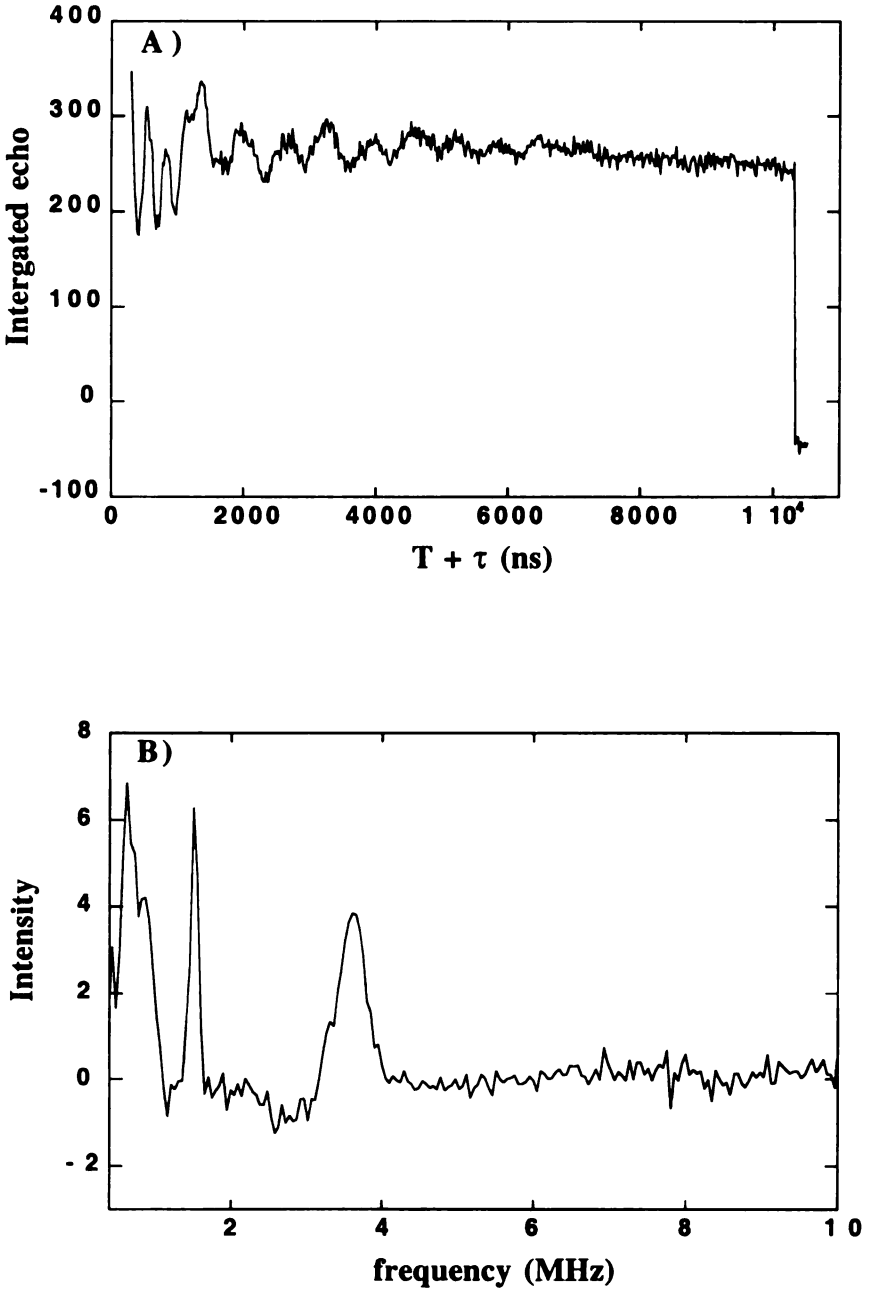

Figure 4.6. Representative experimental ^{14}N-ESEEM spectra for the type-2 copper (T1D Fet3). Spectrum (A) was collected at B_o = 2690 Gauss and for τ = 260ns. Spectrum (B) is the cosine Fourier transform of (A). Other measurement condition are: microwave frequency, 8.78 GHz; microwave power (43 dB); sample temperature, 4.2 K.

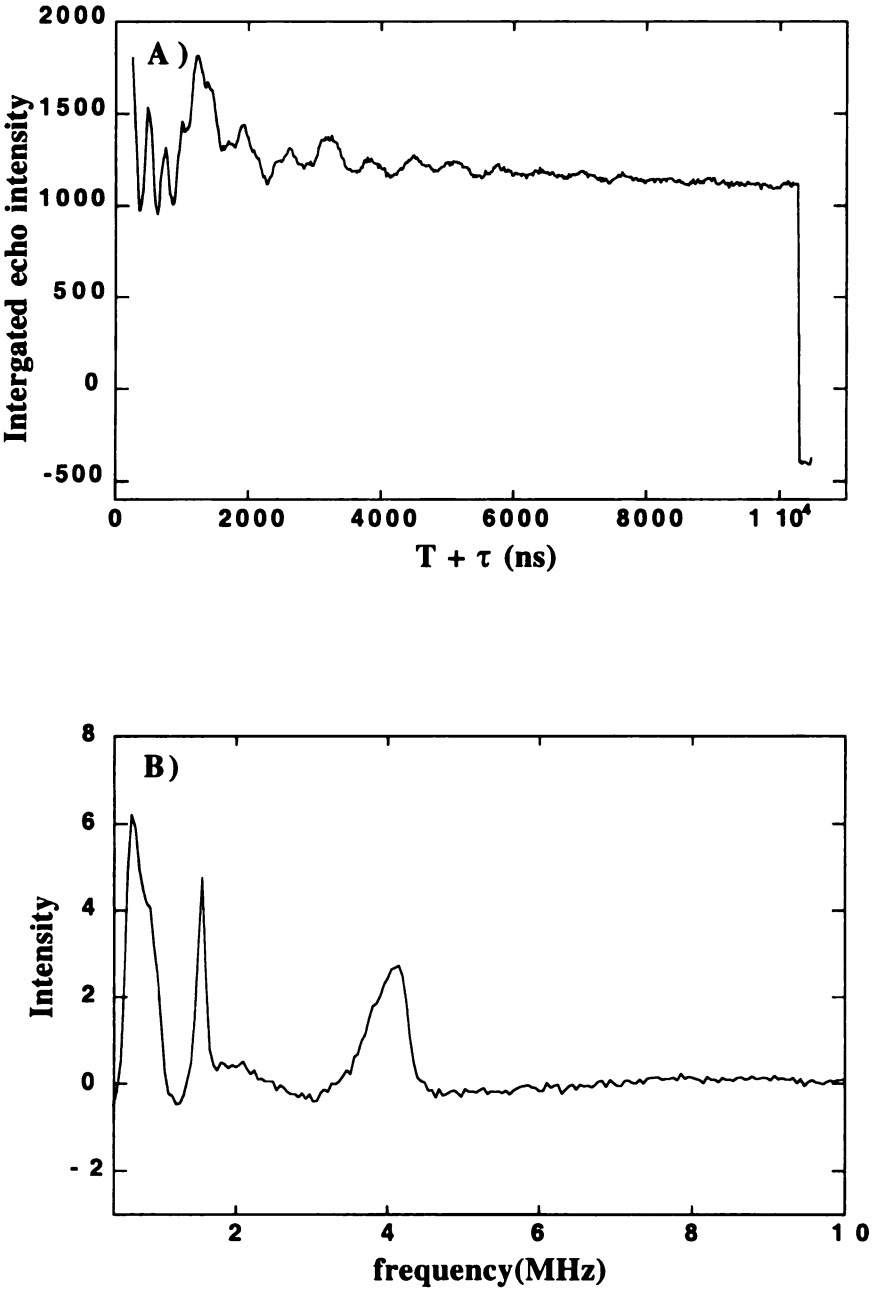

Figure 4.7. Representative experimental ^{14}N-ESEEM spectra for the type-2 copper (T1D Fet3). Spectrum (A) was collected at B_o = 3050 Gauss and for τ = 230ns. Spectrum (B) is the cosine Fourier transform of (A). Other measurement condition are: microwave frequency, 8.78 GHz; microwave power (43 dB); sample temperature, 4.2 K.

The nuclear Larmor frequency. The consequence of this condition is depicted in Figure 4.8. Because the nuclear Zeeman and hyperfine interactions cancel one another in one of the electron spin manifolds, the electron spin energy levels are split by the ^{14}N nuclear quadrupole interaction (NQI). Consequently, three sharp lines are observed in the low frequency region of the spectrum. In the other manifold where the nuclear Zeeman and the electron-nuclear hyperfine interaction are additive, a single, broad double quantum transition is expected at about four times the nuclear Zeeman frequency.

This condition of "exact cancellation"[2,27] enables us to estimate the quadrupole coupling constant, e^2qQ, and the NQI asymmetry parameter, η, by assigning the three low-frequency peaks to the zero-field NQI resonance frequencies:

$$\nu_0 = \frac{e^2qQ(\eta)}{2}$$

$$\nu_- = \frac{e^2qQ(3-\eta)}{4}$$

$$\nu_+ = \frac{e^2qQ(3+\eta)}{4}.$$

From the positions of the experimental peaks and using the above equations we obtained our first estimate of $\eta = 0.75$ and $e^2qQ = 1.60$ MHz. The position and shape of the broad peak near 4 MHz are determined by the symmetry and strength of the hyperfine interaction, and by the relative orientation of the hyperfine and NQI tensors.

Figure 4.8. (A) Energy diagram describing 'exact cancellation condition' for I = 1. (B) Typical ESEEM spectrum of ^{14}N following exact cancellation condition.

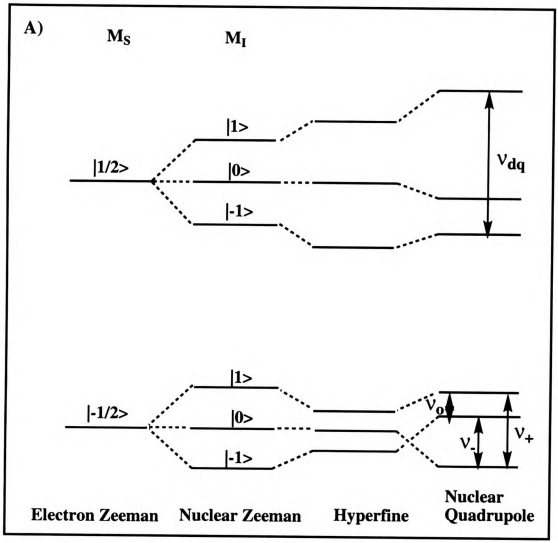
A)
M_S
M_I
|1>
|1/2>
|0>
|-1>
ν_{dq}
|1>
|-1/2>
|0>
|-1>
ν_0
ν_-
ν_+
Electron Zeeman
Nuclear Zeeman
Hyperfine
Nuclear Quadrupole

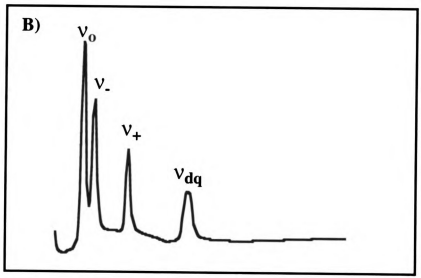
B)
ν_0
ν_-
ν_+
ν_{dq}

Figure 4.9 and 4.10 illustrate various simulations of the ^{14}N-ESEEM data obtained for the type 2 copper site in Fet3p. Figure 4.9 shows comparisons between experiment (solid lines) and theory (dashed lines) for data collected at $g_{\|}$, while a parallel set of comparisons is made for $g_{\perp}$ on Figure 4.10. In spectra 4.9a and 4.10a, our calculations assumed one equatorially bound histidine imidazole ligand having an isotropic hyperfine coupling constant (A_{iso}) of 1.75 MHz and effective dipole-dipole radius, r_{eff} of 3.0Å. In contrast, simulations 4.9(4.10)b-d were generated with the assumption that there are two equatorial imidazoles bound to the type 2 Cu(II). Simulations 4.9b and 4.10b assume two magnetically equivalent imidazoles while c and d consider two magnetically inequivalent equatorial imidazole ligands. All of these simulations show minor peaks that range from 2.2 - 3.2 and that arise from linear combinations of the narrow peaks resolved at 0.6, 0.9 and 1.5 MHz. These combination lines are a consequence of the product rule and were not resolved in our ESEEM study of the type 2 site of Fet3p. The simulations of Figure 4.9/4.10b-d were generated for two reasons. Recent X-ray crystallographic studies of two other multicopper oxidases, ascorbate oxidase (AO)[28,29] and human ceruloplasmin (hCp)[30], identified two histidines close to the type 2 copper sites in these proteins. Furthermore, sequence analysis indicated the presence of a homologous type 2 copper site in Fet3p.[31,32] Indeed, this analysis was used to design the mutagenesis strategy that did, in fact, result in the successful production of the T1D and T2D mutants used here and elsewhere.[23] Our simulations, however, indicate that only one histidine imidazole is coordinated equatorially to the type 2 copper in Fet3p despite the likelihood that both histidines are present at that site.

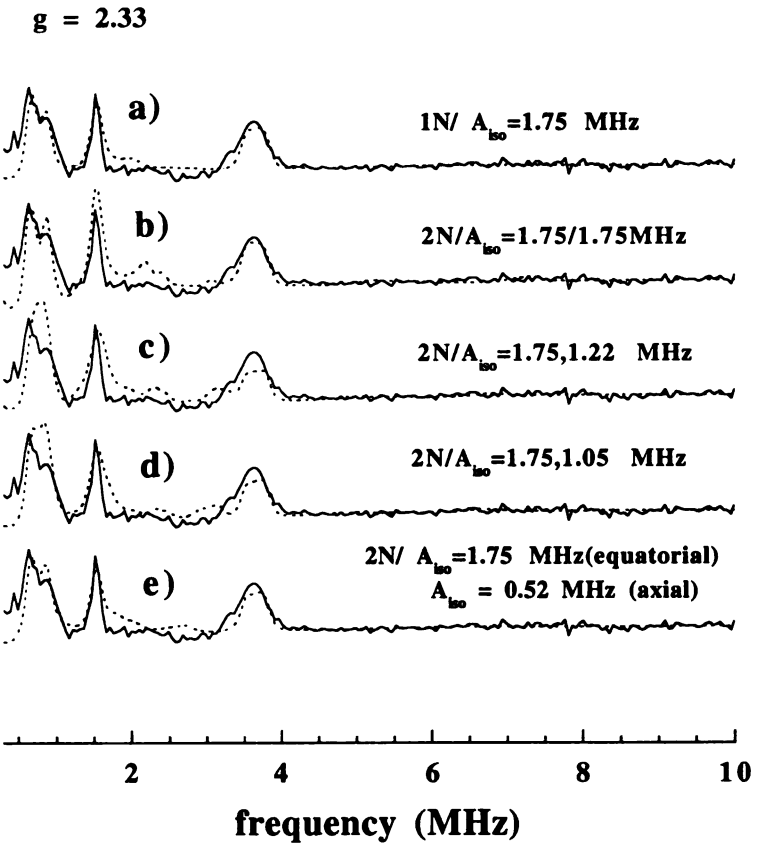

Figure 4.9. Determination of number of histidyl imidazole ligands for the type-2 center of Fet3. The simulation (dotted lines) models and parameters are listed in Table 4.1. The stimulated-echo ESEEM (solid lines) and simulations (dotted lines) were collected at g = 2.33 using a τ-value of 260 ns. Other common experimental conditions common to the ESEEM measurements are given in Figure 4.6. The simulation given for (a) considers only one coupled nitrogen, those shown for simulations of (b)-(e) are for 2 coupled nitrogens with Hamiltonian parameters being given in Table 4.1.

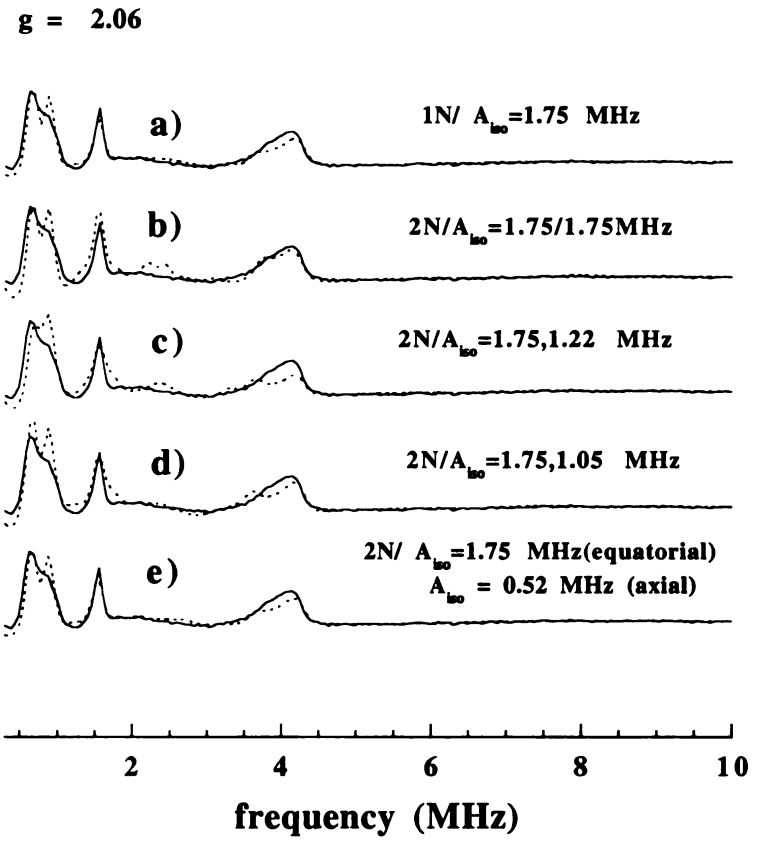

Figure 4.10. Determination of number of histidyl imidazole ligands for the type-2 center of Fet3. The simulation (dotted lines) models and parameters are listed in Table 4.1. The stimulated-echo ESEEM (solid lines) and simulations (dotted lines) were collected at g = 2.06 using a τ-value of 230 ns. Other common experimental conditions common to the ESEEM measurements are given in Figure 4.7. The simulation given for (a) considers only one coupled nitrogen, those shown for simulations of (b)-(e) are for 2 coupled nitrogens with Hamiltonian parameters being given in Table 4.1.

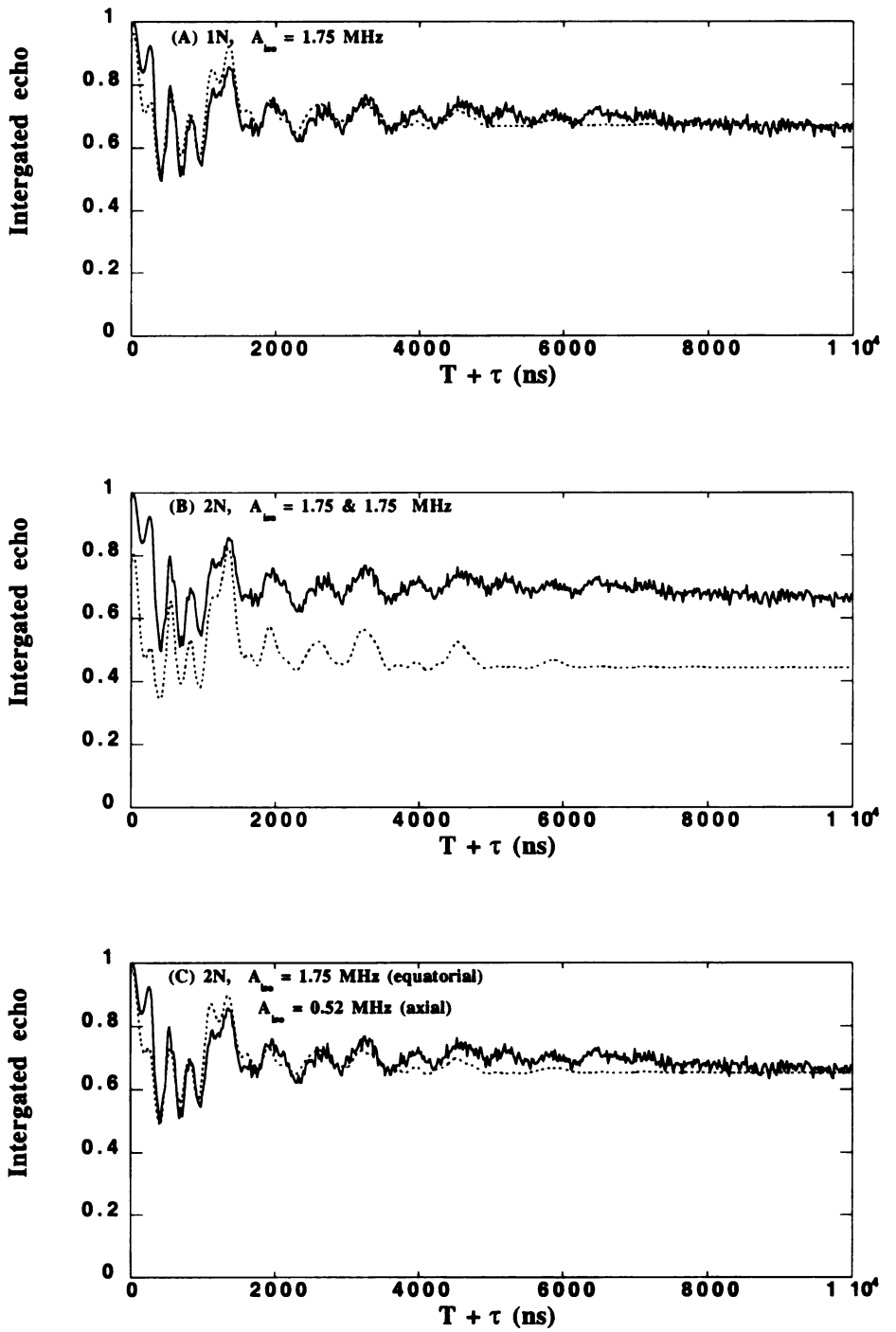

Figure 4.11. Time-domain computer simulations (dashed lines) of the normalized ^{14}N ESEEM data collected for T1D Fet3 protein at g = 2.33. Trace A is for one equatorially coordinated histidyl imidazole ligand (A_{iso} = 1.75 MHz and r_{eff} = 3.0 Å). Simulation B assumes two magnetically equivalent histidyl imidazole ligand. Trace C assumes one equatorial and one axial (A_{iso} = 0.52 MHz and r_{eff} = 3.2 Å) histidyl q imidazole ligands. Other parameters are listed in Table 4.1.

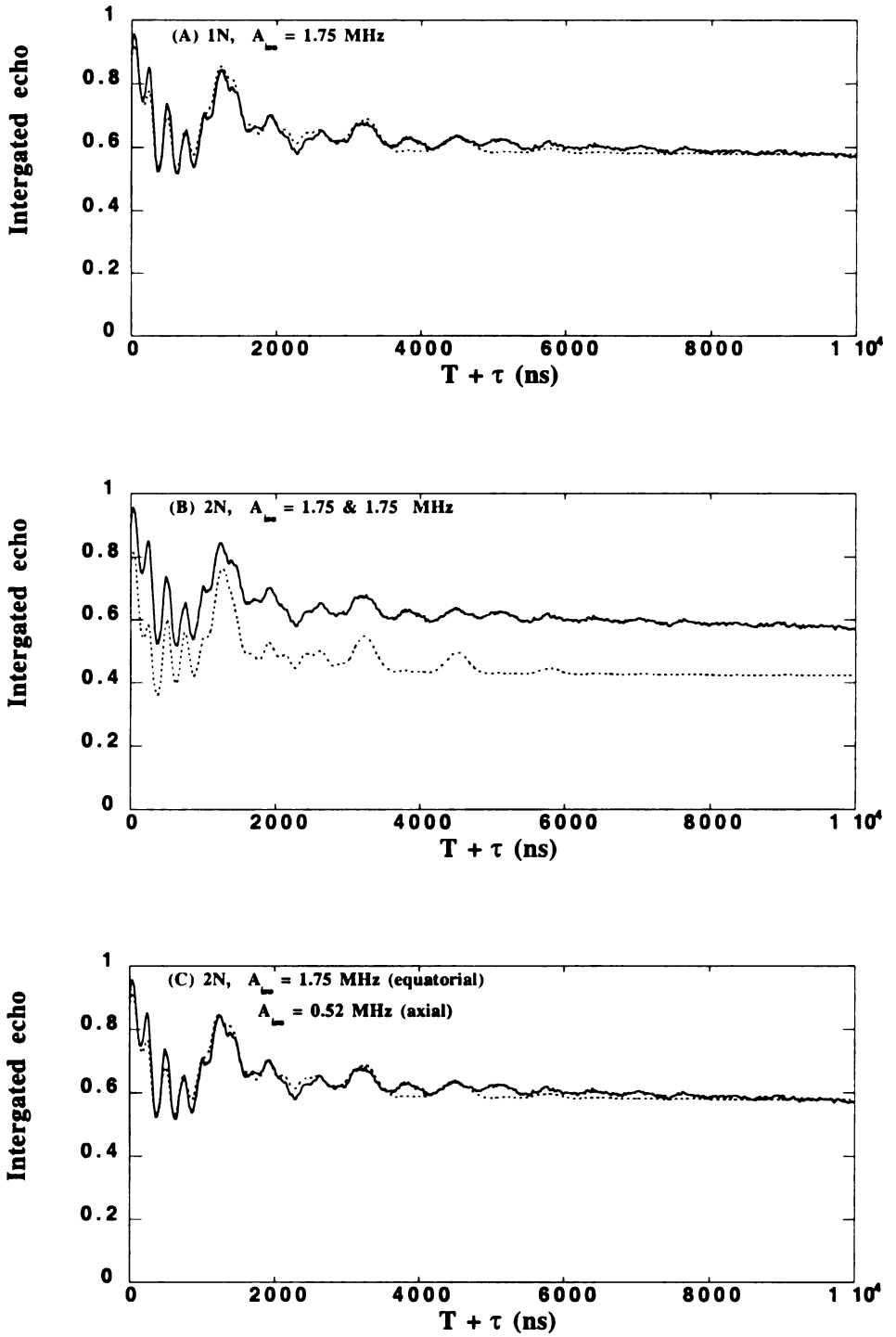

Figure 4.12. Time-domain computer simulations (dashed lines) of the normalized ^{14}N ESEEM data collected for T1D Fet3 protein at g = 2.06. Trace A is for one equatorially coordinated histidyl imidazole ligand (A_{iso} = 1.75 MHz and r_{eff} = 3.0 Å). Simulation B assumes two magnetically equivalent histidyl imidazole ligand. Trace C assumes one equatorial and one axial (A_{iso} = 0.52 MHz and r_{eff} = 3.2 Å) histidyl imidazole ligands. Other parameters are listed in Table 4.1.

Table 4.1 Ligand hyperfine parameters for the stimulated echo ESEEM simulations aimed at the determination of number of histidine ligands covalently bonded to the type 2 center of Fet3 (Fig. 4.9 and 4.10). α,β, and γ are the Euler angles that relate the principal axis system of the nuclear-quadrupole interaction to the Cu(II) g-tensor axes. θ_N and ϕ_N accomplished this transformation for the hyperfine tensor.

	a		b		c		d		e	
ligand	N1	N2	N1	N2	N1	N2	N1	N2	N1	N2
A_{iso}(MHz)	1.75	-	1.75	1.75	1.75	1.22	1.75	1.05	1.75	0.52
r_{eff} (Å)	3.0	-	3.0	3.0	3.0	3.0	3.0	3.2	3.0	3.2
θ_N,ϕ_N	90°,0°	-	90°,0°	90°,90°	90°,0°	90°,90°	90°,0°	0°,0°	90°,0°	0°,0°
e^2qQ	1.58	-	1.58	1.58	1.58	1.58	1.58	1.55	1.58	1.55
η	0.83	-	0.83	0.83	0.83	0.83	0.83	0.85	0.83	0.85
α,β,λ	20°,39°,0°	-	20°,39°,0°	20°,39°,0°	20°,39°,0°	20°,39°,0°	20°,39°,0°	0°,45°,65°	20°,39°,0°	0°,45°,65°

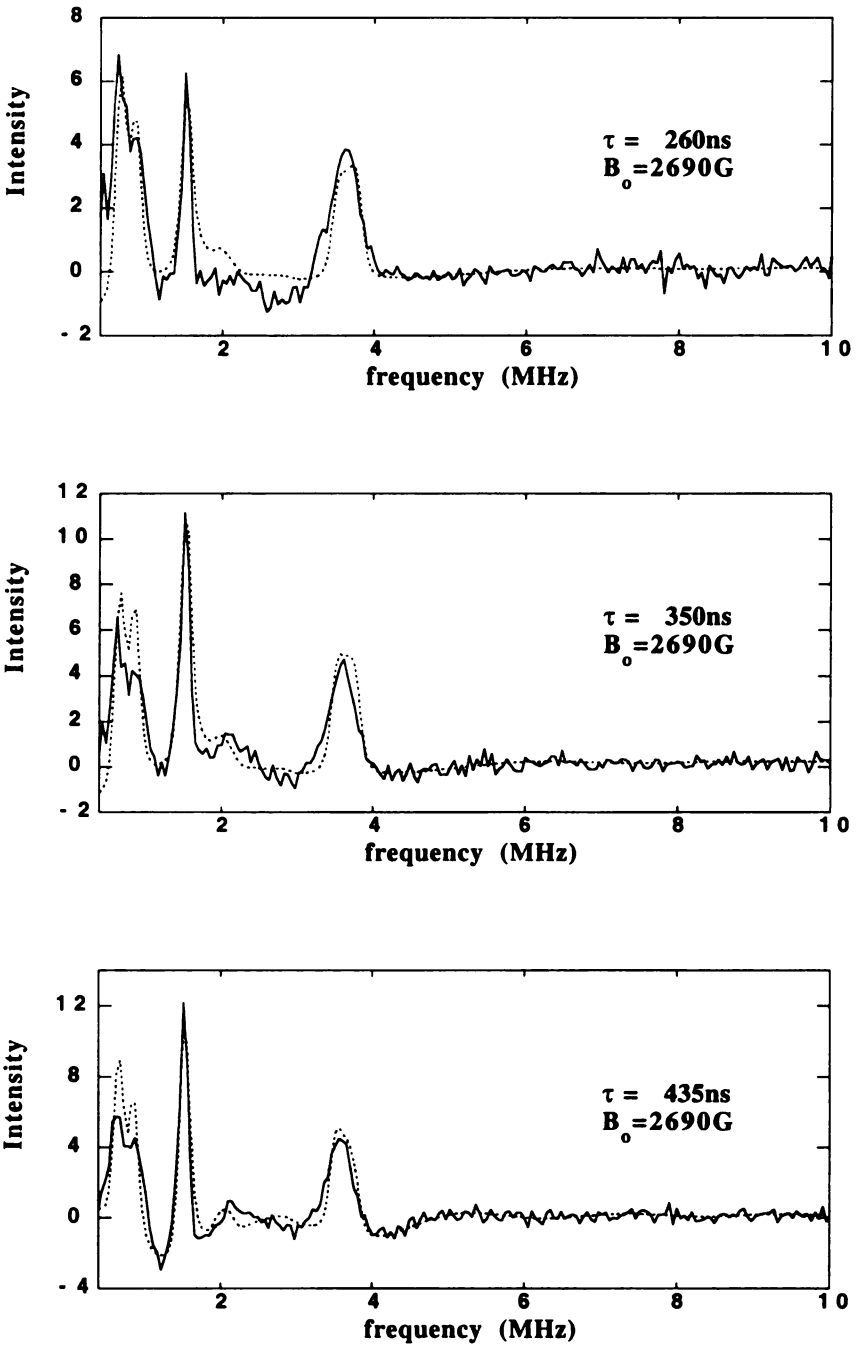

Figure 4.13A. T1D Fet3 ESEEM data and computer simulations at B_o = 2690G for different τ values: A) 260ns, B) 350ns, C) 435ns. Hamiltonian parameters are the same as in Figure 4.9a in which one magnetic ^{14}N nucleus couples with the electron spin.

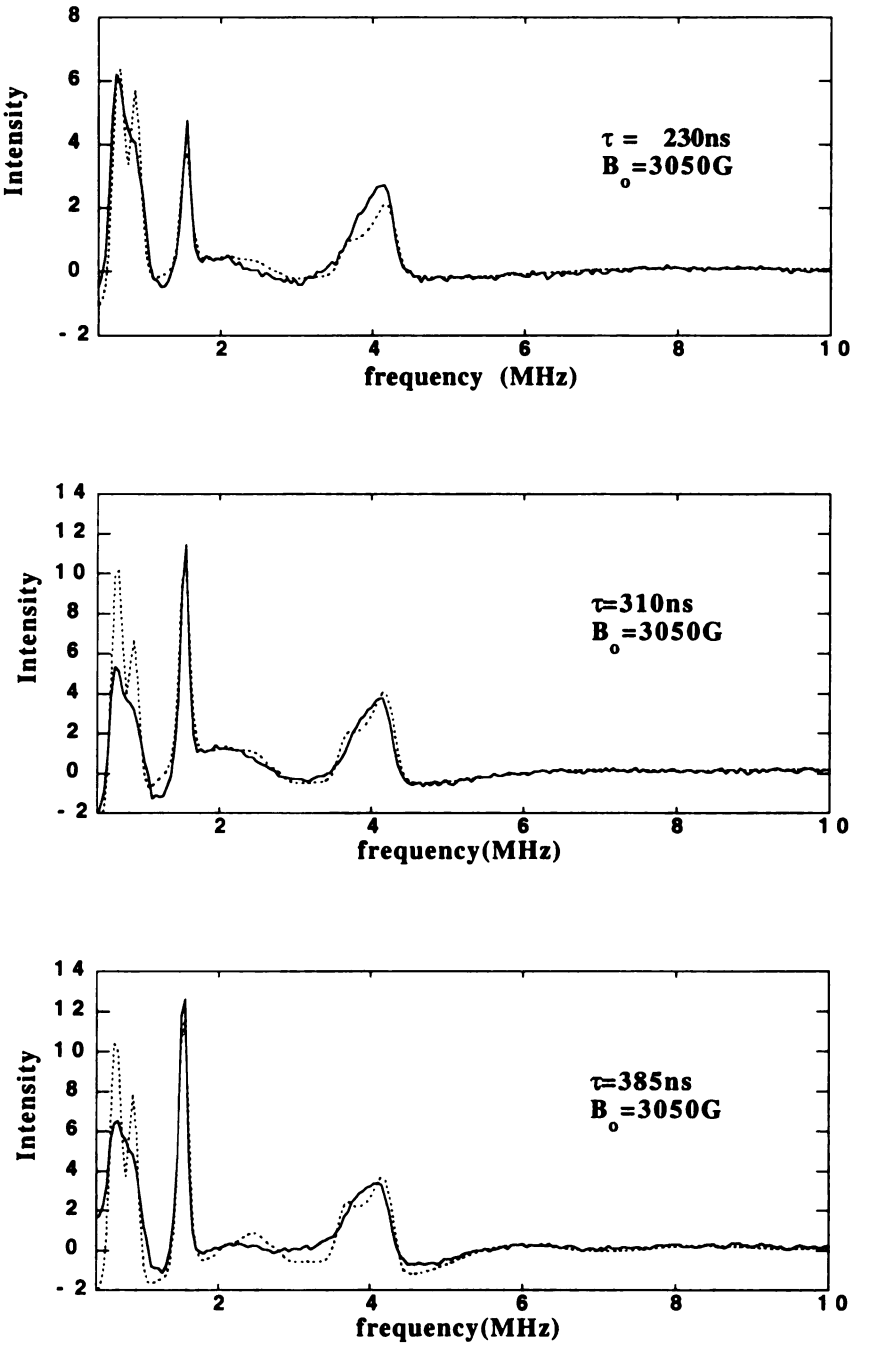

Figure 4.13B T1D Fet3 ESEEM data and computer simulations at B_o = 3050G for different τ values: A) 230ns, B) 310ns, C) 385ns. Hamiltonian parameters are the same as in Figure 4.10a in which one magnetic ^{14}N nucleus couples with the electron spin.

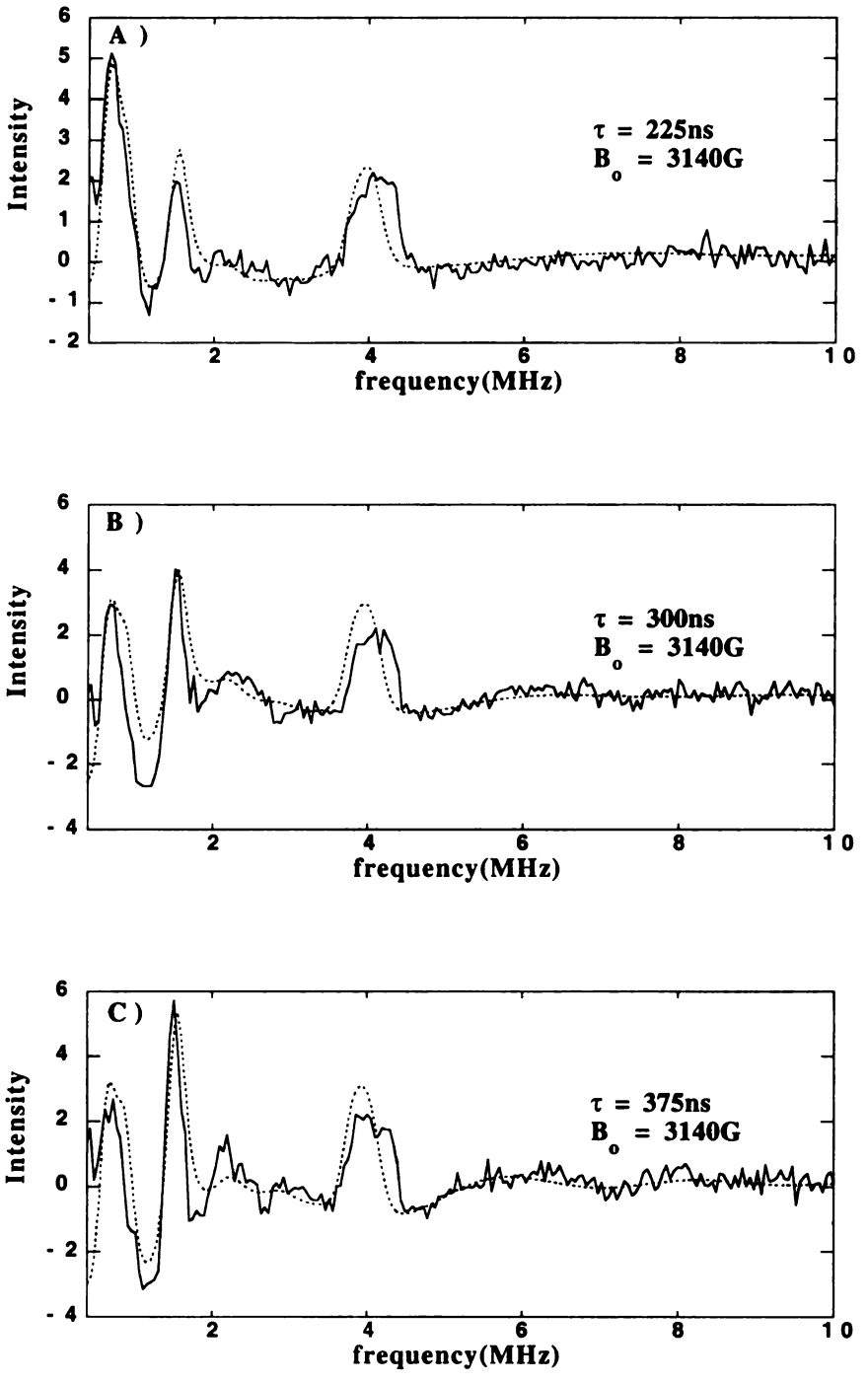

Figure 4.13C. T1D Fet3 ESEEM data and computer simulations at B_o = 3140G for different τ values: A) 225ns, B) 300ns, C) 375ns. Other Hamiltonian parameters are the same as in Figure 4.13 A and B in which one magnetic ^{14}N nucleus couples with the electron spin.

Axial histidine imidazoles have a very weak hyperfine interaction (less than 1 MHz for the directly coordinated nitrogen) so they yield only a shallow modulation that is easily obscured by ^{14}N at exact cancellation.[33] Therefore, the contribution of an axial histidine ligand to the modulation of the electron spin magnetization at the type 2 Cu(II) would be obscured if an equatorially bound histidine was present as well. To test this inference, a simulation was performed for one axial and one equatorial histidine ligand (Fig. 4.9/4.10e). As expected, simulations a and e show only modest differences. These simulations indicate that if a second histidine is present as an inner sphere ligand at the type 2 Cu(II) in Fet3p, it is most likely axially coordinated. One of these ligands would be His81, since its substitution in the T2D mutant does result in loss of the copper atom. The other is most likely His416, based on the sequence alignments with the other multicopper oxidases. A test of this prediction by mutagenesis has not been performed.

Spectra obtained at different τ's for each field are shown in Figures 4.13A-C. These spectra show the effect of the choice of τ on the intensity of the low frequency peaks. The 1.6 MHz peak grew in intensity with respect to other peaks as τ was increased. This trend is true for three B_o setting. Simulation curves (dotted lines) replicate the this trend, thus adding confidence to our simulation parameters.

4.4.2.2 T2D Fet3p

^{14}N-ESEEM data for the type 1 Cu(II) site were collected from T2D Fet3p samples. These are shown in Figure 4.14 and 4.15. Spectra taken at $g_{||}$ (2825G, Figure 4.14) show peaks at 0.4, 0.7, 0.8, 1.4, 1.6, 3.2 and 3.5 MHz. In the $g_{\perp}$ region

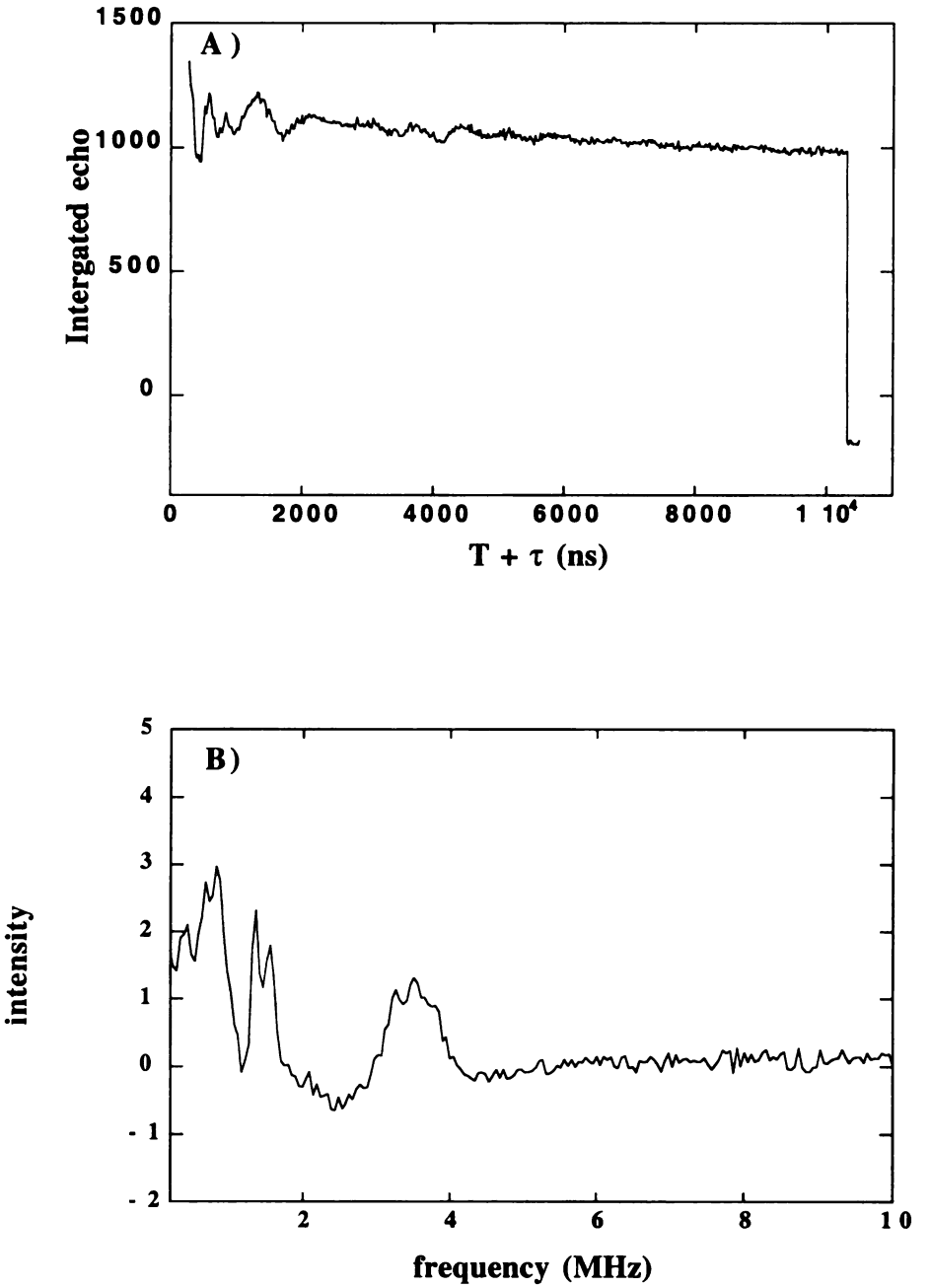

Figure 4.14. Representative experimental ^{14}N-ESEEM spectra for the type-1 copper site (T2D Fet3). Spectrum (A) was collected at B_o = 2825 Gauss and for τ = 250ns. Spectrum (B) is the cosine Fourier transform of (A). Other measurement conditions: microwave frequency, 8.836 GHz; microwave power, 43 dB; sample temperature, 4.2K.

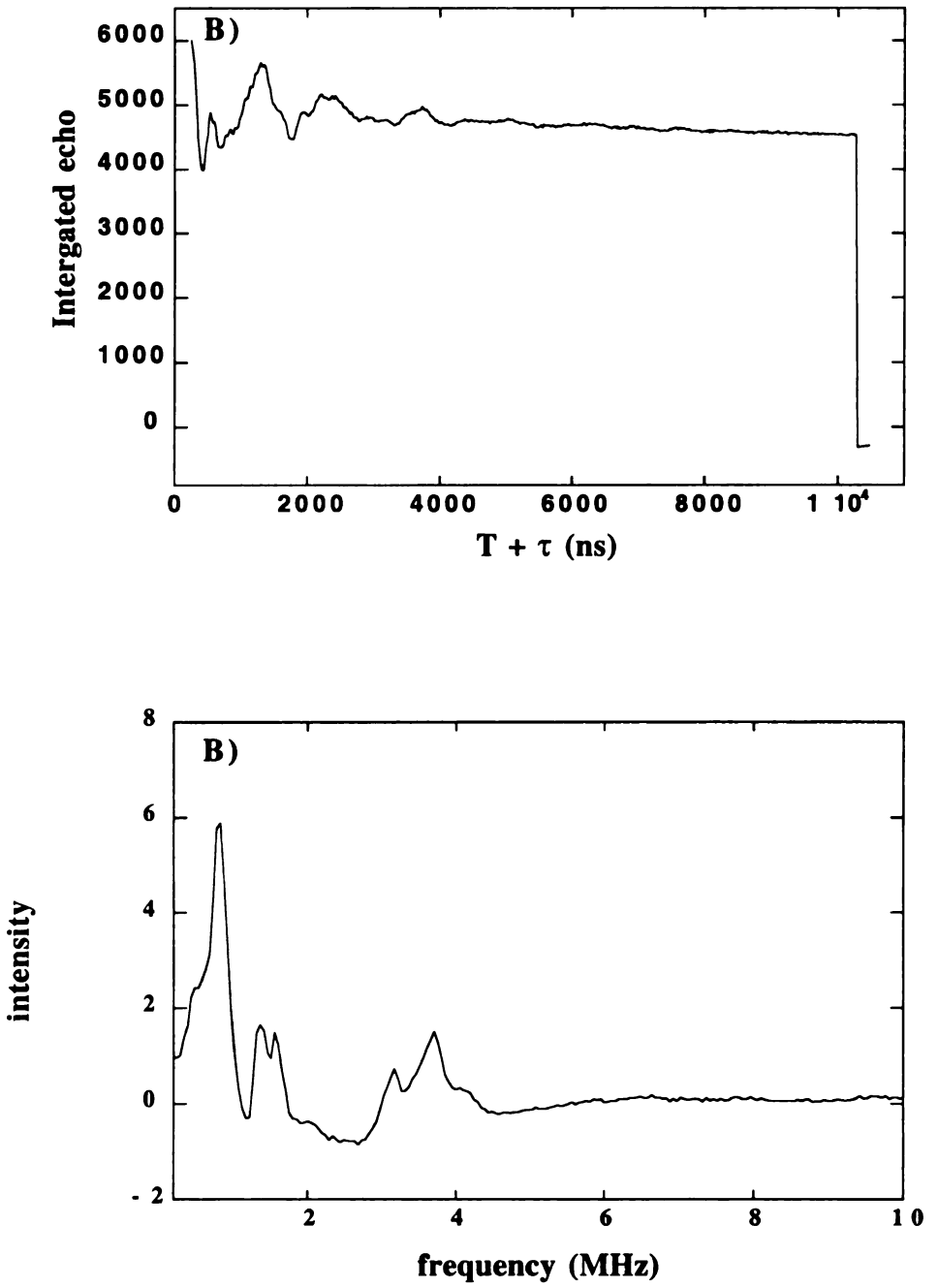

Figure 4.15. Representative experimental ^{14}N-ESEEM spectra for the type-1 copper site (T2D Fet3). Spectrum (A) was collected at B_o = 3090 Gauss and for τ = 230ns. Spectrum (B) is the cosine Fourier transform of (A). Other measurement conditions: microwave frequency, 8.836 GHz; microwave power, 43 dB; sample temperature, 4.2K.

(3090G, Figure 4.15), ^{14}N-ESEEM the peaks are found at 0.5,0.8, 1.4, 1.6, 3.2, 3.6 and 4.1 MHz.

The number of ESEEM frequencies was greater than what one would expect for either a single equatorially-bound histidine imidazole, or for two magnetically equivalent ones. Therefore, simulations were based on the assumption that there are two magnetically inequivalent histidine ligands at the type 1 site in Fet3p. Generally, type 1 or blue Cu(II) sites, feature two histidine and one cystiene ligands that conform to a trigonally distorted tetrahedral array, and differ only in their "axial" ligation. Assuming that the observed modulation intensities require a coupling near exact cancellation, we were able to estimate two sets of quadrupole coupling constants, e^2qQ and η. The sharp peaks at 0.4, 0.8 and 1.4 MHz observed at 2825 G were considered as a first set of quadrupole peaks, while the frequency components at 0.7, 0.8 and 1.6 MHz comprised the second set. The position and the width of the double quantum peak were estimated by adjusting A_{iso} and the r_{eff}. Both the relative amplitudes of the lower peaks and the appearance of the additional features in the double quantum peak are very dependent on orientation of the lab field with respect to HFI tensor and the NQI tensor principal axes.

Figure 4.16 shows the best simulations (dotted lines) of ^{14}N-ESEEM data for the type 1 Cu(II) site in T2D Fet3p at both the $g_{\|}$ and $g_{\perp}$ regions. The proposed histidine imidazole ligands (designated His1 and His2) have the same hyperfine tensor principal values (A_{iso} (1.47 MHz) and r_{eff} (2.50 Å)) for their remote nitrogen. They differ only in their tensor orientation with respect to the Cu g-tensor and NQI parameters. For His1, e^2qQ = 1.35 MHz and η = 0.55, while for His2, e^2qQ = 1.60

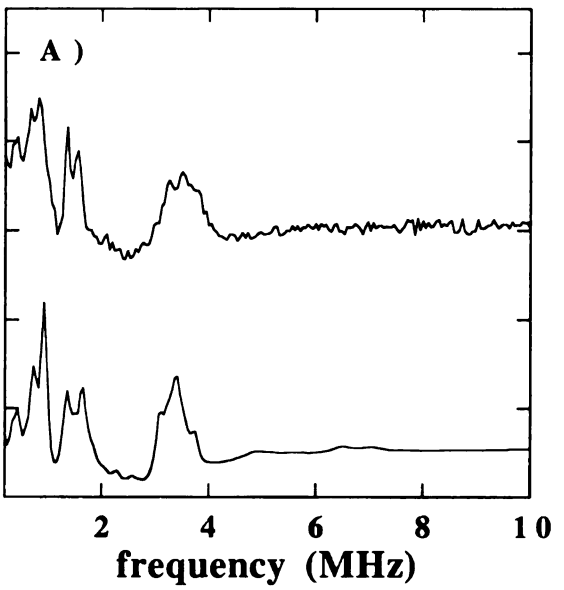

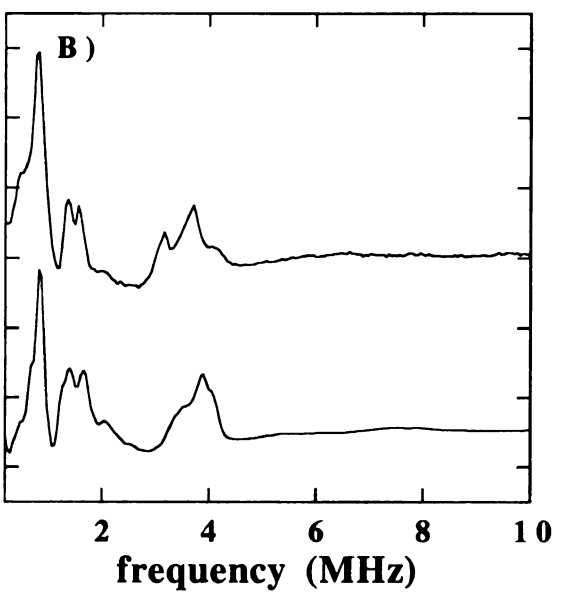

Figure 4.16. Determination of number of histidyl imidazole ligands for the type-1 center of Fet3. The stimulated-echo ESEEM (solid lines) (A) were collected at g = 2.23 using a τ-value of 250 ns, while that of (B) were collected at g = 2.04 using a τ-value of 227 ns. Other common experimental conditions common to the ESEEM measurements are given in Figures 4.14 and 4.15. The Hamiltonian parameters used to calculate the simulation (dotted lines) curves are given in Table 5.2.

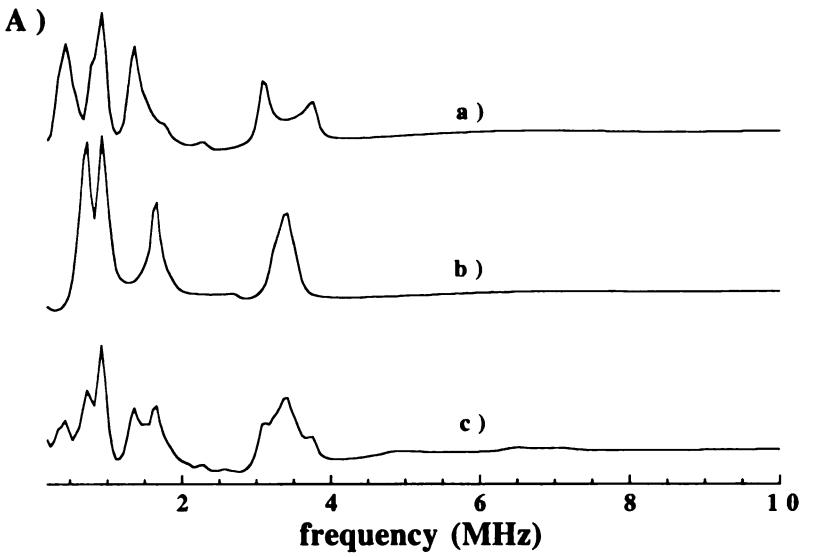

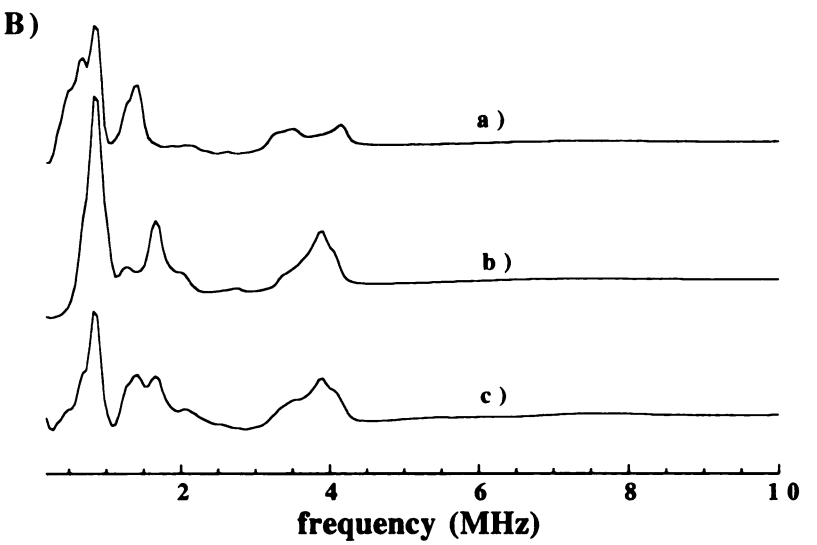

Figure 4.17. Computer simulations for single nucleus, a) N1 and b) N2 for static magnetic fields, 2825G(A) and 3090G(B). Spectra c in A and B are ESEEM product of ESEEM functions of N1 and N2. Hamiltonian parameters used to generate a and b are found in Table 4.2.

Table 4.2. Ligand hyperfine parameters for stimulated ESEEM simulations for the histidine ligands of the type 1 site in Fet3. The simulations are shown in Figure 4.16.

ligand	N1	N2
A_{iso}(MHz)	1.47	1.47
r_{eff}(Å)	2.50	2.50
θ_N, ϕ_N	±71°,180°	±97°,77°
e^2qQ	1.35	1.60
η	0.55	0.80
α,β,λ	70°,90°,0°	0°,90°,60°

MHz and η = 0.80. These NQI parameters are assigned to the uncoordinated ^{14}N of the histidyl imidazole ligands. X-ray crystal structures of multicopper oxidases, AO,[28,29] hCp[30] and laccase[34] and mononuclear blue copper oxidases, plastocyanin[35], and azurin[36-38] indicate that the type 1 copper is coordinated by the $^{14}N\delta$ of the histidyl imidazole. We assume this to be the case for type 1 copper site in Fet3p as well. Previous studies showed a small variation in the NQI parameters of type 1 copper centers (e^2qQ=1.40-1.49 MHz, η = 0.90-.94) as compared to those observed in type 2 copper centers (e^2qQ = 1.4 -1.8, η = 0.48-0.98).[39,40] It has been suggested that these ^{14}N difference may arise in part from the inequivalence of histidyl imidazole ligands when the remote nitrogen is of the δ versus ε type.[39] However, numerical replication of the ESEEM data on T2D Fet3p was unsuccessful

using the modest range of NQI coupling parameters that typify δ versus ε nitrogens. More likely, the difference in NQI parameters measured for the two histidyl imidazole ligands of T2D Fet3p stems from the extent and/or strength of the hydrogen bond involving the distal N-H of the ligands. Based on the study by Jiang et al.[40], we would expect the N-H of His2 (e^2qQ = 1.60 MHz, η = 0.80) to be hydrogen bonded more strongly than the equivalent N-H of His1 (e^2qQ = 1.35 MHz, η = 0.55).

Recent X-band ESEEM data on single crystals of azurin from *Pseudomonas aeroginosa* revealed two sets of NQI parameters, e2qQ = 1.43 MHz and η=0.95 for His117 and e2qQ=1.37, η=0.86 MHz for His46.[41] The X-ray-crystal structure of this protein revealed that His46 is hydrogen bonded to the carbonyl oxygen of Asp10, whereas His117 is hydrogen-bound to a water molecule.[37,38,42] His117 is protuding through a surface in a shallow depression, called the hydrophobic patch, and is experimentally proven by site-directed mutagenesis to be involved in electron transfer.

The imidazole rings of the histidine ligands at the type 1 Cu(II), predicted to be His413 and His489, also differ in their orientation with respect to the Cu^{+2} g-tensor principal axes. The data indicate that one imidazole has the principal axis of its hyperfine coupling ±20° from the xy plane (values of θ_n= 70° or 109°, ϕ_n =180°), while the other has this principal axis ±7° with respect to the xy plane (values θ_n=83° or 97°, ϕ_n =77°). These orientation angles are consistent with the distortion from square-planar geometry that is characteristic of the trigonally distorted tetrahedral geometry

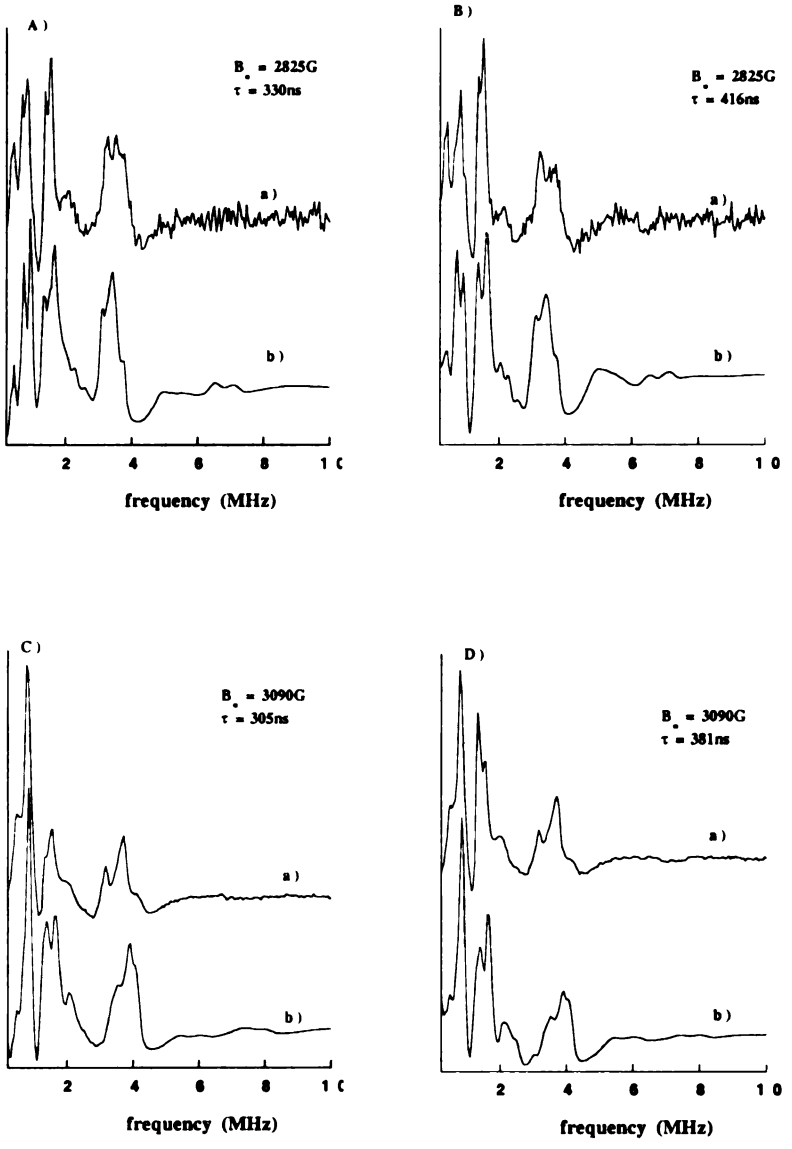

Figure 4.18. ^{14}N ESEEM data for T2D Fet3p (a) and computer simulations (b) at various τ values.

found at type 1 sites. In AO, the homologous His ligands (residues 445 and 512), together with Cys507, are arrayed on one side of the trigonal plane. Met517 is the apical ligand with its sulfur atom at the long apex of a distorted trigonal pyramid. Fet3p, like laccase[34], has a Leu residue at the homologous point in its primary sequence and therefore is most likely to have a trigonal rather than trigonal pyramidal type 1 copper site geometry.

4.4.2.3 Comparison of ^{14}N Hyperfine Interactions at the Type 1 and Type 2 Cu(II) in Fet3p

The observed A_{iso} (1.47 MHz) for the type 1 Cu(II) is smaller than that for the equatorially-bound histidine at the type 2 Cu(II) (A_{iso} = 1.75 MHz). Previous ENDOR studies have developed an inverse correlation between the magnitude of the isotropic hyperfine coupling due to the directly bound nitrogen and the amount of tetragonal distortion of the complex towards a tetrahedral geometry.[43] These studies showed that a deviation from square planar geometry results in the reduction of the overlap of the Cu^{+2} $d_{x^2-y^2}$ orbital occupied by the unpaired spin with the coordinating nitrogen σ orbital leading to a decrease of the hyperfine coupling constant. Colaneri *et al.*[44] provided an explanation for this observed decrease in A_{iso}. Tetrahedral distortion would result in a decrease of the spin density of the directly coordinated nitrogen σ orbital but at the same time an increase in the delocalization of spin into the π imidazole ring or the C-N bond orbitals. Combined with the decrease in the overlap of the nitrogen σ and copper $d_{x^2-y^2}$ orbitals, these changes in the electronic structure would result in the observed decrease in nitrogen isotropic hyperfine coupling.

Irrespective of the precise mechanism for this correlation, the difference in A_{iso} values for the type 1 and type 2 sites in Fet3p conforms to the expected geometry of each site. If A_{iso} for the directly coordinated nitrogen decreases with tetrahedral distortion, we would also expect A_{iso} for the remote nitrogen to decrease.

4.5 Summary

Simulations of the ^{14}N ESEEM spectra of T1D and T2D Fet3p showed that the observed modulations are due to remote nitrogen of histidyl ligands. In the T1D enzyme, one equatorial histidine is coordinated to the type 2 copper site. An axial histidine might also be present. Two magnetically inequivalent histidine ligands that are disposed ~10° below the equatorial plane, could be present in the type -1 copper site of Fet3p. These two histidine are different in their NQI values. The difference is explained by the degree of hydrogen bonding involving the remote nitrogen.

List of References

1)Mims, W. B.; Peisach, J. *Biochemistry* **1976**, *15*, 3863-3869.

2)Mims, W. B.; Peisach, J. *J. Chem.Phys.* **1978**, *69*, 4921-4930.

3)Mims, W. B.; Peisachs, J. *J. Biol. Chem.* **1979**, *254*, 4321-4323.

4)Mondovi, B.; Graziani, M. T.; Mims, W. B.; Oltzik, R.; Peisach, J. *Biochemistry* **1977**, *16*, 4198-4202.

5)Kosman, D. J.; Peisach, J.; Mims, W. B. *Biochemistry* **1980**, *19*, 1304-1308.

6)Fee, J. A.; Peisach, J.; Mims, W. B. *J. Biol. Chem.* **1981**, *256*, 1910-1914.

7)Zweier, J. L.; Peisach, J.; Mims, W. B. *J. Biol. Chem.* **1982**, *257*, 10314-10316.

8)McCracken, J.; Pember, S.; Benkovic, S. J.; Villafranca, J. J.; Miller, R. J.; Peisach, J. *J. Am. Chem. Soc.* **1988**, *110*, 1069-1074.

9)Hasset, R. F.; Yuan, D. S.; Kosman, D. J. *J. Biol.Chem.* **1998**, *273*, 23274-23282.

10)Nilges, M. J. ; Ph.D. Thesis; University of Illinois: Urbana, Illnois, 1979.

11)Belford, R. L.; Nilges, M. J. *Computer Simulation of Powder Spectra*; Belford, R. L.; Nilges, M. J., Ed.: Denver, Colorado, 1979.

12)Maurice, A. M. ; Ph.D. Thesis; University of Illinois: Urbana, Illinois, 1980.

13)McCracken, J.; Sin, D.; Dye, L. *Appl. Magn. Reson.* **1992**, *3*, 305-316.

14)Mims, W. B. *J. Magn. Reson.* **1984**, *59*, 291-306.

15)Mims, W. B. *Phys. Rev. B* **1972**, *5*, 2409-2419.

16)Mims, W. B. *Phys. Rev. B* **1972**, *6*, 353-3545.

17)Hurst, G. C.; Henderson, T. A.; Kreilick, R. W. *J. Am. Chem. Soc.* **1985**, *107*, 7294-7299.

18)Hurst, G. C.; Henderson, T. A.; Kreilick, R. W. *J. Am. Chem. Soc.* **1985**, *107*, 7299-7303.

19)Poole, C. P.; Farach, H. A. *The Theory of Magnetic Resonance*; Wiley-Interscience: New York, 1972.

20)Hoffman, B. M.; Martinsen, J.; Venters, R. A. *J. Magn. Reson.* **1984**, *59*, 110-123.

21)Hutchison, C.; B, M. D. *J. Chem. Phys.* **1977**, *66*, 3311-3330.

22)De Groot, A.; Evelo, R.; Hoff, A. *J. Magn. Reson.* **1986**, *66*, 331-343.

23)Blackburn, N. J.; Ralle, M.; Hasset, R.; Kosman, D. J. *Biochemistry* **2000**, *39*, 2316-2324.

24)Atherton, N. M. *Electron Spin Resonance*; Ellis Horwood Limited: New York, 1973.

25)McGarvey, B. R. *Electron Spin Resonance of Transition-Metal Complexes*; in Transition Metal Chemistry, Carlin, R. L. ed.; Marcel Dekker, Inc.: New York, 1966; Vol. 3, pp 89-201.

26)Avigliano, L.; Davis, J. L.; Graziani, M. T.; Marchesini, A.; Mims, W. B.; Mondovi, B.; Peisach, J. *FEBS Letters* **1981**, *136*, 80-84.

27)Flanagan, H. L.; Singel, D. J. *J. Chem. Phys.* **1987**, *87*, 5606-5616.

28)Messerschmidt, A.; Rossi, A.; Ladenstein, R.; Huber, R.; Bolognesi, M.; Gatti, G.; Marchesini, A.; Petruzelli, R.; Finazzi-Agro, A. *J. Mol. Biol.* **1989**, *206*, 513-529.

29)Messerschmidt, A.; Ladenstein, R.; Huber, R.; Bolognesi, M.; Avigliano, L.; Petruzzelli, R.; Rossi, A.; Finazzi-Agro, A. *J. Mol. Biol.* **1992**, *224*, 179-205.

30)Zaitzeva, I.; Zaitzev, V.; Card, G.; Moshkov, K.; Box, B.; Ralph, A.; Lindley, P. *J. Biol. Inorg. Chem.* **1996**, *1*, 15-23.

31)de Silva, D. M.; Askwith, C. C.; Eide, D.; Kaplan, J. *J. Biol. Chem.* **1995**, *270*, 1098-1101.

32)Askwith, C.; Eide, D.; Van Ho, A.; Bernard, P. S.; Li, L.; Davis-Kaplan, S.; Sipe, D. M.; Kaplan, J. *Cell* **1994**, *76*, 403-410.

33)Cornelius, J. B.; McCracken, J.; Clarkson, R. B.; Belford, R. L. *J. Phys. Chem.* **1990**, *94*, 6977-6982.

34)Ducros, V.; Brozowski, A. M.; Wilson, K. S.; Brown, S. H.; Ostergaard, P.; Schneider, P.; Yaver, D. S.; Pedersen, A. H.; Davies, G. J. *Nat. Struct. Biol.* **1998**, *5*, 310-316.

35)Guss, J. M.; Freeman, H. C. *J. Mol. Biol.* **1983**, *169*, 521-563.

36)Norris, G. E.; Anderson, B. F.; Baker, E. *J. Am. Chem. Soc.* **1986**, 2784-2785.

37)Baker, E. N. *J. Mol. Biol.* **1988**, *203*, 1071-1095.

38)Nar, H.; Messerschmidt, A.; Huber, R. *J. Mol. Biol.* **1991**, *218*, 427-447.

39)Goldfarb, D.; Fauth, J. M.; Farver, O.; Pecht, I. *Appl. Magn. Reson.* **1992**, *3*, 333-351.

40)Jiang, F.; McCracken, J.; Peisach, J. *J. Am. Chem. Soc.* **1990**, *112*, 9035-9044.

41)van Gastel, M.; Coremans, W. A.; Jeuken, L. J. C.; Canters, G. W.; Groenen, E. J. J. *J. Phys. Chem. A* **1998**, *102*, 4462-4470.

42)Colaneri, M. J.; Vitali, J.; Peisach, J. *Biochemistry* **2000**, *39*, 584-591. Based on the ESEEM studies and X-ray crystal structures of some biological and model type 1 and type 2 copper complexes, Colaneri *et al* . suggested that for $\eta \geq 0.9$ the distal nitrogen is hydrogen bonded to water molecule, while $\eta < 0.9$, the remote N is likely hydrogen bonded to the carbonyl oxygen of the backbone or side chain of protein.

Further simulations was done with one of the histidines of the Fet3p assigned to have $\eta = 0.90$ for its remote nitrogen. At one τ value, experimental data were fairly replicated for both magnetic field settings. However, at higher τ the experimental data were poorly matched.

43)Iwaizumi, M.; Kudo, T.; Kita, S. *Inorg. Chem.* **1986**, *25*, 1546-1550.

44)Colaneri, M. J.; Potenza, J. A.; Schugar, H. J.; Peisach, J. *J. Am. Chem. Soc.* **1990**, *112*, 9451-9458.

Chapter 5

^{2}H ESEEM: Water Ligation to and Accessibility of the Type-1 and Type-2 Copper Sites in Fet3p

The nature ligands and their arrangement at the metal center in metalloproteins determine the reactivity and function of the metal center. In chapter 4, the histidine ligation to type 1 and type 2 centers in the Fet3 protein was determined. In these chapter, water ligation to these copper centers is considered.

The coordination of metal by an exogenous ligand, water and its accessibility to water solvent can be determined by ESEEM. One way of determining this is by making use of the attributes of the sum-combination ($\upsilon_\alpha + \upsilon_\beta$) peak. Sum combination peaks are resolved in two and four-pulse ESEEM because the electron spin echoes are modulated not only by the fundamental frequency at the alpha and beta electron spin manifolds but by the sum and difference of these fundamental frequencies.[1-3] Non-coordinating water has a ^{1}H-ESEEM frequency spectrum characterized by overlapping fundamental nuclear modulation frequencies, υ_α and υ_β, centered at proton nuclear Zeeman frequency, υ_H and a narrow sum-combination peak centered at $2\upsilon_H$. Previous ENDOR/ESEEM studies on some metal-aquo complexes revealed that the protons of covalently bonded water have hyperfine interactions that are highly anisotropic.[4-7] As a result of this anisotropy, υ_α and υ_β will give rise to powder pattern lineshapes that span a range of ~20MHz about υ_H and the sum-combination peak, ($\upsilon_\alpha + \upsilon_\beta$) will shift from $2\upsilon_H$. This anisotropic peak is shifted from the twice the Larmor frequency of proton by an amount equal to[8],

$$\Delta \cong \left(\upsilon_\alpha + \upsilon_\beta\right) - 2\upsilon_H = \frac{9A_\perp^2}{16\upsilon_H} \tag{5.1}$$

Equation 5.1 was derived for an isotropic g and axial hyperfine interaction where $A_\perp$ is the perpendicular component of the hyperfine tensor ($A_\perp = A_{xx} = A_{yy}$). The absence of the shifted peak, therefore, signifies absence of axially and/or equatorially coordinated water to Cu(II).

Water coordination and accessibility can also be established by D_2O-exchange experiments.[9,10] Here, ESEEM data are collected for systems in D_2O and H_2O buffer under similar conditions. Ratio of the ESEEM function of a system in D_2O buffer over a system in H_2O is obtained to yield ESEEM function that is dominated by exchangeable deuterium and protons. Because the nuclear g factor, g_n, of protons is 6.5 time larger than deuterium, the modulation frequencies from each nucleus-type occur in regions that do not interfere with one another. This technique was used in this study to determine water ligation and solvent accessibility of the type-1 and type-2 copper sites in Fet3p. D_2O-exchange experiment does not only allow us to identify coordinated water but also assess the contribution of ambient/matrix water to the ESEEM function. We were able to determine the nearest solvent water to metal center and describe the distribution of ambient water that accounts for the observed two-pulse quotient modulation function. The ratio envelopes suggest that both the type 1 and type 2 sites are readily accessible to water. However, the type 2 is more open than the type 1 site. The consequence of this difference will be discussed. Moreover, water is an inner-sphere ligand to only the type 2 copper site with one axial and one equatorial D_2O. The ^2H modulation function of the type 1 copper site is

due entirely to ambient deuterons with the nearest metal-to-deuteron distance being 3.7Å.

5.1 Experimental Procedures

Construction of Fet3p mutants and production of soluble protein. Fet3p variants in D_2O buffer were prepared similarly as those in H_2O buffer as described in Chapter 4.

CW-EPR. Continuous-wave EPR spectra of the Fet3p and its variants were obtained at X-band on a Bruker ESP-300E EPR spectrometer equipped with an Oxford ESR-900 liquid helium cryostat.

ESEEM. Pulsed EPR experiments were performed on a home-built spectrometer described previously.[11] Two-pulse data were collected at X-band using a reflection cavity that employed a folded stripline resonant element. All experiments were performed at liquid helium temperature, 4.2 K.

5.2 ^{2}H Interaction and Simulation

Water ligation to type-1 and type-2 copper sites was determined using two-pulse ($\pi/2$-τ–π) ESEEM measurements and the D_2O-exhange protocol.[9] These experiments are based on the product rule[1,12] for two-pulse ESEEM where the modulation function (E_{mod}) for a discrete paramagnetic center consists of a product of the modulation functions of each nucleus coupled to the center.

$$E_{mod}(I_1,I_2..I_n) = E_{mod}(I_1)\, E_{mod}(I_2)\ldots E_{mod}(I_n) \qquad (5.2)$$

Division of the ESEEM data of D_2O-exchanged enzyme by parallel data sets collected for enzyme in aqueous buffer will yield a quotient function dominated by the exchangeable deuterons.

$$E_{mod} = \frac{E_{mod}(^2H)}{E_{mod}(^1H)} . \tag{5.3}$$

The effect of ambient D_2O on the modulation function was also investigated. Ambient water is treated as statistically distributed in a series of non-coordination concentric shells with r_{min} as the distance of water deuterons nearest to the metal center.[13,14] In our calculation, there are ten shells that are incremented in equal steps of $1/r^3$. The contribution of ambient water can be approximated to be equal to,

$$E_{mod,avg} = V(r_1,\tau)^{n1} \times V(r_2,\tau)^{n2} \times V(r_3,\tau)^{n3} .... \tag{5.4}$$

where $V(r,\tau) = \int_0^{\pi} V_{mod}(r,\tau,\theta)d\theta$.[13,14] (5.5)

The n_i in the modulation function V represents the number of deuterium nuclei in an ^{i}th shell and is assumed to be equal to $(f)(\rho_N)(r^3_{i+i}-r^3_i)$ where f is a factor whose value depends on how the copper site is exposed to water and ρ_N is the mean number of deuterium nuclei per unit volume which is calculated to be 0.067 D/Å^3. The resulting average modulation function, E_{modavg} may then be incorporated into the modulation function arising bound water ligands using the product rule.

Equations 5.4 and 5.5 are derived using spherical model, an approximation to the equations ,

$$\langle E_{mod} \rangle = \sum_i \rho_i V_{mod,i} \tag{5.6a}$$

$$\langle E_{mod} \rangle = \sum_j \rho_j \prod_i^n V_{mod,i,j} . \tag{5.6b}$$

The above equations are modulation functions for disordered systems such as frozen solutions and powder samples with 5.6a describing one magnetic nucleus interacting with the electron spin and 5.6b for more than one. In both equations, ρ_i represents the weighting factor or probability for a spin in the ^{i}th orientation with respect to a reference axis. Equations 5.6a is equivalent to

$$\langle E_{\text{mod}} \rangle = \frac{1}{4} \int_0^{2\pi} \int_0^{\pi} V(\theta) \sin\theta d\theta d\phi, \tag{5.7a}$$

with $\rho_i = \frac{1}{4} \sin\theta d\theta d\phi$. Similarly we can write 5.6b as

$$\langle E_{\text{mod}}{}^n \rangle = \frac{1}{4} \int_0^{2\pi} d\phi \int_0^{\pi} \prod_1^n V(\theta) \sin\theta d\theta. \tag{5.7b}$$

In order to calculate (5.7b), one needs to know the geometry of nuclei around the paramagnetic center. The geometry can be approximated as spherical with the magnetic nuclei randomly oriented along the sphere of radius r_{eff}. This random arrangement allows the reversal of arrangement of the order of operation in (5.7b), so that equation (5.7b) becomes,

$$\langle E^n_{\text{mod}} \rangle = \left[\frac{1}{4} \int_0^{2\pi} d\phi \int_0^{\pi} V(\theta) \sin\theta d\theta \right]^n = \left[\langle V_{\text{mod}} \rangle \right]^n \tag{5.8}$$

which is essentially equivalent to equation (5.4). In our calculations, the electron spin is assumed to be quantized along the direction of the z-component of the external magnetic field and the angle θ represents the angle made by vector r, the distance of separation between the nuclear spin and electron spin, with the applied magnetic field. The consequence of this assumption will be discussed.

5.3 Results

CW-EPR. Figure 5.1A,B, and C are CW-EPR of the wild type, T2D and T1D Fet3 protein in D_2O buffer, respectively. The spectra are similar to the spectra observed for each sample in H_2O buffer. Therefore, no significant changes occurred in the copper sites when the Fet3p samples were deuterated.

T1D Fet3p

The two-pulse ESEEM spectra collected at $g_\perp$ (B_o = 3055 Gauss) and τ = 250 ns for T1D Fet3p in D_2O- and H_2O-based buffers are shown in Figures 5.2A and 5.2B, respectively. The ^2H contribution to these data can be obtained by dividing the data of spectrum Fig. 5.2A by that of Fig. 5.2B. These ratioed values are given in Figure 5.2C. Two periodicities are observed in the quotient envelope, one occuring at ~500 ns corresponding to the second harmonic and the other at ~250 ns corresponding to the fundamental or Larmor frequency of ^2H.

T2D Fet3p

The ratio-envelope 2-pulse ESEEM data obtained at $g_\perp$ (B_o = 3090 Gauss) for the type 1 Cu(II) site in T2D Fet3p is shown in Figure 5.3 C. It is was calculated by dividing trace 5.3 A over 5.3 B. In contrast to T1D Fet3p, the modulation of the quotient envelope of T2D Fet3p is shallow. Also, no apparent second harmonic is observed.

Figure 5.1. Continuous-wave EPR spectra of (A) wild-type Fet3, (B) type 2 depleted (T2D) Fet3 and, (C) type 1 depleted (T1D) Fet3 protein in D_2O buffer. For (A), measurement conditions were: microwave frequency, 9.48GHz; microwave power, 2mW; modulation frequency, 100kHz; modulation amplitude, 4.014G; temperature, 15.6K. For (B), measurement condition were: microwave frequency, 9.48GHz; microwave power, 2mW; modulation frequency, 100kHz; modulation amplitude, 4.014G; temperature, 21K. For (C), measurement conditions were: microwave frequency, 9.48GHz; microwave power, 2mW; modulation frequency, 100kHz; modulation amplitude, 4.014G; temperature, 15.6K.

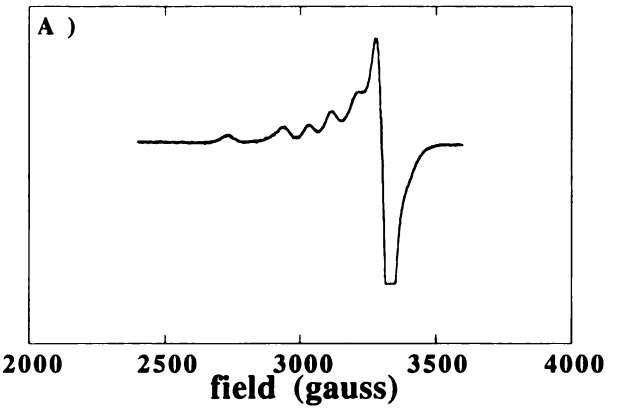
A)
2000
2500
3000
3500
4000
field (gauss)

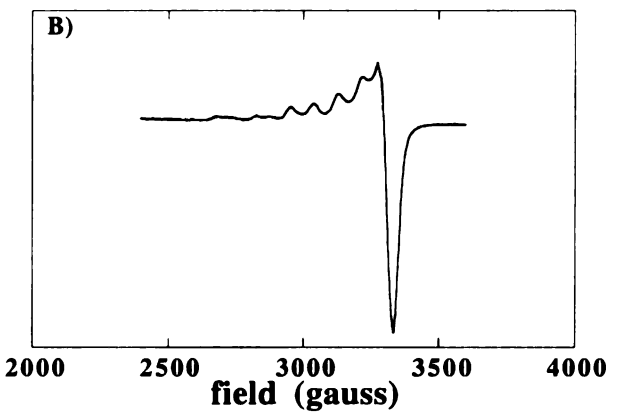
B)
2000
2500
3000
3500
4000
field (gauss)

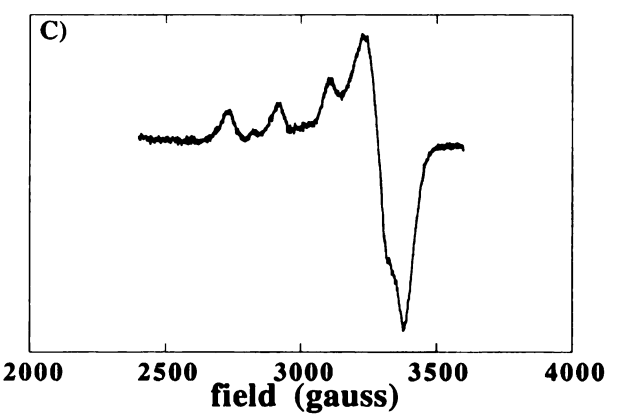
C)
2000
2500
3000
3500
4000
field (gauss)

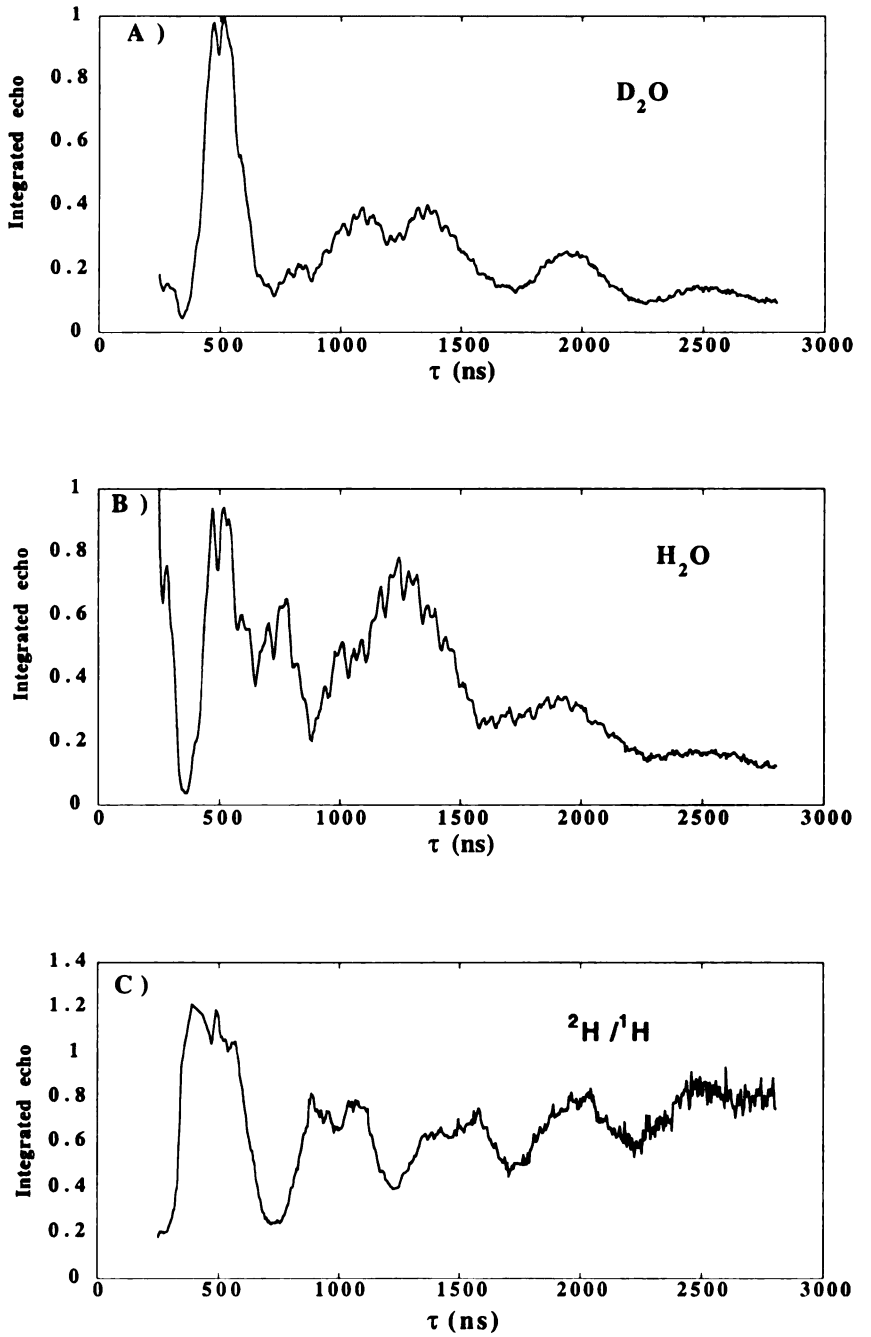

Figure 5.2. Two-pulse ^{2}H-ESEEM experimental traces for type-2 copper site in Fet3 protein (T1D). (A) Two-pulse ESEEM data in D_2O buffer, measurement conditions: ν = 8.79GHz; microwave power, 44dB; B_o = 3055 G and τ = 250ns. (B) Two-pulse ESEEM for T1D in H_2O buffer, measurement conditions are the same as A. (C) Quotient (A/B) modulation envelope of T1D Fet3p.

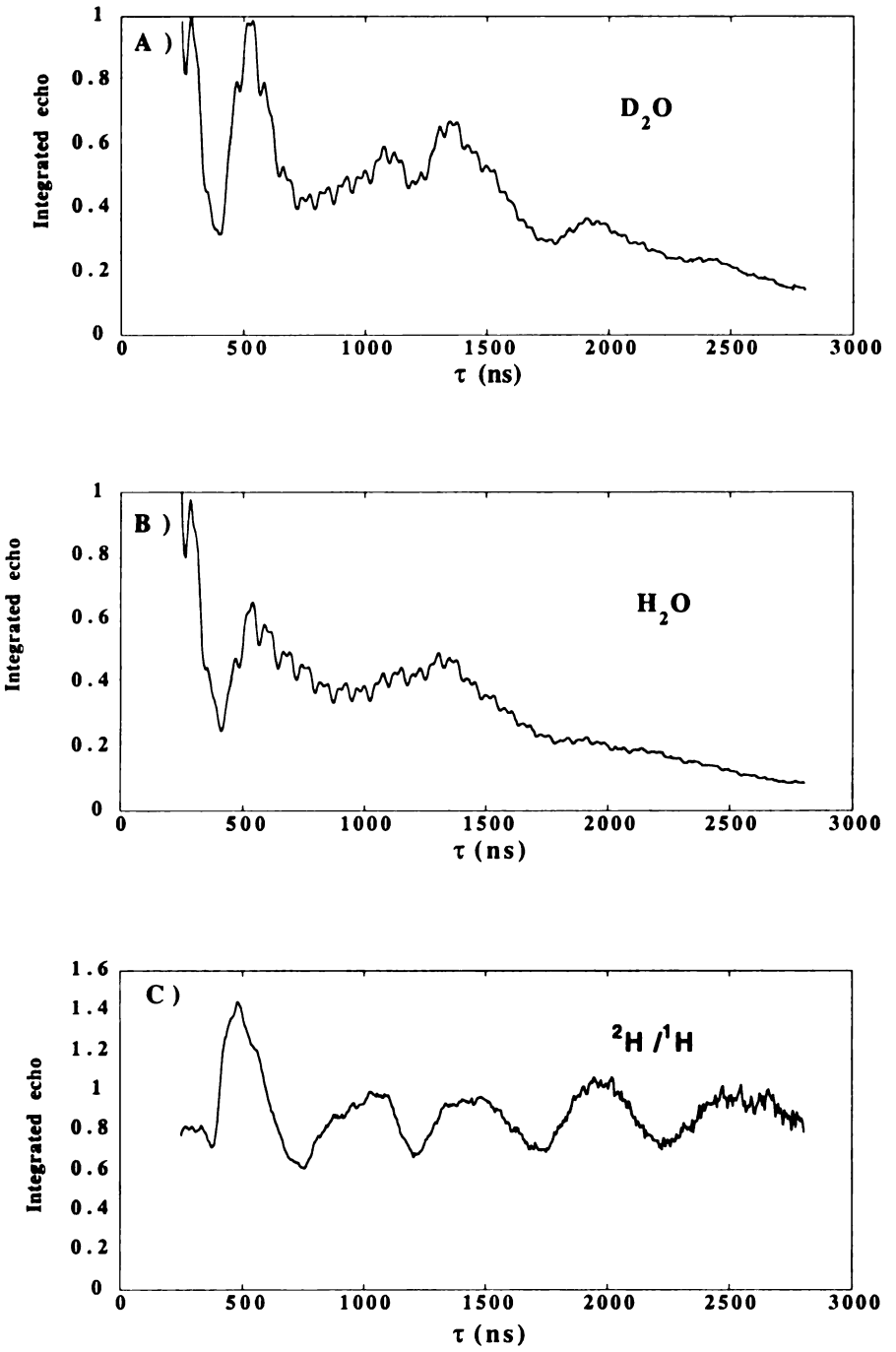

Figure 5.3. Two-pulse ^{2}H-ESEEM experimental traces for type-1 copper site in Fet3 (T2D Fet3p). (A) Two-pulse ESEEM data in D_2O buffer, measurement conditions: ν = 8.79GHz; microwave power, 44dB; B_o = 3090 G and τ = 250ns. (B) Two-pulse ESEEM for T2D in H_2O buffer, measurement conditions are the same as A. (C) Quotient (A/B) modulation envelope of T2D Fet3p.

5.4 Discussion

5.4.1 Theoretical ^{2}H-ESEEM Traces for Ambient, Axial and Equatorial Water

For qualitative comparison of the experimental ratioed envelope, the theoretical modulation functions for equatorial, axial and ambient water are shown in Figures 5.4A, B and C, respectively. Traces A and B were generated using the measured principal hyperfine values of axial and equatorial water protons by Atherton and Horsewill in their single-crystal Electron Nuclear Double Resonance (ENDOR) study of $Cu(H_2O)_6^{+2}$ in $Mg(NH_4)_2(SO_4)_4 \bullet 6H_2O$ salt.[4] Trace C, the ESEEM spectrum for unbound D_2O, was computed using a purely dipolar axial hf-tensor ($A_{xx} = A_{yy} = -0.2$ MHz, $A_{zz} = 0.4$ MHz, $r_{eff} \sim 4.0$ Å). A principal feature of these theoretical functions is the strong second harmonic that occurs at a period of 250 ns due to equatorial water (trace A). This second harmonic is less pronounced for an axially bound water (trace B) and it is further diminished in the case of ambient water (trace C).

These theoretical traces were generated using a Fortran ESEEM program, TPSPN1 for isotropic g-factor. The ESEEM program calculates the ESEEM function using equation that spatially averages all orientations over a unit of sphere,

$$\langle E_{\mathrm{mod}} \rangle = \frac{1}{4} \int_0^{2\pi} \int_0^{\pi} E(\theta) \sin\theta \, d\theta \, d\phi. \tag{5.9}$$

An isotropic g-tensor leads to an assumption of the quantization of the electron spin along the z-direction of the applied magnetic field. This approximation can also be used for g-tensor with small anisotropy at higher field where the spin tends to align

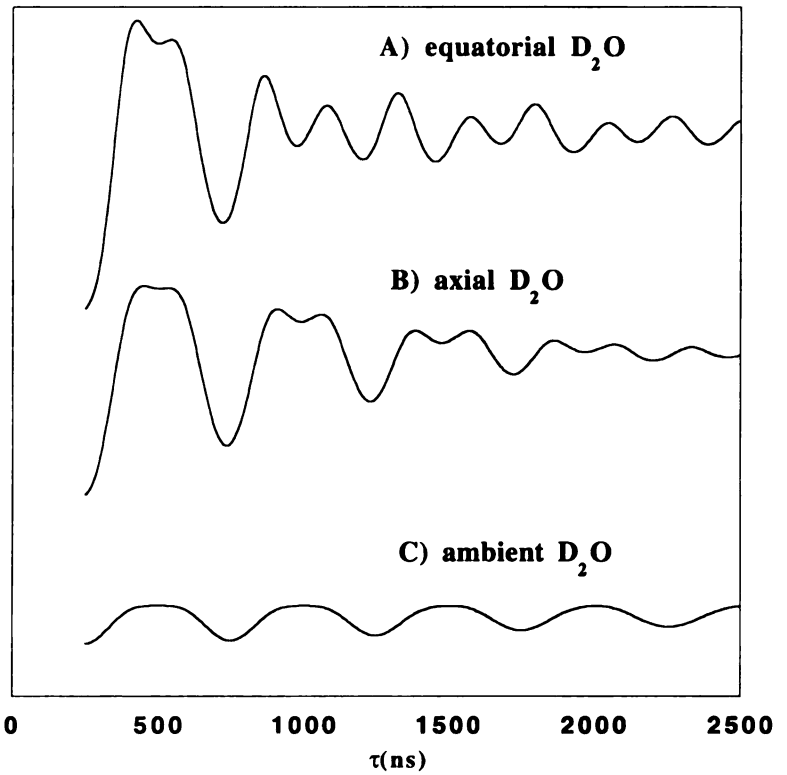

Figure 5.4. Theoretical two-pulse ^2H ESEEM traces for (A) equatorial, (B) axial and (C) ambient water. Hamiltonian parameters for ESEEM simulations for equatorial D_2O: A_{xx} = -0.6, A_{yy} = -1.2, A_{zz} = 1.4 MHz, g_n = 0.85741, magnetic field = 3055 G, τ = 250ns, e^2qQ = 0.22 and η =0.5. Parameters for axially bound D_2O are the same except for the hyperfine tensor, A_{xx} = -0.5, A_{yy} = -0.6, A_{zz} = 1.1 MHz. For ambient D_2O, A_{xx} = -0.2, A_{yy} = -0.2, A_{zz} = 0.4 MHz which corresponds to an r_{eff} of 4Å.

with the external magnetic field. Using this assumption, the dipolar contribution to the hyperfine interaction can be calculated to be

$$T = \frac{g_e g_n \beta_e \beta_n}{r^3}, \tag{5.10}$$

where g_e is the g value at that field. For the copper complex considered in this work, the high field region corresponds to the $g_\perp$ region of the CW-EPR spectrum where transitions involving all the four Cu(II) nuclear sublevels may contribute to the ESEEM. To test the validity of this approximation, ESEEM traces generated by an angle-selection program, ANGTPSPN1, similar to program described in Chapter 4 are compared with traces calculated by spatial averaging over a unit of sphere, TPSPN1. Figure 5.5 and 5.6 are for case of axial water ligation. Solid lines were calculated by TPSPN1 while dotted lines were calculated by ANGTPSPN1. Figure 5.5 considers only echo modulation due to the hyperfine interaction. The contribution of NQI to modulation is considered in Figure 5.6. For the dashed lines in Figures 5.5A and 5.6A, $\theta_N = 0°$, $\phi_N = 0°$ were assumed , while in Figures 5.5B and 5.6B assumed that $\theta_N = 35°$, $\phi_N = 0°$. A close agreement between TPSPN1 and ANGTPSN1 is evident in Figure 5.5 B and Figure 5.6 B. This implies that the Cu-O and O-H bonds make an angle of 125° and the two O-H bonds, and angle of 110°. Additional assumption made on the calculation of Figure 5.6B was that the NQI principal axis system (PAS) is coincident with HFI PAS (i.e, NQI Euler angle $\beta = 35°$ for counterclockwise rotation along z.) Comparison for water coordinated equatorially are described in Figure 5.7 and 5.8 . Again close agreement is achieved when θ_H=125° (35° off the Cu-O bond) and HFI and NQI PAS are coaxial.

Figure 5.5. Comparison of ^{2}H-ESEEM traces calculated by angle-selection (ANGTPSPN1, dotted curves) and spatial orientation averaging (TPSPN1, solid curves) for D_2O axially coordinated to copper. All the traces are calculated with $A_{iso} = 0.15$ MHz, $r_{eff} = 2.8$Å and no NQI contribution. Additional parameters needed to generate the dashed curves are diagonal elements of the g-tensor and A-tensor of copper: $g_{xx} = g_{yy} = 2.05$, $g_{zz} = 2.25$, $A_{xx} = A_{yy} = 35$ MHz, and $A_{zz} = 586$ MHz. Dotted trace 5.4A has θ_D, $\phi_D = 0°,0°$. Dashed trace 5.4B has θ_D, $\phi_D = 35°,0°$.

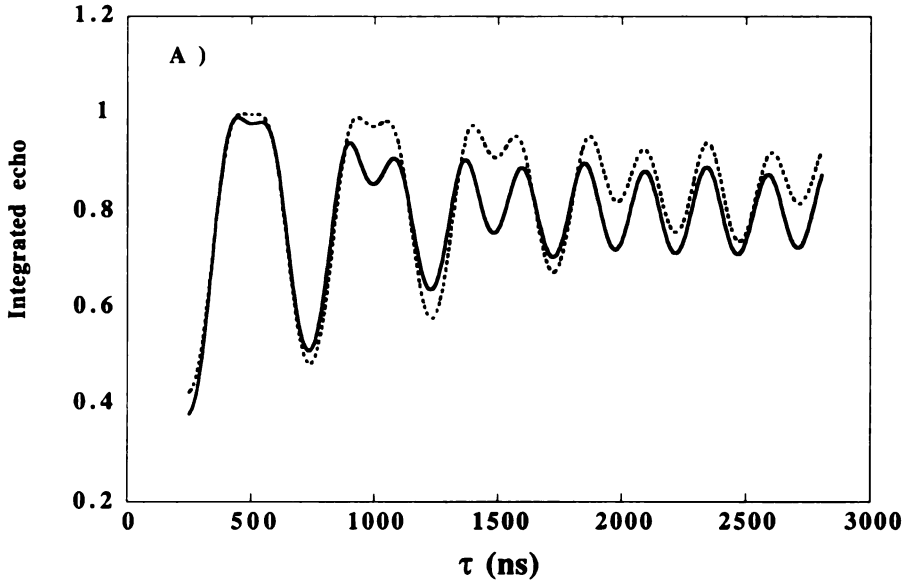
A)
Integrated echo
1.2
1
0.8
0.6
0.4
0.2
0
500
1000
1500
2000
2500
3000
τ (ns)

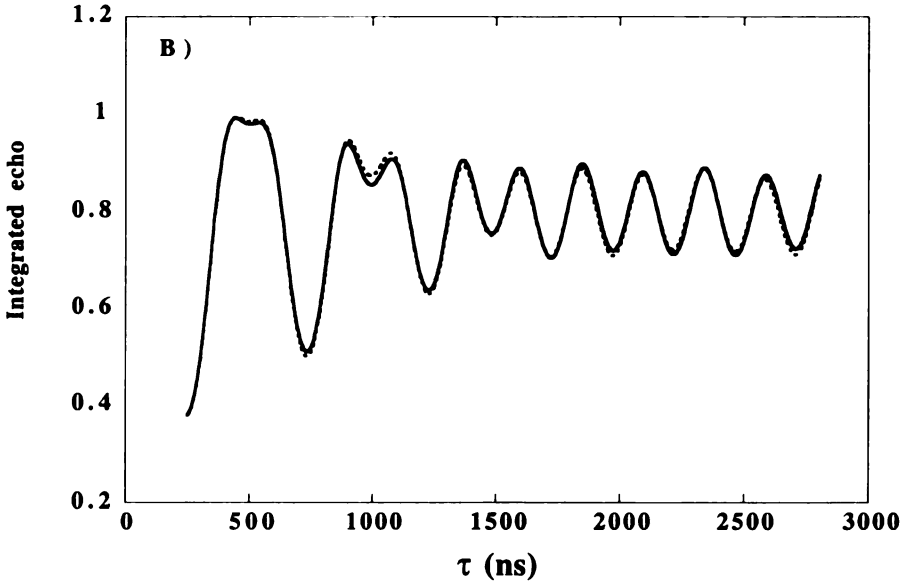
B)
Integrated echo
1.2
1
0.8
0.6
0.4
0.2
0
500
1000
1500
2000
2500
3000
τ (ns)

Figure 5.6. Comparison of ^{2}H-ESEEM traces calculated angle-selection (ANGTPSPN1, dotted curves) and spatial orientation averaging (TPSPN1, solid curves) for D_2O axially coordinated to copper. ^{2}H NQI is included ($e^2qQ = 0.22$ MHz, $\eta = 0.50$). Dashed curve 5.5A assumes θ_D, $\phi_D = 35°,0°$ and NQI Euler angle coincident with the g PAS ($\alpha = \beta = \gamma = 0$). Dashed curve 5.5B assumes θ_D, $\phi_D = 35°,0°$ and NQI Euler angle coaxial with HFI PAS ($\alpha = \gamma = 0$, $\beta = 225°$). All other parameters are the same as in Figure 5.5

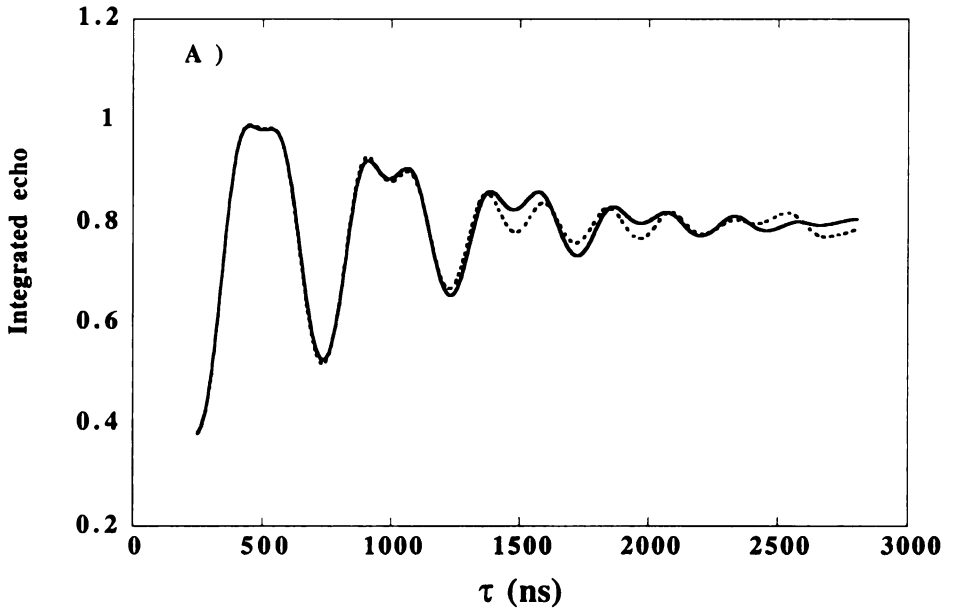
A)
Integrated echo
1.2
1
0.8
0.6
0.4
0.2
0
500
1000
1500
2000
2500
3000
τ (ns)

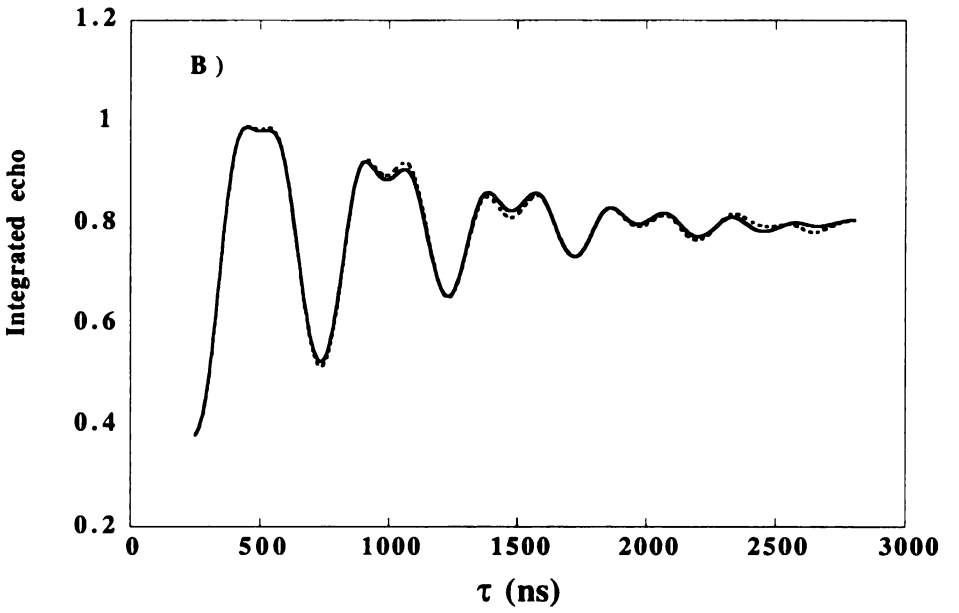
B)
Integrated echo
1.2
1
0.8
0.6
0.4
0.2
0
500
1000
1500
2000
2500
3000
τ (ns)

Figure 5.7. Comparison of ^{2}H-ESEEM traces calculated by angle-selection (ANGTPSPN1, dotted curves) and spatial orientation averaging (TPSPN1, solid curves) for D_2O equatorially ligated to copper. All the traces are calculated with A_{iso} = -1.0 MHz, r_{eff} = 2.5 and no NQI contribution. Additional parameters needed to generate dotted curves are diagonal elements of the g-tensor and A-tensor of copper: $g_{xx} = g_{yy} = 2.05$, $g_{zz} = 2.25$, $A_{xx} = A_{yy} = 35$ MHz, and $A_{zz} = 586$. Dotted trace 5.6A has $\theta_D, \phi_D = 90°,0°$. Dotted trace 5.4B has $\theta_D, \phi_D = 125°,0°$.

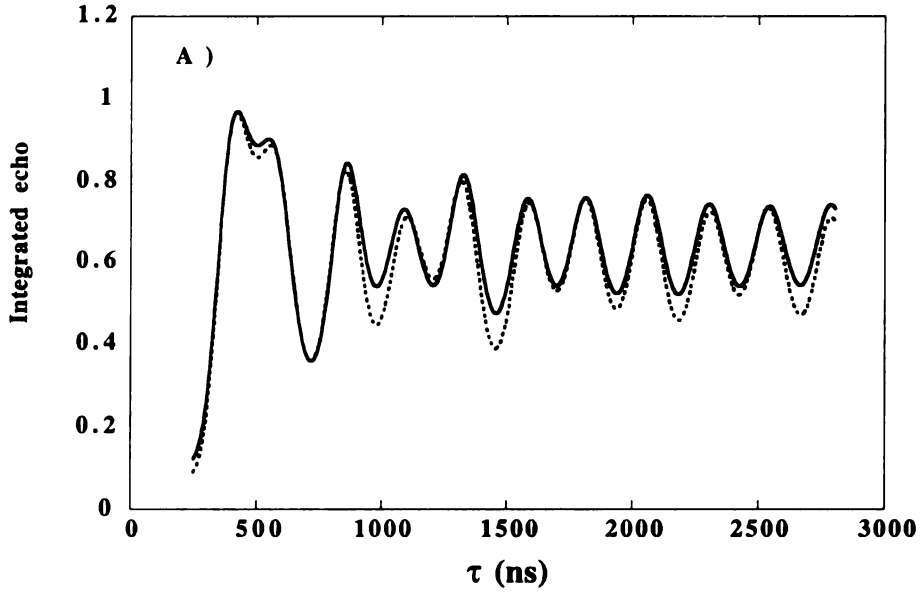
A)
Integrated echo
1.2
1
0.8
0.6
0.4
0.2
0
0
500
1000
1500
2000
2500
3000
τ (ns)

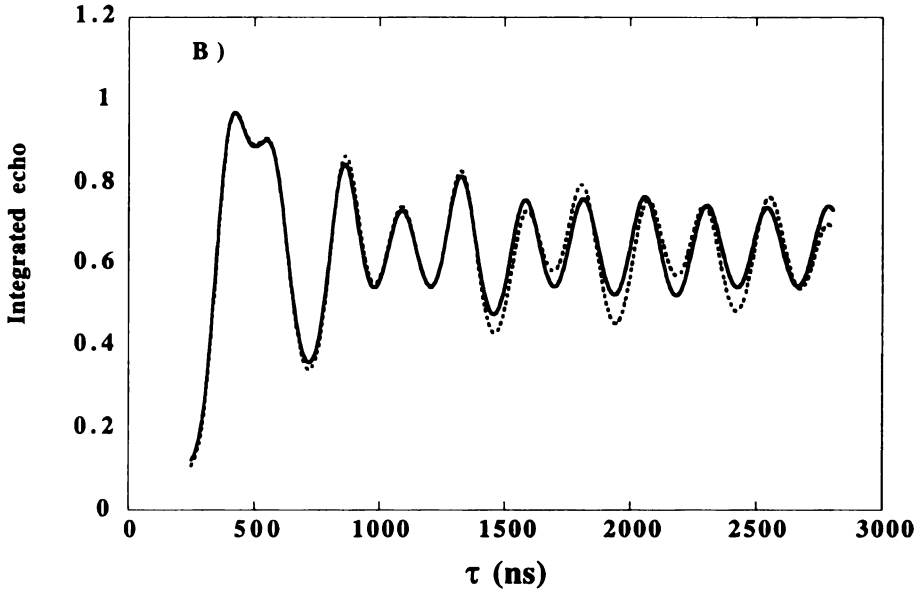
B)
Integrated echo
1.2
1
0.8
0.6
0.4
0.2
0
0
500
1000
1500
2000
2500
3000
τ (ns)

Figure 5.8. Comparison of ^{2}H-ESEEM traces calculated angle-selection (ANGTPSPN1, dotted curves) and spatial orientation averaging (TPSPN1, solid curves) for D_2O equatorially coordinated to copper. ^{2}H NQI is included ($e^2qQ = 0.22$ MHz, $\eta = 0.50$). Dotted curve 5.7A assumes θ_D, $\phi_D = 90°,0°$ and NQI Euler angles, ($\alpha = \gamma = 0$, $\beta = 270°$). Dotted curve 5.7B assumes θ_D, $\phi_D = 125°,0°$ and NQI Euler angles ($\alpha = \gamma = 0$, $\beta = 325°$). All other parameters are the same as in Figure 5.7

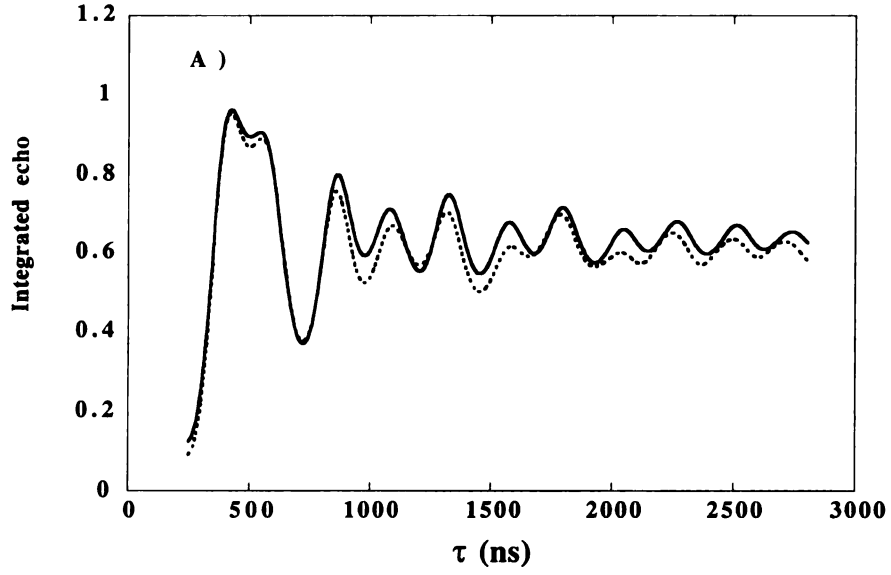
A)
Integrated echo
1.2
1
0.8
0.6
0.4
0.2
0
0
500
1000
1500
2000
2500
3000
τ (ns)

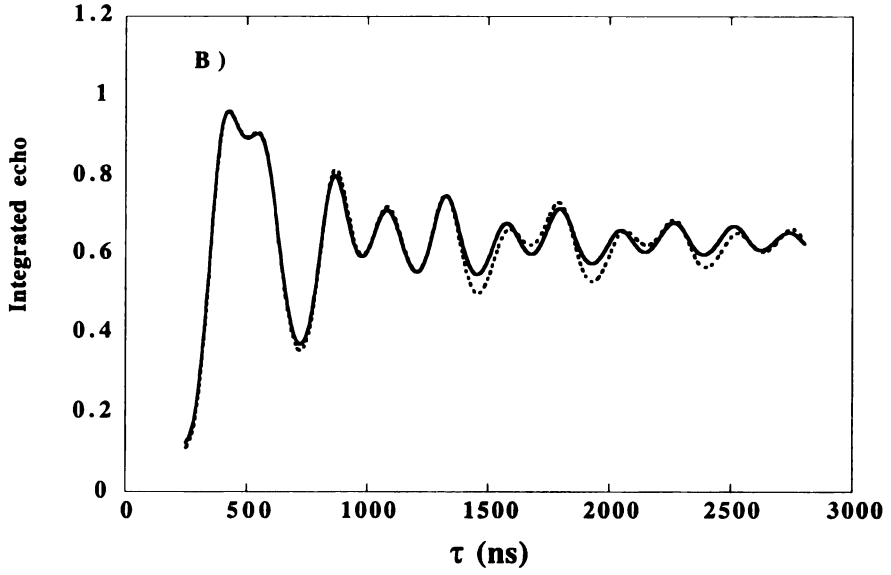
B)
Integrated echo
1.2
1
0.8
0.6
0.4
0.2
0
0
500
1000
1500
2000
2500
3000
τ (ns)

5.4.2 Frequency Domain Spectra of Ambient, Axial and Equatorial D_2O

Figure 5.9 shows an energy level diagram for the splitting of electron alpha and beta spin manifold due to HFI. The diagram neglects the contribution of NQI which for deuterium ($e^2qQ = 0.22$, $\eta \cong 0.50$)[15] is small and negligible. In the alpha electron spin manifold, the two transition, ω_{ab} and ω_{bc} are $\omega_{ab} \cong \omega_{bc} = \omega_{\alpha}$. This is true for the beta manifold as well. The nuclear modulation, ω_{α} and ω_{β}, manifest themselves in the frequency domain spectrum as a broad line centered about the ^2H Larmor frequency, ω_D. Additional NQI will shift and broaden ω_{α} and ω_{β} by an amount, $\Delta\omega_{nqi}$. In addition to this fundamental frequency, sum combination peak with negative phase will be observed. In our system, the nuclear Zeeman interaction is greater than HFI and NQI so that the sum combination peak is primarily broadened by the NQI.

The effect of the increasing the dipolar interaction is shown for the case of ambient, axial and equatorial D_2O in Figure 5.10. Broadening of the fundamental frequency is accompanied by the faster decay of the fundamental harmonic compared to the second harmonic (refer to Figure 5.4).

5.4.3 Analysis of T1D Fet3p Data

The data for the type 2 site differ from the model calculations, but show features in common with all those patterns. The depth of modulation observed for T1D Fet3 protein is similar to that predicted for equatorially bound water while the appearance of the sum combination frequency is more in line with that of an axially

Figure 5.9. Splitting of m_S electron spin level by the nuclear Zeeman and hyperfine interaction of nearby nucleus with I=1. Quadrupole interaction is neglected

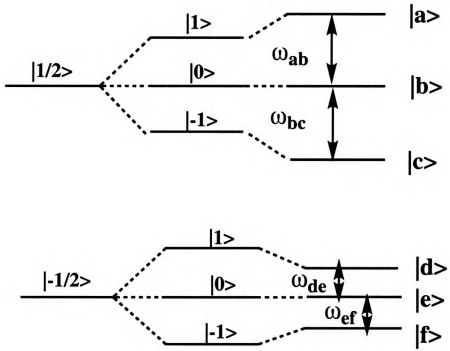

small or negligible contribution of NQI

$\omega_{ab} = \omega_{bc} = \omega_{\alpha}$

$\omega_{de} = \omega_{ef} = \omega_{\beta}$

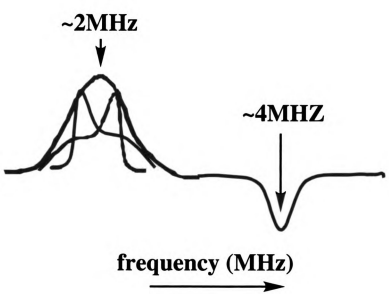

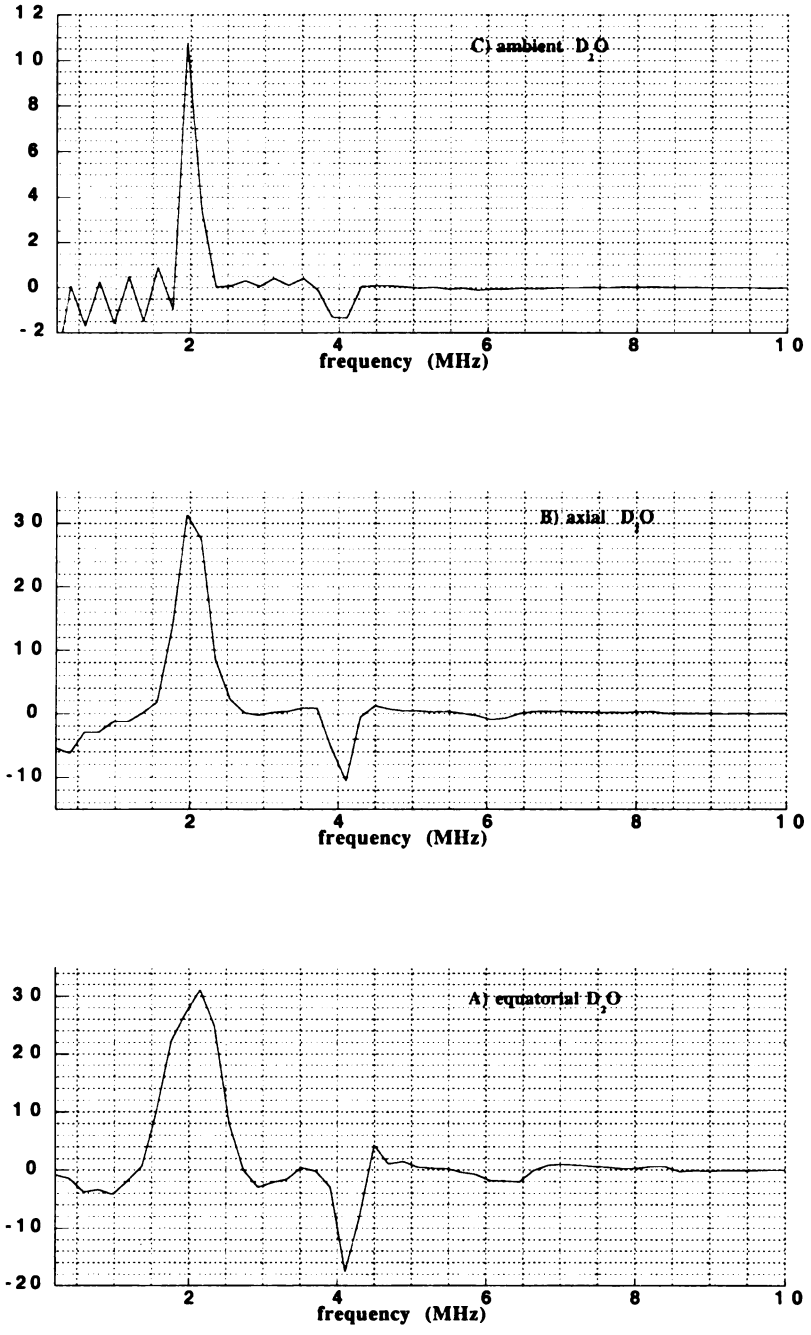

Figure 5.10. Broadening of the fundamental frequency as function of distance of water deuterons. Traces, (A) equatorial, B) axial and, C) ambient D_2O, are Fourier transform of the simulations shown in Figure 5.3.

bound water ligand. The damping of the lower frequency, 2MHz, modulation is matched best by the predicted function for the ambient water simulations. Overall, the ESEEM data were best fit by a simulated function that takes into account the contribution of a distribution of ambient water from r_{eff} = 4.0Å to 8.6Å in addition to one axial and one equatorial water. This simulation is given in Figure 5.11A (dotted line).

Another way of discriminating the contributions of deuterium coming from axial water from those due to equatorial water is to ratio the relative amplitudes of the fundamental ^2H frequency (2 MHz) and sum-combination frequency (4 MHz) as measured from the ESEEM spectra and described by Hegg *et al.*[16] The ratio technique is based on the broadening effect of the electron-nuclear hyperfine interaction on the fundamental frequency of ^2H. Because the sum-combination feature is broadened only by the small NQI of deuterium, it provides an internal standard for gauging the damping or the linewidth of the fundamental frequency. For T1D Fet3p, the experimental $\nu_D/2\nu_D$ ratio is 4.1, well outside the range of ratios given for several water coordination schemes listed in Table 1 of the paper by Hegg *et al.*. According to that work, an equatorial D_2O should give a $\nu_D/2\nu_D$ ratio of about 1.5, an axial D_2O, 2.5, and a combination of the two, 2.0. The large $\nu_D/2\nu_D$ observed here could be attributed to the contribution of a large population of ambient water that was not taken into account by Hegg *et al* in their calculations.

A tabulation of the theoretical $\nu_D/2\nu_D$ peak ratios that includes the effect of ambient water is given in Table 5.1. Ambient water is assumed to be uniformly distributed [$n_i = (4\pi/3)(\rho_N)(r^3_{i+i}-r^3_i)$] in a series of ten concentric non-coordinating

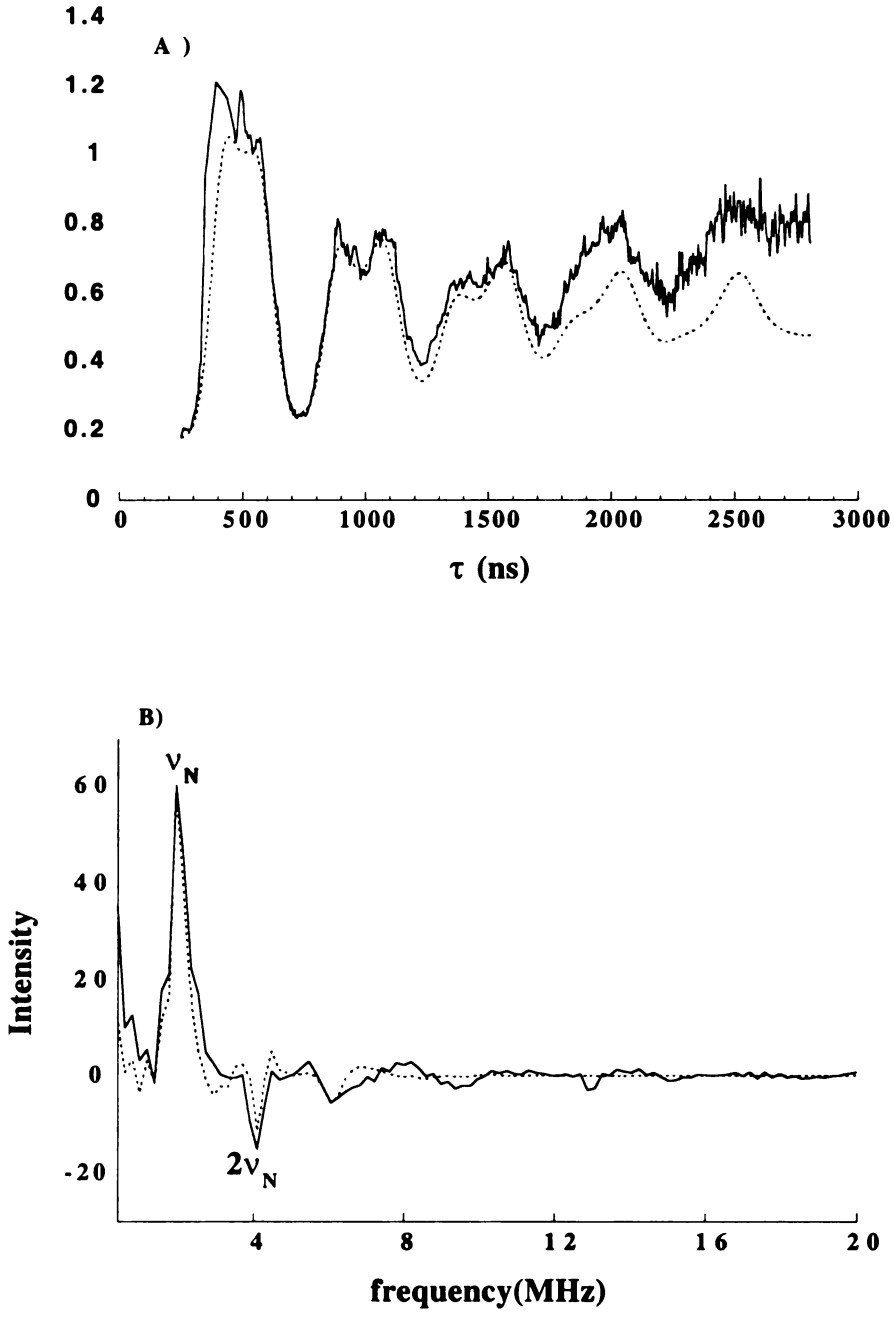

Figure 5.11. Computer simulation (dotted) of (A)time and (B)frequency domain ^{2}H-ESEEM data (solid) of T1D Fet3p. Calculated ESEEM traces assume a product of the modulation function of one axial D_2O, one equatorial D_2O and a distribution (n_i = $(4\pi/3)(\rho_N)(r^3_{i+i}-r^3_i)$) of ambient D_2O.

Table5.1. Tabulated ratios of the amplitudes of the peaks at the deuterium Larmor frequency (ν_D) with the corresponding sum combinations peaks at twice the Larmor frequency. Peak amplitudes were measured directly from ESEEM frequency. The distribution of ambient water was modelled assuming the nearest non-coordinating water to be 4.0Å from the Cu center and $n_i = (4\pi/3)(\rho_N)(r^3_{i+i}-r^3_i)$.

Model	$\frac{\text{Peak at 2 MHz}}{\text{Peak at 4 MHz}}$
Type -1 depleted Fet3 (expt.)	4.0
One axial D_2O	2.8
One equatorial D_2O	1.7
One equatorial and one axial D_2O	2.0
one axial/distribution of water	7.5
one equatorial/distribution of water	3.8
One equatorial/one axial/distribution of water	4.1

shells. The ratio, 4.1, that is closest to the experimental peak ratio, 4.0, corresponds to the modulation function that results from a contribution of one equatorial water, one axial water and a distribution of ambient water. The effect of one ambient water on the modulation function is negligible, however, the cumulative effect of a large population of ambient waters will greatly affect the resulting modulation function so that the effects of strong dipolar interaction (from bound waters) on the $\nu_D/2\nu_D$ ratios are partially masked. Therefore, unlike the Cu-substituted TfdA protein studied by

Hegg *et al*, the type 2 Cu(II) in Fet3p is more open to solvent water. This exposure, in turn, allows the solvent to have a more pronounced effect on the ^2H modulation.

5.4.4 Analysis of T2D Fet3p

The observed damping of the 2 MHz frequency in ^2H-ESEEM trace of T2D Fet3p (Fig. 5.3C) was modest indicating that an axial or ambient deuteron coupling was possible. Axial D_2O or OD^- coordination can be ruled out based on the observed depth of modulation and decay of the echo envelope. On the other hand, a single ambient water could not account for the experimental modulation depth, suggesting that a distribution of water molecules interacts with the type 1 Cu(II) also. Simulation (Figure 5.12) assuming a distribution of water with $n_i = (2\pi/3)(\rho_N)(r^3_{i+i}-r^3_i)$ reproduced the observed depth of modulation. The experimental $\nu_D/2\nu_D$ ratio is 8.1. From Table 2, the theoretical $\nu_D/2\nu_D$ ratio that correlates best with the observed ratio for T2D Fet3p corresponds to the simulation that assumes a contribution of ambient water distributed according to $n_i = (2\pi/3)(\rho_N)(r^3_{i+i}-r^3_i)$.

The simulation indicates that the type 1 Cu(II) in Fet3p has no covalently bonded water as would be predicted for this type of copper site. This is also supported by the absence of split peaks in the sum combination frequency of the proton two-pulse ESEEM of T2D fet3p (Figure 5.13). In contrast, the T1D fet3p has pronounced shift peak.

The nearest non-coordinating water is about 3.75 (± 0.25) Å from the metal center. The study by Mims, Davis and Peisach on the accessibility of type 1 copper sites to water suggests that the simulation that reproduced the depth of modulation of

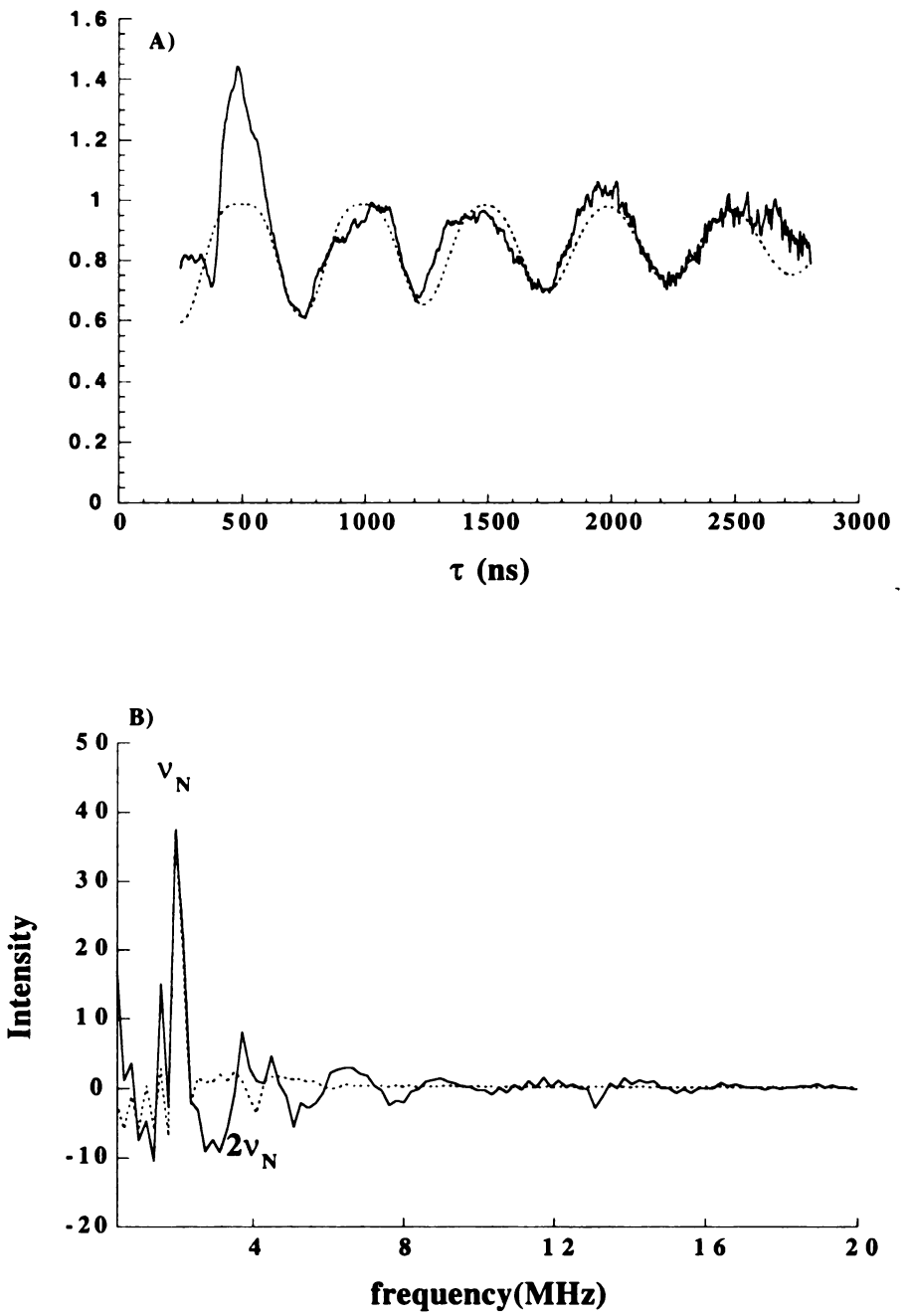

Figure 5.12. Computer simulation (dotted) of (A)time and (B)frequency domain ^{2}H-ESEEM data (solid) of T1D Fet3p. The ESEEM traces were generated using the modulation function of a distribution ($n_i = (2\pi/3)(\rho_N)(r^3_{i+i}-r^3_i)$) of ambient D_2O. No covalent waters were included.

Table 5.2. Experimental and stimulated peak ratios of the amplitude of the deuterium fundamental frequency to its sum-combination frequency for the type 1 center of Fet3.

Model	Nearest distance of ambient water to copper center (Å)	$\frac{\text{Peak at 2 MHz}}{\text{Peak at 4 MHz}}$
Type -2 depleted Fet3		8.1
Axial /distribution of water	4.0	6.2
Equatorial/distribution of water	4.0	4.1
Distribution of water (f=2π /3)	4.0	8.0
Distribution of water (f=2π /3)	3.7	7.9
Distribution of water (f=2π /3)	3.5	7.9

the type 1 Cu(II) in Fet3p corresponds to a geometric model in which one-half (surface) of the coordination sphere is exposed to ambient water (hemispherical model).[9] The absence of an OH^- or water ligation in type-1 copper and the limited access of water solvent to type-1 copper compared to type-2 copper might play a role in the tuning of reduction potential of type-1 copper. Water is a hard ligand and will favor Cu^{+2} over Cu^{+1}. A more hydrophobic environment would tend to stabilize Cu^{+1} because of its low charge. The more positive reduction potential would help facilitate the proposed electron transfer function of this metal cofactor.

5.5 Effect of Distal N-D on the Modulation Function

In both variants, the effect of the exchangeable proton of the remote nitrogen of the histidyl imidazole was also considered. The hyperfine coupling constant of

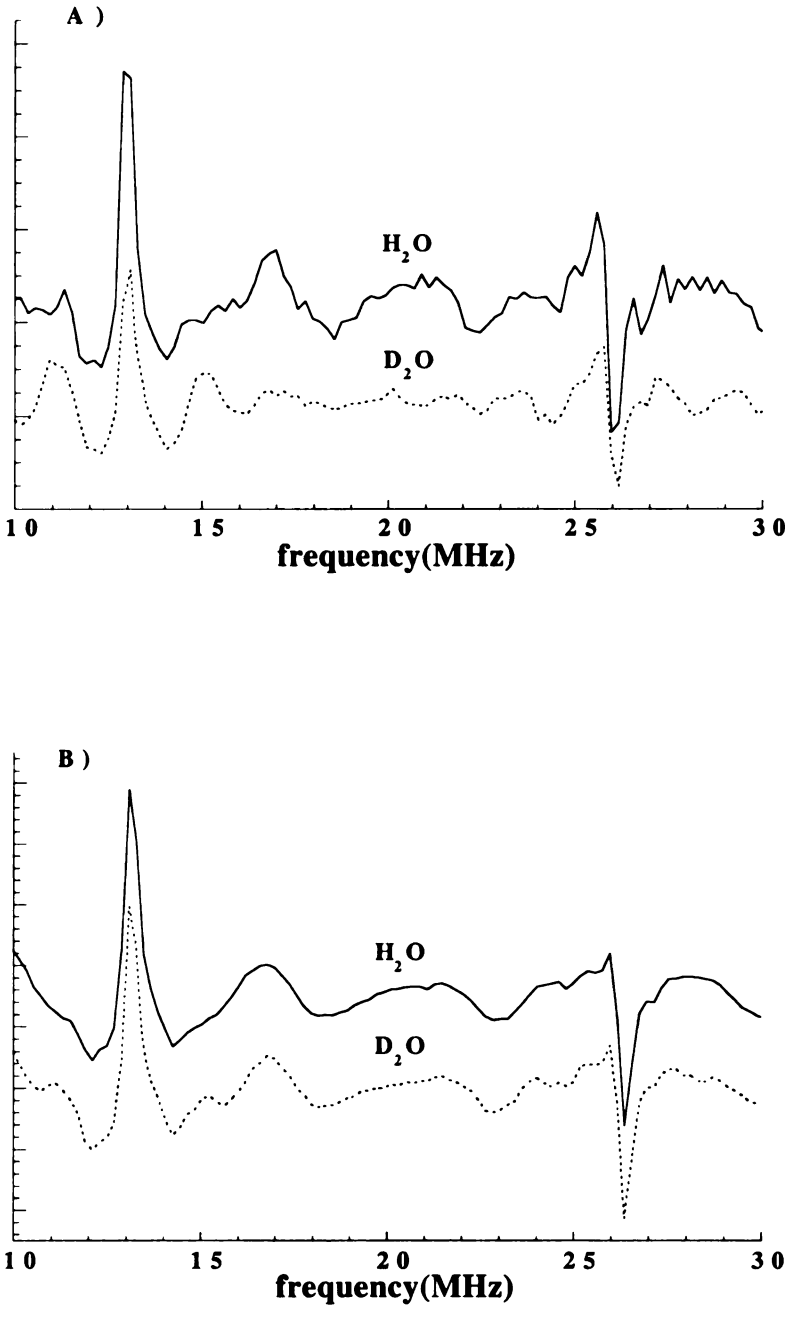

Figure 5.13 Frequency ESEEM data of T1D and T2D Fet3p in H_2O and D_2O buffer system showing only the modulation frequencies due to proton nucleus.

the exchangeable ^{1}H is predominantly isotropic ($A_{iso}(^{1}H) \leq 5.5$ MHz, $A_{iso}(^{2}H \leq 0.85$ MHz).[17,18] Assuming that the effective dipolar distance of the this hydrogen is about 6Å, the contribution of the through space interaction to the ^{2}H hyperfine coupling constant is 0.06 MHz. Thus, the effect of the exchangeable proton of the remote-imidazole nitrogen to the damping of the fundamental frequency of the ^{2}H is negligible compared to the contribution of the ambient water.

5.6 Summary and Conclusion

Combining the ^{14}N ESEEM results discussed in chapter 4 and the ^{2}H ESEEM in this chapter, structures of the type 1 and type 2 copper sites can be proposed. ESEEM measurements have allowed us to identify some of the type-1 and type-2 copper site ligands for the Fet3 protein. The type -2 copper has one strongly bound histidyl imidazole ligand, while the type-1 has two histidyl imidazole ligands as predicted by sequence analysis. Deuterium-exchange experiments show that both copper sites are solvent accessible and that ambient water must be included in the ESEEM analysis to account for the observed $\nu_D/2\nu_D$ ratios. Water is bound to type-2 copper at equatorial and axial positions. For the type-1 center, the deuterium modulation function is entirely due to the distribution of ambient water.

D_2O exchange experiment revealed that type 1 copper site in Fet3p is restricted to solvent access. Simulation of the two-pulse ESEEM data suggests the type 1 site assumes hemispherical model in which one-half of the surface is exposed to ambient to water. This model is consistent with the known protein structures that include type 1 copper sites. In all of these systems, the copper atom is shielded from

direct water coordination by the protein fold and associated side chain ligation. This shielding is irrespective of the coordination number, which can vary from three to five depending on the specific type 1 copper-containing protein. Among the multicopper oxidases this coordination number is either 3 (laccase, Lc)[19] or 4 (AO, hCp)[20-22]; the four-coordination in the latter two proteins is due to the thiosulfur of a Met residue that is replaced by Leu in laccase as it is in Fet3p. As discussed above, the type 1 Cu(II) site in Fet3p is most similar to that of laccase.

On the other hand, type 1 sites do differ in the extent to which they are buried in the protein. The type1 Cu site of azurin features histidine imidazole ligand whose distal (NE2) nitrogen is at the surface of the protein exposed to solvent. In azurin, the removal of this histidine by mutagenesis can be functionally complemented by addition of exogenous N-methylimidazole.[23,24] In azurin, there is strong support for the hypothesis that this imidazole is the site of entry of the electron from the reducing substrate.[25]

Structural analysis has shown that the corresponding histidine side chain in Lacasse, residue 494, is solvent exposed. In contrast, the type 1 Cu(II) site, and the homologous His1045 in hCp is completely buried (numbering referenced to the encoded ATG, not the processed protein). On the basis of sequence alignment and the known structures of Laccase, hCp, and AO, the potentially solvent-exposed type 1 Cu(II) ligand in Fet3p is His489. These features of the type 1 sites in Lac, hCp and Fet3p are illustrated in Scheme 1, structures A-C, respectively. The ESEEM data on the type 1 site in Fet3p indicate the coordinating imidazoles are not magnetically equivalent, perhaps due to differences in H-bonding. Furthermore, the presence of

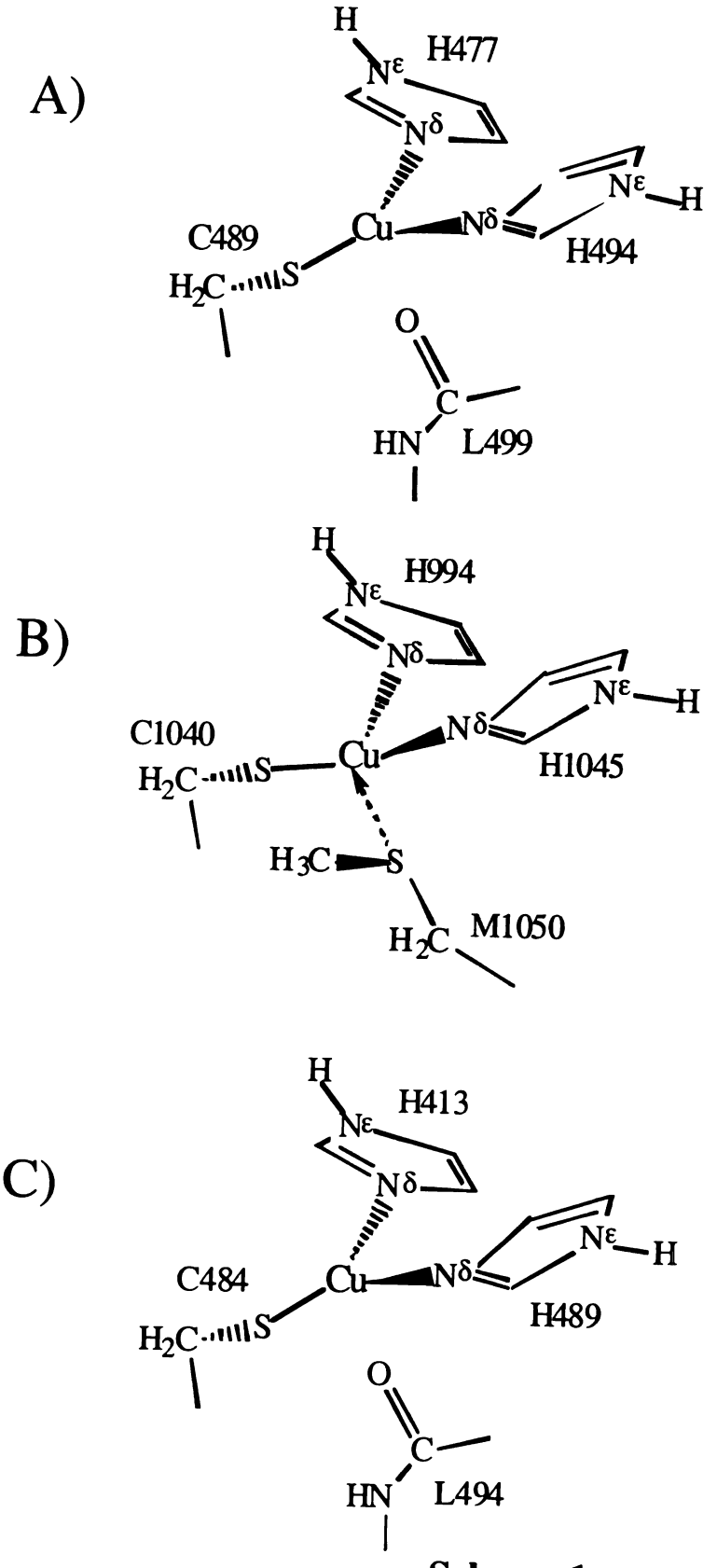
A)
H
Nε
H477
Nδ
Nε
H
C489
Cu
Nδ
H494
H2C
S
O
C
HN
L499
B)
H
Nε
H994
Nδ
Nε
H
C1040
Nδ
H2C
S
Cu
H1045
H3C
S
H2C
M1050
C)
H
Nε
H413
Nδ
Nε
H
C484
Cu
Nδ
H2C
S
H489
O
C
HN
L494

Scheme 1

significant ambient water, most likely distributed asymmetrically, suggests that this site in Fet3p (structure C)is more similar to the type 1 site in Laccase (structure A) and more exposed to solvent than the corresponding site in hCp (structure B). Thus, the unique activity that hCp and Fet3p have towards Fe(II) as the reducing substrate does not obviously depend on a strictly homologous and unique type 1 copper site. Indeed, given the apparent differences between the Fet3p and hCp type 1 sites, that would likely be reflected in differences in reduction potential and electron transfer rates, the two enzymes may very likely use a different mechanism of electron transfer from the Fe(II) substrate. If this is true, then the specificity these two enzymes have towards Fe(II) would have to arise from features of the proteins and not the nature of the "active sites." Lindley and co-workers have presented some evidence in support of a model that this activity is due to a specific $Fe^{2+/3+}$ binding site in an Asp/Glu-rich channel adjacent to His1045.[26] However, this hypothesis has not been experimentally tested further.

In summary, the ^{14}N and ^{2}H ESEEM data conform to an asymmetrically solvent-exposed model of the type 1 Cu(II) site in Fet3p in two ways. First, the distal N-H of His489 would be in a hydrophilic environment, most likely H-bonded to solvent. In contrast, the second histidine imidazole at this site, from His413 based on sequence alignment, would be buried in a non-polar environment that was solvent inaccessible. This would account for the asymmetry ascribed to the two histidine imidazoles at the Fet3p type 1 Cu(II) site by the ESEEM analysis outlined above. Furthermore, the solvation of the HE2 proton on His489 would account for the presence of the ambient water required by the ^{2}H-ESEEM simulations.

The ESEEM measurements were perhaps most revealing about the type 2 copper site in Fet3p. The data indicate that this copper has only one strongly bound, equatorial histidine imidazole ligand. On the other hand, sequence analysis showed that Fet3p contained both His residues found at the type 2 sites in the other multicopper oxidases. Furthermore, the crystal structures of two of them, AO and hCp, provided strong evidence for equatorial coordination by both of these side chains. The structure of AO also indicated the presence of a single equatorial water molecule bound at the type 2 Cu(II). In contrast, the ESEEM data are best fit by a model that has two water molecules bound directly to the type 2 Cu(II) in Fet3p. One of these waters is bound at an equatorial position while the other appears to be axial.

Although we found only one histidine strongly bound to the type 2 Cu(II) in Fet3p, a second histidine might be axially coordinated. Even if this were the case, however, the structure of the Fet3p type 2 site would be markedly different than what is seen in the crystal structures of its homologs. In both AO and hCp, the N-Cu-N atoms define a plane. Thus, in these proteins the histidine imidazoles are either both equatorial or both axial; most certainly they are the former. As noted above, the structure of AO indicates also the presence of a coordinated water that could be either equatorial or axial, again depending on the axis assignment. Reasonably, the occupancy by water of an equatorial site might be sufficiently larger than at an axial one and thus be sufficiently electron dense for detection by x-ray crystallography. A model that depicts the type 2 Cu(II) coordination in AO is shown in Scheme 2, structure A. In contrast, the ESEEM analysis strongly indicates that the type 2 Cu(II) in Fet3p has one equatorial histidine imidazole, one equatorial water, one axial water,

and potentially an additional axial histidine. This is a new view of the type 2 Cu(II) in a trinuclear cluster. It is illustrated in Scheme 2, structure B.

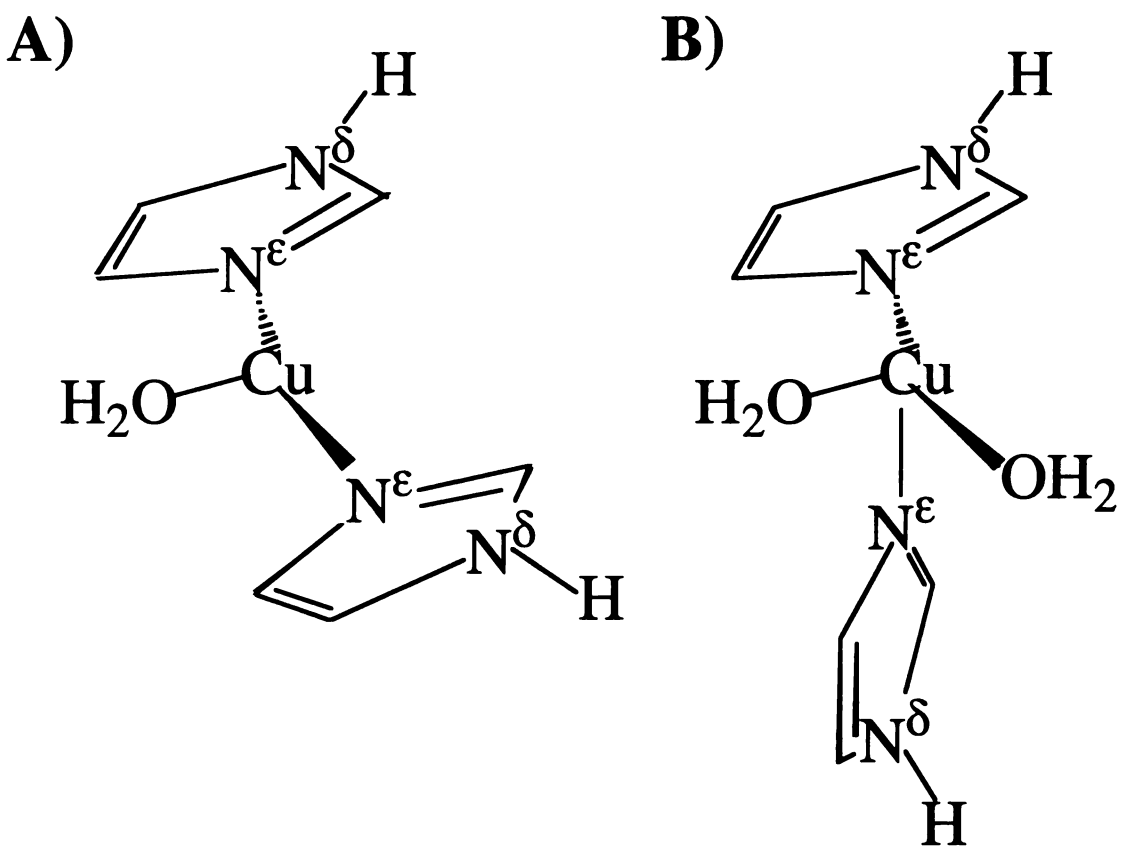

Scheme 2

List of References

1)Mims, W. B. *Phys. Rev. B* **1972**, *5*, 2409-2419.

2)Tyryshkin, A. M.; Dikanov, S. A.; Goldfarb, D. *J. Magn. Reson.* **1993**, *A 105*, 271-283.

3)Lee, H.-I.; McCracken, J. *J. Phys. Chem.* **1994**, *98*, 12861-12870.

4)Atherton, N. M. *Mol. Phys.* **1979**, *37*, 1349-1361.

5)Gerfen, G.; Hanna, P.; Chasteen, N. D.; Singel, D. J. *J. Am. Chem. Soc.* **1991**, *113*, 9513-9519.

6)McCracken, J.; Friedenberg, S. *J. Phys. Chem.* **1994**, *98*, 467-473.

7)Tyryshkin, A. M.; Dikanov, S. A.; Evelo, R. G.; Hoff, A. J. *J. Chem. Phys.* **1992**, *97*, 42-49.

8)Reijerse, E. J.; Dikanov, S. A. *J. Chem. Phys.* **1991**, *95*, 836-845.

9)Mims, W. B.; Davis, J. L.; Peisach, J. *Biophys. J.* **1984**, *45*, 755-766.

10)McCracken, J.; Peisach, J.; Dooley, D. M. *J. Am. Chem. Soc.* **1987**, *109*, 4064-4072.

11)McCracken, J.; Shin, D.; Dye, J. L. *Appl. Magn. Reson.* **1992**, *3*, 305-316.

12)Dikanov, S. A.; Shubin, A. A.; Parmon, V. N. *J. Magn. Reson.* **1981**, *42*, 474-487.

13)Mims, W. B.; Davis, J. L. *J. Chem. Phys.* **1976**, *64*, 4836-4846.

14)Mims, W. B.; Peisach, J.; Davis, J. L. *J. Chem. Phys.* **1977**, *66*, 5536-5550.

15)Waldstein, P.; Rabideau, S. W.; Jackson, J. A. *J. Chem. Phys.* **1964**, *41*, 3407-3411.

16)Hegg, E. L.; Whiting, A. K.; Saari, R. E.; McCracken, J.; Hausinger, R. P.; Que, L. J. *Biochemistry* **1999**, *38*, 16714-16726.

17)Van Camp, H. L.; Sands, R. H.; Fee, J. A. *J. Chem. Phys.* **1981**, *75*, 2098-2107.

18)Roberts, J. E.; Cline, J. F.; Lum, V.; Freeman, H.; Gray, H. B.; Peisach, J.; Reinhammer, B.; Hoffman, B. *J. Am. Chem. Soc.* **1984**, *106*, 5324-5330.

19)Ducros, V.; Brozowski, A. M.; Wilson, K. S.; Brown, S. H.; Ostergaard, P.; Schneider, P.; Yaver, D. S.; Pedersen, A. H.; Davies, G. J. *Nat. Struct. Biol.* **1998**, *5*, 310-316.

20)Messerschmidt, A.; Rossi, A.; Ladenstein, R.; Huber, R.; Bolognesi, M.; Gatti, G.; Marchesini, A.; Petruzelli, R.; Finazzi-Agro, A. *J. Mol. Biol.* **1989**, *206*, 513-529.

21)Messerschmidt, A.; Ladenstein, R.; Huber, R.; Bolognesi, M.; Avigliano, L.; Petruzzelli, R.; Rossi, A.; Finazzi-Agro, A. *J. Mol. Biol.* **1992**, *224*, 179-205.

22)Zaitzeva, I.; Zaitzev, V.; Card, G.; Moshkov, K.; Box, B.; Ralph, A.; Lindley, P. *J. Biol. Inorg. Chem.* **1996**, *1*, 15-23.

23)den Blaauwen, T.; Kamp, v. d.; Canters, G. W. *J. Am. Chem. Soc.* **1991**, *113*, 5050-5052.

24)den Blaauwen, T.; Canters, G. W. *J. Am. Chem. Soc.* **1993**, *115*, 1121-1129.

25)van de Kamp, M.; Floris, R.; Hali, F. C.; Canters, G. W. *J.Am. Chem. Soc.* **1990**, *112*, 907-908.

26)Lindley, P. F.; Card, G.; Zaitseva, I.; Zaitsev, V.; Reinhammar, B.; Selin, L.; Yoshida, K. *J. Biol. Inorg. Chem.* **1997**, *2*, 454-463.